Simon Pöllath

Reciprocal and real space imaging of static and dynamically excited magnetic skyrmions and chiral magnetic textures

Dissertation

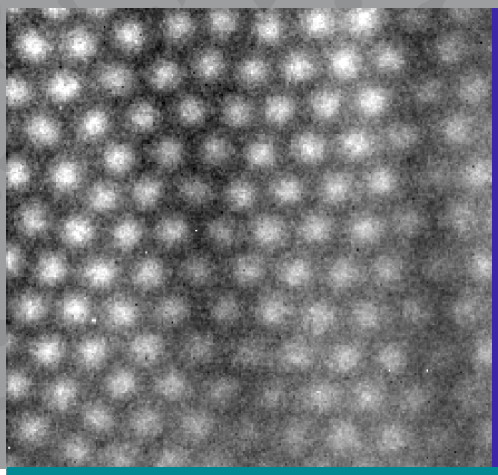

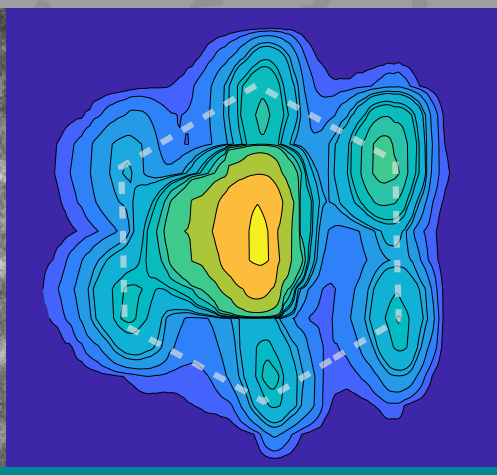

Universität Regensburg

FAKULTÄT FÜR PHYSIK

Reciprocal and real space imaging of static and dynamically excited magnetic skyrmions and chiral magnetic textures

DISSERTATION ZUR ERLANGUNG DES DOKTORGRADES DER NATURWISSENSCHAFTEN (DR. RER. NAT.) DER FAKULTÄT PHYSIK

DER UNIVERSITÄT REGENSBURG

vorgelegt von *Simon Pöllath*
aus Weiden i.d.OPf.

im Jahr 2020

Promotionsgesuch eingereicht am:	06.07.2020	
Die Arbeit wurde angeleitet von:	Prof. Dr. Josef Zweck	
Prüfungsausschuss:	Vorsitzender:	PD Dr. J. D. Urbina
	1. Gutachter:	Prof. Dr. J. Zweck
	2. Gutachter:	Prof. Dr. C. Back (TUM)
	Weiterer Prüfer:	Prof. Dr. D. Weiss
Datum Promotionskolloquium:	22.10.2020	

Contents

1 Introduction

In 2009, Mühlbauer et al. reported the first experimental observation of magnetic skyrmions in the material MnSi with small angle neutron scattering (SANS) [1]. Since then, skyrmion research developed to a large and active field in solid state physics with a total of over 2500 publications up to June 2020.

So what is a magnetic skyrmion? In a nutshell, it is a particular alignment of the magnetization vector field $\boldsymbol{M}(\boldsymbol{r})$ of a ferromagnetic material. The spin structure of a skyrmion is depicted in Fig. 1.1. As can be seen, the magnetization in the center is aligned antiparallel to the magnetization at the edges of the skyrmion. In between lies the skyrmion wall, where the spin structure is reminiscent of a vortex or whirl. The reason for the great interest in this peculiar structure lies in its extraordinary properties. First of all, typical skyrmion sizes are in the order of 10 to 100 nm, which makes them usable in nano-scaled devices. Considering magnetic storage, the small size allows to use skyrmions as information carriers with a large data density [2–4]. Along with that, the skyrmion has an inherent topological protection, which means that its spin structure is protected from external influences like thermal fluctuations by a finite energy barrier. This is beneficial as a potential information carrier needs to possess a data retention at room temperature of more than 10 years [5]. Further, skyrmions can be moved by electrical currents, temperature gradients and magnons which provides a large set of interaction [6–8]. For the electrical case, the critical current density at which the skyrmions start to move can be as low as $1 \times 10^6\,\mathrm{A\,m^{-2}}$, which represents an energy efficiency that could meet the requirement of today's electronics that focus more and more on mobility and eco-friendliness [9].

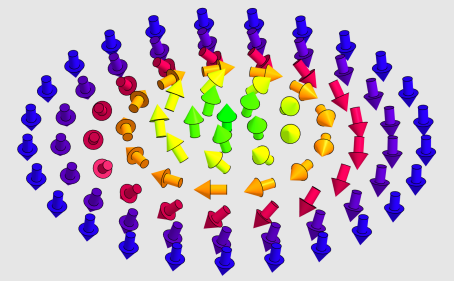

Fig. 1.1.: Magnetization structure of a skyrmion.

A variety of applications that utilize the unique properties of the skyrmions have been proposed. The most prominent one is the skyrmion racetrack [10–15]. Different concepts exist - a common design is a strip of skyrmion-hosting material with a width in the order of the skyrmion size. An electrical current is sent through the strip which pushes a train of skyrmions through it. The individual skyrmions in the train act as information carriers and effectively make the device a shift register.

There are also different proposals like the use of a skyrmion as a nano-oscillator, which uses the skyrmion eigenmodes to produce on-chip microwave signals [16–19]. Other ideas aim at the established semiconductor industry and propose to construct skyrmion based logic devices or skyrmion transistors [18, 20].

Admittedly, the feasibility of these concepts is still to be proven, however, important steps have been made towards a real application. While the skyrmions found first required a temperature below 30 K, today, materials are known that host skyrmions even beyond room temperature [21–25]. In fact, a whole zoo of different skyrmion types, with structures that deviate from the one shown in Fig. 1.1, has been experimentally discovered [22, 26–29]. The lifetime of skyrmions was further explored and entropy-related limitations of the topological energy barrier were reported [30–34]. Additionally, multiple ways to create or delete skyrmions with electrical current/heat pulses or with externally-applied magnetic field protocols have been found [21, 31, 35–39]. The skyrmion motion induced by electrical and magnon currents as well as magnetic field gradients has been studied [9, 40–43] and the skyrmion eigenmodes were identified and measured [44–47].

Undoubtedly, Lorentz transmission electron microscopy (LTEM) played an important role in achieving these goals as it emerged as one of the most important real-space skyrmion imaging techniques [48]. It is also a large part of this thesis. The other experimental part shows resonant elastic X-ray scattering (REXS) off skyrmions which was further combined with ferromagnetic resonance (FMR) measurements [49–51].

This thesis consists of three parts. The first one introduces the fundamental theoretical concepts of magnetism that is necessary to understand the energetic origin of skyrmions and the subsequent parts. A selection of magnetic phases that are observed in skyrmion hosting materials is presented. In the second part, reciprocal space measurements in terms of REXS on the material Cu_2OSeO_3 are presented. It starts with the theoretical basics of the technique. Then, static REXS measurements of the magnetic phases of Cu_2OSeO_3 are shown. Finally, the REXS technique is extended with FMR experiments which allows to study the system's magnetic resonances with an unambiguous assignment to the magnetic phase. This novel technique is called REXS-FMR. The third part of the work covers real space imaging of magnetic skyrmions in terms of LTEM. A theoretical introduction of the used LTEM techniques is given. A model that describes the LTEM contrast formation is applied to the skyrmion texture and ways to extract its structural parameters from LTEM measurements are given. Finally, LTEM measurements on Cu_2OSeO_3 and room-temperature skyrmion hosting Pt/Co/W and Pt/Co/Tb multilayer stacks are presented. Each chapter begins with its own introduction which gives a more detailed overview of the respective contents.

2 Theoretical concepts

This chapter introduces the fundamental theoretical concepts to understand the essential magnetic concepts of chiral magnetic textures. It starts off by introducing the micromagnetic energies that are responsible for the formation of the chiral magnetic structures investigated experimentally. The different energy terms are combined successively which will lead to different chiral magnetic ground states. The individual properties of the structures are explained alongside. These elaborations are then put in a thermodynamic context by the discussion of the magnetic phase diagrams (by means of externally applied magnetic fields and finite temperatures) of the chiral magnetic materials studied in this work.

Finally, the magnetostatic considerations are supplemented by dynamical aspects with the introduction of the Landau-Lifshitz-Gilbert equation. It describes the magnetization's temporal evolution outside of its equilibrium state.

2.1 Magnetism of magnetic skyrmions

2.1.1 Micromagnetic energies

In this section, the micromagnetic energies are introduced that occur in the magnetic systems that are investigated in this thesis. The interplay of those contributions are responsible for the complex spin formations in chiral magnetic phases introduced in section 2.1.2 and help to interpret the experimental results.

To theoretically describe a chiral magnet that hosts different magnetic phases, an extended Hamiltonian within a classical 3D Heisenberg model is used. For this, a three dimensional set of lattice sites i with an associated dimensionless unit spin vector $\hat{\boldsymbol{S}}_i$ is assumed. The interaction between two lattice sites i and j consists of various energy terms expressed via some atomistic terms which will be introduced in this section. In this work only magnetic structures that show smooth variations of $\hat{\boldsymbol{S}}$ or the magnetization $\boldsymbol{M}$ across many lattice sites are investigated. In chiral magnets, the magnetic modulation length describes the distance at which the magnetization $\boldsymbol{M}$ has performed a full rotation. As an example, the skyrmion hosting material Cu_2OSeO_3, discussed in sections 3.2 or 4.3, possesses a magnetic modulation length of $\approx 62\,\mathrm{nm}$, which represents a line density of 278 magnetic moments per modulation length, resulting in an angular variation of $\approx 23\,\mathrm{mrad/lattice\ site}$ [52–54]. In such

cases, a continuum formulation of the individual atomistic energy terms is desirable and will be given alongside. Continuum theory allows for micromagnetic simulations on system sizes that greatly exceed the computational capabilities of atomistic simulations.

Exchange interaction

The most famous spin interaction when considering ferromagnets is probably the Heisenberg exchange energy [55]

$$H = -\frac{1}{2}\sum_{\substack{i,j \\ i\neq j}} J_{ij}\hat{\boldsymbol{S}}_i \cdot \hat{\boldsymbol{S}}_j \ . \tag{2.1}$$

As already mentioned $\hat{\boldsymbol{S}}_i$ is the atomic spin operator associated to lattice site i and J_{ij} is the exchange integral that defines the type of exchange coupling between lattice sites i and j. That leads to a parallel spin alignment (ferromagnetic, see Fig. 2.1A) for positive and antiparallel alignment (antiferromagnetic) for negative J_{ij}. This energy is the outcome of an interplay between Coulomb interaction and the Pauli exclusion principle. The latter dictates that the total wave function consisting of orbital and spin wave functions for two electrons must be antisymmetric under exchange of electrons (fermions) [56, 57]. For an antisymmetric orbital wave function, the average distance of two electrons is larger compared to the symmetric case because the antisymmetric wave function becomes zero for identical electron positions. Because of this, the Coulomb energy is reduced and a symmetric spin-wave function with parallel spins is preferred. This effect is countered by an increased kinetic energy of the antisymmetric orbital wave function which is spatially more confined due to the electron's mutual avoidance. Therefore only systems where the gain in Coulomb energy wins over the loss in kinetic energy will become ferromagnetic. Above the critical Curie temperature T_c, the ferromagnetic order is destroyed by thermal fluctuations and a paramagnet is obtained [5, 56–59].

The Heisenberg exchange interaction is insufficient for the description of a chiral magnet and the general expression for a two-site exchange energy

$$H_\mathrm{ex} = -\frac{1}{2}\sum_{\substack{i,j \\ i\neq j}} \hat{\boldsymbol{S}}_i^\dagger \boldsymbol{J}_{ij}\hat{\boldsymbol{S}}_j \ , \tag{2.2}$$

needs to be used [60]. Here $\boldsymbol{J}_{ij}$ is the general exchange tensor which can be decomposed into

$$\boldsymbol{J}_{ij} = J_{ij}\boldsymbol{I} + \boldsymbol{J}_{ij}^\mathrm{as} + \boldsymbol{J}_{ij}^\mathrm{s} \ . \tag{2.3}$$

The first part is the isotropic exchange from Eq. (2.1) with the identity tensor $\boldsymbol{I}$. The discrete isotropic exchange constant $J_{ij} = \frac{1}{3}\,\mathrm{Tr}(\boldsymbol{J}_{ij})$ is the dominant term and is usually in the order of 10 to 100 meV [60]. The second part is the anisotropic antisymmetric exchange tensor that is given by

$$\boldsymbol{J}_{ij}^{\mathrm{as}} = \frac{1}{2}\left(\boldsymbol{J}_{ij} - \boldsymbol{J}_{ij}^{\dagger}\right) . \tag{2.4}$$

Finally, the traceless anisotropic symmetric exchange tensor is defined by

$$\boldsymbol{J}_{ij}^{\mathrm{s}} = \frac{1}{2}\left(\boldsymbol{J}_{ij} + \boldsymbol{J}_{ij}^{\dagger}\right) . \tag{2.5}$$

In the following, only isotropic and antisymmetric exchange will be considered, as they sufficiently describe the investigated systems [60]. In fact, Eq. (2.3) can be obtained from a tight binding model with spin-orbit coupling as small perturbation with the three terms given in Eq. (2.3) being the zeroth to second order terms of perturbation [5, 61].

Isotropic symmetric exchange interaction

As already mentioned, the first part of the expansion (2.3) resembles isotropic exchange interaction given in Eq. (2.1). Assuming ferromagnetic ordering and a smooth variation of the spins, a continuum version of (2.1) can be formulated. For this, only nearest neighbor interaction is considered and homogeneous exchange, i.e. $J_{ij} = J$, is assumed. The resulting continuum exchange energy is then [56, 57]

$$E_{\mathrm{ex}} = A_{\mathrm{ex}} \int_V \left[(\nabla m_x)^2 + (\nabla m_y)^2 + (\nabla m_z)^2\right] \,\mathrm{d}V . \tag{2.6}$$

Here, the spins were replaced by the unit magnetization vector $\boldsymbol{m} = \boldsymbol{M}/M_{\mathrm{s}}$ with saturation magnetization M_{s}. The isotropic exchange constant is given by $A_{\mathrm{ex}} = JS^2 Z_{\mathrm{nn}}/2a_{\mathrm{nn}}$ with nearest neighbor count Z_{nn} and distance a_{nn} which is valid for simple cubic (sc), body centered cubic (bcc) and face centered cubic (fcc) lattices [56]. Naturally, this energy is minimized by a uniform magnetization configuration.

Dzyaloshinskii-Moriya interaction

In Eq. (2.3), the anisotropic antisymmetric exchange interaction appears as a first order perturbation term which was shown by Moriya in 1960 but was already empirically found by Dzyaloshinskii in 1957 [5, 61, 62]. This is why the antisymmetric exchange interaction is also called Dzyaloshinskii-Moriya interaction (DMI). Mag-

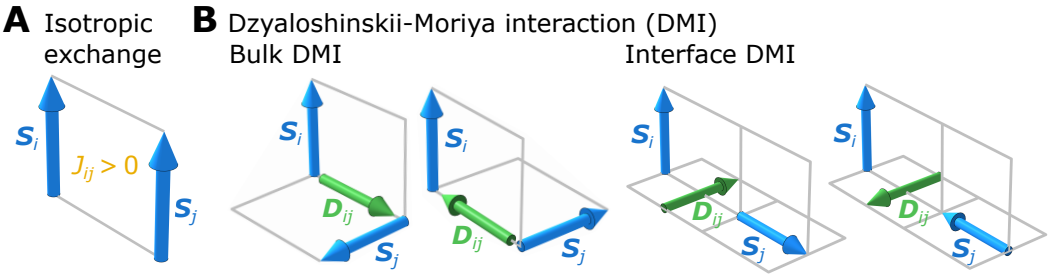

Fig. 2.1.: Preferred spin orientation for **(A)** isotropic direct exchange interaction with $J_{ij} > 0$ (ferromagnetic) and **(B)** DMI for orientations of $\boldsymbol{D}_{ij}$ along the connection vector of the lattice sites (bulk DMI) and perpendicular to it (interface-DMI).

netic systems with DMI therefore must show spin-orbit coupling. The affiliated tensor introduced in Eq. (2.4) can be rewritten as

$$\boldsymbol{J}_{ij}^{\mathrm{as}} = \begin{pmatrix} 0 & -D_{ij}^{z} & D_{ij}^{y} \\ D_{ij}^{z} & 0 & -D_{ij}^{x} \\ -D_{ij}^{y} & D_{ij}^{x} & 0 \end{pmatrix} , \tag{2.7}$$

with the definition of the DMI-vector $\boldsymbol{D}_{ij} = \left(D_{ij}^{x}, D_{ij}^{y}, D_{ij}^{z}\right)^{\mathsf{T}}$. The corresponding DMI-energy E_{DMI} can then be expressed as a scalar product of $\boldsymbol{D}_{ij}$ with the cross product of interacting spin pairs i and j which gives the commonly known term that was also found by Dzyaloshinskii

$$E_{\mathrm{DMI}} = -\frac{1}{2} \sum_{\substack{i,j \\ i \neq j}} \boldsymbol{D}_{ij} \left(\hat{\boldsymbol{S}}_i \times \hat{\boldsymbol{S}}_j \right) . \tag{2.8}$$

In general, this interaction favors perpendicular alignment of $\hat{\boldsymbol{S}}_i$ and $\hat{\boldsymbol{S}}_j$ and changes sign upon spin exchange. The latter is a very important feature as it leads to a preferred spin winding direction or preferred chirality, which is eponymous for the chiral magnets investigated in this thesis.

The key ingredient that defines the resulting spin texture is the magnitude and orientation of the DMI-Vector $\boldsymbol{D}_{ij}$. In order to obtain $\boldsymbol{D}_{ij} \neq 0$, the central point of the lattice sites i and j cannot be a center of inversion. Such magnetic systems are said to have a broken inversion symmetry. The orientation of $\boldsymbol{D}_{ij}$ can essentially be derived from symmetry arguments. Precise rules for this can be found in the work of Moriya [61] or more detailed work [5]. Note that unlike the usually homogeneous exchange interaction with the scalar J, $\boldsymbol{D}_{ij}$ strongly depends on the lattice sites i and j. There is not just a single DMI vector for a whole sample. Fortunately, the complex rules can be condensed into two major classes of DMI that already cover

the description of an essential part of known skyrmion hosting materials and the materials investigated in this thesis.

The first type of DMI can be found in materials that belong to the non-centrosymmetric space group $P2_13$ of the B20-compounds. Here, the inversion symmetry is broken by the crystal lattice geometry itself. The most prominent examples for materials in this class are the metal MnSi [1], the semiconductor $Fe_xCo_{1-x}Si$ [48, 63], the metal FeGe [64] or the multiferroic insulator Cu_2OSeO_3[1] [52, 54, 66]. For these systems, $\boldsymbol{D}_{ij}$ is parallel to the connection vector of interacting lattice sites, which is usually referred to as bulk DMI. The preferred orientations for two spins that only interact via bulk DMI is shown on the left side of Fig. 2.1B. As can be seen, the sign of $\boldsymbol{D}_{ij}$ determines the rotational sense (chirality) of the system. As before, a continuum approximation of the bulk DMI can be obtained by only considering nearest neighbor interaction and a uniform DMI vector length $D_{ij} = D$. The resulting energy reads

$$E_{\mathrm{DMI}}^{\mathrm{bulk}} = D_{\mathrm{bulk}} \int_V [\boldsymbol{m} \cdot (\nabla \times \boldsymbol{m})] \, \mathrm{d}V \, . \tag{2.9}$$

The bulk DMI constant is given by $D_{\mathrm{bulk}} = -DS^2/a_{\mathrm{nn}}^2$ for a continuum formulation on a simple cubic lattice.

The second type of DMI is found in thin multi-layers of magnetic materials. Here, the inversion symmetry of the lattice is broken at the interface of the magnetic material, due to the change in type or structure of neighboring atoms. Therefore, it is called interface-DMI. Examples that show interface-DMI are polycrystalline thin-film stacks of Pt/Co/(Ir,Tb,W,Ta) [25, 38, 67–69] or ultrathin films of Ni/Fe/Cu(001) [5]. From these examples, an important requirement is seen which is that the top and bottom adjacent materials of the magnetic layer must differ, as otherwise the mirrored geometry creates the exact same DMI with opposite sign as the other surface. This leads then to a DMI compensation. The DMI vectors of a system with interface-DMI is perpendicular to the connecting vectors of the lattice sites of two interacting spins. Furthermore, they lie inside the surface plane [5, 60]. The preferred spin alignment for the two possible directions of $\boldsymbol{D}_{ij}$ is shown on the right side of Fig. 2.1B. The continuum approximation for the interface-DMI energy of a cubic lattice interface is given by

$$E_{\mathrm{DMI}}^{\mathrm{int}} = D_{\mathrm{int}} \int_A [m_z \cdot \nabla \boldsymbol{m} - (\boldsymbol{m} \cdot \nabla) m_z] \, \mathrm{d}A \, . \tag{2.10}$$

[1] Cu_2OSeO_3 does not belong to the $P2_13$ space group, however the arrangement of the effective magnetic moments is the same as in the other B20 materials which allows an identical description [65].

Here, $D_{\mathrm{int}} = -DS^2/a_{\mathrm{nn}}$ is the interface-DMI constant and $\hat{\boldsymbol{z}}$ is parallel to the interface normal. Note that in this case, the integration is over the interface A, i.e. the integrand is a 2D energy density.

Zeeman energy

The Zeeman energy describes the fundamental interaction of a magnetic moment with an externally-applied magnetic field H_{ext} that has its minimum for parallel alignment. The Zeeman energy in continuum approximation reads

$$E_{\mathrm{Zee}} = -\mu_0 M_{\mathrm{s}} \int_V \boldsymbol{H}_{\mathrm{ext}} \cdot \boldsymbol{m} \, \mathrm{d}V \, . \tag{2.11}$$

Magnetic anisotropy

The energy of a uniformly magnetized system typically depends on its orientation with respect to the crystal structure. This phenomenon is called crystalline anisotropy and is the result of spin-orbit coupling, i.e. the coupling of the spin moment with the orbital moment. The latter has fixed directions relative to the crystal structure which may be caused by the crystal structure (magnetocrystalline anisotropy), interfaces/surfaces (interface/surface anisotropy) or crystalline strain (magnetoelastic anisotropy) [57].

The essential results from these different types of anisotropy are uniaxial and cubic anisotropy. Uniaxial anisotropy energy in continuum approximation is given by

$$E_{\mathrm{a,u}} = K_{\mathrm{u}} \int_V \left[1 - (\boldsymbol{m} \cdot \hat{\boldsymbol{u}})^2\right] \, \mathrm{d}V \, , \tag{2.12}$$

and describes the preferred orientation of $\boldsymbol{m}$ along the unit vector $\hat{\boldsymbol{u}}$ with uniaxial anisotropy constant K_{u} [57].

The cubic anisotropy energy reads

$$E_{\mathrm{a,c}} = K_{\mathrm{c}} \int_V \left(1 - m_x^4 - m_y^4 - m_z^4\right) \, \mathrm{d}V \, , \tag{2.13}$$

which expresses favored orientation of $\boldsymbol{m}$ along one of the cubic lattice vectors parallel to m_x, m_y or m_z. Note that these expressions need to be adjusted depending on the system's easy axes. An axis where $E_{\mathrm{a,u}}$ or $E_{\mathrm{a,c}}$ is minimal, is also referred to as an easy axis and the axis along maximal energy is referred to as a hard axis.

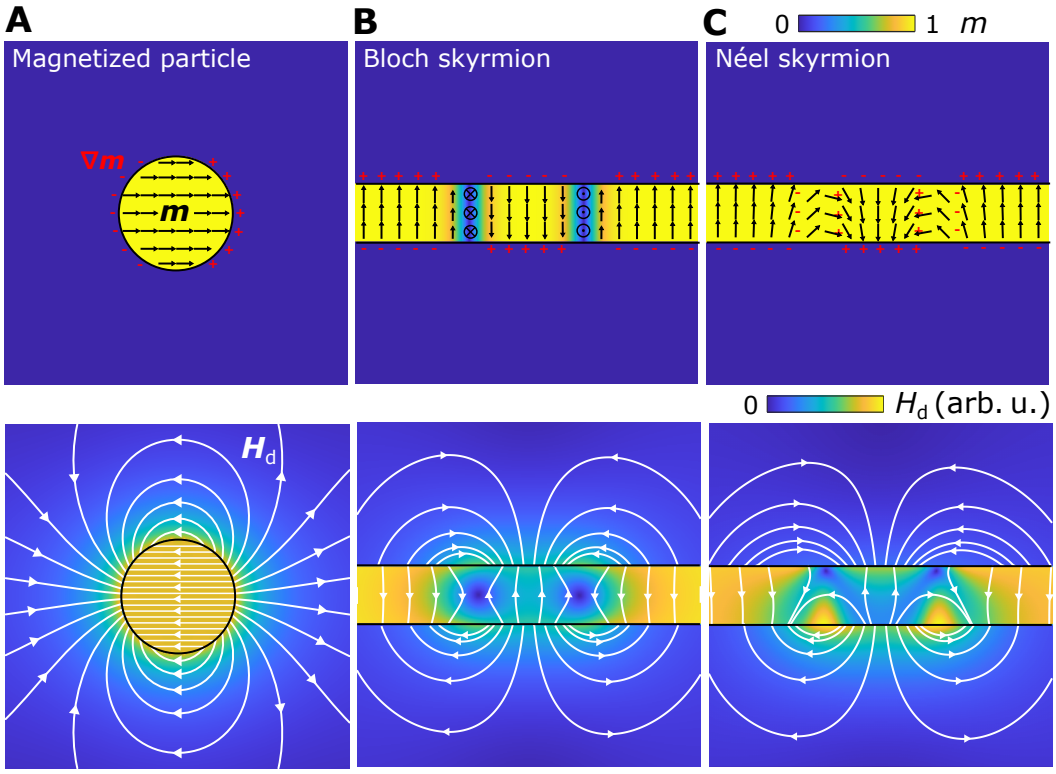

Fig. 2.2.: Three examples for spin magnetization structures producing magnetostatic fields. The top row is the spin structure for **(A)** a uniformly magnetized circular particle and the cross sections of **(B)** a Bloch and **(C)** a Néel Skyrmion. The red signs indicate the magnetic charges resulting of a local divergence of $\boldsymbol{m}$. The bottom row features the respective demagnetizing/stray fields.

Magnetostatic energy and fields

The magnetic moments inside a medium have associated dipolar fields which interact with each other via Zeeman energy. Compared to nearest neighbor interactions, this interaction is a long range effect. The treatment of these fields is done by considering Maxwell's equation $\nabla \cdot \boldsymbol{B} = 0$ including $\boldsymbol{B} = \mu_0(\boldsymbol{H} + \boldsymbol{M})$, which gives

$$\nabla \boldsymbol{H} = -\nabla \boldsymbol{M} \, . \tag{2.14}$$

Without external magnetic fields, $\boldsymbol{H}$ is called the magnetostatic field $\boldsymbol{H}_\mathrm{d}$ of a given $\boldsymbol{M}$. From Eq. (2.14), it becomes apparent that the divergence of $\boldsymbol{M}$ acts as magnetic charges or the sinks and sources of $\boldsymbol{H}_\mathrm{d}$. In analogy to the Gaussian law of electrostatics and the associated electric potential, a magnetic scalar potential φ_m with $\boldsymbol{H}_\mathrm{d} = -\nabla\varphi_\mathrm{m}$ is defined. This potential can be computed from Poisson's equation

$$\Delta\varphi_\mathrm{m} = -\nabla \boldsymbol{M} \, , \tag{2.15}$$

using the Laplace operator Δ. As an example, Eq. (2.15) is numerically solved for a 2D circular particle with uniform magnetization which is shown in Fig. 2.2A. The top part shows the magnetization structure. The color coding corresponds to the length of the magnetization inside the visible plane. The magnetization has a non-vanishing divergence at the particle's edges whose normal have a component along $\boldsymbol{m}$. These magnetic surface charges $\nabla \boldsymbol{m}$ are indicated with the red $\pm$ signs. The bottom part of the figure shows $\boldsymbol{H}_\mathrm{d}$ for the particle. Color represents the component of $\boldsymbol{H}_\mathrm{d}$ in the displayed plane. Inside the sample, $\boldsymbol{H}_\mathrm{d}$ is uniform and aligned anti-parallel to $\boldsymbol{m}$, which is why it is called demagnetizing field. Outside of the sample, $\boldsymbol{H}_\mathrm{d}$ is called magnetic stray field. It can be shown that the demagnetization field inside a uniformly magnetized ellipsoid is always anti-parallel to $\boldsymbol{m}$ and its magnitude can be analytically computed [56, 57]. Note that the plotted field lines do not necessarily reflect increased magnitude of $\boldsymbol{H}_\mathrm{d}$ with the density of field lines and are sometimes not continuously drawn throughout the sample edges, which might be slightly confusing in particular in Figs. 2.2B,C.

The energy E_d related to the magnetostatic field is [56, 57]

$$E_\mathrm{d} = -\frac{1}{2}\mu_0 M_\mathrm{s} \int_V (\boldsymbol{m} \cdot \boldsymbol{H}_\mathrm{d}) \, \mathrm{d}V \, . \tag{2.16}$$

It can be interpreted as the Zeeman energy of the magnetization with its demagnetizing field, as $\boldsymbol{m}$ will be zero outside of the sample. However, it should be emphasized that this energy already includes the energy contribution of the stray field [5, 56, 57].

Two more examples of magnetostatic fields shall be given here as they will be helpful for arguments in the experimental part of this work. The first, shown in Fig. 2.2B, is a cross-section of the spin configuration of a magnetic Bloch skyrmion in a thin sample, which will be further discussed in section 2.1.2. It basically consists of three areas with uniform magnetization that will produce magnetic surface charges at the sample surface. The domain or skyrmion wall is of Bloch type, i.e. $\boldsymbol{m}$ rotates perpendicular to the image plane, in which direction the sample is assumed to be infinite for the calculation[2]. As can be seen, the stray field that emerges from the surface charges connect above the domain walls. The demagnetizing field is essentially vertical inside the sample and vanishes at the skyrmion wall. For transmission electron microscopy (TEM) investigations, an important feature is that $\boldsymbol{H}_\mathrm{d}$ above and below the horizontal line in the center of the sample is antisymmetric, which leads to the fact that the integrated magnetostatic field along the vertical axis is zero. Note that the magnetostatic energy (2.16) is generally decreased by avoiding

[2] Clearly, this does not represent a skyrmion anymore but will qualitatively produce equivalent stray fields.

the creation of magnetic charges. This is also called pole-avoidance principle. In the thin film, E_d is minimized when $\boldsymbol{M}$ is uniform and lies within the sample plane. The dependence of E_d with the direction of $\boldsymbol{M}$ with respect to the sample geometry is called shape-anisotropy.

The last example, displayed in Fig. 2.2C, shows the cross-section of a magnetic Néel Skyrmion which is equivalent to the Bloch skyrmion with the difference that the spins in the skyrmion wall rotate inside the image plane which is called a Néel wall. Due to this, magnetic volume charges are created within the sample, which will lead to a horizontal demagnetizing field antiparallel to $\boldsymbol{m}$ inside the wall. As can be seen, the stray fields above and below the sample are not symmetric as in Fig. 2.2B. Due to this, the integrated magnetic induction along the vertical direction in Fig. 2.2C is reduced by $\boldsymbol{H}_\mathrm{d}$ at the wall positions, which is again important for TEM investigations.

2.1.2 Magnetic textures in chiral magnets

Chiral magnets possess a rich variety of modulated magnetic textures that are the result of the energetic interplay between the five interactions that were introduced in the last chapter. In this section, the most important spin textures that can be found in chiral magnetic systems are introduced. The presence of a particular phase depends on the individual strengths of the magnetic parameters (like A_ex, $D_\mathrm{bulk}/D_\mathrm{int}$, M_s or $K_\mathrm{u}/K_\mathrm{c}$), externally-applied magnetic fields H_ext and sample geometry.

Helical and Cycloidal phase

At first, a chiral magnetic material without anisotropies, magnetostatic interactions and external magnetic fields is considered. In this situation, the relevant energies are direct exchange and DMI $E = E_\mathrm{ex} + E_\mathrm{DMI}$. As direct exchange favors parallel and DMI perpendicular alignment of adjacent spins, the combination of both interactions results in a slight spin canting at an angle γ as displayed on the left side of Fig. 2.3A for bulk, and Fig. 2.3B for interface-DMI. A simple energy minimization gives

$$\gamma_{ij} = \frac{D_{ij}}{J_{ij}} \,. \tag{2.17}$$

Extending this argumentation to a line of spins, a spin helix with a pitch or propagation vector $\boldsymbol{q}_\mathrm{h}$ is obtained for bulk DMI as shown on the right side of Fig. 2.3A. For interface-DMI a spin cycloid, shown in Fig. 2.3B, is obtained. Respectively, the cases for both signs of DMI are presented. The chirality or handedness describes the winding direction of the spins when following $\boldsymbol{q}_\mathrm{h}$. It can directly be seen how the sign of the DMI-vector changes chirality of the spin helix/cycloid. In a 3D

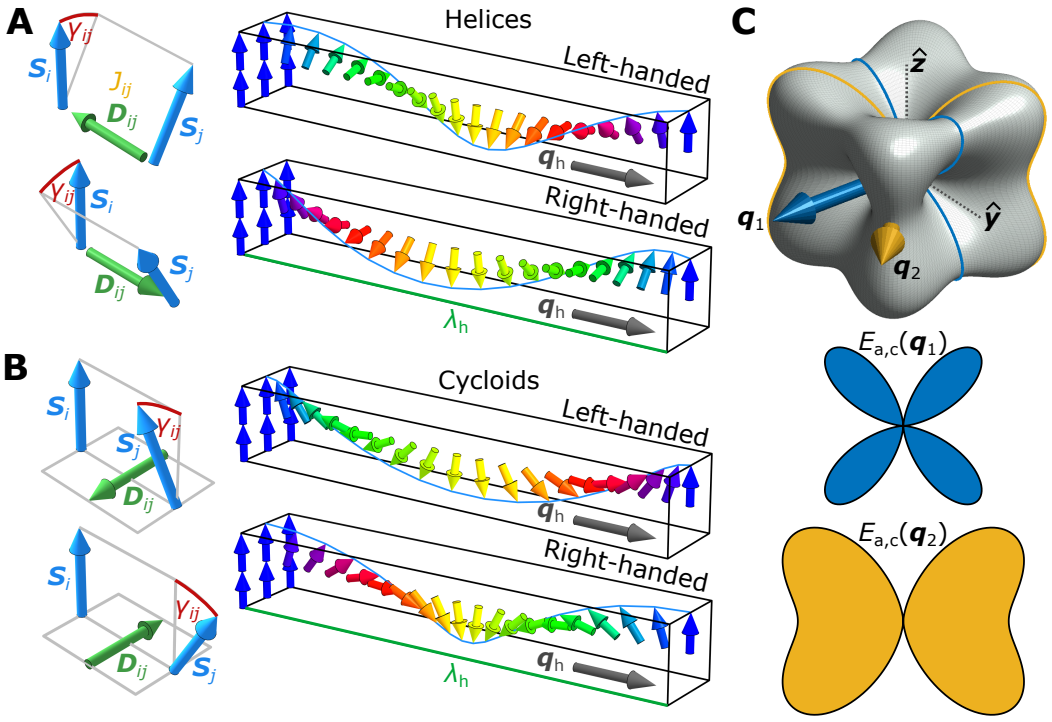

Fig. 2.3.: Spin configuration in the helical and cycloidal phase. On the left side, the energetic minimum of two spins that are coupled with direct exchange and **(A)** bulk or **(B)** interface-DMI is shown for each sign of D. The right side shows the helical or cycloidal phase that results from the respective interaction. **(C)** Cubic anisotropy energy plotted radially with respect to the direction of $\boldsymbol{m}$. Two $\boldsymbol{q}_\mathrm{h}$-vectors representing spin helices and associated helix directions as trajectory on the magnetic energy surface are shown. The respective enclosed areas shown below are proportional to anisotropy energy.

material, the sample planes normal to $\boldsymbol{q}_\mathrm{h}$ show a uniform magnetization, which is also indicated on the left side of the helices/cycloids in Fig. 2.3. This spin structure is referred to as helical/cycloidal phase. From continuum theory, it is possible to derive the energetically optimal q_h and the helix length λ_h using the ansatz

$$\boldsymbol{m}(\mathbf{r}) = \cos(q_\mathrm{h}\, z)\, \hat{\boldsymbol{x}} + \sin(q_\mathrm{h}\, z)\, \hat{\boldsymbol{y}}\ , \tag{2.18}$$

for a spin helix propagating along the z-axis ($\boldsymbol{q}_\mathrm{h} \parallel \hat{\boldsymbol{z}}$). Minimizing exchange energy (2.6) plus DMI energy (2.9) for the spin helix (2.18) gives the magnitude of $\boldsymbol{q}_\mathrm{h}$

$$q_\mathrm{h} = \frac{2\pi}{\lambda_\mathrm{h}} = \frac{D}{2A}\ . \tag{2.19}$$

This holds for spin helices and $D = D_\mathrm{bulk}$ as well as cycloids and $D = D_\mathrm{int}$. Therefore, measuring the helix length e.g. by LTEM or scattering experiments, the

Compound	λ_h (nm)	T_c (K)	Ref.
$Fe_{0.5}Co_{0.5}Si$	90 (bulk, ≈50 nm)	43.5	[48, 70–72]
MnSi	19 (bulk)	29.5	[1]
Cu_2OSeO_3	62 (bulk), 70 (150 nm), 50 (≈100 nm)	58.8	[52, 54, 73]
FeGe	70 (<50 nm)	≈280	[64]
GaV_4S_8	18 (bulk, 200 to 700 nm)	13	[74]
$Co_{10}Zn_{10}$	185 (bulk)	462	[24]
$Mn_{1.4}Pt_{0.9}Pd_{0.1}$	135 (50 to 100 nm)	≈400	[22]

Tab. 2.1.: Magnetic modulation lengths and critical temperatures for prominent chiral magnetic materials. The number in brackets after the helix length indicates sample thickness.

ratio of DMI to direct exchange interaction strength is directly given. Values for λ_h are typically in the range of 10 to 100 nm. A selection of prominent chiral magnetic materials and their modulation length as well as T_c is given in Tab. 2.1.

In materials with cubic magnetic anisotropy, the propagation vector $\boldsymbol{q}_\mathrm{h}$ tends to align such that $\boldsymbol{q}_\mathrm{h}$ is along an easy axis. This is not completely obvious, but can easily be understood, e.g. by looking at a cubic anisotropy energy $E_\mathrm{a,c}$ given in Eq. (2.13). Fig. 2.3C shows $E_\mathrm{a,c}(\boldsymbol{m})$ plotted radially, with respect to the direction of the unit magnetization $\boldsymbol{m}$. Here, the easy axes go through the valleys in the side of the cube-like structure, as indicated by the dashed lines. Now a spin helix with bulk DMI is considered. As an example, two $\boldsymbol{q}_\mathrm{h}$-vectors $\boldsymbol{q}_1$ and $\boldsymbol{q}_2$ are drawn in the schematic. As $\boldsymbol{m} \perp \boldsymbol{q}_\mathrm{h}$ in the case of a spin helix, the magnetization winds around the energy surface as indicated by the blue and orange path. The enclosed area of this path is then proportional to the cubic anisotropy energy of the spin helix. Comparing the two examples given, it becomes clear that the blue area associated with $\boldsymbol{q}_1$ is smaller and is indeed one of the six ground states for the shown cubic anisotropy. Further, λ_h is independent from the anisotropy as it will only affect the frequency of the trajectory around the energy landscape.

Conical and Field Polarized Phase

In the last section, direct exchange, DMI and anisotropy energies are considered and a helical phase is obtained. Now, an externally-applied magnetic field $\boldsymbol{H}_\mathrm{ext}$ is included in terms of Zeeman energy. First, the spin helix from before that is created by bulk DMI and isotropic exchange is considered. Under $H_\mathrm{ext} > 0$, $\boldsymbol{q}_\mathrm{h}$ aligns parallel to $\boldsymbol{H}_\mathrm{ext}$ while maintaining its magnitude. This configuration would increase the Zeeman energy which, however, is compensated by a slight spin tilt towards $\boldsymbol{H}_\mathrm{ext}$. Then, the winding of $\boldsymbol{m}$ is not on a circle, but on a cone, as it is shown in Fig. 2.4A.

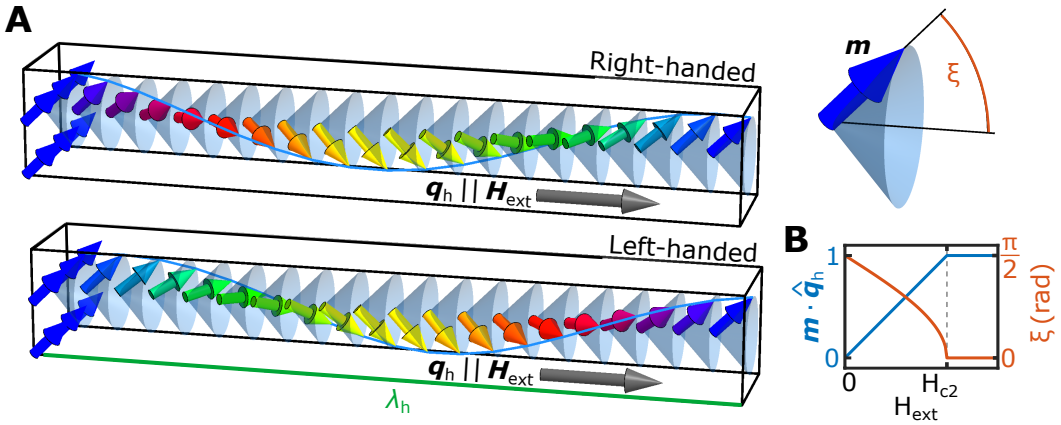

Fig. 2.4.: **(A)** Spin structure of the conical phase for both chiralities of bulk DMI. **(B)** Dependence of the cone angle ξ in dependence on the externally-applied magnetic field.

This phase is therefore called conical phase. Note that the description of the conical phase here is limited to bulk DMI, as present scientific work essentially only covers this case. Interface DMI is a 2D effect limited to thin film materials, where such a conical phase is hardly observable.

The conical tilt angle ξ can be determined by minimizing $E(m_{\mathrm{cone}}) = E_{\mathrm{Zee}} + E_{\mathrm{DMI}} + E_{\mathrm{ex}}$ using an ansatz for a tilted spin helix

$$\boldsymbol{m}(\boldsymbol{r}) = \sqrt{1 - m_{\mathrm{cone}}^2}\, \cos\left(q_{\mathrm{h}} z\right) \cdot \hat{\boldsymbol{x}} + \sqrt{1 - m_{\mathrm{cone}}^2}\, \sin\left(q_{\mathrm{h}} z\right) \cdot \hat{\boldsymbol{y}} + m_{\mathrm{cone}} \cdot \hat{\boldsymbol{z}} \tag{2.20}$$

with $m_{\mathrm{cone}} = \boldsymbol{q}_{\mathrm{h}} \cdot \boldsymbol{m} = \cos(\xi)$ and $\boldsymbol{q}_{\mathrm{h}} \parallel \hat{\boldsymbol{z}}$. The equilibrium value for m_{cone} is then given by [60, 75]

$$m_{\mathrm{cone}} = \begin{cases} cos(\xi) = \frac{H_{\mathrm{ext}}}{H_{\mathrm{c2}}} & \text{for } H_{\mathrm{ext}} < H_{\mathrm{c2}} \\ 1 & \text{for } H_{\mathrm{ext}} \geq H_{\mathrm{c2}} \end{cases}, \tag{2.21}$$

with the second critical field

$$\mu_0 H_{\mathrm{c2}} = \frac{D_{\mathrm{bulk}}}{2 A_{\mathrm{ex}} M_{\mathrm{s}}}\,. \tag{2.22}$$

The component of $\boldsymbol{m}$ along $\boldsymbol{H}_{\mathrm{ext}}$ increases linearly up to H_{c2} above which the magnetization is saturated and all spins are parallel to the applied magnetic field. This state is called uniform, saturated or field-polarized phase. Eq. (2.21) is plotted in Fig. 2.4B.

Naturally, there must be also a first critical field H_{c1} which appears when considering anisotropies at weak external fields. Upon application of weak magnetic fields along an arbitrary direction, the spin helices that may originally appear in

domains of different $\boldsymbol{q}_\mathrm{h}$-orientation for a 3D material at $H_\mathrm{ext} = 0$, must reorient and travel along the anisotropic energy landscape (e.g. shown in Fig. 2.3C) that is further deformed by the upcoming Zeeman energy [1, 76, 77]. The trajectory of $\boldsymbol{q}_\mathrm{h}(\boldsymbol{H}_\mathrm{ext})$ can be rather complex, depending on the applied field direction [76]. The conical phase with $\boldsymbol{q}_\mathrm{h} \parallel \boldsymbol{H}_\mathrm{ext}$, upon which the above mathematical description and (2.21) is applicable, is reached at the first critical field H_c1.

Magnetic skyrmions

The most prominent spin texture and major topic of this work is the magnetic skyrmion. Before discussing the energetic requirements, the skyrmion structure is introduced. Analogous to helices and cycloids that arise for different DMIs and chiralities, there are also different spin arrangements for skyrmions. The ones for the most common skyrmion types are displayed in Fig. 2.5. The shown isolated skyrmions have a cylindrical symmetry with $m_z(\boldsymbol{r}) = m_z(r)$. At $r \to \infty$, the magnetization points along the external magnetic field[3] assumed to be parallel to $\hat{\boldsymbol{z}}$. Approaching $r \to 0$, the spins start to rotate in a circular domain wall until the magnetization is anti-parallel to $\boldsymbol{m}(r \to \infty)$ at the skyrmion core at $r = 0$. A skyrmion radius R, at which $\boldsymbol{m}(R) \cdot \hat{\boldsymbol{z}} = 0$, can be defined. The skyrmion wall is the area that connects the uniform magnetization parallel to $\boldsymbol{m}(r \to \infty)$ and the skyrmion core. The different types of skyrmion walls are the result of the different types and signs of DMI. The interface-DMI leads to a skyrmion wall that is comparable to a Néel wall of common magnetic domains. For this reason, these types of skyrmions (Fig. 2.5A) are called Néel skyrmions. Bulk DMI results in Bloch-like skyrmion walls and the name Bloch skyrmions (Fig. 2.5B). The skyrmion polarity is defined by the sign of $\boldsymbol{m}(0) \cdot \hat{\boldsymbol{z}}$. Mathematically, the skyrmion can be described using a vorticity, which is 1 for the shown skyrmion types, and a helicity ψ which is 0 or π for Néel and $\pi/2$ or $3\pi/2$ for Bloch skyrmions [78]. The helicity is the angle of the skyrmion wall magnetization with respect to the radial direction, which can also be seen in Fig. 2.5. The two possible values of ψ for Bloch or Néel skyrmions are often called the two skyrmion chiralities. This mathematical description is introduced in more detail in section 4.2.2. For different values of the vorticity, additional new classes of skyrmions can be introduced, e.g. with a vorticity of -1, anti-skyrmions can be described that were also discovered experimentally [22]. However, this is not further discussed in this thesis. Also note that the spin structure of the Bloch skyrmions for $r < R$ is equivalent to a magnetic vortex [79, 80], which is why the name vortex often appears in the skyrmion context.

[3] Magnetic anisotropies are ignored here.

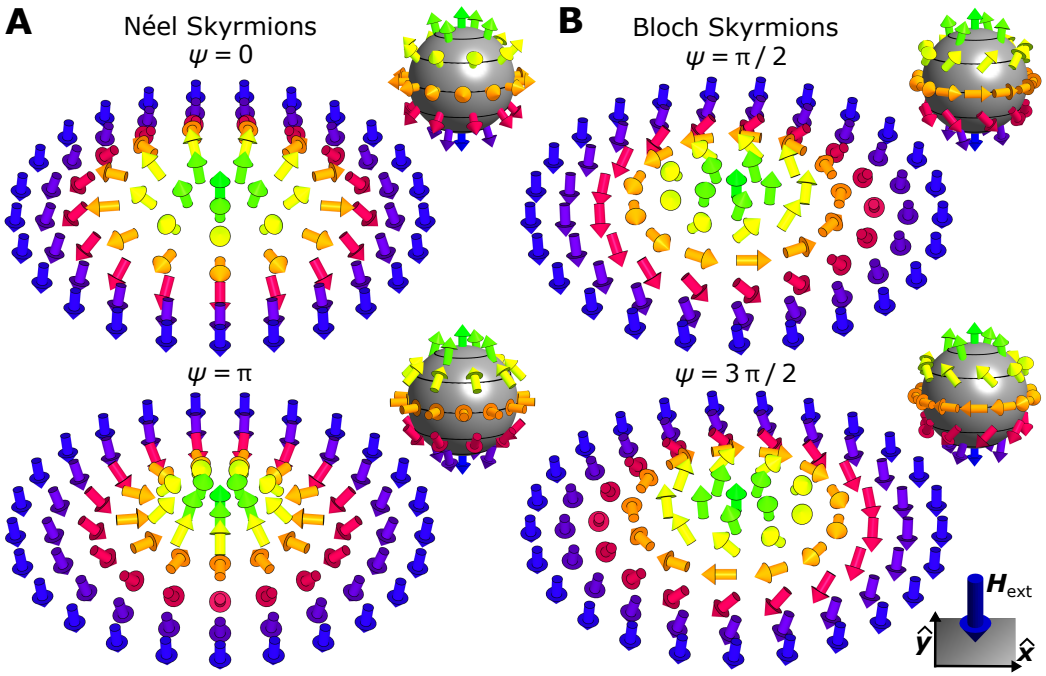

Fig. 2.5.: Spin structures of isolated magnetic **(A)** Néel skyrmions with interface-DMI and **(B)** Bloch skyrmions with bulk DMI. Each type corresponds to a different skyrmion helicity ψ. The inset shows the spins mapped to a unit sphere.

An important feature of the skyrmion spin structure is the so-called topological protection. In an infinite system, this means the absence of a continuous transformation on $\boldsymbol{m}$ from the skyrmion spin structure to the uniform state. Any continuous transition eventually results in a discontinuity of $\boldsymbol{m}(\boldsymbol{r})$ which due to the exchange interaction represents an energy barrier that is infinite in continuum theory but of course finite for a real system as the lattice constant of the real spin lattice does not approach zero [30, 32, 81]. The topological protection is often used as a selling point for skyrmion research, as it renders the picture of a stable magnetic quasi-particle that is protected against external influences which makes it a viable candidate for future data storage applications [11, 12, 14, 16, 20].

In the same context, the topological winding number or topological charge N_{sk} is often introduced. For any given direction $\hat{\boldsymbol{v}}$, a location $\boldsymbol{r}_\perp = (x, y)^\mathsf{T}$ within the skyrmion structure can be found where $\boldsymbol{m}(\boldsymbol{r}_\perp)$ is parallel to $\hat{\boldsymbol{v}}$. Therefore, $\boldsymbol{m}$ can be mapped to the unit sphere S^2. These mappings are shown in the insets of Fig. 2.5. They can be obtained by virtually grabbing the skyrmion at its edges with both hands and wrapping it around a sphere. The grabbed edges are combined at the bottom of the sphere. The topological winding number N_{sk} counts how many times a spin structure can be wrapped around the sphere. In the given examples, each skyrmion

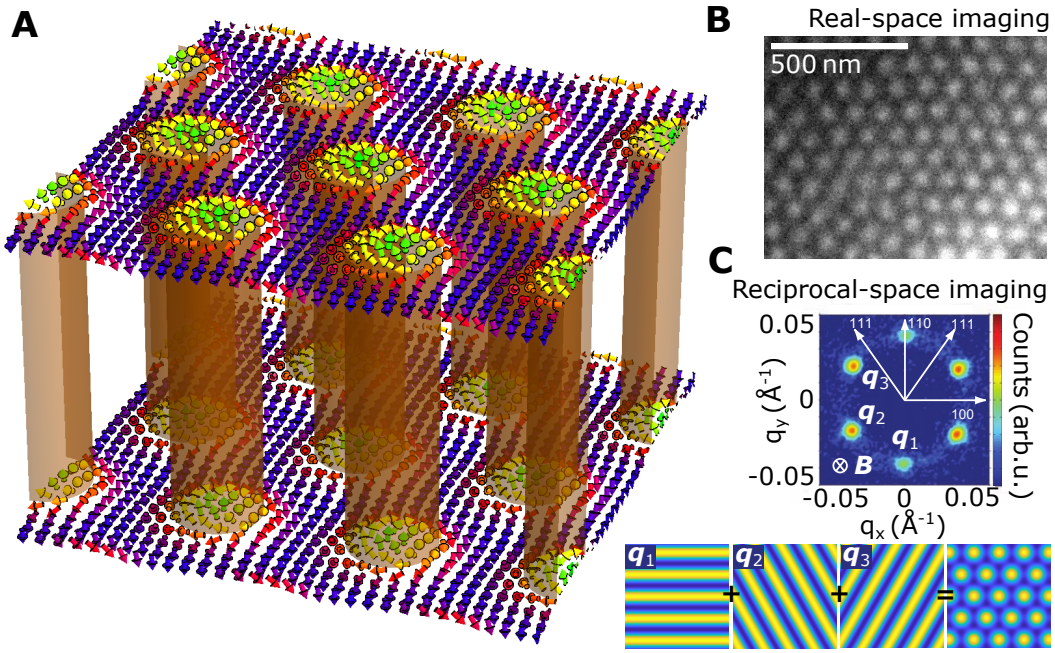

Fig. 2.6.: **(A)** Spin structure of a hexagonal Bloch skyrmion lattice. **(B)** Real-space Fresnel Lorentz TEM image of a Bloch skyrmion lattice in $Fe_{0.5}Co_{0.5}Si$. **(C)** Reciprocal-space image of a Bloch skyrmion lattice in MnSi obtained by SANS. Two opposing spots represent a single spin helix and their sum gives the hexagonal lattice as depicted below. The scattering image in (C) is reprinted with permission from [1].

has an absolute winding number of one, as seen from the insets in Fig. 2.5. The winding number Nsk can be calculated by the following integration [78, 82, 83]

$$N_{\mathrm{sk}} = \frac{1}{4\pi} \int_{\mathrm{A}} \boldsymbol{m} \cdot \left(\frac{\partial \boldsymbol{m}}{\partial x} \times \frac{\partial \boldsymbol{m}}{\partial y} \right) \mathrm{d}x \, \mathrm{d}y \, . \tag{2.23}$$

In systems that contain many skyrmions which are neither created nor annihilated, N_{sk} is a conserved quantity. Note that the mapping shown in the inset of Fig. 2.5A for $\psi = 0$ is sometimes referred to as “hedgehog” or “hairy sphere”. Further note that as the presented skyrmion structures in Fig. 2.5 all have an absolute topological winding number of one, they are topologically equivalent, and can be continuously transformed into each other [78, 83].

Another interesting property of the skyrmion can be found when studying the skyrmion-electron interaction. When an electron traverses laterally through the skyrmion structure, its spin direction adapts to the magnetization profile. This continuous tilting of an angular momentum leads to a counteracting force that acts on the skyrmion and the electron itself. In the theoretical description, the skyrmion is associated with a quantized magnetic flux. When the skyrmion moves due to the current, it therefore creates an emergent electric field, in analogy to

Faraday's law of induction. This field is transverse to the electron direction. The electron or skyrmion deflection can be detected in tailored topological or skyrmion Hall-effect measurements [6, 84–86] or from the skyrmion motion in real space [87, 88]. This is also called the emergent electrodynamics of the skyrmion spin structure [6]. The manipulation of skyrmions with electric currents at low current densities ($1 \times 10^6\,\mathrm{A\,m^{-1}}$) is an incentive to use skyrmions in spintronics applications for data storage, like the frequently proposed skyrmion racetrack devices [9, 11–13]. Such a racetrack can not only be operated at current densities that are two orders of magnitude lower than previously proposed domain wall racetracks, but are also not known to suffer from domain wall deformation and slowdown for large currents [42, 89, 90].

In a real system with bulk DMI, the skyrmions do not appear isolated but in a hexagonal lattice state. A sketch of this is shown in Fig. 2.6A. As can be seen, the 3D skyrmion spin structure is independent of the z-component, resulting in skyrmion tubes inside the bulk, which is comparable to the flux tubes inside a superconductor. The lattice can be imaged in real space using e.g. Fresnel LTEM, which is discussed later in chapter 4. A micrograph of the skyrmion lattice of $Fe_{0.5}Co_{0.5}Si$ is shown in Fig. 2.6B. The energetic interplay of DMI and Exchange that is seen so directly for the case of the spin helix seems to be a bit concealed for the skyrmion lattice at first glance. However, the energetic signature of the spin helix is still present in the skyrmion lattice. To see this, three spin helices can be assumed, with their $\boldsymbol{q}_\mathrm{h}$ in the same plane and at an angle of 60° with respect to each other. The superposition of these three helices essentially describes the skyrmion lattice, which is indicated for m_z at the bottom of Fig. 2.6C. This is also the reason why magnetic scattering experiments conducted on a skyrmion lattice show the famous six-fold pattern, which is displayed in the top part of Fig. 2.6C. The image is taken from the initial small angle neutron scattering (SANS) experiment that led to the discovery of magnetic skyrmions in MnSi [1]. The helix length of the three helices is identical to the previously calculated λ_h. Therefore, the skyrmion lattice constant a_sk is given by

$$a_\mathrm{sk} = \frac{2}{\sqrt{3}} \cdot \lambda_\mathrm{h} \approx 1.15 \cdot \lambda_\mathrm{h}\ . \tag{2.24}$$

2.1.3 Magnetic phase diagrams of chiral magnets

In this section, the magnetic phase diagrams of chiral magnets are introduced by putting the spin structures from the last section in a thermodynamic context. The description begins with the most prominent phase diagram for bulk chiral magnets of the space-group $P2_13$ of the B20-compounds and discusses their modifications for thin films. Subsequently, another family of chiral magnetic textures is introduced.

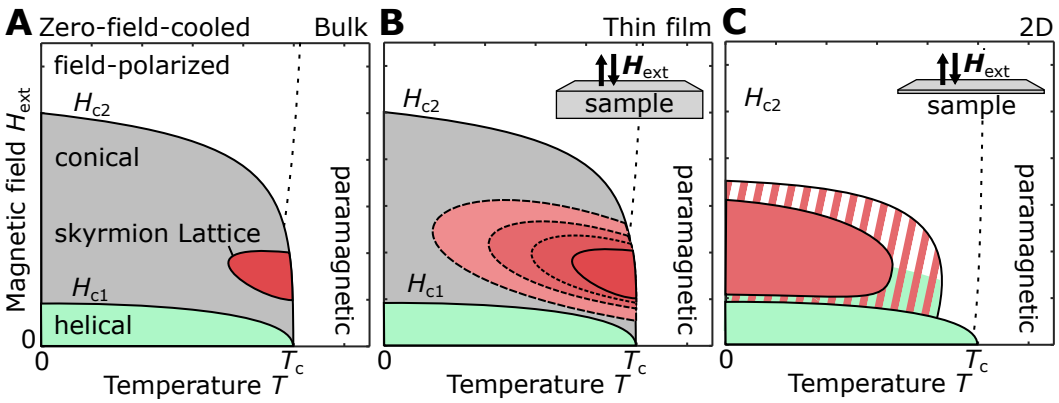

Fig. 2.7.: **(A)** Qualitative magnetic phase diagram of a B20 chiral magnet. **(B)** Magnetic phase diagram of a thin film B20 chiral magnet for applied external magnetic fields perpendicular to the film. With decreasing thickness, the skyrmion lattice state extends and the conical state vanishes. **(C)** In a 2D film, the conical is not present and mixed phases are found.

These are, besides direct exchange and DMI, also stabilized by magnetic anisotropy and magnetostatic energy.

Phase diagram of the B20 compounds with the P2$_1$3 space-group

A magnetic phase diagram shows the presence of a magnetic phase with respect to temperature T and externally-applied magnetic field H_{ext}. The general phase diagram for B20 materials with the P2$_1$3 space-group is qualitatively shown in Fig. 2.7A. These materials are referred to as B20 chiral magnets. The shown phase diagram is obtained when cooling the sample below the Curie temperature T_{c} at zero externally-applied magnetic field and a subsequent adiabatic increase to different fields. Afterwards, the sample is heated. During this, the present phases or phase boundaries are recorded. This phase diagram is labeled zero-field-cooled (ZFC). In general, the phase diagram shows a strong hysteresis which means that the locations where the phases are observed will change in dependence on the magnetic history or the trajectory through phase space [31, 71, 81, 91].

Below T_{c}, the system becomes ferromagnetic and at zero magnetic field, the helical phase is present, which is expected from the energetic discussion of the last section. The formation of helical domains with differently oriented $\boldsymbol{q}_{\mathrm{h}}$ is possible. For example in Cu_2OSeO_3, differently aligned helical domains are observed with $\boldsymbol{q}_{\mathrm{h}} \parallel \langle 001 \rangle$. These directions are the easy axes of the cubic anisotropy which explains the alignment from the discussion in 2.1.2 [51, 54, 76].

When an external magnetic field is applied, the $\boldsymbol{q}_{\mathrm{h}}$-vectors of the helical domains travel according to the energy landscape until $\boldsymbol{q}_{\mathrm{h}} \parallel \boldsymbol{H}_{\mathrm{ext}}$ [76]. This is completed for $H_{\mathrm{ext}} = H_{\mathrm{c1}}$ and the magnetic system transforms to the conical phase. This can only

be a second order phase transition if H_{ext} is applied in one of the high symmetry directions [77]. Upon further increase of the magnetic field, the net moment of the conical phase increases until the saturated or field-polarized state is reached at H_{c2}.

A last small phase space pocket is found at intermediate magnetic fields and temperatures just below T_{c}. It hosts the hexagonal Bloch skyrmion lattice state. In fact, this phase was already known prior to its identification as the skyrmion spin state and was labeled A-phase, which is also a common name [92]. The phase transition from the skyrmion to the conical phase is of second order [1, 84]. Helical, conical and skyrmion phase are also called the magnetically modulated phases.

The magnetic phase diagram can be reconstructed from a classical 3D Monte Carlo simulation. Surprisingly, it is sufficient to include only three energy contributions, namely direct exchange, DM and Zeeman interaction [93]. Nevertheless, the simulated phase diagram, based on such a modest energy functional, already shows quite a large universality within the bulk chiral magnets [1, 54, 63, 91, 94]. As this is a Monte Carlo simulation, it is also possible to conclude that the skyrmion lattice state is actually not a thermodynamic ground state of the system at zero temperature, but is only a thermally activated state.

For real-space observation of skyrmions in TEM, the B20 samples must be mechanically thinned down to around 100 nm. It turns out that this procedure significantly alters the phase diagram. The discussion here is limited to magnetic fields applied along the sample normal, which is the common measurement condition for skyrmion imaging in TEM. The first difference is that with decreasing thickness, the skyrmion pocket extends to lower temperatures, while the conical phase is suppressed, which is indicated by the dashed lines in Fig. 2.7B [64]. Approaching a 2D system, the conical phase completely vanishes and the skyrmion lattice phase becomes the ground state of the system. This is easily understood, as a 2D system cannot show a spin rotation along $\hat{\boldsymbol{z}}$ as the conical $\boldsymbol{q}_{\mathrm{h}}$-vector would be parallel to the external field and therefore normal to the sample plane. Approximately, the conical phase vanishes once the film thickness is smaller than the helix length for $T = 0\,\mathrm{K}$ [70, 95, 96]. A second difference is related to this issue and concerns the orientation of the helical domains. In 2D, the helical $\boldsymbol{q}_{\mathrm{h}}$-vectors are constrained to the sample plane. Classical Monte-Carlo simulations for an actual 2D system give a phase diagram which is qualitatively shown in Fig. 2.7C. The conical phase is absent and it shows a mixed skyrmion/helical and skyrmion/field-polarized phase [48, 97, 98].

Phase diagram for perpendicularly magnetized thin layers

In the bulk B20 chiral magnets, the stability of the magnetically modulated phases is essentially explained by three energy contributions, namely isotropic exchange, DMI

and Zeeman energy. Another class of materials that is investigated in this thesis are thin ($\approx 1\,\mathrm{nm}$) films of ferromagnets (like Co or CoFeB) sandwiched between two different heavy metal layers (like Pt and Ir, Ta, W, MgO or Tb) with strong spin-orbit coupling [21, 25, 67, 99, 100].

At the interface, spin-orbit coupling leads to a strong magnetic uniaxial anisotropy perpendicular to the film which favors a uniform spin state parallel or antiparallel to the sample normal. While such a state satisfies anisotropy and isotropic exchange energy, it leads to the generation of magnetic surface charges and associated magnetostatic fields and energy as discussed in section 2.1.1. To compensate this, the system introduces magnetic stripe domains which will lead to flux closure that will decrease the magnetostatic energy as shown in Fig. 2.2B, C. On the other hand this competes with a positive exchange energy within the domain wall [5, 101]. In reality, the stripe domains are usually disordered and show a labyrinthine pattern, an example is shown in Fig. 2.8A.

Once an external magnetic field is applied parallel to the sample normal, domains with magnetization parallel to the field will extend, and antiparallel ones will shrink. At some field, the stripe domains fragment and further shrink towards circular objects. These circular domains are called bubble domains. From energy minimization, it is expected that a hexagonal lattice of bubbles has a lower energy than the stripe phase above a critical field [102, 103]. In reality, the bubble phase rarely shows a perfect hexagonal lattice and the arrangement is rather amorphous [5, 102]. Without DMI, the bubbles have Bloch walls of arbitrary chirality, like shown in Fig. 2.8B. Such systems were extensively studied in the 1970s, where the magnetic bubble memory was a promising successor of magnetic core memory. The technique ultimately vanished with the introduction of the Flash Random Access Memory (RAM) at the end of the 1980s [104]. The phase diagram of a bubble system is qualitatively shown in Fig. 2.8C. This matches theoretical expectations and is also confirmed experimentally e.g. in ultrathin Fe or Ni on Cu(001) [5, 102, 103, 105].

The difference of such bubble hosting materials to the ones investigated in this thesis is the presence of a large interface-DMI at the ferromagnet - heavy metal layer interface. It can be nearly as strong as the direct Heisenberg exchange [36]. As already mentioned, it is important that the top- and bottom layer are different materials, as otherwise this would create an opposite sign of D_{int} from the mirrored geometry and lead to DMI compensation. To obtain a net DMI, the heavy metals are chosen such that the respective spin-orbit couplings lead to different DMI magnitudes. They even can be additive, as shown by Moreau-Luchaire et al. for Pt/Co/Ir trilayers and sketched in Fig. 2.8D [25]. The DMI can strongly alter the observed magnetic structures. Dependent on its magnitude, the stripe domains become more narrow

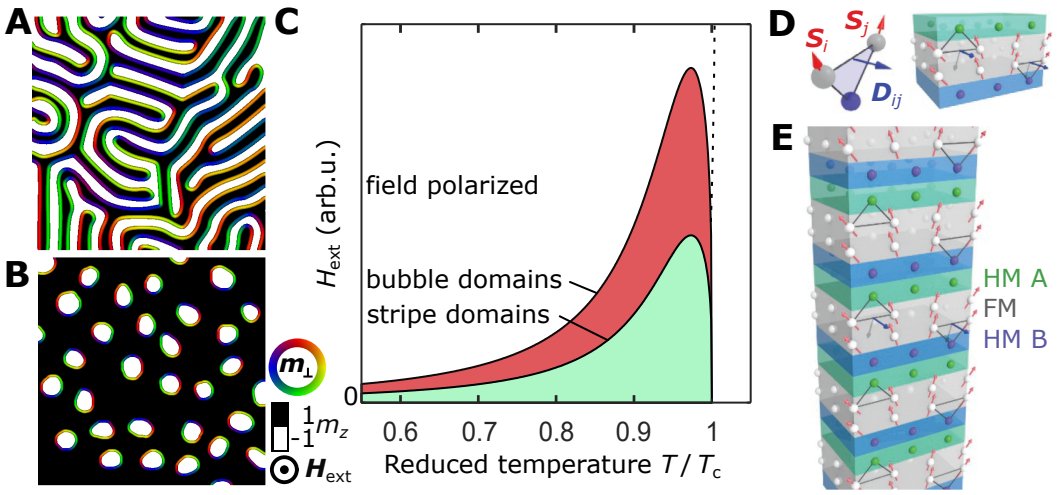

Fig. 2.8.: **(A)** Stripe domains in a perpendicularly magnetized thin film. Color represents in-plane magnetization (see color-wheel) and black/white areas mark magnetization pointing uniformly along the sample normal. The stripe to domain wall width is chosen arbitrarily for better visualization. **(B)** Bubble domains in a finite externally-applied magnetic field. The bubbles have Bloch walls and their chiralities are arbitrary. **(C)** Magnetic phase diagram of a perpendicularly magnetized ultrathin film obtained from a theoretical model [102]. The externally-applied magnetic field is parallel to the sample normal. **(D)** The shown interface-DMI at the bottom and top interface of a ferromagnetic layer (FM) between two different heavy metals (HM A, HM B) is additive. **(E)** In a multilayer stack of trilayers shown in D, the magnetization pattern is repeated in stacking direction [106]. Panel (A) is based on data in [107]. Panel (B) is based on data in [5]. Panels (D) and (E) are slightly modified versions of image in [25].

and approach a cycloidal structure as it was shown in Fig. 2.3B. In contrast to the bubble materials, the interface-DMI favors domain walls of the Néel type instead of the Bloch type. This also applies to the bubbles that now show circular Néel walls and can shrink to sizes below 100 nm, while equivalent systems without DMI would not show magnetic bubbles smaller than 1 µm [25]. Furthermore, all bubbles have the same chirality - they become monochiral - due to the DMI. Topologically, the bubbles in these systems are equivalent to the one of a Néel skyrmion and also the structure is essentially the same as the one of Néel skyrmions found in other skyrmion-hosting materials, mainly due to the reduced size of the skyrmion core. This is why these objects are mostly referred to as skyrmions [21, 25, 67, 99, 100], although this is an ongoing debate [108–110]. In this thesis, they will be referred to as Néel skyrmions and the stripe phase will be referred to as cycloidal phase.

The trilayer systems can also be stacked in multilayers as shown in the sketch in Fig. 2.8E. Due to magnetostatic coupling and Ruderman-Kittel-Kasuya-Yosida (RKKY)-interaction, the magnetic layers may show the same magnetization in the $\hat{z}$-direction along the stack [25, 106]. Due to this, the effective magnetic volume is

increased which potentially leads to en enhanced skyrmion stability and in addition to an increased TEM image contrast as discussed in section 4.2. A more detailed description on RKKY interaction can be found e.g. in [56, 57].

2.2 Magnetization dynamics

In section 2.1, the static spin structures of chiral magnets in equilibrium are shown. Now, the theoretical formalism for the dynamics of a magnetization structure that is subject to a changing energy landscape is introduced. The total energy density of a chiral magnet can be written as

$$\epsilon_{\mathrm{total}}(\boldsymbol{M}) = \frac{1}{V} E_{\mathrm{total}} = \frac{1}{V}\left(E_{\mathrm{ex}} + E_{\mathrm{DMI}}^{\mathrm{bulk/int}} + E_{\mathrm{Zee}} + E_{\mathrm{a,u/c}} + E_{\mathrm{d}}\right) , \tag{2.25}$$

using Eqs. (2.6), (2.9), (2.10), (2.11), (2.12), (2.13) and (2.16). In the equilibrium case or a local energy minimum, changing $\boldsymbol{M}$ will increase $\epsilon_{\mathrm{total}}$, leading to $\nabla_{\boldsymbol{M}} \epsilon_{\mathrm{total}} \neq 0$ with $\nabla_{\boldsymbol{M}} = \left(\frac{\partial}{\partial M_x}, \frac{\partial}{\partial M_y}, \frac{\partial}{\partial M_z}\right)^{\mathsf{T}}$. An effective field

$$\boldsymbol{H}_{\mathrm{eff}} = -\nabla_{\boldsymbol{M}} \epsilon_{\mathrm{total}} , \tag{2.26}$$

is defined, which is parallel to $\boldsymbol{M}$ in the magnetic ground state [111]. The temporal evolution of $\boldsymbol{M}(t)$ in a non-equilibrium situation is given by the Landau-Lifshitz-Gilbert (LLG) equation [112–114]

$$\frac{\partial \boldsymbol{M}}{\partial t} = -\gamma \mu_0 \left(\boldsymbol{M} \times \boldsymbol{H}_{\mathrm{eff}}\right) + \frac{\alpha}{M_{\mathrm{s}}} \left(\boldsymbol{M} \times \frac{\partial \boldsymbol{M}}{\partial t}\right) . \tag{2.27}$$

Here, $\gamma = \left|\frac{ge}{2m_{\mathrm{e}}}\right|$ is the gyromagnetic ratio, e the electron charge, m_{e} electron mass and g the Landé factor. The first term leads to a precession of $\boldsymbol{M}$ around $\boldsymbol{H}_{\mathrm{eff}}$, as shown in Fig. 2.9A. The second term is a phenomenological damping term that allows for energy dissipation via a positive magnetic damping parameter α. Combined with the precession term, a spiraling trajectory towards $\boldsymbol{H}_{\mathrm{eff}}$ is obtained, as displayed in Fig. 2.9B. Further terms can be added to the LLG to account for instance the interaction of $\boldsymbol{M}$ with spin-polarized currents via spin-transfer torques.

As a further example, the trajectory of $\boldsymbol{M}(t)$ in the cubic anisotropic potential given in Eq. (2.13) is shown in Fig. 2.9C. For this, Eq. (2.27) is iteratively solved using the classic Runge-Kutta method (RK4) with $\mu_0 = \gamma = M_{\mathrm{s}} = 1$, $\alpha = 0.09$ and a timestep of $\delta t = 0.001$ [115]. In contrast to Fig. 2.9A, B, the effective field is not constant. Just like in Fig. 2.3C, the vector direction from the center to the surface of the cuboid structure represents the direction of $\boldsymbol{M}$ and its magnitude is proportional

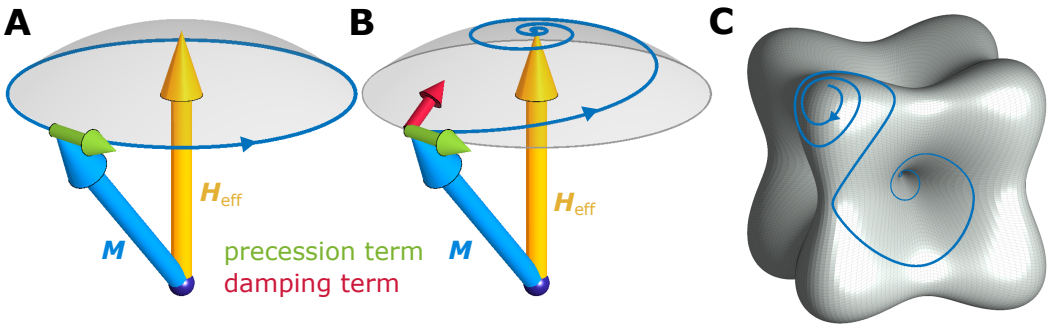

Fig. 2.9.: Visualization of the Landau-Lifshitz-Gilbert (LLG) equation. **(A)** Only considering the precession term of the LLG, the magnetization precesses around a constant effective field and does not relax. **(B)** Including the damping term, the magnetization spirals towards the effective field. For a better visualization, the effective field and the precession and damping term vectors were scaled. **(C)** The trajectory of the magnetization in a cubic anisotropy potential. The parameters for the simulation are given in the main text.

to the cubic anisotropy energy density $\epsilon_{\text{a,c}}$. It can nicely be seen how the curvature of the energy landscape makes $\boldsymbol{M}$ spiral outwards for the initially given $\boldsymbol{M}(t = 0)$. Once $\boldsymbol{M}$ reaches a direction where the curvature inverts, the precession direction changes and the trajectory becomes an inward spiral that ends in one of the six global energy minima.

In section 3.3 of this work, Eq. (2.27) is numerically solved to study the excited states of Bloch skyrmions. As this is a non-uniform or textured magnetic system, the magnetic body is divided into a grid and $\boldsymbol{H}_{\text{eff}}$ must be calculated locally to solve Eq. (2.27). For this, various pieces of software exist as e.g. the open-source framework MuMax3 [116].

3 Reciprocal-space imaging of skyrmion excitations

This chapter covers the imaging of magnetic skyrmions and their excitations in reciprocal-space by means of magnetic resonant elastic x-ray scattering (REXS). After the introduction of the experimental setup and some theoretical considerations about the technique, scattering experiments on the static chiral magnetic textures in Cu_2OSeO_3 are shown. This includes helical, conical and hexagonal skyrmion lattice phases, as well as the second low-temperature skyrmion phase that was recently discovered in Cu_2OSeO_3 [117–119].

Once the theoretical and experimental groundwork is established, measurements of the Ferromagnetic Resonance (FMR) are added. First, the three fundamental skyrmion excitations are introduced by means of micromagnetic simulations. The micromagnetic constants used for Cu_2OSeO_3 used to model the chiral magnet produce a phase diagram found in experiments [54]. Within this model, the skyrmion lattice phase is excited by means of a time-dependent magnetic field, and the three fundamental modes are identified and discussed [44, 45]. Subsequently, FMR experiments using REXS are presented. The three skyrmion modes, as well as helical and field-polarized resonances, are captured. The detection of FMR by means of REXS establishes a new technique for FMR-measurements that is called REXS-FMR. It extends conventional FMR experiments by elemental and reciprocal space sensitivity of REXS. The ability to select specific $\boldsymbol{q}_\mathrm{h}$-vectors in FMR experiments can be beneficial in systems that show a complex magnetic environment e.g. due to a coexistence of multiple modulated magnetic phases or differently oriented domains.

Large parts of this chapter are published in Ref. [51].

3.1 Magnetic Resonant Elastic X-Ray Scattering off Cu_2OSeO_3

This section contains the basic theoretical concepts to understand the experimental reciprocal space mapping of the static chiral magnetic textures discussed in section 3.2. It further provides a groundwork for the additional FMR measurements that are performed simultaneously to the scattering, which will be introduced in section

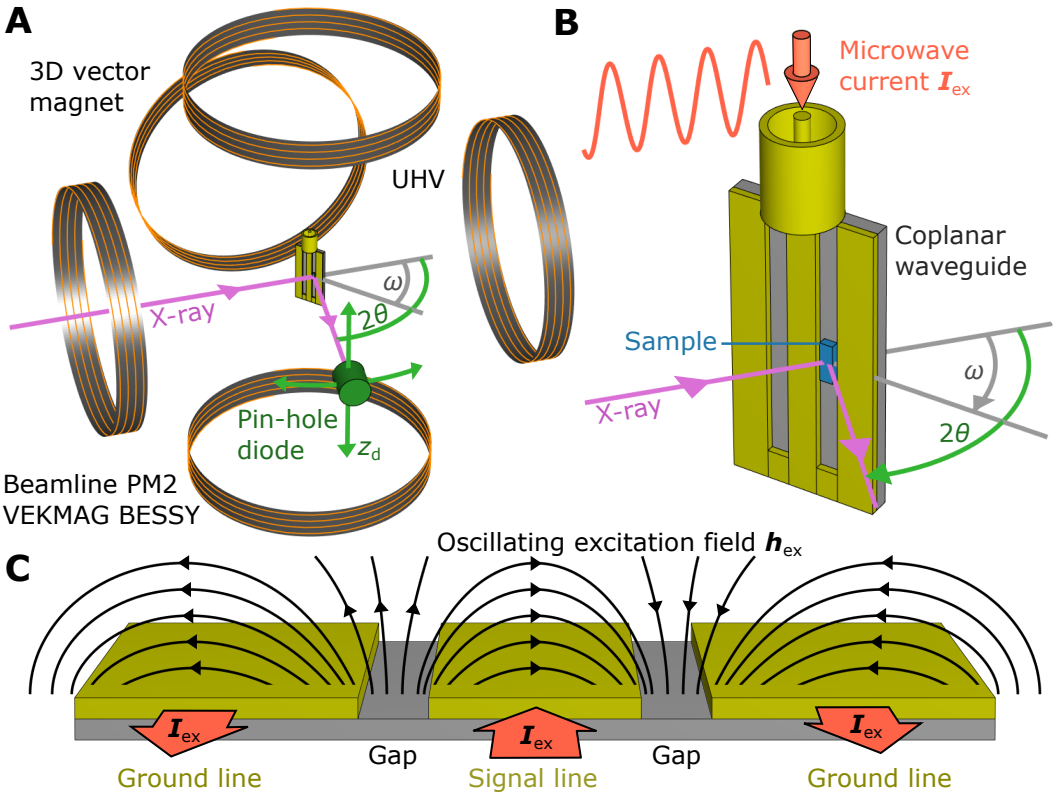

Fig. 3.1.: Experimental setup for the REXS-FMR experiments. **(A)** The X-ray is scattered off the sample and detected with a movable pin-hole diode. A 3D vector magnet allows an application of external magnetic fields along arbitrary directions. **(B)** The sample is placed on a coplanar waveguide through which a microwave current $\boldsymbol{I}_{ex}$ can be driven. **(C)** The coplanar waveguide generates an oscillating magnetic field $\boldsymbol{h}_{ex}$ that follows $\boldsymbol{I}_{ex}$ in time. This field is used to magnetically excite the sample.

3.3. It will cover the general measurement setup that is used throughout these experiments and will also give insight into the scattering conditions and related geometries. The explanations do not cover the general case but will be rather close to the experimental conditions presented afterwards. The intention is not to convey a complete description of (magnetic resonant elastic) X-ray scattering theory. For this, a variety of literature exists - a subset is given by Refs. [120–123].

3.1.1 Experimental setup

The experimental work is carried out at the beamline PM2 at BESSY II in Berlin using the VEKMAG end station. In the following, only parts of the setup that are relevant for the specific experiments, are introduced. For a more comprehensive description of the experimental capabilities of VEKMAG, the reader is referred to Ref. [124].

A sketch of the experimental setup is shown in Fig. 3.1A. The collimated x-ray beam with variable energy enters the ultra-high-vacuum (UHV) chamber and is focused onto the sample surface to a spot with a diameter in the order of 100 µm. The sample holder is connected to a cryostat which can cool the sample to temperatures around 10 K for this particular holder. Furthermore, the sample can be linearly moved along all three Cartesian directions and can be rotated by an angle ω around the normal vector of the scattering plane $\boldsymbol{k}_\mathrm{i} \times \boldsymbol{k}_\mathrm{f}$ as indicated. The scattered photon beam is captured using an X-ray sensitive diode behind a pinhole with a diameter of 300 µm. The diode can be rotated around $\boldsymbol{k}_\mathrm{i} \times \boldsymbol{k}_\mathrm{f}$ by an angle 2θ and translated along $\boldsymbol{k}_\mathrm{i} \times \boldsymbol{k}_\mathrm{f}$, i.e. change its z-position z_d. In total, three exchangeable diodes can be mounted in the chamber and a charge-coupled device (CCD) camera can be used for transmission experiments (not shown). The sample is situated between three pairs of superconducting coils. In combination, they form a 3D vector magnet, which means that arbitrary magnetic field directions at the sample site can be established. The maximal magnetic induction of 9 T along the beam direction and 1 T along an arbitrary direction is more than sufficient for the study of Cu_2OSeO_3 with $\mu_0 H_{c2} \approx 120\,\mathrm{mT}$ around $T = 0\,\mathrm{K}$ [54].

The sample is mounted on a coplanar waveguide as shown in Fig. 3.1B. Using a microwave feed-through, the sample can be magnetically excited. The working principle of the coplanar waveguide is illustrated in Fig. 3.1C. The current $\boldsymbol{I}_\mathrm{ex}$ through the central strip (signal line) flows opposite to the lateral strips (ground lines). An electric (not shown) and magnetic field $\boldsymbol{h}_\mathrm{ex}$ is generated on top and in the space between the strips (gap) as shown. The time dependence of the fields follows the oscillations of the applied current. If the excitation matches the resonance frequency of the magnetic system, ferromagnetic resonance (FMR) can be observed. In this state, the spins precess around their equilibrium position, comparable to the situation shown in Fig. 2.9A [125, 126]. The field distribution $\boldsymbol{h}_\mathrm{ex}(\boldsymbol{r})$ that is displayed in Fig. 3.1C is calculated using the lengthy Karlqvist equation which is found e.g. in Ref. [127].

3.1.2 Magnetic X-ray scattering

Before considering dynamic situations like the one discussed in section 3.3, the scattering off static magnetic structures is considered. As already mentioned, this description will be very close to the experimental situation in Cu_2OSeO_3 and will not generally be applicable. To begin with, a hypothetical sample, containing a mono-$\boldsymbol{q}_\mathrm{h}$ helical domain along $[100]$-direction is considered, which is shown in Fig. 3.2A. Naturally, the spin helix is magnified for the figure and does not represent its actual dimensions. For a qualitative understanding of the scattering condition,

the Laue-condition is considered. It says that the process of diffraction requires the difference vector $\Delta\boldsymbol{k}$ of initial and final photon wave vector $\boldsymbol{k}_\mathrm{i}$ and $\boldsymbol{k}_\mathrm{f}$ to be equal to a reciprocal lattice vector $\boldsymbol{G}_{hkl}$. For elastic scattering $\boldsymbol{k}_\mathrm{i} = \boldsymbol{k}_\mathrm{f}$, this is equivalent to Bragg's law. For resonant scattering off magnetically modulated structures, the magnetically scattered peaks appear as satellite peaks of the structural Bragg peaks [49, 50, 121, 128–130]. In this case, the Laue condition can be extended to [50]

$$\Delta\boldsymbol{k} = \boldsymbol{k}_\mathrm{f} - \boldsymbol{k}_\mathrm{i} = \boldsymbol{G}_{hkl} \pm \boldsymbol{q}_\mathrm{h} \,. \tag{3.1}$$

The attribute resonant in the scattering context means that the x-ray wavelength is tuned such that electrons from a single core level are excited to the Fermi level. In the case of 3d-ferromagnets this is from the $2p\frac{1}{2}$ (L_2 edge) or $2p\frac{3}{2}$ (L_3 edge) levels. The circularity of the x-rays and the selection rules determine the spin type of the electron to be excited. As the density of states at the Fermi level of a ferromagnet differs for each of the two spin directions, the photon absorption depends on the magnetization of the sample. This effect is called X-ray circular magnetic dichroism (XMCD) [120, 131, 132]. Regular Bragg scattering is explained by a constructive interference of different beam paths that occur due to the reflection from parallel lattice planes. The effect is therefore based on the periodicity of the atomic lattice or the periodicity of the charge distribution that follows the crystal structure. The periodicity of a magnetic spin helix is also connected to the atomic lattice, although λ_h is much larger than the lattice constant. For a spin helix, this can be pictured as a 1D magnetic superlattice. Considering this, it is plausible that the photons in the magnetically sensitive scattering experiment are also scattered from the periodic magnetization distribution [121].

For now, Bragg scattering on the (001)-Bragg peak of the previously introduced artificial sample is considered. To use the Ewald construction on Eq. (3.1), the modulation vectors $\boldsymbol{q}_\mathrm{h}$ have to be imposed on the reciprocal space lattice [128]. The modulation vector magnitude of Cu_2OSeO_3 is $q_\mathrm{h} = 0.1\,\mathrm{nm}^{-1}$ and the used photon energy at the L_3 edge is 931 nm which corresponds to $k_\mathrm{i} = 4.7\,\mathrm{nm}^{-1}$. Therefore, the reciprocal space positions $\boldsymbol{G}_{001} \pm \boldsymbol{q}_\mathrm{h}$ are close to $\boldsymbol{G}_{001}$. The reciprocal space in the vicinity of $\boldsymbol{G}_{001}$ is shown in Fig. 3.2B.

The Ewald construction for this situation is shown in Fig. 3.2C. The incident wave vector k_i ends in the origin of reciprocal space (gray dot). The three points at (001) are indicated with the same coloring as in Fig. 3.2B. When the sample is tilted around $[010]$ by an angle ω, the whole reciprocal space is rotated in the same manner. Elastic scattering $k_\mathrm{i} = k_\mathrm{f}$ defines the Ewald sphere. Once one of the three reciprocal points lies on the Ewald sphere for a specific tilt value of the sample, scattering occurs. Fig. 3.2C shows three different situations during a typical ω rocking scan.

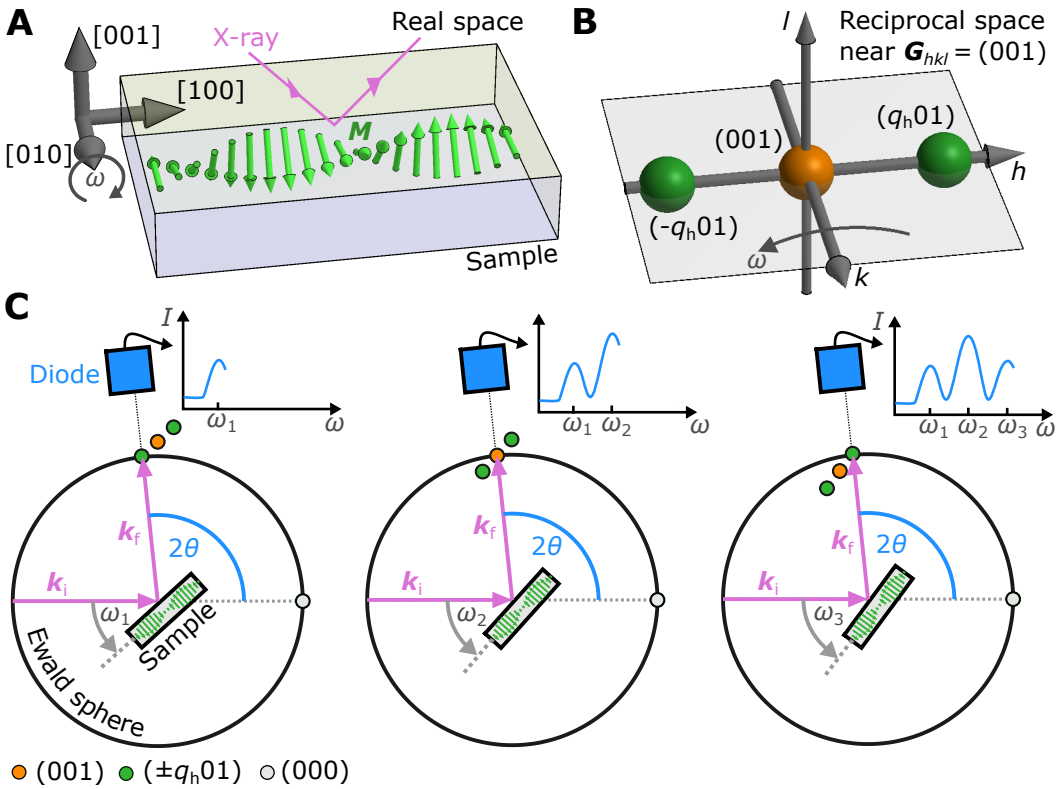

Fig. 3.2.: Ewald construction of REXS on a helical phase in Cu_2OSeO_3. **(A)** Sample orientation with an example helical magnetization structure (enlarged). **(B)** Reciprocal space in the vicinity of (001). The helical modulation vectors $\pm\boldsymbol{q}_\mathrm{h}$ are imposed onto the reciprocal lattice. **(C)** Ewald construction for scattering off the sample in (A). The sample is rotated around $[010] \parallel \hat{\boldsymbol{x}}$. Three situations for increasing angles $\omega = \omega_1 < \omega_2 < \omega_3$ are shown. In the three panels, the scattering condition is successively fulfilled for each one of the three reciprocal space positions shown in (B). In this example, the diode would detect three intensity maxima during the ω-rocking scan as indicated by the insets. Images in (C) are inspired by the supplementary material in [50].

The sample orientation and spin structure is indicated by the rectangle in the center of the sphere. In the situation on the left, the scattering condition is fulfilled for $(-q_\mathrm{h}01)$ and an intensity maximum is measured in the diode signal as indicated in the inset graph. When further increasing ω, the scattering condition for (001) and $(+q_\mathrm{h}01)$ is fulfilled and two more peaks show up successively while tracking the diode signal. Note that this reflection scattering geometry is quite untypical e.g. when coming from an electron scattering background with TEM. Here, the sample tilt gives a rotation of the scattering condition ensemble in Fig. 3.2B around (000), which leads to the dipping of the three vectors into the Ewald sphere. During the ω scan, the three points in Fig. 3.2B are not rotated around the drawn k-axis, but around (000), as indicated by the low curvature of the circular arrow.

From this, it becomes clear that the magnetically scattered beams appear as side-peaks or satellite-peaks around the structural Bragg peak. This description explains the geometry of the scattering experiment, however it lacks the description of the scattered intensity of the individual peaks and their individual (magnetic) contributions. A detailed mathematical discussion on this issue can be found in Ref. [121]. It is applied later in section 3.3 and appendix A.1. Note that for the three presented scattering conditions, the diode angle 2θ is not adjusted while ω changes. This is not a general case and only possible for the specific geometry used in the experiment, where all three scattered beams are captured due to the diode's finite acceptance angle.

3.2 Experimental static reciprocal imaging of modulated phases in Cu_2OSeO_3 using Resonant Elastic X-ray Scattering

In this section, the experimental data is presented. After the experimental parameters are given, the phase diagram of Cu_2OSeO_3 is shown. With that in mind, reciprocal maps of the helical, conical and hexagonal skyrmion lattice phase are successively shown. To aid the qualitative understanding of the observed patterns, sketches similar to the ones in Fig. 3.2 are included. Finally, a reciprocal space map of the novel low-temperature (LT) skyrmion phase is shown. On this phase, real-space imaging has been attempted in section 4.3.

The Cu_2OSeO_3 sample is grown by A. Aqeel[1] using the chemical vapor transport method. It is cut to a cuboid of dimensions $1.8 \times 0.5 \times 0.5\,\mathrm{mm}^3$. It is oriented such that the edges are parallel to $[110]$, $[1\bar{1}0]$ and $[001]$. One of the two large surfaces, parallel to (001), is mechanically polished. With the polished side facing top, the sample is placed into the gap of a shorted coplanar waveguide. The waveguide has a gap width of 1 mm. The relative scale in Fig. 3.1B is close to the real physical situation. The sample is inserted such that its surface slightly protrudes the top surface of the waveguide. Comparing with Fig. 3.1C, the excitation field $\boldsymbol{h}_{\mathrm{ex}}$ is therefore expected to be a mixture of in- and out-of-plane components. The out-of-plane excitation, however, is dominant. Once the sample is transferred into the UHV chamber, the circularly polarized photons are tuned to the Cu L_3 edge which corresponds to a photon energy of 931.1 eV [133]. As already explained in the last section, magnetic scattering from modulated spin structures occurs in the vicinity of structural Bragg scattered peaks. As the soft X-ray wave vector is fixed to $4.7\,\mathrm{nm}^{-1}$,

[1] Physik-Department, Technische Universität München, Garching, 85748, Germany.

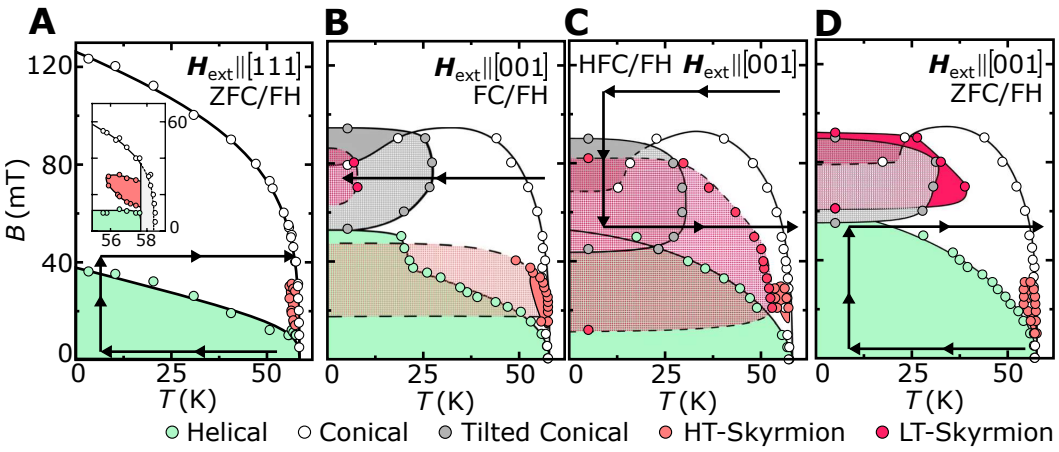

Fig. 3.3.: Magnetic phase diagrams of bulk Cu_2OSeO_3 for different histories of externally-applied magnetic field and temperature. **(A)** ZFC phase diagram with $\boldsymbol{H}_{\mathrm{ext}} \parallel [111]$ obtained by SANS. The sample is cooled at zero externally-applied magnetic field to lowest possible temperatures. Then the field is increased to a certain value before the sample is field-heated (FH) above T_{c} and the process is repeated for a different magnetic field. The inset shows a magnification for T close to T_{c} and gives a better view of the skyrmion pocket. **(B)** Field-cooled (FC) phase diagram for $\boldsymbol{H}_{\mathrm{ext}} \parallel [001]$. Here, the sample is cooled for different finite field values. The two novel tilted conical and low-temperature skyrmion phases emerge due to the different direction of $\boldsymbol{H}_{\mathrm{ext}}$. **(C)** High-field cooled (HFC) phase diagram for $\boldsymbol{H}_{\mathrm{ext}} \parallel [001]$. The sample is cooled for $H_{\mathrm{ext}} > H_{\mathrm{c2}}$. Then it is decreased to a certain value before the sample is field-heated. **(D)** Zero-field cooled phase diagram for $\boldsymbol{H}_{\mathrm{ext}} \parallel [001]$. The inset in (A) is reprinted with permission from [54]. The other graphs are also slightly modified versions reprinted with permission from [117].

the large lattice parameter of Cu_2OSeO_3 limits the selection to the (001)-Bragg peak. The spacing of the (001) planes is $d_{001} = 0.8925\,\mathrm{nm}$ which gives $G_{001} = 7.1\,\mathrm{nm}^{-1}$ [53]. Bragg's law gives the scattering angle $2\theta = 96.5°$. For a visualization, revisit Fig. 3.2C which is close to the actual geometry. Note that scattering from the (001) lattice planes is actually crystallographically forbidden for the space group $P2_13$. The peak can, however, be observed when the scattering takes place in resonance. The exact reason for this is still not completely understood [50, 128, 134].

The X-ray is focused onto the sample surface with a spot diameter of $\approx 100\,\mu\mathrm{m}$. The scattered photons are captured with the photo-diode. The diode angle 2θ and the sample angle ω are initially tuned to obtain maximum Bragg intensity. Starting in the paramagnetic phase, the sample is cooled below $T_{\mathrm{c}} \approx 58\,\mathrm{K}$ at zero applied magnetic field. The magnetic phase diagram obtained from small angle neutron scattering (SANS) for a zero-field cooled sample of Cu_2OSeO_3 is shown in Fig. 3.3A [117]. For $\boldsymbol{H}_{\mathrm{ext}} \parallel [111]$, it has the shape of the generic phase diagram presented in section 2.1.3. The arrows indicate the trajectories through phase space that are followed to obtain the phase diagram. At $H_{\mathrm{ext}} = 0\,\mathrm{mT}$ and $T = 30\,\mathrm{K}$, the helical

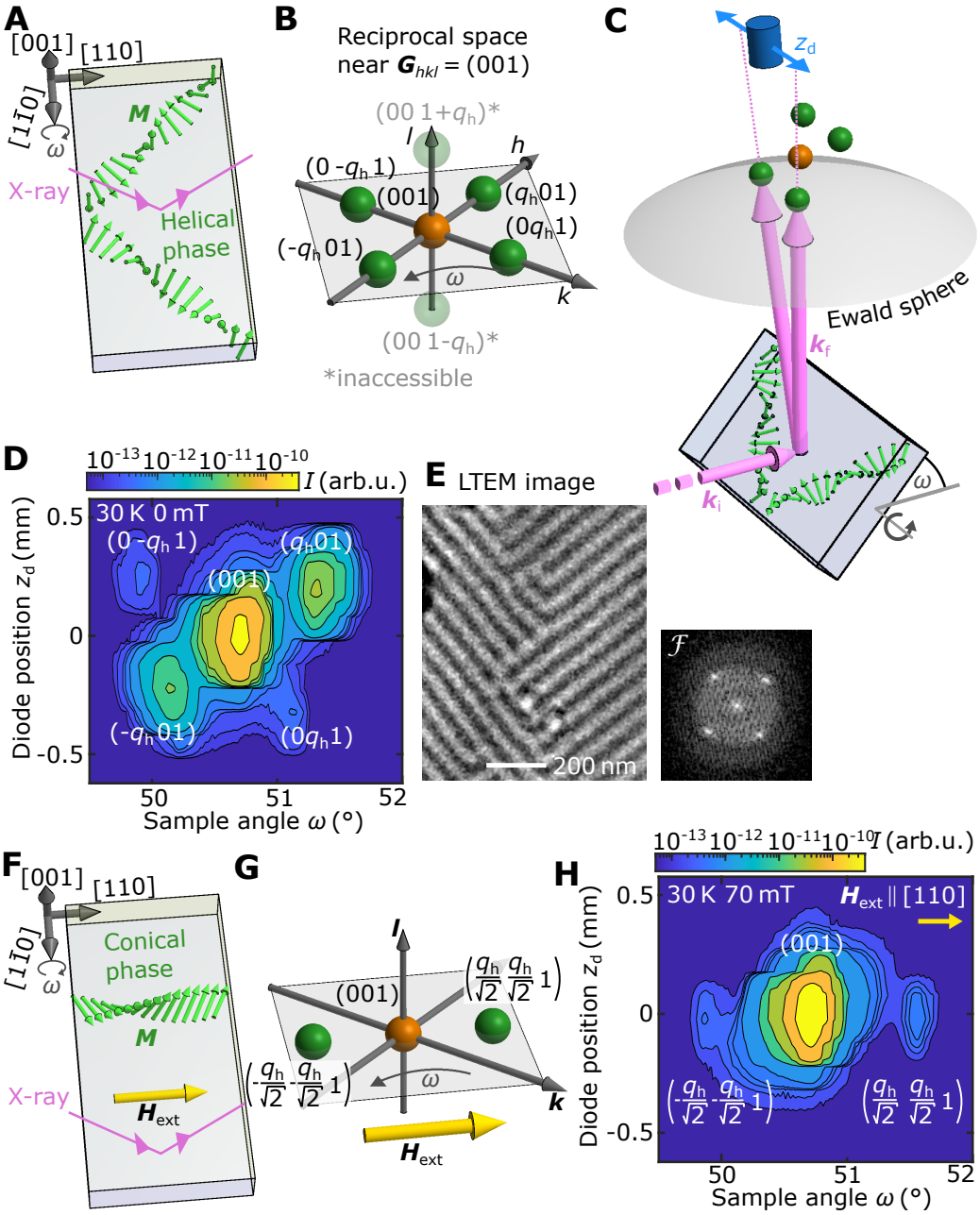

Fig. 3.4.: Reciprocal space maps of helical and conical phase. **(A)** Sample geometry with two indicated helical domains. **(B)** Reciprocal space near (001) with imposed helical q_h-vectors. **(C)** Ewald construction for scattering condition drawn in 3D. **(D)** Experimental reciprocal space map obtained by REXS. **(E)** LTEM micrograph showing domain boundary of two differently oriented helical domains in Cu_2OSeO_3, which explains the emergence of more than two helical peaks at the same time. The inset is an FT of the image and shows four side peaks like the scattering data. **(F)** Sample geometry with a conical phase with q_h parallel to the applied magnetic field. **(G)** Reciprocal space near (001) with imposed conical modulations. **(H)** Experimental reciprocal space map of the conical phase. The TEM image in (E) is median filtered with a kernel of 3×3 pixel^2 and subsequently Gaussian filtered with $\sigma = 2$ pixel.

phase is present. In Cu_2OSeO_3, the $\boldsymbol{q}_\mathrm{h}$-vectors of the helical phase align parallel to the $\langle 001 \rangle$ directions, which are the easy axes of the cubic anisotropy in the system. Fig. 3.4A shows a sketch of the sample containing two helical domains with $\boldsymbol{q}_\mathrm{h}$ within the sample plane. As the (001)-Bragg peak is measured, the $\boldsymbol{q}_\mathrm{h}$-vectors of the helical phase need to be imposed on the (001)-reciprocal space vector as shown in Fig. 3.4B. The four green spheres in the plane originate from the domains drawn in Fig. 3.4A. The additional two spheres represent helical domains with $\boldsymbol{q}_\mathrm{h}$ parallel to the sample normal which in principle are also present. However, they cannot be measured for this setup without further diode adjustment. This is skipped as it does not possess further relevance. Only the in-plane $\boldsymbol{q}_\mathrm{h}$-domains are considered in the following.

The scattering condition can be understood from the explanations given in section 3.1. However, in contrast to the 2D problem considered in Fig. 3.1C, here the reciprocal satellite vectors around $[001]$ lie on a plane. Therefore, the sketch needs to be extended to 3D, which is briefly illustrated in Fig. 3.4C. As can be seen for the given sample tilt ω, the reciprocal space vectors $(0\,{-}q_\mathrm{h}\,1)$ and $(-q_\mathrm{h}01)$ fulfill the scattering condition at the same time. Therefore in addition to ω, it is also necessary to scan the diode height z_d in order to measure all four satellite peaks. In the experiment, ω-scans are recorded for different values of z_d. The resulting intensity scan is therefore no longer 1D as in Fig. 3.1C but a 2D intensity distribution like the one shown in Fig. 3.4D. As expected, it shows the structural Bragg peak in the center and the four satellite peaks that represent the in-plane helical domains. At $T = 30\,\mathrm{K}$, the helical satellite peak intensity is around two orders of magnitude weaker than the Bragg peak intensity. The different satellite peak intensities of the two opposing pairs can be explained by a varying helical domain population that is sampled by the x-ray spot. In this case, ω samples the $[110]$ and z_d the $[1\bar{1}0]$-direction in reciprocal space. It should be noted that this is actually the first successful magnetic scattering experiment that has been performed at the VEKMAG end-station.

A few peculiarities about these maps should be mentioned. The first is the horizontal lines that are especially prominent at the top and bottom of the Bragg peak, e.g. in Fig. 3.4D. These are interpolation artifacts as the shown map section only consists of 18 ω-scans for different values of z_d. A second issue is that the map becomes distorted for large absolute values of z_d as the diode movement is linear and not spherical around the sample. A third problem concerns the elliptical distortion of the peaks, which is not solely a result of plotting an angle versus a length. In fact, the reciprocal resolution along $[110]$ (ω) is larger compared to $[1\bar{1}0]$ (z_d). This is a result of the finite pin-hole diameter of the diode. As already mentioned, the diode angle 2θ is kept constant during the scan as all helical spots can still be captured this way (compare Fig. 3.1C). This, however, is not generally possible and requires

the right interplay of pin-hole diameter, magnitude of $\boldsymbol{q}_\mathrm{h}$, photon wave vectors and a short sample-detector distance (here 20 mm). In fact, as 2θ is not adjusted, larger pin-holes would enable a more consistent measurement of the full peak extents as the peak width in ω-direction is governed by the respective broadening of the scattering condition in reciprocal space. Oppositely, the pin-hole diameters directly influence the resolution in z_d-direction, as the scattering condition is not changed during a z_d-scan. Therefore, the intensity peaks are convoluted with a pulse function that has the width of the pin-hole diameter along z_d. This means that the diode size needs to be chosen small enough that the resolution in z_d is sufficient to separate the peaks, while it is large enough to still capture all peaks in ω direction. Despite these problems, the peaks are still well separable and as the ultimate goal is not to produce the historically most accurate measurements of the modulated phases in reciprocal space but to measure FMR, the quality of the obtained maps are sufficient. For accurate maps of reciprocal space, CCD camera measurements are much more suited, also considering that the measurement time of $\approx 3\,\mathrm{h/map}$ leaves the data vulnerable to slow drifts of the setup or unexpected beam shutdowns.

As the illustration of the two domains in Fig. 3.4A is rather vague, an actual real-space Fresnel LTEM image of such a two-domain state in Cu_2OSeO_3 is presented in Fig. 3.4B. The measurement is made on an equivalent crystal, also grown by A. Aqeel. The orientation of the two domains is rotated by 90° with respect to each other. The two domains are separated by a domain boundary that consists of defects like stripe endings or 90° stripes. Interestingly, such defects can possess half of a topological charge as shown in Ref. [135]. The Fourier transform (FT) in the inset shows the spots equivalently to the scattering data, although the central spot is not related to the Bragg peak, of course.

After application of an external magnetic field of 70 mT, the presence of the conical phase is expected from the phase diagram in Fig. 3.3A. As $\boldsymbol{q}_\mathrm{h}$ will align parallel to the external magnetic field, it is applied in $[110]$-direction in order to be able to capture the wave vector of the conical phase with the established setup. A sketch of this is shown in Fig. 3.4F. The corresponding reciprocal space in the vicinity of (001) with the reciprocal satellite points $(\pm q_\mathrm{h}/\sqrt{2}\,\pm q_\mathrm{h}/\sqrt{2}\,1)$ is shown in Fig. 3.4G. The experimental reciprocal space map of the conical phase is displayed in Fig. 3.4H.

To probe the skyrmion phase, the sample needs to be heated to temperatures just below T_c. A magnification of the phase space in this area is shown in the inset of Fig. 3.3A [54]. Note that for 1 K below T_c, the system is already ferromagnetic but no distinct magnetic modulations are visible from scattering experiments. This is sometimes referred to as fluctuation dominated phase, to indicate that in this phase thermal fluctuations destroy any long range order. To find the right temperature

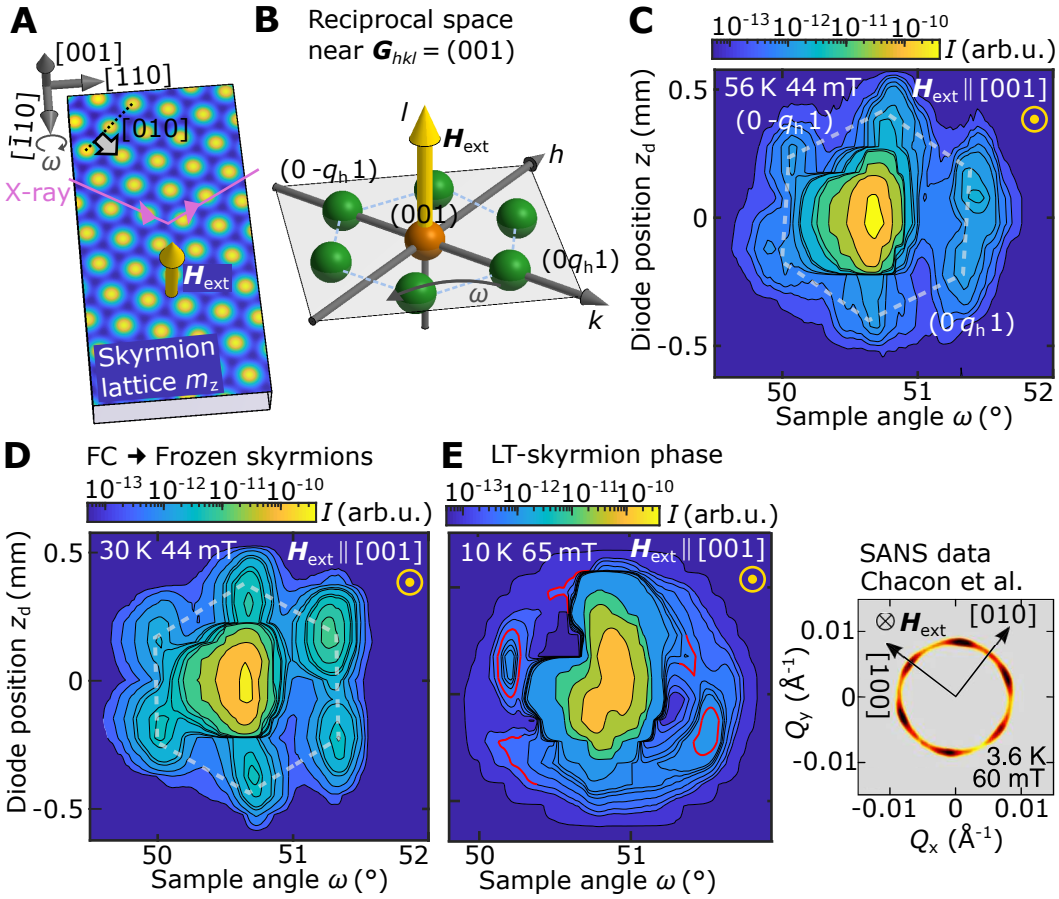

Fig. 3.5.: Reciprocal space maps of skyrmion and LT-skyrmion phase. **(A)** Sample geometry and indicated skyrmion lattice. **(B)** Reciprocal space near (001) with imposed skyrmion $\boldsymbol{q}_h$-vectors. **(C)** Experimental reciprocal space map obtained by REXS for skyrmion phase and **(D)** field-cooled skyrmion phase. **(E)** Experimental reciprocal space map of LT-skyrmion phase and SANS data for comparison. The SANS data in (E) is taken from [117].

calibration of the setup, the intensity of one of the helical peaks is observed during heating. Once the intensity vanishes, $T_c \approx 58\,\mathrm{K}$ is found. To find the skyrmion phase, the temperature is set to 56 K. Due to the long acquisition times of a map, choosing the right field to find the skyrmions pocket can actually become time-consuming and it is preferred to avoid the acquisition of many maps at different magnetic fields. Also the phase diagrams, like the one shown in Fig. 3.3A, are not perfectly reliable, as different sample shapes can lead to deviations. With the present setup, the best technique found is to tune ω and z_d to one of the helical peaks and conduct an out-of-plane field scan. As also one of the three skyrmion modulation directions are fixed to $[010]$ [54], there is basically a 50 % chance of finding a skyrmion signature during the scan. This way, it is possible to set the field to a value at the center of the

skyrmion pocket, where the peak intensity and the distance to phase borders are largest.

A sketch of the sample geometry with a skyrmion phase is depicted in Fig. 3.5A. In this example, one of the modulation directions is attached to the $[010]$ direction. The external field $\boldsymbol{H}_{\mathrm{ext}}$ is applied along the sample normal such that all $\boldsymbol{q}_{\mathrm{h}}$-vectors of the skyrmion phase lie inside the (001)-plane. The corresponding reciprocal space near (001) is shown in Fig. 3.5B. In this example, the reciprocal space positions that correspond to the skyrmion lattice state are at $[0, \pm q_{\mathrm{h}}, 1]$, $[\pm\sqrt{3}q_{\mathrm{h}}/2, \pm q_{\mathrm{h}}/2, 1]$ and $[\pm\sqrt{3}q_{\mathrm{h}}/2, \mp q_{\mathrm{h}}/2, 1]$. An experimental reciprocal map of the skyrmion lattice at $T = 56\,\mathrm{K}$ and $\mu_0 H_{\mathrm{ext}} = 44\,\mathrm{mT}$ is displayed in Fig. 3.5C. The six satellite peaks lie on the edges of a hexagon and are clearly discernible although their intensity is lowered by around an order of magnitude in comparison to the measured intensity of the helical phase shown previously, which is due to the increased temperature that dictates a lower saturation magnetization.

Recently, it was discovered that the phase diagram of Cu_2OSeO_3 drastically changes when the external magnetic field is applied along one of the easy $\langle 100 \rangle$ axes [117]. For this case, strong deviations from the general phase diagram of the B20 chiral magnets, discussed in section 2.1.3, were observed, even though Cu_2OSeO_3 follows it perfectly for $\boldsymbol{H}_{\mathrm{ext}} \parallel [111]$ (compare Fig. 3.3A). In Fig. 3.3B, a so called field-cooled phase diagram is displayed for $\boldsymbol{H}_{\mathrm{ext}} \parallel [001]$ [117]. It is obtained by cooling the sample at different constant external magnetic fields while tracking the magnetic phases using SANS. Note that an overlap of phases represents coexistence. For further details, please refer to Ref. [117].

The first difference of this phase diagram to the one shown in Fig. 3.3A is that the narrow temperature range of the skyrmion pocket is extended to lower temperatures. This is actually not a consequence of $\boldsymbol{H}_{\mathrm{ext}} \parallel [001]$ but a sample history dependent observation in many of the B20 chiral magnets [63, 136–138]. A map of such a frozen skyrmion lattice is shown in Fig. 3.5D. It is obtained by cooling a skyrmion lattice like the one shown in Fig. 3.5C[2] to $T = 30\,\mathrm{K}$ while maintaining a constant field of 44 mT. The satellite peaks of the super-cooled skyrmion lattice show an increased intensity by an order of magnitude and become more distinguishable.

The even more striking new features of the phase diagram are the two newly observed phases at low temperatures and magnetic fields below but close to H_{c2}. One of the new phases is the tilted conical phase. It is metastable and accompanies the emergence of a second new low-temperature (LT) skyrmion phase. In H_{ext}-T-space, this LT skyrmion phase is disconnected from the high-temperature (HT) skyrmion phase and is stabilized due to the magnetocrystalline anisotropies in Cu_2OSeO_3 [117,

[2] It is not directly obtained from this particular map, which can be seen from the different orientation of the spots.

118]. In SANS, the LT-skyrmion phase appears as a circular signature around the zero-beam and can be partly transformed to a six-spot pattern by a field inclination of around 15° away from $[001]$, as shown on the right side of Fig. 3.5E. This indicates that the skyrmion lattice at such low temperatures is highly frustrated and does not possess long range order. For a re-creation in terms of REXS, the sample is field-cooled to $T \approx 10\,\mathrm{K}$ at $H_{\mathrm{ext}} = 65\,\mathrm{mT}$, which gives the most consistent results. FMR measurements by Aqeel et al. suggest that slow field oscillations in the LT-skyrmion phase can enhance the long-range LT-skyrmion order [139]. Therefore, the field is oscillated one hundred times between 65 and 100 mT with $100\,\mathrm{mT\,s^{-1}}$. Afterwards, the field is inclined by $20°$ away from and back to $[001]$ to obtain the REXS map displayed on the left side of Fig. 3.5E. The ring around the Bragg peak is clearly visible, the six spot pattern, however, remains elusive. There is some spot like structure which is indicated with the red markings. This map is the closest to the SANS measurements published in Ref. [117]. Although the data is promising, no FMR measurements on this phase are shown later due to the imperfect result. Nevertheless, the REXS data can serve as a motivation for the LTEM imaging on (001)-Cu_2OSeO_3 performed in section 4.3.

3.3 Resonant Elastic X-ray Scattering Ferromagnetic Resonance

In this section, the REXS measurements on resonantly excited magnetic skyrmions in Cu_2OSeO_3 are presented. In the beginning, micromagnetic simulations are shown, using a model that is close to the experimental system. This approach has two benefits: First, it can give quantitative expectations for the experiments presented afterwards. Second, it is an educational way to introduce the skyrmion eigenmodes, which was intentionally skipped up to this point.

After this theoretical introduction, the experimental results are presented. The FMR-eigenfrequencies of the field-polarized, helical and skyrmion phase are measured by recording the external magnetic field dependence of the Bragg or satellite peak intensity and comparing cases with active to inactive excitation field $\boldsymbol{h}_{\mathrm{ex}}$. These scans are repeated for different excitation frequencies. Actually, this is the foundation of a novel technique labeled REXS-FMR, which is capable of an element- and magnetic phase selective measurement of the ferromagnetic resonance.

3.3.1 Skyrmion eigenmodes

For a theoretical description and introduction of the skyrmion eigenmodes, micromagnetic simulations are conducted. The proposed micromagnetic model includes exchange, bulk DMI, magnetic cubic anisotropy and Zeeman energy. The required micromagnetic energy constants are conveniently taken from Janson et al., who calculated them using ab-initio calculations for Cu_2OSeO_3 at $T = 50\,\mathrm{K}$, which is close to the actual experimental temperature of 56 K [65]. A simulation grid with $512 \times 512 \times 1$ cells ($\hat{\boldsymbol{x}} \times \hat{\boldsymbol{y}} \times \hat{\boldsymbol{z}}$) and periodic boundary conditions in all three directions are imposed. The physical grid dimensions are set to $115 \times 100 \times 0.22\,\mathrm{nm}^3$, such that a spin helix with $\boldsymbol{q}_\mathrm{h} \parallel \hat{\boldsymbol{y}}$ and $\lambda_\mathrm{h} = 50\,\mathrm{nm}$ as well as a hexagonal skyrmion lattice with one of its $\boldsymbol{q}_\mathrm{h} \parallel \hat{\boldsymbol{y}}$ can fit inside the grid without imposing a geometrical frustration by the periodic boundary conditions. The grid containing the latter two configurations is depicted in Fig. 3.6A for a subsampling of 8. The cell line density of 225 cells $/q_\mathrm{h}$ is large. The easy axes of the magnetic cubic anisotropy are fixed such that they are parallel to $\hat{\boldsymbol{z}} \parallel [001]$, $\hat{\boldsymbol{y}} \parallel [100]$ and $\hat{\boldsymbol{x}} \parallel [010]$. The simulations and energy calculations are performed using the MuMax3 framework [116]. To verify that the expected equilibrium value of $\boldsymbol{q}_\mathrm{h}$ is correct, the periodic boundary conditions are omitted and a helical phase with variable λ_h is manually generated and the total energy density ϵ_total is calculated. This is done for both signs of D_bulk. The resulting dependencies are plotted in Fig. 3.6B. Unsurprisingly, the energetic minimum is found for $\lambda_\mathrm{h} \approx 50\,\mathrm{nm}$ for $D_\mathrm{bulk} > 0$, as targeted by the ab-initio calculations [52, 65]. The spin configuration at the minimum energy is the one shown in Fig. 3.6A, as indicated by the triangle.

Before studying the resonant excitations of this system, the phase diagram at $T = 50\,\mathrm{K}$ is briefly consulted, to find an external magnetic field value where the skyrmion state is stable. Note that the temperature is considered only by adjusted magnetic constants like reduced M_s and not e.g. by an additional random thermal noise that is added to $\boldsymbol{m}$, which is sometimes done for these kinds of simulations. The energy density with respect to an externally applied magnetic field along $\hat{\boldsymbol{z}}$ is calculated for the helical, skyrmion and field-polarized phase. The initial spin structure of helical and skyrmion phase is manually generated and further relaxed for each magnetic field value such that it reaches a local minimum. Note that the helical phase cannot relax to the skyrmion or field-polarized phase in the proposed magnetic field range because it is also topologically protected as there are no sample edges due to the periodic boundary conditions. The resulting energy densities are plotted in Fig. 3.6C. With increasing external field, the spin configuration with minimum energy changes from helical to skyrmion to field-polarized phase. Note that the conical phase is not considered as it cannot be fitted into the grid for

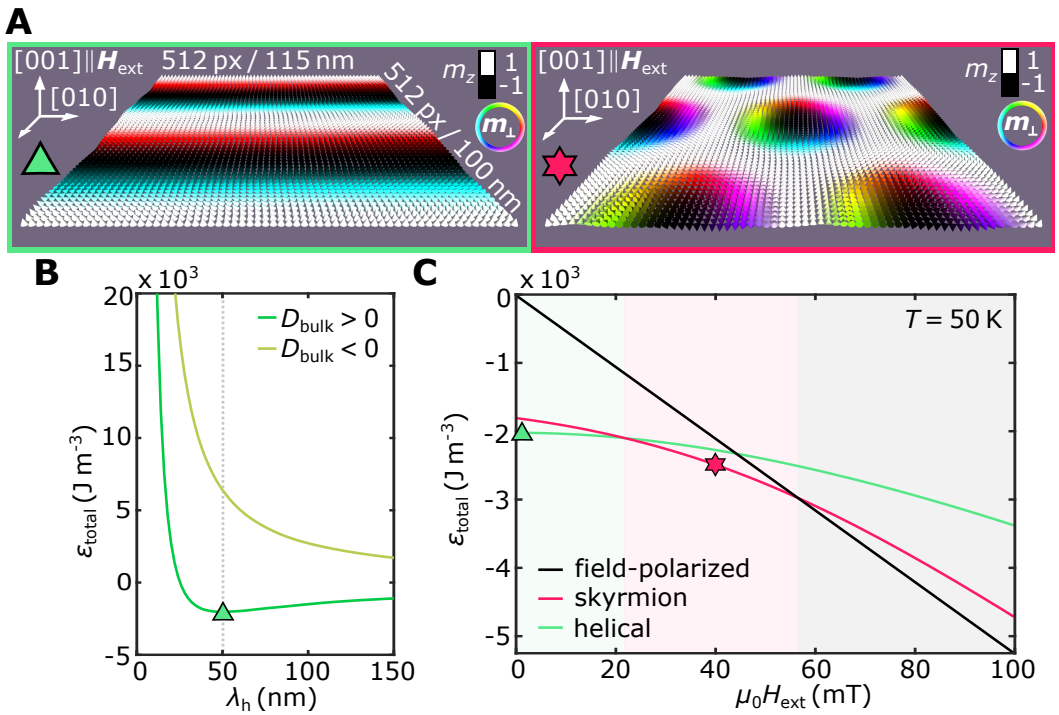

Fig. 3.6.: Energetics of the micromagnetic model for Cu_2OSeO_3. **(A)** Simulation grid dimensions and orientation. The left side shows the helical and right side the skyrmion phase with $\boldsymbol{q}_h$ oriented such that the spin structures fit into the grid's periodic boundary conditions. **(B)** Energy density for the helical phase with respect to λ_h omitting periodic boundary conditions. The minimum energy is found for $D_{bulk} > 0$ and $\lambda_h = 50\,nm$. **(C)** Energy density of helical, skyrmion and field-polarized phase with respect to externally applied magnetic field $\mu_0 \boldsymbol{H}_{ext} \parallel [001]$.

$\boldsymbol{H}_{ext} \parallel \hat{z}$. It is expected that not the skyrmion but the conical phase is the actual ground state of the system for reasons discussed in section 2.1.3. To simulate a realistic skyrmion state, an external magnetic field value in the center of the range where the energy density of the skyrmion state is below the energy density of the helical and field-polarized phase is chosen, as this should be where the thermally activated skyrmion pocket is found. Although the conical phase is not considered, the transition fields from helical to skyrmion and skyrmion to field-polarized phase are in good agreement with the experimental phase diagram shown in Fig. 3.3D.

In the following, the skyrmion phase is magnetically excited and the resonances are studied. For this, an external field of 40 mT is selected which is in the center of the calculated skyrmion phase range in Fig. 3.6C. The respective spin structure is depicted on the right side of Fig. 3.6A and marked with a star. The magnetic damping factor is set to $\alpha = 8 \times 10^{-3}$, as suggested by measurements of Stasinopoulos et al. [140]. To obtain the eigenfrequencies of the skyrmion lattice, the relaxed equilibrium skyrmion state is excited with a 10 ps long magnetic field pulse with an amplitude of

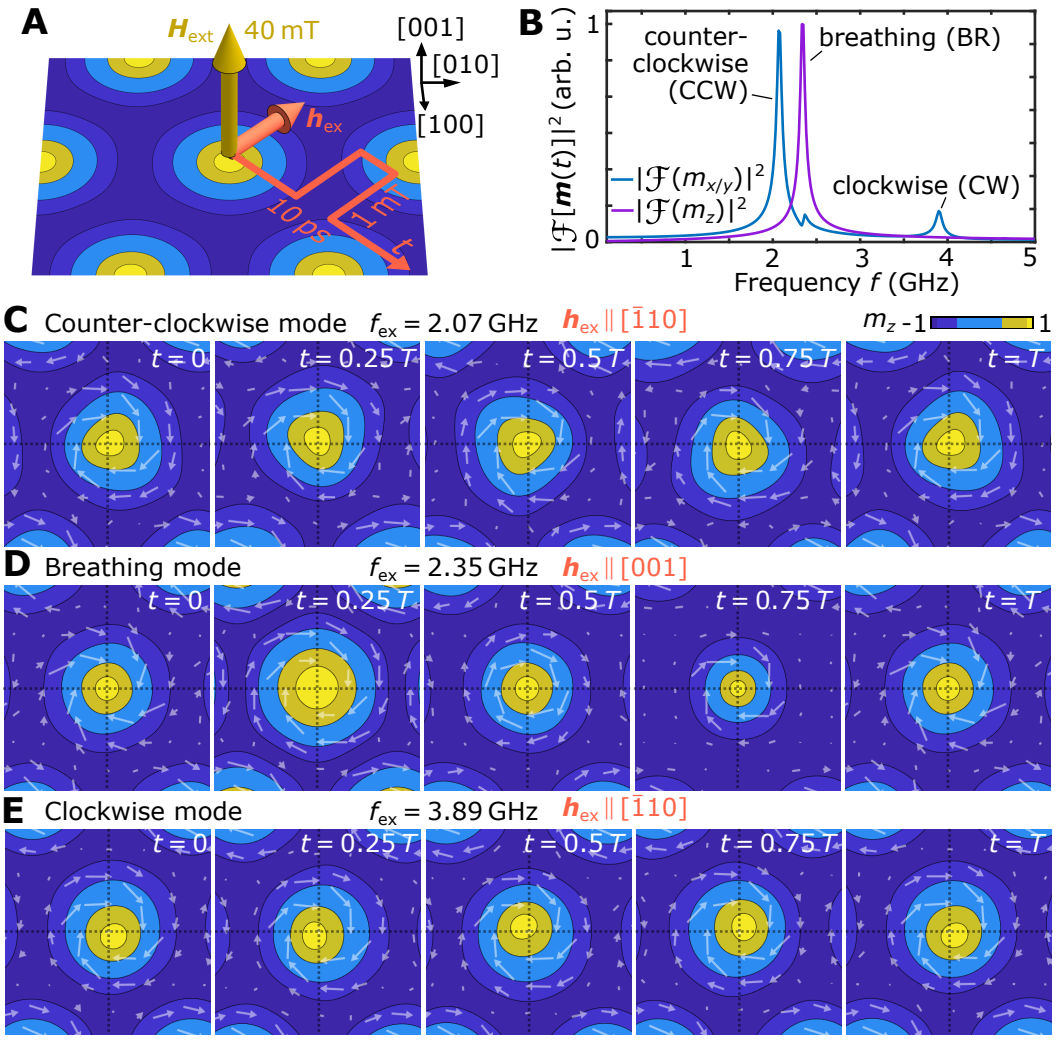

Fig. 3.7.: Simulated skyrmion resonance modes in Cu_2OSeO_3. **(A)** Magnetic field pulse for an even excitation of the system. **(B)** The calculated frequency spectrum of the magnetization's response shows three resonance peaks in the GHz range. **(C)** Simulated skyrmion structure for one oscillation period of the counter-clockwise mode during continuous excitation. Shown are m_z-isolines and arrows that represent the in-plane components of $\boldsymbol{m}$. **(D)** Breathing mode. **(E)** Clockwise mode.

1 mT along $[1\bar{1}0]$ as illustrated in Fig. 3.7A. The field pulse direction is not aligned with an in-plane symmetry axis of the skyrmion lattice, which could lead to an exclusion of certain excitations. The frequency spectrum of the delta-like excitation pulse is constant up to excitation frequencies of 5.9 GHz with a deviation of less than 1 %, which should give an equal excitation of eigenmodes with an eigenfrequency below that value. The response of the system after the pulse is recorded for 60 ns. The temporal evolution of the mean magnetization components of the whole system

shows a decaying sinusoidal-like behavior which is similar to the amplitude of a relaxing damped harmonic oscillator.

A spectral analysis of the damped magnetization precession to its equilibrium state reveals the eigenfrequencies of the skyrmion structure. The absolute square of the Fourier transforms of the mean magnetization components are plotted in Fig. 3.7B. The lateral magnetization components $m_{x/y}$ show two prominent resonances and an additional third one which is less pronounced but more visible in the spectrum of m_z. Ordered from low to high frequencies, these resonance modes are called counter-clockwise (CCW), breathing (BR) and clockwise (CW) mode [44, 45, 47]. Note that although the excitation pulse spectrum is essentially constant in the range of the excitation frequencies, the excitation response of the individual mode strongly depends on the orientation of the excitation field $\boldsymbol{h}_{\mathrm{ex}}$. If $\boldsymbol{h}_{\mathrm{ex}}$ is tuned parallel to $\hat{\boldsymbol{z}}$, the peak of the breathing mode spectrum is increased by a factor of 1.6, while the other two modes are not excited at all and their peaks disappear.

To visualize the three modes and understand their naming, the system is subsequently excited at each of the resonance frequencies. For the CCW mode, a sinusoidal excitation field $\boldsymbol{h}_{\mathrm{ex}}$ with a frequency $f_{\mathrm{ex}} = 2.07\,\mathrm{GHz}$ and an amplitude of 1 mT is applied along $[\bar{1}10]$ direction. After a settling time of around 25 ns, the system oscillates evenly. Snapshots during one oscillation period T are shown in Fig. 3.7C. The skyrmion is triagonally distorted and its core is shifted to one side of its equilibrium position; that is marked with the dashed cross. During the oscillation, the skyrmion revolves around $\hat{\boldsymbol{z}}$ in counter-clockwise direction.

For the breathing mode, the excitation frequency is set to $f_{\mathrm{ex}} = 2.35\,\mathrm{GHz}$ and the excitation field is aligned $\boldsymbol{h}_{\mathrm{ex}} \parallel [001]$ due to the enhanced Q-factor in this direction. After 35 ns, the snapshots in Fig. 3.7D are again recorded for one oscillation period. The mode starts at a situation that looks similar to the equilibrium configuration. At $t = 0.25T$, the skyrmion core and shell expands which is well visible from the m_z-isolines. Then, it shrinks to a minimum size at $t = 0.75T$ and grows again until it reaches the initial configuration of the process. This evolution of growing and shrinking resembles a breathing motion.

Finally, the last mode is recorded applying $f_{\mathrm{ex}} = 3.89\,\mathrm{GHz}$ and $\boldsymbol{h}_{\mathrm{ex}} \parallel [\bar{1}10]$. It is displayed in Fig. 3.7E and shows a displacement of the skyrmion core to one side and of the skyrmion wall to the opposite side. During the period, it rotates in clockwise direction. Besides this rotation, the m_z-isolines remain static, which explains why the CCW and CW modes are not visible in the spectrum of m_z in Fig. 3.7B.

Note that the identification and measurement of the three fundamental skyrmion modes is reported in several publications [44–47, 140–143]. The intention here is to introduce the resonant modes and supply a simulation that gives the expected resonance frequencies tailored for Cu_2OSeO_3.

3.3.2 Measurement of ferromagnetic resonance in Cu_2OSeO_3 using REXS

In this chapter, the ferromagnetic resonance in Cu_2OSeO_3 is studied in terms of REXS. This novel method is referred to as REXS-FMR. At first, the FMR measurements on the field-polarized phase at $T = 15\,\mathrm{K}$ are presented. For $H_{\mathrm{ext}} > H_{\mathrm{c2}} \approx 125\,\mathrm{mT}$, no magnetically modulated phase is present, which means that only the structural Bragg peak is accessible. A magnetic field scan with $\boldsymbol{H}_{\mathrm{ext}} \parallel \boldsymbol{k}_{\mathrm{i}}$ of the (001)-Bragg peak intensity is displayed in Fig. 3.8A (gray curve). Because the Bragg peak intensity comprises a magnetic contribution, $I\left(\boldsymbol{H}_{\mathrm{ext}}\right)$ looks similar to a hard axis loop. It is clearly visible that the hysteresis is not symmetric with respect to $I(0)$. This is because the magnetization contribution consists of terms that depend linearly and quadratically of $\boldsymbol{M}$, which can lead to such an asymmetry. Assuming a strictly linear dependence of the net magnetization $\boldsymbol{M}(\boldsymbol{H}_{\mathrm{ext}})$ for $H_{\mathrm{ext}} < H_{\mathrm{c2}}$ like in Eq. (2.21), an estimation for the actual dependence of $M(H_{\mathrm{ext}})$ can be extracted from the intensity scan using the formalism from Refs. [121, 130]. This is demonstrated in appendix A.1 for the shown case.

Nevertheless, already from this curve, the kinks at H_{c2} are clearly visible and mark when the system undergoes saturation and forms the field-polarized state. Further, slight slope changes for $H_{\mathrm{ext}} < H_{\mathrm{c2}}$ indicate phase transitions to the helical phase, which are described in more details in Refs. [54, 118, 144]. In order to study FMR, the excitation field $\boldsymbol{h}_{\mathrm{ex}}$ at a constant frequency f_{ex} ($= 4.5\,\mathrm{GHz}$ in the shown case) is repeatedly switched on and off at each magnetic field value. For both cases, the intensity is recorded using an integration time of 3 s. In contrast to the recording of two independent magnetic field scans, this way, the measurement is less subject to drifts of the scattering setup. Further, it is expected that the sample temperature stays more constant in contrast to a case where the microwave power is switched on all the time. This procedure also allows the conclusion that the magnetization state reproducibly switches from the excited to its equilibrium configuration for each field step. Typical excitation field magnitudes at the sample surface are in the order of 3 to 8 µT, dependent on f_{ex}, which is estimated using the Karlqvist equation [127].

The red curve for a switched-on excitation field in Fig. 3.8A shows clear deviations from the gray curve at $H_{\mathrm{ext}} \approx \pm 170\,\mathrm{mT}$. These features are attributed to the ferromagnetic resonance of the field-polarized phase. The normalized signal difference $(I_{\mathrm{on}} - I_{\mathrm{off}})/(I_{\mathrm{on}} + I_{\mathrm{off}})$ shown in Fig. 3.8B is of the order of 2 %. This corresponds to a reduction of the net magnetization by around 6.5 %, using the extracted $I\left[\boldsymbol{M}(\boldsymbol{H}_{\mathrm{ext}})\right]$ dependence from appendix A.1. This M reduction corresponds to a precession angle of around 21°, which is quite large for FMR but is still plausible considering the low effective damping factor $\alpha \approx 1 \times 10^{-4}$ reported for Cu_2OSeO_3 [140, 145]. An

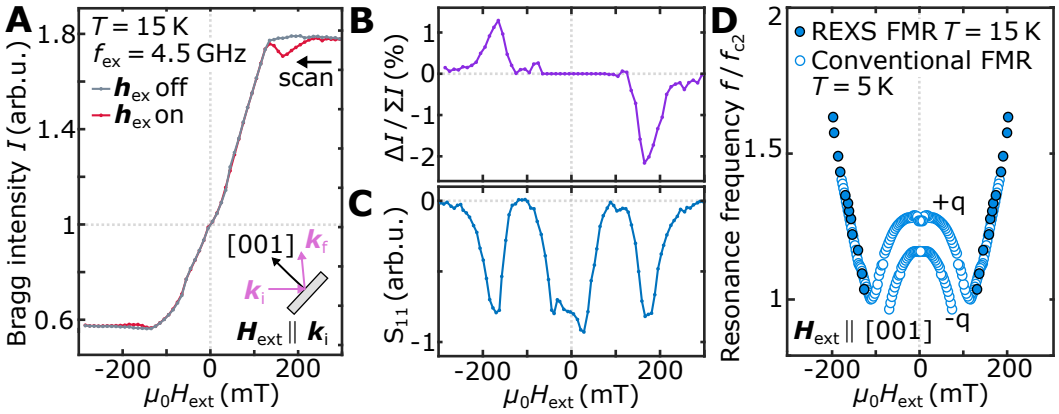

Fig. 3.8.: REXS-FMR on the (001) Bragg peak in Cu_2OSeO_3. **(A)** Applied magnetic field dependence of the Bragg peak intensity. At each point, the excitation field is turned off (gray curve) and on (red curve) successively. **(B)** Relative Change of the Bragg intensity under excitation. **(C)** Reflected microwave power simultaneously obtained. The absorption features around $H_{\mathrm{ext}} = 0\,\mathrm{mT}$ are attributed to the $\pm q$-modes of the helical phase. **(D)** Field dependence of the resonance frequencies obtained from the field-polarized phase with REXS-FMR in comparison to a conventional FMR measurement.

attribution of this change to heating effects would require the system to heat up and cool down by 13 K in less than a second between each switching of $\boldsymbol{h}_{\mathrm{ex}}$. Such a large temperature change seems also quite implausible as it would interfere with the REXS-FMR measurements on the skyrmion phase which has a narrow temperature width of around 2 K, presented later.

Simultaneously to the REXS-FMR measurement, a quantity that is proportional to the power of the reflected microwaves S_{11} is recorded by using a microwave circulator in combination with a Schottky-diode. This corresponds to a conventional FMR measurement, where FMR is detected by observing the absorbed microwave power when the system gets excited. The respective plot is displayed in Fig. 3.8C. The two resonances of the field-polarized phase are clearly visible. In addition, microwave power is absorbed around zero magnetic field, which corresponds to the excitations of the helical phase. No indications for these excitations are present in the Bragg peak intensity. As shown later, this does not mean that REXS-FMR is unable to detect the resonances of the helical phase, it rather highlights the feature of REXS-FMR to selectively study a specific magnetic phase.

In the following, the method is compared to conventional FMR on a similar Cu_2OSeO_3 crystal. For this, the external magnetic field direction is set parallel to $[001]$ and one of the resonance features in Fig. 3.8A is tracked for different values of f_{ex}. The resulting resonance frequencies are plotted in Fig. 3.8D using filled symbols. As a comparison, conventional FMR measurements based on microwave power-loss spectroscopy are included in the plot using the open symbols. These

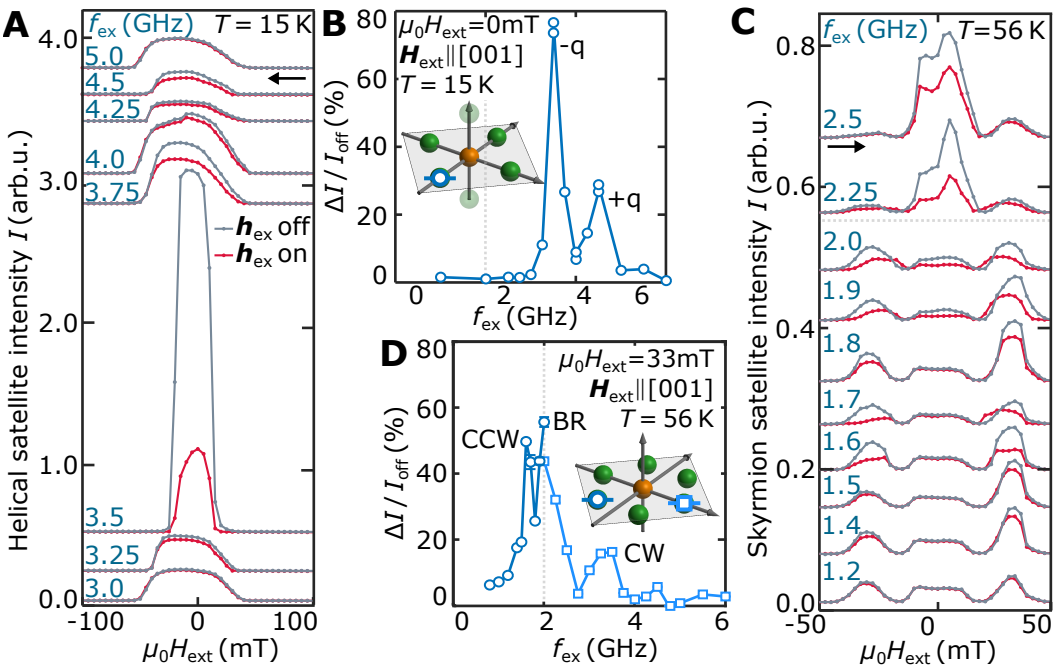

Fig. 3.9.: REXS-FMR on the helical and skyrmion lattice phase of Cu_2OSeO_3. **(A)** Magnetic field scans at a helical reciprocal space location for different values of f_{ex}. At each field step, data is recorded for inactive (gray curve) and active (red curve) excitation field. **(B)** Relative change of the helical spot intensity with applied excitation field at zero applied magnetic field. The inset shows the selected helical peak for the measurement. The two peaks correspond to the helical $+q$ and $-q$ modes. **(C)** Magnetic field scans at a skyrmion reciprocal space location for different excitation frequencies. The finite intensity around zero magnetic field arises from a helical reciprocal point that partly overlaps with the skyrmion one. **(D)** Relative reduction of the skyrmion peak intensity at $\mu_0 H_{ext} = 33\,\mathrm{mT}$. The inset shows the skyrmion peaks used in the measurement. At the dashed line, the setup is modified (see text) and the measured skyrmion peak is changed. Three maxima are observed that correspond to the CCW, BR and CW skyrmion modes.

measurements are performed by A. Aqeel[3] on an equivalent Cu_2OSeO_3 crystal at $T = 5\,\mathrm{K}$. To ensure comparability among the different temperatures of the two techniques, the resonance frequency axis is normalized with the resonance frequency f_{c2} at $H_{ext} = H_{c2}$. The measured resonance positions obtained by REXS-FMR are in excellent agreement with the field-polarized branch ($H_{ext} > H_{c2}$) obtained by conventional FMR. The dependence resembles a Kittel-like trend which matches the fact that the magnetization is uniform in this state. Therefore it is best described by the existent FMR-theory. However, as this is not the main interest of this study, the reader is referred to existent literature like Refs. [57, 125, 146–148]. Note that the graph is mirrored to match the field range of the other panels in that figure.

[3]Physik-Department, Technische Universität München, Garching, 85748, Germany.

The conventional FMR data also shows the field-dependence of the resonance frequencies of the helical and conical phase. Two mode branches are visible, which are called $+q$ and $-q$ modes as indicated. These are basically magnons[4] with $\boldsymbol{k}_{\mathrm{magnon}} = \pm\boldsymbol{q}_{\mathrm{h}}$; a more detailed description including a visualization can be found e.g. in Ref. [45]. To measure these modes with REXS-FMR, the scattering condition is adjusted to capture one of the helical satellite peaks, while maintaining a temperature of 15 K. The measurement protocol is equivalent to the one described before, at each magnetic field step, the helical satellite peak intensity is recorded with the excitation field turned on and off successively. The integration time is increased to 10 s. Magnetic field scans along $[001]$ for different values of f_{ex} are shown in Fig. 3.9A. Naturally, a finite helical spot intensity is only obtained below H_{c1}, when the helical phase is present.

Actually, the observed intensity scan contradicts the naive expectations. Starting in the field-polarized phase with $\boldsymbol{H}_{\mathrm{ext}} \parallel [001]$, one would expect that the $\boldsymbol{q}_{\mathrm{h}}$-vector of the conical and helical phase maintains a $[001]$-direction upon magnetic field reduction, as the other possible $\langle 100 \rangle$ easy anisotropy axes are behind an energy barrier, as explained around Fig. 2.3 in section 2.1.2 [76]. As already discussed, a magnetic modulation $\boldsymbol{q}_{\mathrm{h}} \parallel [001]$ cannot be accessed in the present scattering configuration and no in-plane modulations are expected. Still, a finite helical intensity is measured when decreasing the field from the saturated state. The reason for this is attributed to the novel LT-skyrmion phase that is up to now unique to Cu_2OSeO_3 within the class of the B20 chiral magnets. Fig. 3.3C shows a high-field-cooled (HFC) phase diagram. It is obtained by cooling the sample at $H_{\mathrm{ext}} > H_{\mathrm{c2}}$. Subsequently, the external magnetic field is lowered and the occurring phases are recorded using SANS. Compared to the ZFC phase diagram with $\boldsymbol{H}_{\mathrm{ext}} \parallel [111]$ in Fig. 3.3A, the conical phase at $T = 15\,\mathrm{K}$ is suppressed and is partly substituted with the tilted conical and LT-skyrmion phase [117]. It is possible that the LT-skyrmion phase, that shows no long range order due to its comparatively high energy barrier at low temperatures, decays to a poorly ordered in-plane helical phase which is detected here [31, 51, 81]. There are further indications that the poorly ordered LT-skyrmion phase shows strong susceptibility to resonant excitation which is discussed in the following.

The magnetic field scans in off-resonance condition at 3 GHz and 5 GHz agree with each other, unaffected whether the excitation is turned on or off. This also indicates that heating effects do not influence the measurements off resonance. Once f_{ex} matches the resonance frequency of the helical phase, the satellite intensity is clearly reduced and reproducibly switches between its two values at each field step,

[4] In helimagnets that have no uniform magnetization, magnons are sometimes referred to as helimagnons [45].

which is consistent with the behavior in the field-polarized state discussed before. The reduction is again attributed to the precessional motion of the magnetization. However, it is expected that the recorded intensities for the cases where the excitation is switched off are equivalent, independent of the excitation frequency. However, this is clearly not the case which is most strikingly visible for $f_{\mathrm{ex}} = 3.5\,\mathrm{GHz}$. Here, the satellite intensity increases by an order of magnitude and also the field range, where the helical intensity is observed, is reduced by a factor of about 2. This suggests that the resonant excitation interacts with the LT-skyrmion phase and improves its long-range order, which leads to the increased peak intensity. The reduced field range can then be explained either by an extended phase occupation of the LT-skyrmion phase with long-range order due to resonant excitation, or a sharper reciprocal space occupation of the helical phase due to the improved long range order and a small misalignment between sample plane and the actual field direction [51].

The relative reduction of the helical peak intensity $(I_{\mathrm{off}} - I_{\mathrm{on}})/I_{\mathrm{off}}$ at $\mu_0 H_{\mathrm{ext}} = 0\,\mathrm{mT}$ is plotted in Fig. 3.9B. The helical peak that is used for the measurement is indicated in the inset. The two sharp maxima correspond to the $+q$ and $-q$ helical modes that were already introduced alongside the conventional FMR data in Fig. 3.8D. The resonance frequencies and peak amplitudes are in good agreement with present reports [45, 47]. This measurement shows that in addition to the magnetic phase selection, REXS-FMR is further able to distinguish between differently oriented domains of the helical phase.

Finally, REXS-FMR on the (HT) skyrmion phase is presented. The temperature is tuned to $T = 56\,\mathrm{K}$ and the setup is adjusted such that the scattering condition is fulfilled for one of the skyrmion reciprocal space vectors. The respective external magnetic field scans are shown in Fig. 3.9C. The intensities at $H_{\mathrm{ext}} \approx \pm 30\,\mathrm{mT}$ correspond to the skyrmion phase, while the signatures around 0 mT reflect a reciprocal space vector of the helical phase that partly overlaps with the chosen skyrmion one. Starting at low f_{ex}, the data with and without excitation field are equivalent. Comparing the curves for increased f_{ex}, a clear reduction of the skyrmion peak intensity is observed (e.g. at 1.6 GHz), which is again attributed to the precessional motion of the magnetization. However, the helical peak intensity is not reduced under excitation, as the resonance condition is not yet met. For $f_{\mathrm{ex}} > 1.9\,\mathrm{GHz}$, additional resonance effects of the helical phase are observed.

The measured resonance behavior of the skyrmion phase is further summarized by plotting the relative reduction of the skyrmion peak intensity at $\mu_0 H_{\mathrm{ext}} = 33\,\mathrm{mT}$ in Fig. 3.9D. Note that the discontinuity at $f_{\mathrm{ex}} = 2\,\mathrm{GHz}$ is caused by a necessary change of the microwave circulator which has a range limit at this excitation frequency as well as a change of the skyrmion satellite peak. The used satellite peaks are indicated in the inset by the square and circular symbols. This is also the reason

for the different helical signature for $f_{\mathrm{ex}} > 2\,\mathrm{GHz}$ in Fig. 3.9C. The change to the setup is indicated by dotted gray lines in Figs. 3.9B-D. In the plot, three peaks are clearly visible. They are attributed to the counter-clockwise, breathing and clockwise skyrmion modes, introduced before. Considering that the simulation is slightly off temperature and does not include magnetostatic effects, the measured resonance frequencies are in good agreement with the simulations. The measurement is also in good agreement with literature [45, 47]. Moreover, the height of the maxima is consistent with calculated spectral weight distributions, considering that the coplanar waveguide generates an excitation field which comprises both in-plane, driving the CW and CCW modes, and out-of-plane components, driving the breathing mode [143].

Note that the used photons have a penetration depth of around 30 nm. This means that REXS-FMR is surface sensitive. Recently, skyrmion surface states with a z-dependent skyrmion helicity ψ were reported for Cu_2OSeO_3 [149, 150]. Considering this study, around 25 % of the probed sample volume in the REXS-FMR experiments is expected to contain the aforementioned surface structures. However in FMR, no signatures of these structures that are distinguishable from the regular bulk excitations are found, which indicates that the resonances of the surface states are similar or equal to the bulk skyrmion state or that the surface states might be absent due to a different surface roughness. Admittedly though, the frequency sampling is not that fine.

In summary, the novel x-ray scattering technique REXS-FMR was introduced in this chapter. It combines reciprocal space imaging by means of magnetic REXS and FMR by means of microwave excitation using a coplanar waveguide. The technique has the potential to selectively study the individual magnetic phases and determine the origin of a specific excitation. It allows to unambiguously make the connection between a resonant mode and its underlying magnetic phase. It also inherits the element specific character of REXS. As an example, the magnetic resonances of the helical, field-polarized and skyrmion lattice phase in the cubic chiral magnet Cu_2OSeO_3 are identified by tracking the intensity of the structural (001) Bragg peak and its satellite peaks under microwave excitation. The phase selectivity of REXS-FMR may become particularly useful in systems that show complex magnetic environments and the clear identification of the resonant modes becomes challenging. Examples for this are multidomain skyrmion states in lacunar spinels [74, 151, 152], glassy skyrmion textures in Co-Mn-Zn compounds [24, 153, 154] or the low-temperature skyrmion phase in Cu_2OSeO_3 with its concomitant tilted conical state [117–119].

Besides that, the limits of the technique are potentially not yet reached. A future perspective is a stroboscopic measurement, e.g. of the skyrmion mode dynamics.

The simulations from the beginning of this section suggest that the spot intensity of the gyrating (CW and CCW) modes is oscillating with a phase shift of 60° with respect to each other, while they are expected to be in-phase for the breathing mode, which would allow an unambiguous detection of the three skyrmion modes.

4 Real-space imaging of magnetic skyrmions

In this chapter, real space imaging of magnetic skyrmions and chiral magnetic textures in terms of Lorentz Transmission Electron Microscopy (LTEM) is discussed.

In the first part, the theoretical concepts of LTEM are introduced. After some remarks about the general setup of a transmission electron microscope (TEM), the two LTEM techniques Fresnel and Differential Phase Contrast (DPC) LTEM are explained in more detail.

The second part deals with the theoretical concepts of LTEM imaging of magnetic skyrmions and other chiral magnetic textures. At first, a broad qualitative overview of the Fresnel and DPC LTEM contrast formation of the various chiral magnetic textures is shown. Then, a quantitative description of magnetic electron phase imaging of the skyrmion spin structure is given. The resulting phenomenological relations provide a connection of the TEM contrast to the magnetic skyrmion structure. They are a key requirement for the characterization of engineered skyrmion structures using LTEM, which became one of the most important real space imaging methods of magnetic skyrmions.

In the last part, experimental LTEM data is presented. First, a Cu_2OSeO_3 sample oriented along (001) is measured at temperatures below 50 K with Fresnel and DPC LTEM. These measurements are conducted on an equivalent crystal as the one in chapter 3 and give an additional point in terms of real-space observations. Besides this, room temperature magnetic skyrmion hosting multilayer materials are investigated. In this thesis, the data of a Pt/Co/W and a Pt/Co/Tb multilayer stack are presented. The results clearly show that the character of the room-temperature skyrmions deviates from the low temperature bulk chiral magnets in terms of the magnetic phase diagrams, skyrmion nucleation and pinning.

Parts of sections 4.2.2, 4.2.3 and 4.4.2 are published in [155]. Parts of section 4.4.1 are published in [67].

4.1 Lorentz Transmission Electron Microscopy

Light microscopy is a basic tool in many scientific fields like biology, medical sciences, geology, engineering and physics. The technique, however, possesses a fundamental constraint which is the Abbe diffraction limit given by [156]

$$d = \frac{\lambda}{2n\sin(\theta)} \,. \tag{4.1}$$

Here λ is the light wavelength, n the refractive index of the medium, θ the semi opening angle of the objective, and d is the distance of two separated objects that are imaged. The equation describes the physical limitation of a light microscope's resolution in air which is around half of the wavelength of the used light which can be as small as $\approx 200\,\mathrm{nm}$ for the visible spectrum. Although Ernst Abbe died over 100 years ago, the timeliness of this issue is stressed by the Nobel Prize Committee which awarded the Nobel Prize in chemistry of 2014 to E. Betzing, S. W. Hell and W. E. Moerner who took efforts in surpassing the Abbe limit. Hell and Wichmann describe the theoretical realization of a light microscope with a resolution below the Abbe-limit in their work "Breaking the diffraction resolution limit by stimulated emission: stimulated-emission-depletion fluorescence microscopy" [157]. Five years later, the Stimulated Emission Depletion (STED) microscope is realized experimentally by Klar and Hell [158]. However, the sensational title of Hell's original work should not be taken literally. In fact, every beam in the described microscope exactly follows Abbe's diffraction limit and the technique rather relies on a clever idea to partially deplete an excited volume of fluorescent marker molecules that need to be attached to the actual sample before measurement.

A more direct approach to increase the resolution of microscopes was performed by Ruska and Knoll in the 1930s. Instead of photons, they used electrons for imaging [159]. At a typical energy of 300 keV, the de-Broglie-Wavelength of electrons is $\lambda_\mathrm{e} = 1.97\,\mathrm{pm}$ which is far below inter-atomic distances. A modern Transmission Electron Microscope (TEM) like the *FEI Titan G3 PICO* at the research center in Jülich reaches an information limit below 50 pm [160].

It turned out that a TEM possesses much greater versatility than just high resolution imaging. Today, various experiments can be performed in the same machine. Prominent examples are electron diffraction, energy dispersive x-ray spectroscopy (EDXS), electron energy loss spectroscopy (EELS) or Lorentz TEM (LTEM), which describes the imaging of electric or magnetic fields and includes several sub-techniques.

In this section, the basic working principle of a TEM is explained. Only aspects that are relevant for this thesis are covered. First, the general setup of a TEM is

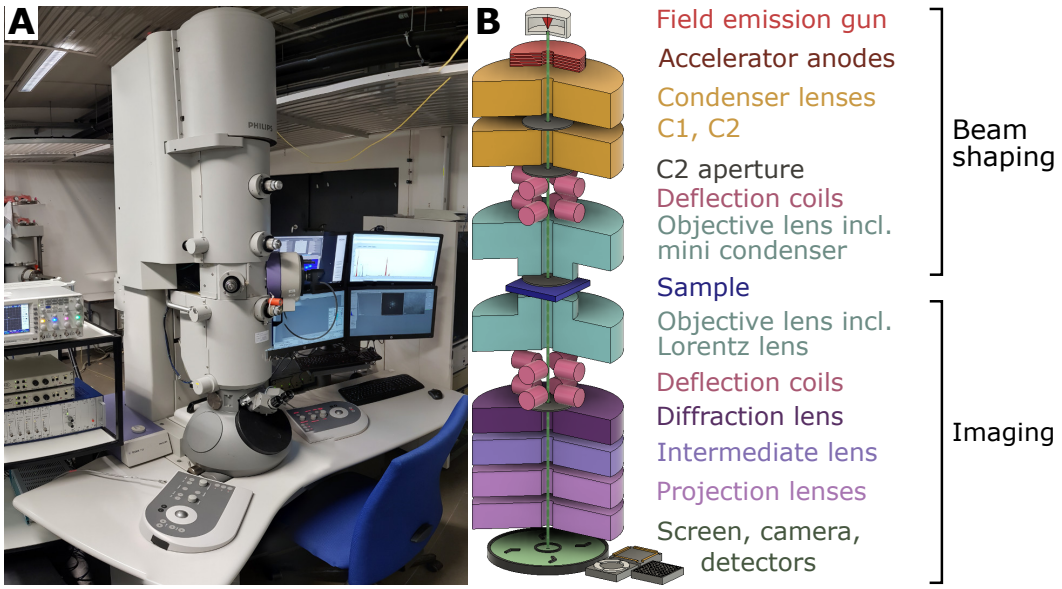

Fig. 4.1.: General setup of a TEM. **(A)** Photograph of the TEM used for the measurements in this thesis. **(B)** Schematic setup of a TEM. The electron beam is extracted from a field emitter and shaped before it is transmitted through the sample. The resulting electron wave is imaged and recorded using a variety of detectors.

given as an overview. Then, more detailed descriptions of the two techniques used for magnetic imaging in this thesis, namely Fresnel and DPC LTEM, are given.

4.1.1 General setup of a TEM

The optical analogue to a TEM is the transmission light microscope as implied by the naming. Unsurprisingly, the actual technical setup is very different. Beside the obvious necessity of a vacuum to enable electron propagation throughout the optics of the machine (the propagation distance is in the order of meters), electrostatic and magnetic lenses have to be used to focus and manipulate the electron beam. The advantage of such a lens is that the focal plane can be adjusted by the electrical current through the coil that produces its magnetic field. A major disadvantage are the large lens aberrations. An insight into the interesting technical details and ideas that are necessary to construct such a machine can be found e.g. in [161, 162]. The model name of the TEM that is used in this work is Tecnai F30 from the manufacturer FEI. A photograph of the machine can be seen in Fig. 4.1A.

A schematic drawing of the optical parts of the TEM is shown in Fig. 4.1B. The electrons tunnel out of the sharp apex ($r \approx 100\,\mathrm{nm}$) of the Tungsten field emission gun (FEG) when an electric field of a few kV is applied [163]. An electrostatic gun lens (not shown) focuses the extracted electrons to a spot before their energy is increased to typical values of 200 keV or 300 keV by the accelerator anodes. A con-

denser system consisting of two condenser lenses (C1 and C2) and two apertures is used to either produce a focused beam for Low Magnification Scanning Transmission Electron Microscopy (LMSTEM) or a parallel beam for the imaging modes (details covered later). The condenser is also used to control the beam intensity/current density that is available on the sample (the beam current is in the order of nA). As electrons are efficiently blocked by matter, TEM samples cannot have arbitrary thicknesses. Usually, it is desired for the electrons not to get scattered multiple times within the sample, which leads to typical sample thicknesses of less than 100 nm as a rule of thumb [162]. The deflection coils are a pair of lenses that can shift and tilt the beam. In combination they are used to translate the beam in the plane perpendicular to the optical axis. The objective lens is a twin lens, i.e. it has an upper and lower part above and below the sample and is the fundamental lens for High Resolution TEM (HRTEM) imaging and High Resolution Scanning TEM (HRSTEM). Inside the gap of the pole pieces and the magnetic field of the objective lens, the actual sample is located. The mini condenser and Lorentz lens are integrated into the objective lens. The Lorentz lens is responsible for the Fresnel LTEM imaging mode which is discussed in section 4.1.2 in more detail. The diffraction lens can be used to image the diffraction pattern of the sample in the focal plane of the objective lens. An intermediate lens and two projection lenses are used to project the image to its desired magnification where it can finally be displayed on a fluorescent screen, a CCD camera or a variety of detectors.

Note that it is intended that the previous explanation might not enable the reader to construct the actual beam path. There are too many different imaging modes and each includes a distinct set of lenses which makes it impossible to explain them consistently in one paragraph. Therefore, the following two sections discuss the two magnetic imaging modes used throughout this thesis in more detail.

4.1.2 Fresnel Lorentz Transmission Electron Microscopy

The idea to use the strong interaction of the electron charge with magnetic fields for magnetic imaging in the TEM was already practically accomplished by Marton in 1948 only few years after the invention of the TEM [164–167]. Nowadays, the term Lorentz TEM includes all TEM techniques that image an intensity variation which arises from the electron phase caused by magnetic or electric fields within a sample. The first actual images obtained by Fresnel LTEM, which is introduced in this section, were presented by Wohlleben [168] and Fuller and Hale [169].

The electron beam path inside the TEM in Fresnel LTEM mode is schematically depicted in Fig. 4.2A. Only essential optical components are drawn. The electrons that are extracted from the FEG are focused to a point (first crossover) that is

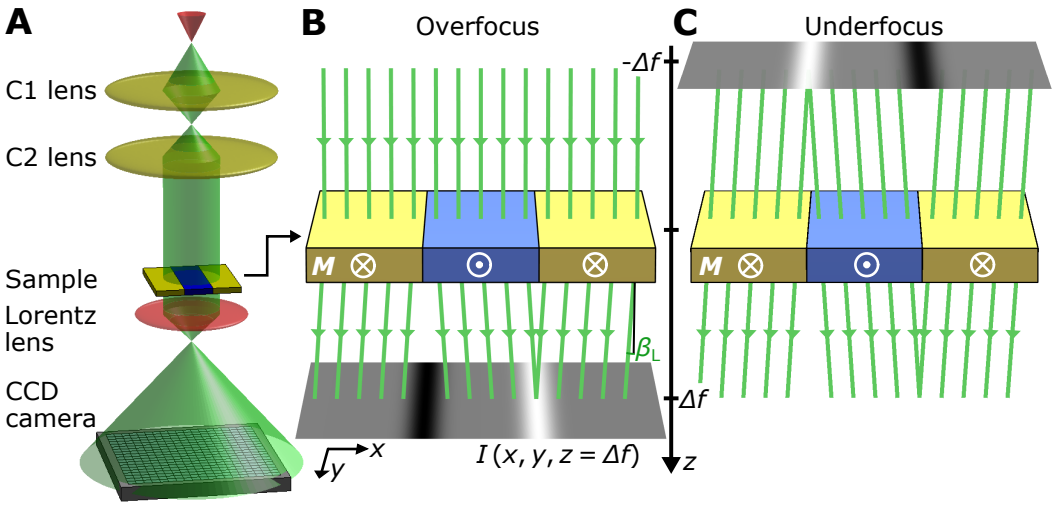

Fig. 4.2.: Qualitative Fresnel LTEM imaging. **(A)** Schematic beam path of a TEM in Fresnel LTEM mode. A parallel beam is created by the condenser system that illuminates the sample. The phase modulated electron wave is imaged using the Lorentz lens. **(B)** In the particle image, electrons that are transmitted through a magnetic sample are deflected due to the Lorentz force. At a distance Δf below the sample, electron density variations in the plane normal to the optical axis occur. This modulated intensity can be imaged in the so-called overfocus of the Lorentz lens. **(C)** When the imaging plane of the Lorentz lens is tuned to be above the sample, a virtual image of the deflected electrons is captured, as described in (B). Compared to the overfocus image, the contrast is inverted.

imaged using the C1 lens (second crossover). This image is in the focal point of the C2 lens which gives a parallel beam just like in a regular condenser of an optical microscope. The parallel beam is transmitted through the sample and the resulting electron wave is imaged using the Lorentz lens. This special lens is situated at a safe distance to the magnetic sample in order to avoid disturbances of the sample's magnetic structure due to the magnetic field of the lens. At maximum excitation, the Lorentz lens introduces a magnetic field of 0.8 mT in the sample plane which can be further compensated using the mini-condenser lens (not shown). The image is projected to its final magnification using a projection lens system (not shown) and is captured with a CCD camera or observed on the fluorescent screen. The objective lens cannot be used for magnetic imaging as it produces magnetic fields around 2 T at the sample position which would saturate most magnetic samples and anyone that is discussed in this thesis. However, the operation of the objective lens at weak excitation currents can be used to study the sample for different magnetic fields. Here, the magnetic field direction is restricted to the optical axis. The only way to introduce magnetic fields within the sample plane is by tilting the sample. This inflexibility can be an issue as described later.

Magnetic imaging in TEM is best understood from a qualitative aspect, using the particle image of electrons. Fig. 4.2B shows the parallel trajectories of incident electrons (green arrows). A hypothetical magnetic sample consisting of three in-plane magnetized domains deflects the transmitted electrons in terms of Lorentz force as illustrated. The deflection angle $\beta_\mathrm{L}(x)$ at the position x of a laterally infinite sample with $\boldsymbol{M} \parallel \hat{\boldsymbol{y}}$ is given by [170]

$$\beta_\mathrm{L}(x) = \frac{e\lambda_\mathrm{e}\mu_0 M_y(x)\tau}{h} \,, \tag{4.2}$$

with sample thickness τ and the y-component of the magnetization $M_y(x)$. At a distance Δf below the sample, the electron intensity normal to the optical axis[1] $I(\boldsymbol{r}_\perp, z = \Delta f)$ is in- or decreased at positions where the domain orientation of the sample changes. This intensity variation can be imaged by setting the Lorentz lens image plane to $z = \Delta f$. One also speaks of a positive defocus or overfocus, classifying the method as a defocus-technique. In reality, such defocus-values can be as large as mm which is large compared to HRTEM where an image with a Δf in the µm range would be called defocused. It is also possible to use negative defoci as shown in Fig. 4.2C. In this case, a virtual image of the backwards extension of the deflected trajectories in Fig. 4.2B is recorded. This is called underfocussing and the respective image contrast is inverted in comparison to the overfocused images.

While the importance of these classical considerations for qualitative contrast formation is undeniable, their validity for more complex magnetic structures or quantitative results is rarely given [167]. A more rigorous description of the resulting image contrast requires an electron treatment as coherent quantum mechanical matter waves. It is possible to describe such waves like optical waves and use Fourier optics to describe their propagation and interaction with lenses including the effect of aberrations [163, 171, 172].

The initial electron wave Ψ_in at the z-position of the sample is described by a plane wave

$$\Psi_\mathrm{in}(\boldsymbol{r}_\perp) = A_0 \exp\left(\mathrm{i}\phi_0 + \mathrm{i}\omega t\right) \,, \tag{4.3}$$

with amplitude A_0, angular frequency ω and a constant phase ϕ_0. Upon magnetic sample interaction, the phase is altered and depends on the lateral coordinates $\boldsymbol{r}_\perp$, i.e. $\phi_0 \rightarrow \phi_\mathrm{m}(\boldsymbol{r}_\perp)$. Assuming that the sample is thin and a pure phase object, A_0 remains constant. This means that beside the interaction of the electron with the magnetic induction of the sample, there are no additional effects like electron

[1] The optical axis is usually chosen to be parallel to $\hat{\boldsymbol{z}}$.

absorption or scattering from the crystal structure. Dropping the time-dependent part, the outgoing wave right below the sample becomes

$$\Psi_{\mathrm{out}}(\boldsymbol{r}_\perp) = A_0 \exp\left[\mathrm{i}\phi_{\mathrm{m}}\left(\boldsymbol{r}_\perp\right)\right] \ . \tag{4.4}$$

In order to calculate the expected Fresnel LTEM contrast for a given magnetic sample, it is necessary to calculate $\phi_m(\boldsymbol{r}_\perp)$. It is known that two electrons that traverse a magnetic sample at $\boldsymbol{r}_1$ and $\boldsymbol{r}_2$ with $\Delta x = |\boldsymbol{r}_2 - \boldsymbol{r}_1|$ acquire a phase-shift $\Delta\phi_{\mathrm{m}}$ according to the enclosed magnetic flux Φ_B of their two paths (that virtually connect at infinite distance to the sample), which gives [167, 170]

$$\Delta\phi_{\mathrm{m}}(\Delta x) = -\frac{e}{\hbar}\Phi_B = -\frac{e}{\hbar}B_\perp\,\tau\,\Delta x \ . \tag{4.5}$$

Here, $B_\perp$ is the projected component of the magnetic induction along the perpendicular direction of $(\boldsymbol{r}_2 - \boldsymbol{r}_1)$ and the optical axis. This linear phase dependence along $\boldsymbol{r}_2 - \boldsymbol{r}_1$ is illustrated in Fig. 4.3A. The lines represent positions of equal phase.

In 1991, Mansuripur presented a convenient way to numerically calculate $\phi_{\mathrm{m}}(\boldsymbol{r}_\perp)$ for a parallel electron beam passing a thin magnetic sample with uniform magnetization along the film thickness at an arbitrary incident angle [173]. For this, Mansuripur computes the vector potential $\boldsymbol{A}(\boldsymbol{r})$ associated with the magnetic sample. This also accounts for the magnetostatic fields in- and outside of the sample. The resulting phase-shift is calculated from prior argumentation. Finally, $\phi_{\mathrm{m}}(\boldsymbol{r}_\perp)$ is given by

$$\phi_m(x,y) = \frac{\mathrm{i}\mu_0 M_{\mathrm{s}} e\tau}{h} \sum_{\substack{m=-\infty \\ n=-\infty \\ mn\neq 00}}^{\infty} \frac{G_{\mathrm{p}}(\tau\boldsymbol{k}_{mn})}{k_{mn}} (\boldsymbol{k}_{mn}\times\hat{\boldsymbol{z}})\cdot[\hat{\boldsymbol{p}}\times(\hat{\boldsymbol{p}}\times\boldsymbol{M}_{mn})]\, e^{2\pi\mathrm{i}\left(\frac{mx}{L_x}+\frac{ny}{L_y}\right)} \ . \tag{4.6}$$

Eq. (4.6) has been converted to SI units from the original work. Here, M_{s} is the saturation magnetization, τ is the sample thickness and L_x, L_y are the lateral dimensions of the sample. The unit vector $\hat{\boldsymbol{p}}$ points along the beam direction. The 2D-reciprocal space vectors $\boldsymbol{k}_{mn}$ are given by

$$\boldsymbol{k}_{mn} = \left(\frac{m}{L_x}\right)\hat{\boldsymbol{x}} + \left(\frac{n}{L_y}\right)\hat{\boldsymbol{y}} \ . \tag{4.7}$$

The coefficients of the magnetization's Fourier series $\boldsymbol{M}_{mn}$ are given by

$$\boldsymbol{M}_{mn} = \frac{1}{L_x L_y} \int_0^{L_x} \int_0^{L_y} \boldsymbol{m}(x,y) \exp\left[-2\pi \mathrm{i}\left(\frac{mx}{L_x} + \frac{ny}{L_y}\right)\right] \mathrm{d}x\,\mathrm{d}y\,, \tag{4.8}$$

with the sample's normalized magnetization vector field $\boldsymbol{m}(x,y)$. Finally, the geometrical factor $G_\mathrm{p}(\tau \boldsymbol{k}_{mn})$ is given by

$$G_\mathrm{p}(\tau \boldsymbol{k}_{mn}) = \frac{1}{(\hat{\boldsymbol{p}}\cdot\boldsymbol{k}_{mn})^2 + (\hat{\boldsymbol{p}}\cdot\hat{\boldsymbol{z}})^2} \frac{\sin\left[\,(\pi\tau\hat{\boldsymbol{p}}\cdot\boldsymbol{k}_{mn})\,/\,(\hat{\boldsymbol{p}}\cdot\hat{\boldsymbol{z}})\,\right]}{(\pi\tau\hat{\boldsymbol{p}}\cdot\boldsymbol{k}_{mn})\,/\,(\hat{\boldsymbol{p}}\cdot\hat{\boldsymbol{z}})}\,. \tag{4.9}$$

These expressions can be computed conveniently using discrete Fourier transforms (FTs) as shown in appendix A.4.

As the phase modification ϕ_m of the electron wave by the magnetic sample is now accessible, the resulting intensity of the Fresnel LTEM image can be calculated using Fourier optics. Fresnel LTEM does not measure ψ_out directly as it does not detect the electron phase but measures a wave intensity. However, $I_\mathrm{out}(\boldsymbol{r}_\perp) = |\Psi_\mathrm{out}|^2 = |A_0|^2$ is constant and does not depend on position. Therefore to obtain magnetic information, Ψ_out is propagated for a distance Δf and the intensity of the resulting electron wave $\Psi_{\Delta f}$ is imaged, which is equivalent to the particle considerations that were discussed with Fig. 4.2B. The wave function $\Psi_{\Delta f}$ can be computed using the Fresnel-propagator [167, 171]

$$\mathcal{P}_{\Delta f} = \frac{1}{\mathrm{i}\lambda_\mathrm{e}\Delta f} \exp\left(\mathrm{i}\pi \frac{x^2+y^2}{\lambda_\mathrm{e}\Delta f}\right)\,, \tag{4.10}$$

with the electron wavelength λ_e. This expression has a compact FT which reads [163, 167]

$$\mathcal{F}(\mathcal{P}_{\Delta f}) = \exp\left[\mathrm{i}\pi\Delta f\lambda_\mathrm{e}(k_x^2+k_y^2)\right]\,. \tag{4.11}$$

Here, k_x and k_y are the reciprocal space vectors. To calculate the propagated wave $\Psi_{\Delta f}$, it is convoluted with $\mathcal{P}_{\Delta f}$ which can be expressed by FTs [163, 167]

$$\Psi_{\Delta f} = \mathcal{F}^{-1}\left[\mathcal{F}(\Psi_\mathrm{out})\cdot\mathcal{F}(\mathcal{P}_{\Delta f})\right]\,, \tag{4.12}$$

with the inverse Fourier transform $\mathcal{F}^{-1}$. Note that $\mathcal{P}_{\Delta f}$ is a quadratic approximation of a spherical wave which means that the latter is only valid close to the optical axis which is given for TEM. The Lorentz lens is used to image $|\Psi_{\Delta f}|^2$. In Fresnel Lorentz electron microscopy, the wave in the back-focal plane Ψ_bfp of the Lorentz lens ($f \approx L_\mathrm{g}$) is given by the Fourier transform of $\Psi_{\Delta f}$ [170, 171].

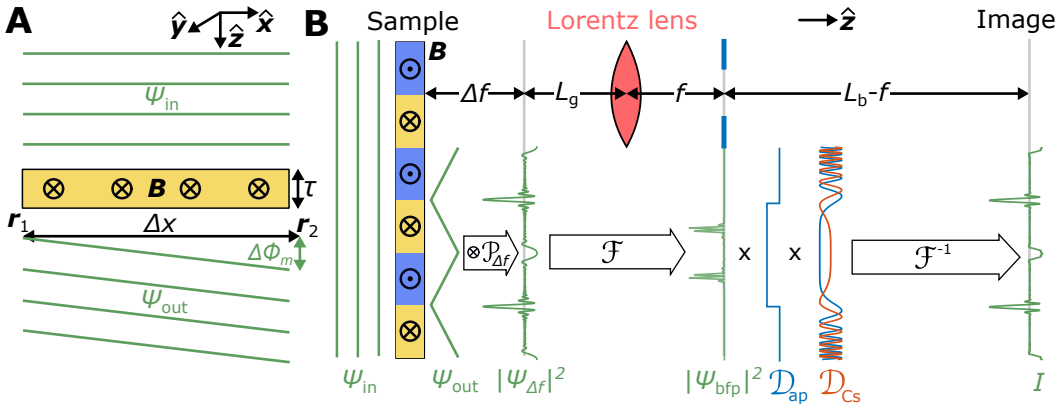

Fig. 4.3.: Electron phase-shift by a magnetic sample and Fresnel LTEM image formation from Fourier optics. **(A)** An incoming plane wave Ψ_{in} is linearly phase- shifted when transmitted through a constant magnetic induction $\boldsymbol{B}$ perpendicular to the optical axis results. **(B)** The electron wave Ψ_{out} that exits the sample is propagated for a distance Δf using the Fresnel Propagator $\mathcal{P}_{\Delta f}$. A Fourier transform gives the electron wave Ψ_{bfp} in the back focal plane of the Lorentz lens, where its complex spherical aberration function $\mathcal{D}_{\mathrm{Cs}}$ (real part drawn in blue and imaginary part drawn in orange color) and an aperture function $\mathcal{D}_{\mathrm{ap}}$ are included by multiplication. Some quantities like $|\Psi_{\Delta f}|^2$ are displayed for intuitive reasons and are not the actual target of the displayed mathematical operations which is why this figure should only be studied in combination with the main text. The square modulus of the inverse Fourier transform of the CTF gives the resulting Fresnel image intensity I. Image (A) is a modified Fig. from Ref. [167]

D. B. Williams and C. B. Carter write that "[...] if the lenses in your own eyes were as good as our best electromagnetic lens, then you'd be legally blind!" [162]. It is therefore reasonable to include aberrations in the contrast formation description[2]. It can be shown that these aberrations can be included by a multiplication of Ψ_{bfp} with additional terms as follows [162, 163, 171]

$$\Psi'_{\mathrm{bfp}}(\boldsymbol{k}_\perp) = \mathcal{F}(\Psi_{\mathrm{out}})\, \mathcal{F}(\mathcal{P}_{\Delta f})\, \mathcal{D}_{\mathrm{ap}}(\boldsymbol{k}_\perp)\, \mathcal{D}_{\mathrm{Cs}}(\boldsymbol{k}_\perp)\,. \tag{4.13}$$

Here, $\mathcal{D}_{\mathrm{ap}}$ accounts for the action of an objective aperture in the back focal plane of the imaging lens and is given by

$$\mathcal{D}_{\mathrm{ap}}(k_x, k_y) = \Theta(k_{\mathrm{ap}} - k_\perp)\,, \tag{4.14}$$

for a circular aperture with radius k_{ap} using the Heaviside function Θ. The spherical aberration of the lens is implemented with [170, 171]

$$\mathcal{D}_{\mathrm{Cs}}(k_x, k_y) = \exp\left[i\,\frac{\pi}{2} C_{\mathrm{s}} \lambda_{\mathrm{e}}^3 (k_x^2 + k_y^2)^2\right]\,. \tag{4.15}$$

[2]Nowadays, spherical and chromatic aberrations can be compensated using correctors, nevertheless the quote is still valid for the lenses themselves.

In this equation, C_s is the lens' spherical aberration coefficient. The objective lens, responsible for high resolution TEM imaging, of the microscope used in this thesis has a C_s in the order of a few mm [162]. In terms of bad optical quality this value is easily beaten by the Lorentz lens with $C_\mathrm{s} \approx 8\,\mathrm{m}$ [172, 174]. However, due to the large defoci used in Fresnel LTEM, the large C_s is often not the resolution limiting term when comparing Eqs. 4.11 and 4.15. The multiplication of $\mathcal{D}_\mathrm{ap}$, $\mathcal{D}_\mathrm{Cs}$ as well as $\mathcal{F}(\mathcal{P}_{\Delta f})$ that accounts for defocus is called contrast-transfer-function (CTF)

$$\mathcal{D}_\mathrm{CTF}(\boldsymbol{k}_\perp) = \mathcal{F}(\mathcal{P}_{\Delta f})(\boldsymbol{k}_\perp)\; A(\boldsymbol{k}_\perp)\; \mathcal{C}(\boldsymbol{k}_\perp)\;. \tag{4.16}$$

It should be noted that additional terms like chromatic aberrations can be included in the CTF but are omitted due to their negligible effect for Fresnel LTEM. To obtain the resulting Fresnel image intensity $I(\boldsymbol{r}_\perp)$, the square modulus of the inverse Fourier transform of Eq. (4.13) is computed [162, 163, 171]

$$I(\boldsymbol{r}_\perp) = \left|\mathcal{F}^{-1}\left[\mathcal{F}(\Psi_\mathrm{out})(\boldsymbol{k}_\perp)\cdot\mathcal{D}_\mathrm{CTF}(\boldsymbol{k}_\perp)\right]\right|^2\;. \tag{4.17}$$

As an overview and a summary, the image formation in terms of Fourier optics described before is schematically shown in Fig. 4.3B. The plane electron wave Ψ_in is phase-shifted by the magnetic induction $\boldsymbol{B}$ of the sample and transforms to Ψ_out which can be calculated using Eqs. (4.6)-(4.9). Ψ_out freely propagates for a distance Δf to the new state $\Psi_{\Delta f}$ which is mathematically achieved by a convolution with the Fresnel propagator $\mathcal{P}_{\Delta f}$ defined in Eq. (4.10). The electron wave in the back-focal-plane of the Lorentz lens Ψ_bfp is obtained by the Fourier transform of $\Psi_{\Delta f}$. To attribute for the spherical aberration of the Lorentz lens and an aperture in the focal plane, Ψ_bfp is multiplied by $\mathcal{D}_\mathrm{Cs}$ and $\mathcal{D}_\mathrm{ap}$. Finally, the resulting wave function which gives the Fresnel image intensity is obtained by an inverse Fourier transform as stated in Eq. (4.17). Note that the mathematical operations in combination with the shown quantities in Fig. 4.3B might lead to confusions. E.g. the Fourier transform to obtain Ψ_bfp is actually applied to $\Psi_{\Delta f}$ and not to $|\Psi_{\Delta f}|^2$ which is displayed for intuitive reasons. Therefore, Fig. 4.3B should only be studied alongside the explaining text.

4.1.3 Differential Phase Contrast Lorentz Transmission Electron Microscopy

The previous section showed how magnetic structures are imaged in an out-of-focus condition. Imaging at a defocus will however also reduce the lateral image resolution. For a defocus of around 50 µm, the lateral resolution is already $> 30\,\mathrm{nm}$ and therefore, depending on the effective magnetic induction of the sample, the technique can be limited to large magnetic structures [175]. A second issue is that

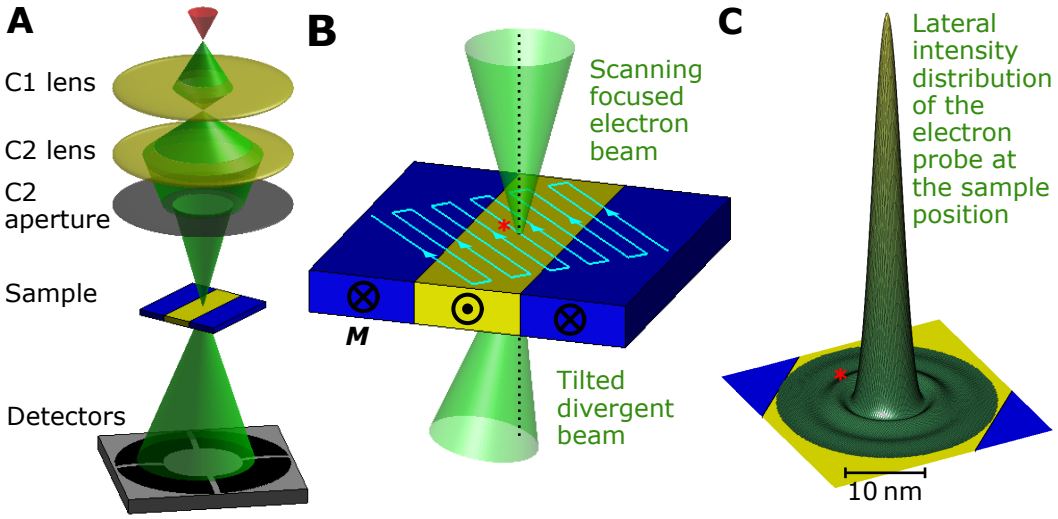

Fig. 4.4.: Qualitative DPC LTEM imaging. **(A)** Schematic beam path of the essential optical parts of a TEM in DPC LTEM mode. The electron beam is focused on the sample where it gets deflected. The deflection is probed locally using a variety of detectors like annular segmented diodes (shown here), position sensitive diodes or fast cameras. **(B)** The electron beam is scanned over the sample and deflected depending on the local magnetic induction. **(C)** Intensity profile of the electron probe.

the TEM is no longer well-calibrated when operated at large defoci, which leads to many operational inconveniences, most prominently the loss of the image's scale. So when absolute physical sizes need to be known, the scalebar has to be tediously calibrated from (non-magnetic) image features of in-focus images for which the scale is calibrated.

A technique that is able to image magnetic fields while staying in focus of the sample is Differential Phase Contrast (DPC) LTEM. The major difference to Fresnel LTEM is that DPC LTEM is a scanning technique, i.e. the beam is focused onto the sample and locally probes the magnetic field. After first proposals in 1974 [176, 177], the technique was experimentally realized by Chapman et al. on magnetic domains of a polycrystalline permalloy film in 1978 [178]. The method was used exclusively for magnetic specimens until it was first applied to the (piezo-) electric field of an InGaN quantum well in 2012 [179]. After further mesoscopic electric field measurements of polarized wurtzite GaAs nano-wires or p-n junctions [180–182], probe-corrected STEM was used to measure the inter-atomic electric fields of $BaTiO_3$ and GaN which established a whole new field of atomic DPC imaging [183, 184]. With the first real space imaging of magnetic Bloch skyrmions using Fresnel-LTEM [48], DPC-LTEM also increased its level of awareness in the magnetism community [69, 185–187].

Fig. 4.4A shows the beam path and the essential optical components for DPC LTEM. Like in Fresnel LTEM mode, the first crossover of the extracted electrons is imaged by the C1 Lens. The C2 lens focuses the beam onto the sample (or creates an image of the second crossover at the sample z-position). The focused beam spot at the sample is called the electron probe. The C2 aperture plays an important role as it controls beam intensity, electron probe size and magnetic field sensitivity (explained later). When the electron beam is transmitted through the sample, a local magnetic induction deflects the outgoing diverging beam. This deflection is the signal of interest for the DPC technique. It is measured using a variety of detectors, the three most prominent are annular segmented diode (shown here[3]) [188], position sensitive diode (PSD) [189] and fast pixelated detector/camera [183]. For the annular segmented diode this works by subtracting the measured electrical current signal of opposing diode segments. More details can be found in Refs. [167, 190–192]. The distance between the sample and the detector is called camera length L_c and can be electron-optically varied using the projection system (not shown). The resulting intensity of the electron wave function that is projected onto the detector is called diffraction disk or Ronchigram. The latter name only applies if the sample is in focus. DPC is a scanning transmission electron microscopy (STEM) technique, i.e. that the focused electron beam is scanned over the sample as shown in Fig. 4.4B. At each scan position, the local deflection of the electron probe is measured which can then be composed to an image when mapping the deflection value to a set of colors (colormap).

As the diffraction limit (4.1) also applies to electrons, the electron probe possesses a finite size. The probe intensity profile is shown in Fig. 4.4C and is given by the well-known Airy pattern

$$I_\mathrm{probe}(r_\perp) = I_0 \left[\frac{2J_1(\alpha_\mathrm{probe}\, r_\perp)}{\alpha_\mathrm{probe}\, r_\perp}\right]^2 , \tag{4.18}$$

with the central spot intensity I_0, the Bessel function of the first kind J_1 and the radial coordinate $\boldsymbol{r}_\perp$. The factor α_probe is given by

$$\alpha_\mathrm{probe} = \frac{2\pi R_\mathrm{C2}}{\lambda_\mathrm{e} L_\mathrm{b}} , \tag{4.19}$$

with the C2 aperture radius R_C2 and the distance from the C2 aperture to the in-focus sample L_b. With $J_1(1.22\pi) \approx 0$, the electron probe radius R_probe defined

[3] There also exist different detector layouts with a varying number of radial and angular segments.

by $I_{\mathrm{probe}}(R_{\mathrm{probe}}) = 0$ is related to the geometrical parameters of the aberration free STEM with

$$R_{\mathrm{probe}} = \frac{1.22\ \lambda_{\mathrm{e}}\ L_{\mathrm{b}}}{2R_{\mathrm{C2}}}\ . \tag{4.20}$$

The uncorrected microscope used in this thesis can produce a minimal probe size of around 10 nm in the LMSTEM mode that is described here. It should be noted that in the HRSTEM mode, atomic sized electron probes can be achieved by focusing the electron beam with the objective lens, situated much closer to the sample, which effectively reduces L_{b}. As already mentioned, this is not applicable to magnetic samples due to the large magnetic fields that are produced by the objective lens at the sample location.

The wave-optical description of LMSTEM starts with the second beam crossover, situated inside the condenser system. A sketch can be found in the top part of Fig. 4.5A. The crossover is treated as a point source which, in reality, is of course not true, but the effect of a broadened source will be discussed in the application of this theory in section 4.2.3. The electron wave Ψ_δ at this point is given by

$$\Psi_\delta(\boldsymbol{r}_\perp) = \delta(\boldsymbol{r}_\perp)\ , \tag{4.21}$$

with the 2D Dirac distribution $\delta(x, y)$. This point source is now imaged using the C2 lens such that the image will be in the sample plane. Therefore, Ψ_δ is first propagated for the object distance L_{g} which is expressed by the trivial convolution with the Fresnel propagator $\mathcal{P}_{L\mathrm{g}}$. In the lens plane, the wave function $\Psi_{\mathrm{C2,in}}$ is

$$\Psi_{\mathrm{C2}}^{\mathrm{in}} = \exp\left(\frac{\mathrm{i}\pi r_\perp^2}{\lambda_{\mathrm{e}} L_{\mathrm{g}}}\right)\ , \tag{4.22}$$

which is the quadratic approximation of a spherical wave as expected [171]. The lens adds an additional focal-length f dependent phase $\phi_f = \frac{\pi r_\perp^2}{\lambda_{\mathrm{e}} f}$ to $\Psi_{\mathrm{C2}}^{\mathrm{in}}$. Further, the effect of the circular C2 aperture with radius K_{C2} is included by the multiplication with an aperture function $\mathcal{D}_{\mathrm{ap}}(k_\perp) = \Theta(K_{\mathrm{C2}} - k_\perp)$. The wave $\Psi_{\mathrm{C2}}^{\mathrm{out}}$ exiting the C2 lens is then given by

$$\Psi_{\mathrm{C2}}^{\mathrm{out}} = \Psi_{\mathrm{C2}}^{\mathrm{in}} \cdot \exp\left(\mathrm{i}\phi_f\right) \cdot \mathcal{D}_{\mathrm{ap}}(k_\perp) = \exp\left(\frac{\mathrm{i}\pi r_\perp^2}{\lambda_{\mathrm{e}} L_{\mathrm{b}}}\right) \cdot \mathcal{D}_{\mathrm{ap}}(k_\perp)\ . \tag{4.23}$$

As expected from a perfect lens, the first part is the quadratic approximation of a spherical wave converging to a point at the image distance L_{b}. For an imperfect lens, deviations from the given ϕ_f have to be included, as indicated by the orange wave-front exiting the C2 lens in Fig. 4.5A. Aberrations only modify and mostly spread the wave function of the resulting electron probe, so they are not explicitly

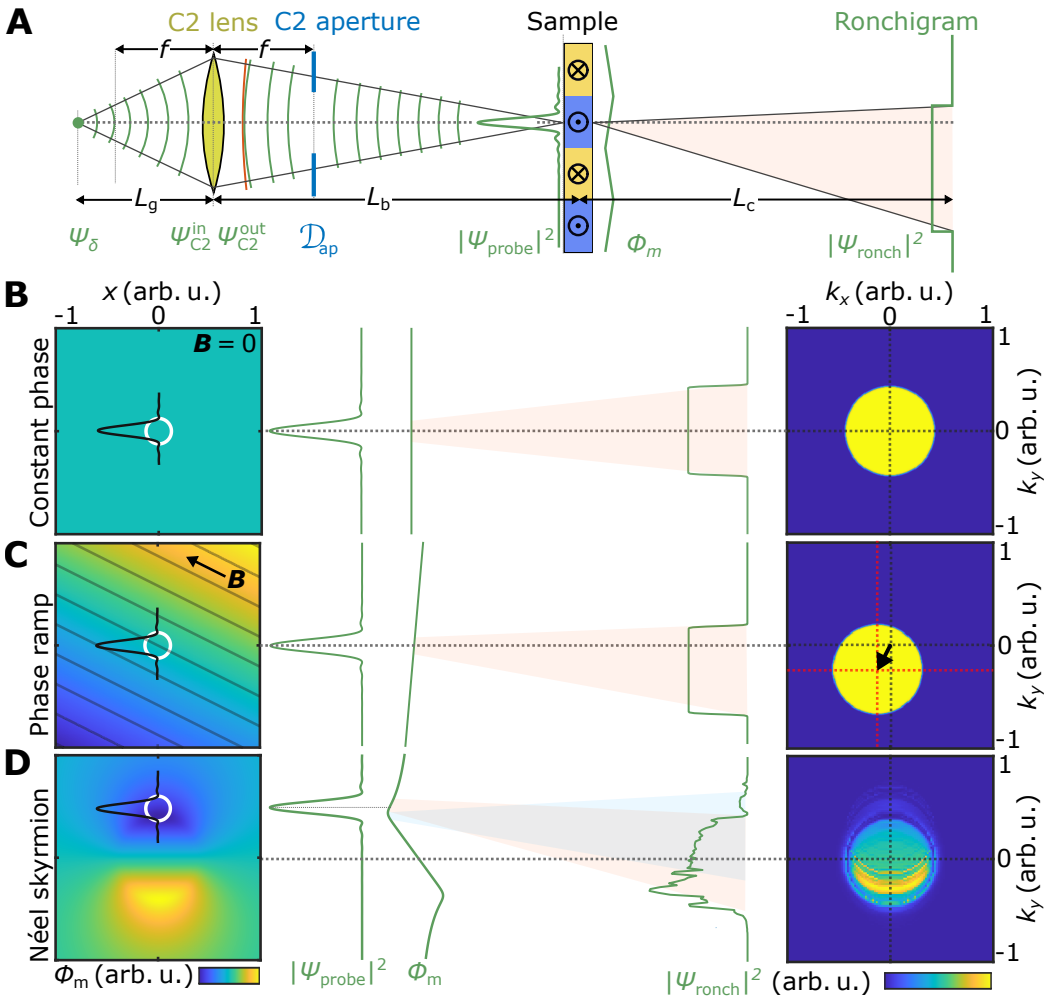

Fig. 4.5.: Wave-optical description of DPC imaging using LMSTEM. **(A)** A point source is imaged using the C2 lens and an aperture. The resulting wave function of the electron probe Ψ_{probe} is phase-shifted by the magnetic induction of the sample. The diverging beam (red shaded) is tilted away from the optical axis due to the phase-shift. The intensity of the wave function Ψ_{ronch} in the plane of observation is called Ronchigram. **(B)** The Ronchigram intensity for a sample without magnetic induction or constant magnetic phase is a centered disk with the shape of the circular aperture. **(C)** A homogeneous in-plane magnetic induction $\boldsymbol{B}$ leads to a shift along the inverted direction of the phase gradient. **(D)** The more complex electron phase shift produced by the tilted magnetization structure of a Néel skyrmion shows no constant phase gradient within the probe area which leads to a redistribution of intensities inside the Ronchigram.

included in this description, as will make sense from the simulations shown later in section 4.2.3. To obtain the electron wave function of the probe Ψ_{probe}, $\Psi^{\mathrm{out}}_{\mathrm{C2}}$ is propagated for the image distance L_{b}. For ideal lenses, it can be shown that Ψ_{probe}

is proportional to the Fourier transform of $\mathcal{D}_{\mathrm{ap}}$, independent of aperture position along the beam path [171]

$$\Psi_{\mathrm{probe}}(\boldsymbol{r}_\perp) \propto \mathcal{F}\left[\mathcal{D}_{\mathrm{ap}}(\boldsymbol{k}_\perp)\right] \ . \tag{4.24}$$

The square modulus of the Fourier transform of a circular aperture is the Airy pattern from expression (4.18). The electron wave is now transmitted through the magnetic sample where it picks up an additional spatially dependent magnetic phase $\phi_{\mathrm{m}}(\boldsymbol{r}_\perp)$. This phase was already discussed in the previous section about Fresnel LTEM and can be computed using Eq. (4.6). The modified wave-function of the probe then propagates for the camera length L_{c} until it reaches the plane of observation. The final wave Ψ_{ronch} can be obtained by using Fraunhofer diffraction in the far field

$$\Psi_{\mathrm{ronch}}(\boldsymbol{k}_\perp) = \mathcal{F}^{-1}\{\,\Psi_{\mathrm{probe}}(\boldsymbol{r}_\perp) \cdot \exp\left[\mathrm{i}\phi_{\mathrm{m}}(\boldsymbol{r}_\perp)\right]\} \ . \tag{4.25}$$

This is valid as typical probe sizes are <10 nm and the electron wavelength is in the pm range while the camera length is in the order of 1 m. For simplicity, the actual scale of Ψ_{ronch} is not given as results of this work only depend on relative shifts. As mentioned before, the observed intensity $|\Psi_{\mathrm{ronch}}|^2$ is called Ronchigram and will, depending on ϕ_{m}, have more or less the character of the aperture shape. For $\phi_{\mathrm{m}} = \mathrm{const}$ and a circular aperture, the Ronchigram is a homogeneously illuminated disc.

To further elaborate on this vague statement, Fig. 4.5B-D shows three different electron phases ϕ_{m}, that originate from different magnetic systems, and their respective Ronchigrams. The left side of Fig. 4.5B shows a constant phase ϕ_{m} that results e.g. from a non-magnetic or perpendicularly (along $\hat{\boldsymbol{z}}$) magnetized sample. The white ring indicates the electron probe radius. With $\phi_{\mathrm{m}} = 0$, the combination of Eq. (4.24) and (4.25) is trivial and the resulting Ronchigram intensity is the aperture function $\mathcal{D}_{\mathrm{ap}}$, centered around the optical axis, as shown on the right side. The central part of the image shows vertical line profiles of Ψ_{probe}, ϕ_{m} for $x = 0$ and Ψ_{ronch} for $k_x = 0$ in remembrance of the right side of Fig. 4.5A.

A sample with uniform in-plane magnetic induction will lead to a linear electron phase ramp ϕ_{m} as shown in Fig. 4.5C. The resulting Ronchigram intensity still has the aperture shape, though it is shifted with respect to the optical axis, as indicated by the arrow. This shift is proportional to the local phase gradient at the electron probe position. This fact is eponymous for Differential Phase Contrast Microscopy and can easily be verified by an inspection of Eqs. (4.24) and (4.25) and the application of the convolution theorem. Assuming a linear phase ramp $\phi_{\mathrm{m}} = ax + by$, instead of the multiplication with $\exp(\mathrm{i}\phi_m)$ in Eq. (4.25), a convolution of the aperture

function $\mathcal{D}_{\mathrm{ap}}$ with $\mathcal{F}\left(\exp\left[i\left(ax+by\right)\right]\right)$ can be conducted. This is a convolution of $\mathcal{D}_{\mathrm{ap}}$ with a laterally shifted delta function, resulting in a Ronchigram of the shifted aperture function.

The third example is the electron phase of a tilted Néel skyrmion, shown in Fig. 4.5D. In this case, the Ronchigram intensity shows striking differences from the aperture function. It is a distribution of disks from different areas on the specimen. Two partial beams which are shifted in opposite directions with respect to the optical axis are shown as an example. Further, there is a redistribution of disk intensity, i.e. the disk is not homogeneously illuminated, which is prominently visible in the line-profile. The reason for this is that the electron phase gradient $\nabla_{\perp}\phi_{\mathrm{m}}$ is not constant inside the electron probe which is indicated in the phase line-profile. The electron probe position is chosen such that the overlap of the probe with ϕ_{m} contains phase gradients in y-direction of opposite sign, which explains the two distinct disks in the Ronchigram. In the region where the two disks overlap, interference leads to the mentioned redistribution of intensity. The effect is even further emphasized by the curvature of ϕ_{m}.

To capture the local electron phase information that is encoded within the Ronchigram, a variety of detectors is available. The most established one is the annular segmented diode that is shown on the bottom of Fig. 4.4A. Before the measurement, the Ronchigram is centered onto the ring such that the diffraction disc has a small overlap of the inner detector edge [191]. The overlap can be controlled by changing the camera length and the C2 aperture size or by using a 3-condenser illumination system as provided by modern microscopes. When the Ronchigram gets shifted off the detector center due to a local phase gradient induced by the sample, the difference signal of opposing diode segments will be proportional to this shift and to the local phase gradient. A detailed detector characterization in terms of linearity, precision and field sensitivity can be found in Refs. [190, 191]. The proportionality of the detector difference signal to the phase gradient is only valid when the diffraction disk is homogeneous as in the situations shown in Fig. 4.5B,C.

As already explained and shown in Fig. 4.5D, a homogeneous Ronchigram cannot be expected once the regarding phase object's size is in the same order as the electron probe diameter. In this case, an inhomogeneous diffraction disk is obtained and the previous relation of Ronchigram intensity and local phase gradient becomes invalid. Müller K. et al. show that the quantum mechanical expectation value for the lateral electron momentum operator $\boldsymbol{p}_{\perp}=\hbar\boldsymbol{k}_{\perp}$ in STEM is given by the center of mass of the Ronchigram intensity [183]

$$\langle\boldsymbol{p}_{\perp}\rangle=\int\Psi_{\mathrm{ronch}}^{*}(\boldsymbol{p}_{\perp})\boldsymbol{p}_{\perp}\,\Psi_{\mathrm{ronch}}(\boldsymbol{p}_{\perp})\,\mathrm{d}p_{x}\,\mathrm{d}p_{y}\,. \tag{4.26}$$

As an example, Müller et al. map the inter-atomic electric fields of $SrTiO_3$ in $[001]$ projection. This material has a spacing of adjacent Sr-columns of $a_{\mathrm{Sr}} \approx 350\,\mathrm{pm}$ and they use an electron probe radius of $R_{\mathrm{probe}} \approx 50\,\mathrm{pm}$. As a_{Sr} and $2R_{\mathrm{probe}}$ have the same order of magnitude, a redistribution of intensities in the Ronchigram intensity is observed, which is captured using a rather slow CCD camera with a frame time of 50 ms. In this example, Müller et al. relate the projected average of the lateral electric field along the electron beam path

$$\boldsymbol{E}_{\perp}^{\mathrm{proj}}(\boldsymbol{r}_{\perp}) = \frac{1}{\tau} \cdot \int \boldsymbol{E}_{\perp}(\boldsymbol{r}_{\perp}, z)\,\mathrm{d}z\,, \tag{4.27}$$

with the center of mass of the Ronchigram [183] which gives

$$-\frac{v}{e\tau}\,\langle \boldsymbol{p}_{\perp} \rangle = \boldsymbol{E}_{\perp}^{\mathrm{proj}} \otimes I_{\mathrm{probe}}\,. \tag{4.28}$$

Here, v is the electron velocity. Therefore, the measured center of mass is directly proportional to the average projected electric field convoluted with the electron probesize.

Today, with a greater prevalence of fast CCD cameras in TEM, this method becomes an established technique in the TEM community for inter-atomic electric field measurement and is widely referred to as 4D-STEM [193, 194]. In fact, Schwarzhuber et al. recently proposed the use of a different detector in TEM, which is called the position sensitive diode (PSD). This detector inherently measures the Ronchigram's center of mass and is able to offset some of the CCD camera's downsides like large pixel dwell time and price [189].

Considering magnetic fields, this discussion seems unnecessary because structures like magnetic domain walls usually extend over more than a thousand atoms. This fact is even the key ingredient for magnetic continuum theory [5]. However, as mentioned before, picometer-sized electron probes are not available for most magnetic structures as LMSTEM needs to be used. Here, probe sizes $>2\,\mathrm{nm}$ (commonly around 10 nm) are expected. With skyrmions smaller than 50 nm, latter considerations become relevant again [36, 52, 71, 74, 195, 196]. From this point of view and in consideration of the ratio of phase variation distance with respect to probe diameter, skyrmions in LMSTEM can be viewed as the magnetic counterparts of atoms in HRSTEM. For this reason, it makes sense to provide the relation of the center of mass of the Ronchigram to the lateral magnetic induction. The calculation is shown in appendix A.2. The result

$$-\frac{1}{e\tau}\langle \boldsymbol{p}_{\perp} \rangle = \left[B_y^{\mathrm{Proj}}(\boldsymbol{r}_{\perp}) \cdot \hat{\boldsymbol{x}} + B_x^{\mathrm{Proj}}(\boldsymbol{r}_{\perp}) \cdot \hat{\boldsymbol{y}} \right] \otimes I_{\mathrm{probe}}(\boldsymbol{r}_{\perp})\,, \tag{4.29}$$

with the average projected lateral magnetic induction

$$\boldsymbol{B}_{\perp}^{\mathrm{Proj}}(\boldsymbol{r}_{\perp}) = \frac{1}{\tau}\int \boldsymbol{B}_{\perp}(\boldsymbol{r}_{\perp}, z)\,\mathrm{d}z\,, \tag{4.30}$$

and $\boldsymbol{B}_{\perp}^{\mathrm{Proj}} = (B_x^{\mathrm{Proj}}, B_y^{\mathrm{Proj}})$ is very similar to the case of electric fields given in Eq. (4.28), however independent of the electron's kinetic energy. This is in agreement with the classical expectation which is also shown in appendix A.2.

4.2 Electron phase imaging theory for magnetic skyrmions and chiral magnetic textures

This section applies the general theoretical considerations about TEM introduced in the previous section to the specific spin structures of skyrmions or other chiral magnetic textures. It starts off with a qualitative description of the Fresnel and DPC LTEM contrast. The intention here is to give an educational overview of possible Bloch and Néel type skyrmion related contrasts in TEM. Afterwards, a quantitative description is given that enables the relation of the skyrmion LTEM contrast to the actual spin structure. This description is then further extended for DPC LTEM and aberration effects are discussed.

4.2.1 Qualitative image contrast of chiral magnetic textures in Lorentz microscopy

This first section qualitatively shows the image contrast that is expected in a Fresnel and DPC Lorentz TEM experiment for the helical and Bloch skyrmion phase of B20 chiral magnets that were introduced in section 2.1.3. Afterwards, these explanations are extended to the cycloidal and Néel skyrmion phases of the heavy metal/ferromagnet/heavy metal multilayer systems discussed in section 2.1.3. Beside schematic drawings, actual microscopy data is presented for each of the two aforementioned techniques.

The description starts with the helical phase which shows a Bloch-type spin winding. As already mentioned, due to the mean free path of high energy electrons, the maximum sample thickness is limited to around 100 nm, which is in the order of the propagation length λ_{h} of the chiral magnets investigated in this thesis. In such a thin film geometry, the direction of the $\boldsymbol{q}_{\mathrm{h}}$-vector of the spin helices is constrained to the sample plane [48, 95]. A sketch of a 2D helical phase is displayed in Fig. 4.6A. The magnetization texture $\boldsymbol{M}$ within the sample is illustrated by the 3D arrows.

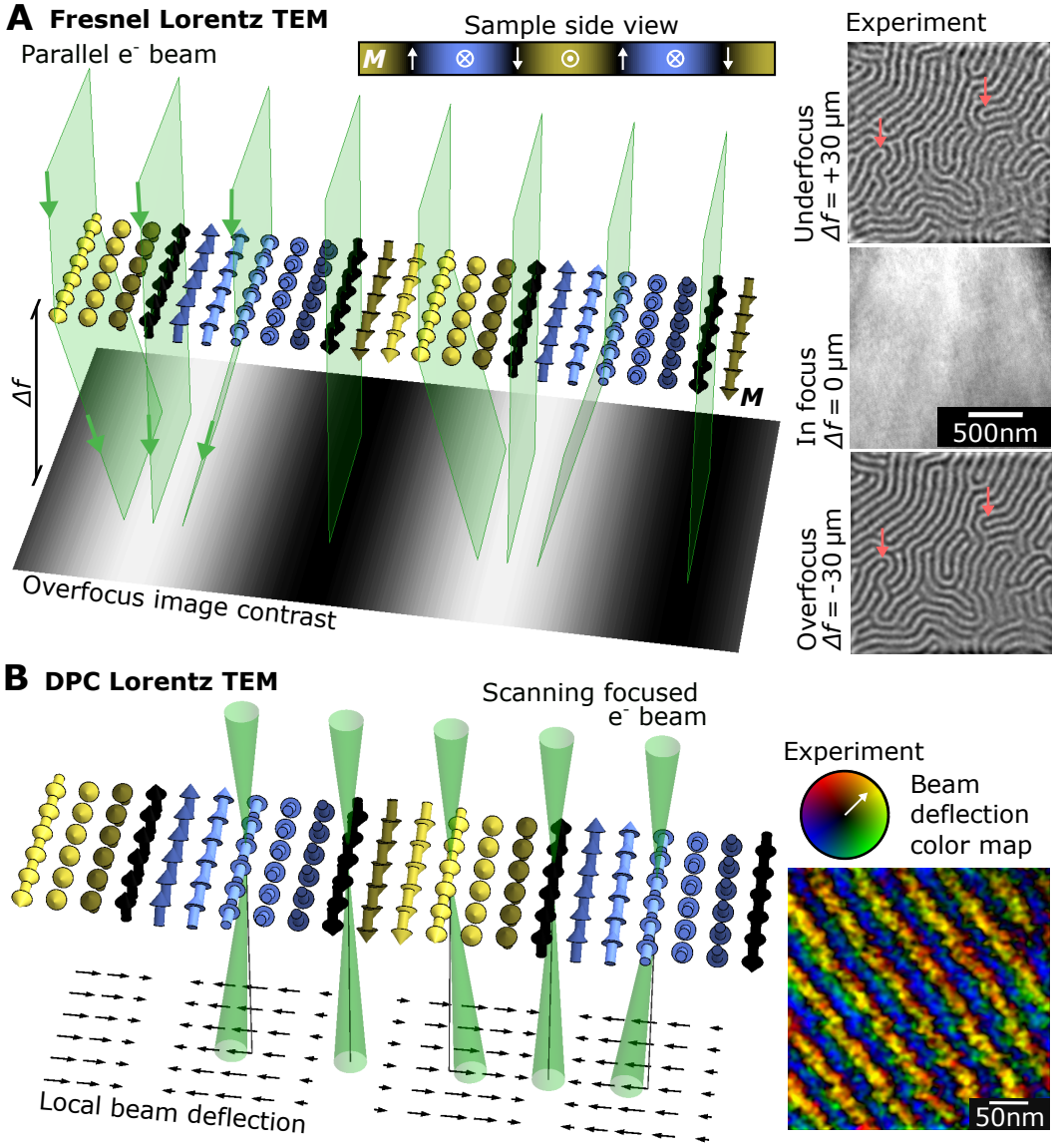

Fig. 4.6.: LTEM imaging of the helical phase. **(A)** Fresnel LTEM imaging of the magnetization structure of a thin magnetic sample containing a helical phase. The green planes show equivalent electron trajectories through the sample. At a distance Δf below the sample, an overfocus image can be obtained (black/white plane). The inset shows a side view of the sample magnetization. On the right, an actual defocus series of the material $Fe_{0.5}Co_{0.5}Si$ is displayed. The magnetic contrast inverts for different signs of Δf and vanishes for $\Delta f = 0$. The arrows mark reference points for an easier comparison. **(B)** Imaging of the helical phase in DPC LTEM. The green cones represent the focused electron beam. Its local deflection is shown below the sample with the black arrows. The image on the right is an actual DPC measurement on Cu_2OSeO_3. Here, color represents the direction and brightness the magnitude of the electron beam deflection as indicated by the color wheel above.

The arrow's coloring highlights the in-plane components of $\boldsymbol{M}$. The inset at the top shows the respective side view of the sample.

Using Fresnel Lorentz TEM at normal incidence, a parallel electron wave is transmitted through the sample with $\boldsymbol{k} \parallel \hat{\boldsymbol{z}}$. For the qualitative description and an easier illustration, the particle image of electrons is considered. In Fig. 4.6A, the front edges of the green planes show the trajectories of the electrons during their transmission. As these trajectories are the same along $\boldsymbol{q}_\mathrm{h} \times \hat{\boldsymbol{z}}$, planes are drawn to represent equivalent paths. Therefore, the drawings should not be confused with an illustration of a plane wave front. As indicated, the electrons get deflected from the spin structure. At some distance Δf to the sample, the lateral electron density shows a stripe pattern that follows the modulation of the magnetization, as indicated by the black/white plane. This electron density is captured by the overfocus image contrast in Fresnel LTEM, as was explained in section 4.1.2 and Fig. 4.2B. Example Fresnel LTEM images of the helical phase of $Fe_{0.5}Co_{0.5}Si$ are displayed on the right side of Fig. 4.6A. The helical phase in the image is not well ordered and shows many defects. As expected, the image intensities of over- and underfocus image are inverted, which is easily visible by comparing the contrast at the reference sites marked by the red arrows. When the image plane is tuned to the sample plane, i.e. $\Delta f = 0$, the magnetic contrast vanishes as shown in the in-focus image. Due to the nature of magnetic lenses in a TEM as well as imperfections of the calibration, different foci also slightly shift and rotate the field of view and can also lead to different magnifications. Therefore, affine transformations are calculated using reference sites and applied to the example images such that image features are located at the same position for each defocus. Furthermore, a bandpass and Gaussian ($\sigma = 3\,\mathrm{pixel}$) filter have been applied to the over- and underfocus images to remove the background and emphasize the contrast reversal. This procedure is conducted for each focus series, presented in this section and is not critical in this qualitative context.

Using DPC Lorentz TEM, the electron beam is focused onto the sample plane. The confined electron probe interacts with local magnetic fields of the sample which lead to a deflection of the diverging electron beam. The electron beam is scanned across the sample and at each position the beam deflection is measured. It is proportional to the local electron phase gradient and the magnetic induction as explained in section 4.1.3. For the helical phase, this is illustrated in Fig. 4.6B. The green cones represent the focused electron beam for five example positions. Equivalently to the previous description, the beam gets deflected by the Lorentz force and the local beam deflection is displayed with the black arrows below the spin structure. As expected, the out-of-plane components of $\boldsymbol{M}$ do not deflect the beam. The image on the right side of the sketch shows an actual DPC measurement of the helical phase

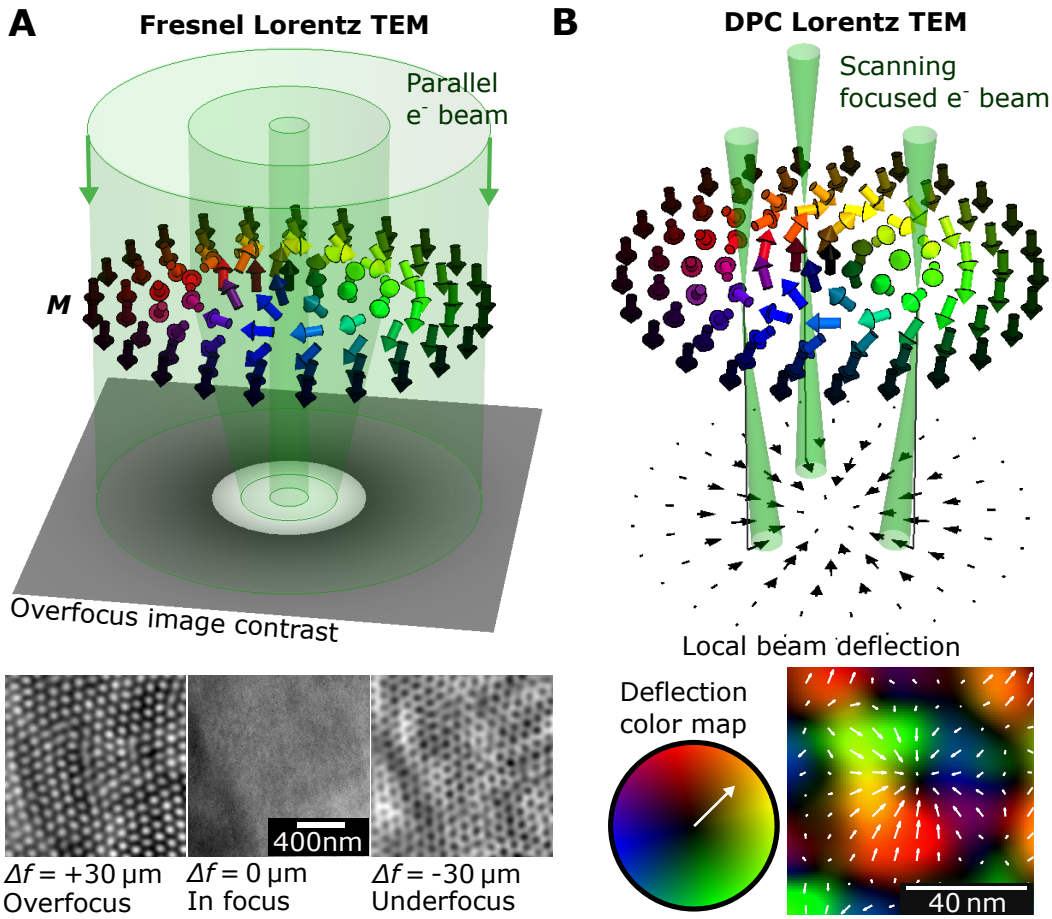

Fig. 4.7.: LTEM imaging of the skyrmion phase. **(A)** Fresnel LTEM imaging of a Bloch skyrmion. The electrons get deflected to the center of the skyrmion by its wall magnetization. The overfocus image sketched below shows a bright spot. The experimental focus series of Cu_2OSeO_3 on the bottom shows a hexagonal lattice of the expected bright spots that change to dark spots for underfocus condition. **(B)** DPC LTEM imaging of a Bloch skyrmion. The local deflection of the focused electron beam at the skyrmion wall points towards the skyrmion center. This matches the experimental image of a skyrmion in Cu_2OSeO_3 shown at the bottom.

of Cu_2OSeO_3. The beam deflection is encoded in color. The color represents the direction and its brightness the magnitude of the beam deflection. This is further indicated by the color wheel shown on top. Note that the color mapping might not be equivalent throughout this thesis and it is advised to always check the respective color wheel that is given for each measurement. Here, e.g. it has been chosen such that the blue and yellow matches the sketch to the left. To reduce some of the noise of the image that is caused by strong charging effects of the insulating material, a polynomial background fit is subtracted and a 3×3 median as well as a Gaussian filter ($\sigma = 4\,\mathrm{pixel}$) is applied.

A quite similar description can be applied to the contrast formation of a Bloch skyrmion. The 3D vectors in Fig. 4.7A show the spin structure of a Bloch skyrmion. The in-plane components are highlighted by color, depending on their direction and magnitude. As the objective lens produces a magnetic field parallel to the beam direction, the skyrmion tubes, shown in Fig. 2.6, are also parallel to the beam for normal electron incidence. In the given example, it can be seen that the electrons that are transmitted through the skyrmion wall get deflected towards its center. Due to this, the Bloch skyrmion can be considered as a nano-lens for electrons. Due to this deflection, at an overfocus $\Delta f > 0$, an increased electron density at the lateral position of the skyrmion core is expected. The overfocus Fresnel image therefore shows the given skyrmion as a bright spot as in the sketch below. One might notice that the spot is surrounded by a dark halo which results from the electron redistribution to the center. An actual micrograph of the skyrmion lattice in Cu_2OSeO_3 shows the same expected contrast. Changing the image plane to a z-value above the sample again leads to an inversion of contrast and the skyrmions appear as black dots.

The DPC measurement follows the latter description, and an electron beam deflection towards the skyrmion center is measured at the skyrmion wall positions, as shown in the sketch of Fig. 4.7B. The experimental image also shows how the wall covers all directions of deflection as visible from the color wheel. This reflects the equatorial spins of the unit spheres in Fig. 2.5B. Note that only one type of Bloch skyrmion chirality is shown in this example. For an inverted DMI constant D_{bulk}, the over- and underfocus images will be exchanged and the local beam deflection will be in opposite direction. This also means that Lorentz TEM is sensitive to the skyrmion chirality and the sign of the DMI.

Now systems with interface DMI, which leads to cycloidal and Néel skyrmion spin structures, are considered. However, the trivial particle description from before is insufficient for the accurate description of the observed images. The particle image can still be applied, however the spin structure needs to be adjusted as described in the following. At the top of Fig. 4.8A, a cycloidal magnetization structure is shown. Naively, it might be expected that the in-plane components of the cycloid lead to a beam deflection which should be visible at least for DPC LTEM. In reality, this is not true which is evidenced by a wave optical consideration. Using Mansuripur's formalism from Eq. (4.6), it can analytically be proven that the phase shift $\phi_{\mathrm{m}}(\boldsymbol{r}_\perp)$ that is obtained by an electron transmitted through a cycloidal spin structure is zero as demonstrated in appendix A.3. Due to this, no contrast can be obtained from such

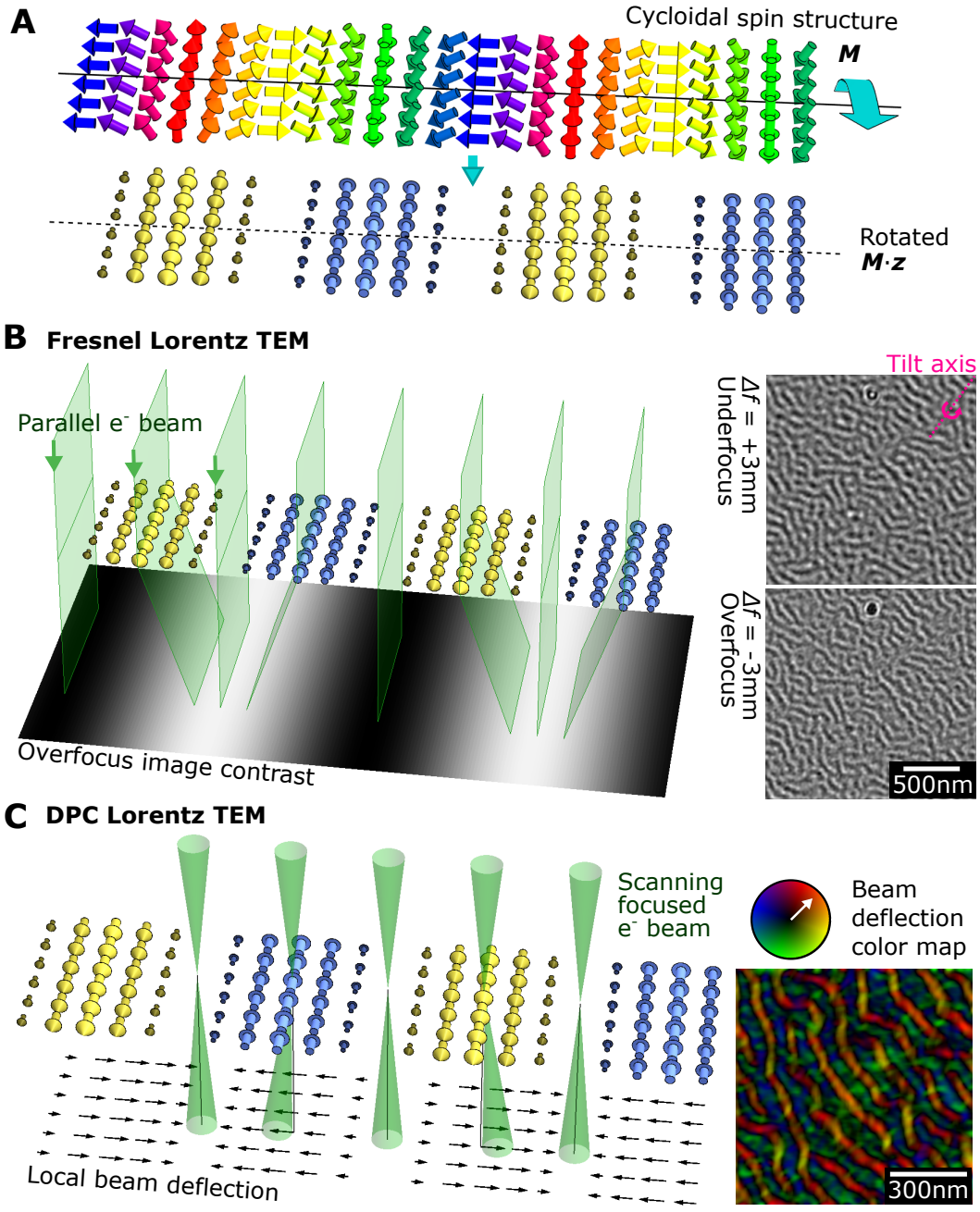

Fig. 4.8.: LTEM imaging of the cycloidal phase. **(A)** The cycloidal spin structure is shown on the top. The in-plane components do not contribute to phase imaging. Tilting the sample around the indicated axis gives in-plane contributions from the out-of-plane spins as sketched at the bottom. **(B)** Fresnel LTEM imaging of the tilted cycloidal phase. The contrast formation is very similar to the helical phase as seen from the experimental data on the right. The diagonal tilt axis orientation is marked inside the top micrograph. **(C)** DPC LTEM imaging of the tilted cycloidal phase and experimental data on the right.

a spin structure. McVitie et al. show that the electron phase can be also expressed as [197]

$$\phi_{\mathrm{m}}(\boldsymbol{r}_{\perp}) = -\frac{e\mu_0\tau}{2hr_{\perp}} \otimes (\nabla \times \boldsymbol{M}) \cdot \hat{\boldsymbol{z}} \; . \tag{4.31}$$

As before, τ is the sample thickness and $\otimes$ is the convolution operator. It directly follows that only magnetization distributions $\boldsymbol{M}(\boldsymbol{r}_{\perp})$ with a curl that has a non-vanishing z-component can be observed with LTEM. However, for both cycloid and Néel skyrmion $(\nabla \times \boldsymbol{M}) \cdot \hat{\boldsymbol{z}} = 0$. To intuitively understand this, the magnetostatic field $\boldsymbol{H}_{\mathrm{d}}$ of a Néel skyrmion needs to be considered, which is shown in Fig. 2.2C. To obtain the electron beam deflection, the magnetic induction needs to be integrated along the $\hat{\boldsymbol{z}}$ according to Eqs. (4.29) and (4.30). At the wall position, the demagnetizing field is opposite to the magnetization direction. Outside the sample, the stray fields are non-symmetric and leave a net contribution that is opposite to the magnetization of the Néel skyrmion wall. In reality, the combination of these effects compensates the contribution of $\boldsymbol{M}$ to the magnetic induction.

Nevertheless, the issue that no LTEM signal is obtained can be overcome by introducing a tilt of the sample with respect to the incident electron beam. This way, the out-of-plane components of the magnetization generate an additional in-plane contribution within the plane of observation. These in-plane components of a cycloid are shown at the bottom of Fig. 4.8A. The rotation is conducted around the tilt axis which is chosen parallel to the propagation vector $\boldsymbol{q}_{\mathrm{h}}$. For this configuration, Eq. (4.31) is non-zero and it is possible to return to the particle image as shown in Fig. 4.8B. The deflection is equivalent to the one for the helical phase shown in Fig. 4.6B and the overfocused Fresnel image shows a stripy pattern. This can also be seen from the experimental data on the right obtained from a multilayer stack of Pt/Co/W that is tilted by 20° around the indicated axis. The same argumentation applies to the DPC LTEM measurement illustrated in Fig. 4.6C and the respective experimental data shown on the right.

From the Fresnel images in Fig. 4.6B it might already be apparent that the black and white contrast fades in some areas. In this context, contrast means the intensity difference of the black and white stripes. This becomes even more striking when looking at the Fresnel image in Fig. 4.9A which is recorded from a tilted (20°) Pt/Co/Tb multilayer sample (details on the sample can be found in section 4.4.2). It shows a disordered stripe phase, i.e. the cycloids are not aligned parallel but in a labyrinthine pattern. Defining a local $\boldsymbol{q}_{\mathrm{h}}$-vector perpendicular to the stripe, the $\boldsymbol{q}_{\mathrm{h}}$ directions are evenly distributed across the image. It is evident that contrast is strongest for stripes with $\boldsymbol{q}_{\mathrm{h}}$ parallel to one of the diagonal directions of the image. This can also be seen from the low frequency section of the Fourier transform shown

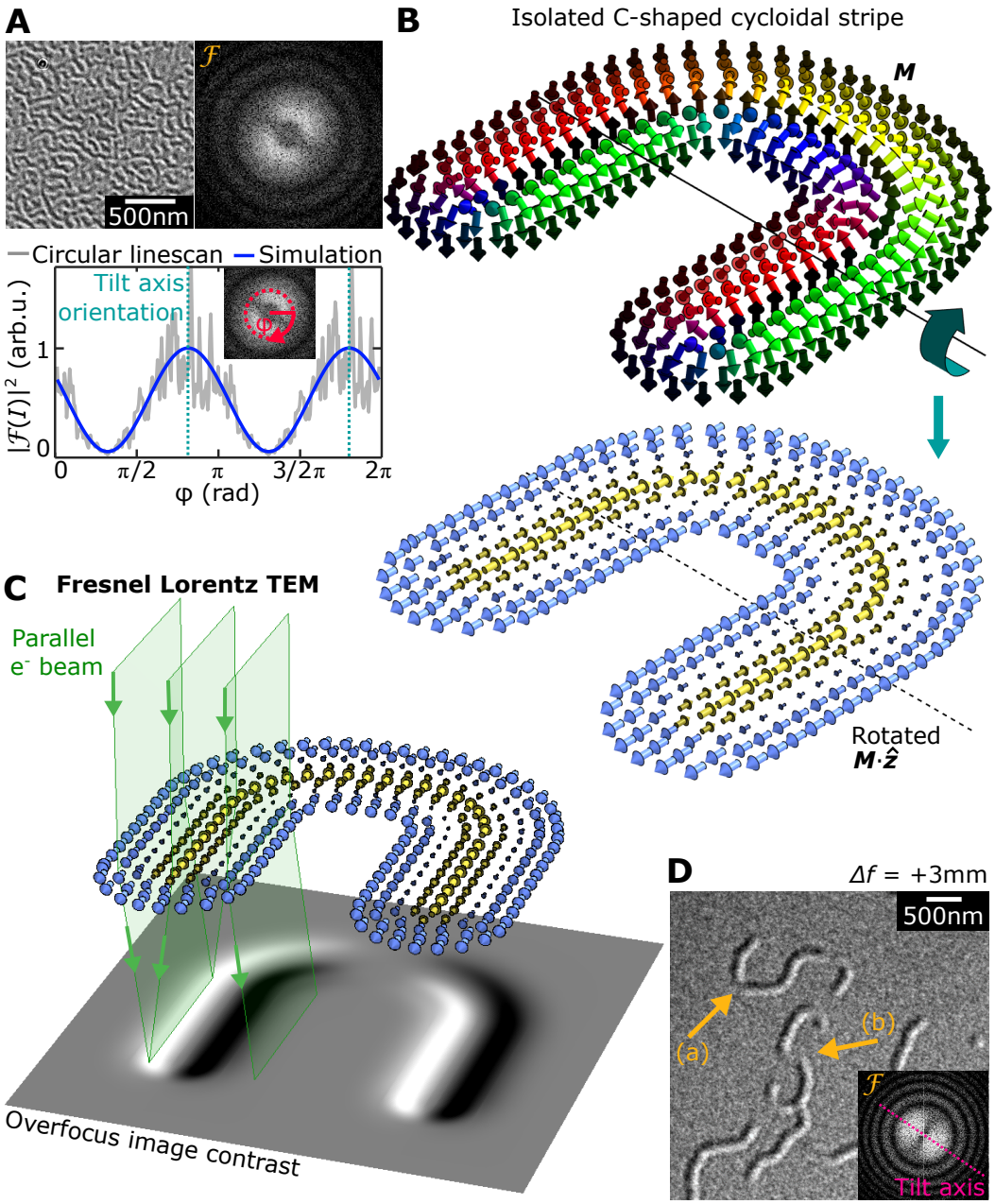

Fig. 4.9.: Cycloidal imaging contrast with respect to tilt axis orientation **(A)** Fresnel micrograph of a disordered cycloidal phase (left) and corresponding Fourier transform (cropped to low frequencies). The plot below shows the circular intensity profile, indicated by the inset. The blue colored line is the theoretically expected dependence (see main text). **(B)** Spin structure of an isolated c-shaped cycloidal stripe (top). Tilting the out-of-plane components as indicated results in the in-plane projections shown below. **(C)** Fresnel imaging of the tilted c-shaped cycloidal stripe. Image contrast vanishes at the c's central part. **(D)** Fresnel LTEM image of isolated cycloidal stripes. Following the contrast along the stripe gives an inversion across the vanishing part for the situation marked with (a). In (b) the contrast does not invert as the stripe maintains its direction with respect to the tilt axis. The tilt axis is indicated in the inset which shows the Fourier transform of the image.

next to the image. Here, the broader inner ring with large intensity features an angular dependence with two maxima along the direction of stripes that show the largest contrast. A circular image profile along the ring with the polar angle φ is shown below as indicated by the inset. Note that images of Fourier transforms (usually) have a logarithmic color scale and a visual comparison of the image to the circular profile might be deceiving. To quantify the angular dependence of the contrast, the Fresnel LTEM image intensity I for different relative orientations of the sample tilt axis and $\boldsymbol{q}_\mathrm{h}$ is simulated. In the simulation, the polar angle of $\boldsymbol{q}_\mathrm{h}$ is called φ and the one of the tilt axis is called κ. A stripy LTEM intensity oscillation is obtained whose amplitude vanishes for $(|\kappa - \varphi| \mod 90°) \to 90°$. The angular dependence of the square modulus of the FT of the images at a k-space radius of $k_\perp = q_\mathrm{h}$ can then be extracted from the simulation

$$|\mathcal{F}(I)|^2 (k_\perp = q_\mathrm{h}, \varphi) \propto |cos(\varphi - \kappa)|^2 \ . \tag{4.32}$$

Here, polar coordinates with the angle φ and radius $k_\perp$ are used (compare with the inset in the bottom of Fig. 4.9A). The result matches the measured circular profile as can be seen from the fit in the data in the bottom of Fig. 4.9A. The inset shows the chosen geometry for φ. This means that LTEM images for tilted cycloids and Néel skyrmions strongly depend on the tilt axis orientation and that the method is insensitive for $\boldsymbol{q}_\mathrm{h}$-vectors that are perpendicular to the tilt axis. Further, by the identification of the maximum value in the respective ring at $k_\perp = q_\mathrm{h}$ in the Fourier transform, the orientation κ of the tilt axis can be determined, as indicated by the dashed line in the plot. The knowledge about the current tilt axis orientation in TEM is often unclear, as a change of TEM magnification can lead to a rotation of the image. Further, the electron transparent membranes where the samples are evaporated onto have a buckling surface which can show intrinsic tilts up to $15°$ [198].

To show the effect more clearly, the spin structure of a single C-shaped cycloidal stripe is considered as shown in Fig. 4.9B. With the same argumentation as before, the in-plane components of the tilted z-components of the magnetization are drawn below. Fresnel LTEM imaging on this structure is illustrated in Fig. 4.9C. As can be seen from the c's endings, the beam deflection leads to a dark and bright overfocus image contrast surrounded by the average gray intensity. However, in the central part of the c, the beam deflection is perpendicular to the local $\boldsymbol{q}_\mathrm{h}$-vector, which is perpendicular to the tilt axis. Due to this, the beams do not meet in the plane of the defocus. Therefore, contrast vanishes for this orientation of the stripe. A second fact is that when following the black/white image feature of the stripe across the short part with vanishing contrast, the edge that was black turns bright and vice

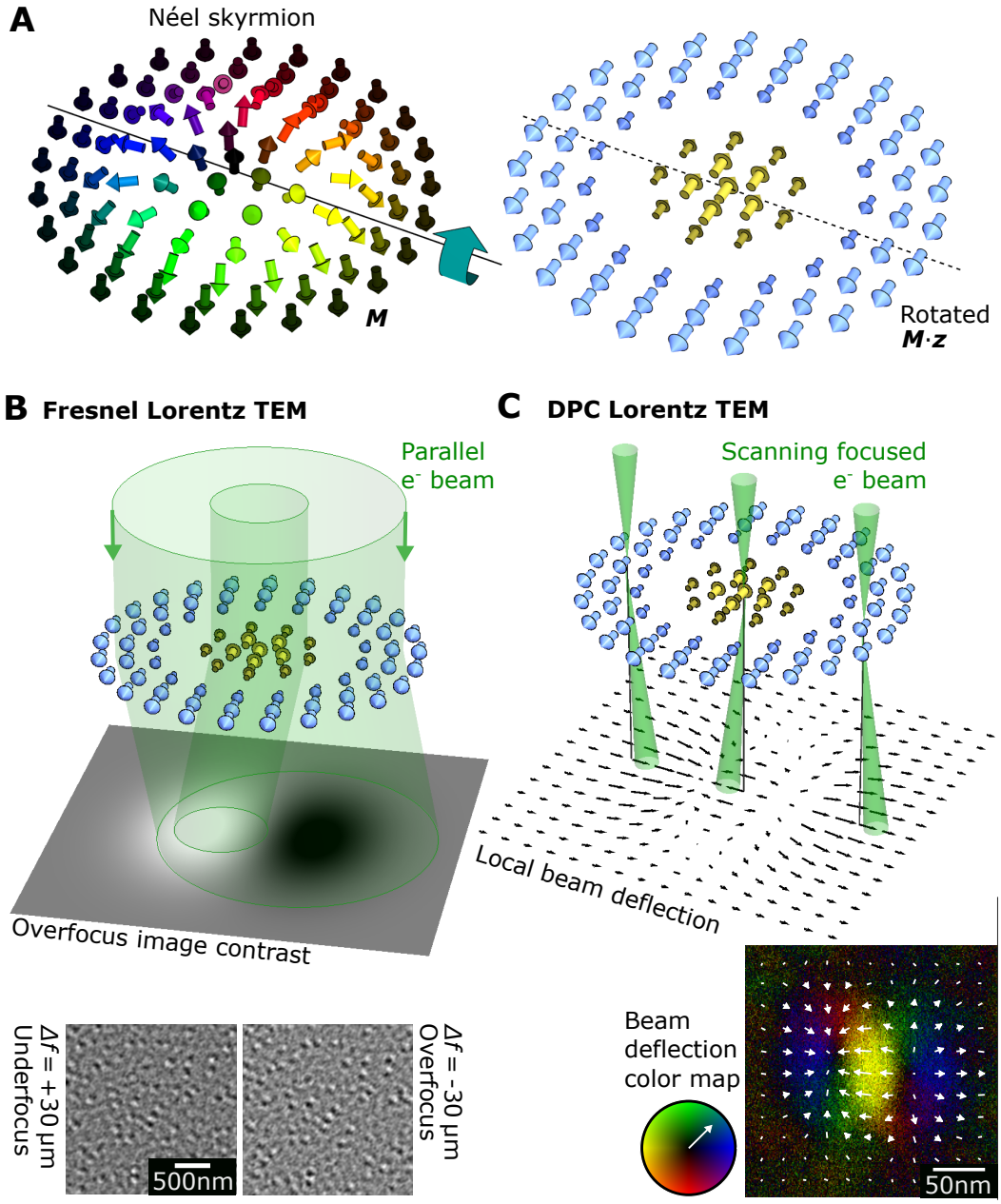

Fig. 4.10.: LTEM Imaging of Néel skyrmions. **(A)** The left side displays the spin structure of a Néel skyrmion. Tilting the out-of-plane magnetization components as indicated results in the in-plane projections shown on the right. **(B)** Fresnel LTEM imaging gives adjacent dark and bright spots when following the tilt axis. An experimental focus series is shown below. **(C)** Electron beam deflection in DPC LTEM meets expectations in the skyrmion core and the polarized part outside the skyrmion. To model the exact deflection structure inside the skyrmion wall that is e.g. seen from the experimental data below, a wave optical needs to be considered.

versa. Considering the spin structure, this is clear. However, in no case should this lead to the conjecture of a changing chirality of the structure, as might be rightfully concluded for the Bloch skyrmion or a helical stripe. In fact, LTEM is not sensitive to the chirality of a Néel skyrmion or isolated cycloidal stripe. It only measures the Néel skyrmion polarity, as the contrast is obtained by the out-of-plane components of the untilted structure. In Fig. 4.9D, a Fresnel image of isolated cycloidal stripes is shown. As demonstrated before, the tilt axis can be identified from the Fourier transform as shown in the inset. The arrow labeled with (a) marks a feature where the contrast inversion is equivalent to Fig. 4.9C. In situation (b), the black/white contrast is not inverted because the projection of the local $\boldsymbol{q}_{\mathrm{h}}$-vector to the tilt axis does not change its sign.

Note that the tilted isolated cycloidal stripe shown in the bottom of Fig. 4.9B is similar to the in-plane magnetization of the so-called 360° domain walls which have been observed since the 1960s [199]. Therefore, the black and white contrast along the stripe in Fresnel images is also featured in these measurements [200]. However, the imaging does not rely on sample tilt as the magnetic domains are already inside the sample plane, which gives an increased contrast due to the relatively large in-plane magnetization.

Finally, LTEM imaging of a Néel skyrmion is discussed. Fig. 4.10A shows its spin structure on the left and the in-plane projection of the tilted out-of-plane magnetization structure on the right. The Fresnel LTEM imaging of this structure is illustrated in Fig. 4.10B. The electron beam deflection is parallel to the sample tilt axis. A dark and bright overfocus image contrast is obtained like in the experimental data on a tilted Pt/Co/Tb sample given below. The beam deflection in DPC LTEM essentially follows this description as seen at the top of Fig. 4.10C and the experimental data below. However, small details like the subtle deflections perpendicular to the tilt axis cannot be explained by the simple particle model and require a wave optical description as shown in section 4.2.3.

For completeness, it should be noted that the field-polarized phase gives no magnetic contrast variation in Fresnel LTEM. In DPC LTEM, it leads at best to a homogeneous beam deflection as it can introduce an electron phase ramp, as shown in Fig. 4.3A in section 4.1.2. In the most common case, the externally-applied magnetic field of the TEM aligns the field-polarized phase parallel to the optical axis and no phase change is introduced at all. In this case, also the $\boldsymbol{q}_{\mathrm{h}}$-vector of the conical phase is aligned parallel to the optical axis. This will also not lead to a Fresnel contrast and might only introduce an electron phase ramp if the sample thickness is no multiple of λ_{h}. Using specialized sample holders which can produce an in-plane magnetic field and align a conical phase parallel to the sample plane, a similar contrast to the helical phase is expected.

4.2.2 Spin structure of isolated magnetic skyrmions in relation to the magnetic electron phase

Lorentz TEM undeniably emerged as one of the most important methods for real-space observation of magnetic skyrmions. Its spatial resolution exceeds the one of optical magnetic imaging like magneto-optical-Kerr-effect (MOKE) microscopy by two orders of magnitude, it allows a faster image-acquisition time than magnetic force microscopy (MFM) or spin-polarized scanning tunneling microscopy (SP-STM) and is more accessible than magnetic X-ray microscopy [21, 81, 201, 202]. The contrast formation however shows a certain complexity, which might already have become apparent from the previous section. Relating the observed image contrast with the actual spin structure is non-trivial and in-principle requires certain knowledge about the saturation magnetization and thickness of the sample as well as various microscopic parameters like aberrations or defocus values. In this section, the magnetic electron phase that is generated by an isolated Bloch or Néel skyrmion is calculated and related to the skyrmion spin structure which is defined by skyrmion radius and skyrmion wall width. These findings can then act as the ground work for the application of the different Lorentz techniques like electron holography, DPC or Fresnel LTEM which share their reliance on the magnetic electron phase but show a different skyrmion contrast and are subject to different aberrations. For DPC LTEM, this is discussed in section 4.2.3.

The first requirement for this quantitative discussion is a suitable skyrmion model which can be used as a basis for the TEM simulations. The choice fell to the isolated skyrmion model proposed by Büttner et al. who extensively study the stability of skyrmions for a large parameter space in their work [33]. The model assumes a cylindrically symmetric skyrmion with polar coordinates $r_\perp$ and φ. The magnetization profile is given by

$$\boldsymbol{m}(r_\perp, \varphi) = \sin\left[\theta(r_\perp)\right]\cos\left(\varphi + \psi\right)\,\hat{\boldsymbol{x}} + \sin\left[\theta(r_\perp)\right]\sin(\varphi + \psi)\,\hat{\boldsymbol{y}} + \cos\left[\theta(r_\perp)\right]\,\hat{\boldsymbol{z}}\,. \tag{4.33}$$

Here, ψ is the skyrmion helicity as already introduced in section 2.1.2 and Fig. 2.5. From Eq. (4.33), it is now also apparent that ψ is the angle between the radial direction and the in-plane magnetization of the skyrmion wall, which is the essential difference between the Bloch and Néel type. The skyrmion wall profile is defined by $\theta(r_\perp)$. Experimental data suggests the following profile [33, 203, 204]

$$\theta(r_\perp; R^*, \Delta^*) = \theta_{\mathrm{DW}}(r_\perp - R^*, \Delta^*) + \theta_{\mathrm{DW}}(r_\perp + R^*, \Delta^*) - (N+1)\frac{\pi}{2}\,, \tag{4.34}$$

$$\theta_{\mathrm{DW}}(r_\perp; \Delta^*) = 2\arctan\left[\exp\left(\frac{r_\perp}{\Delta^*}\right)\right]\,. \tag{4.35}$$

The core polarity $N = \pm 1$ gives the sign of the magnetization's z-component in the skyrmion core, i.e. $\mathrm{sgn}\left[m_z(r_\perp = 0)\right] = N$. The counterintuitive quantity R^* is related to the skyrmion radius R defined by $m_z(R) = 0$ with the expression

$$R^* = \Delta^* \ln\left(\sinh\left(R/\Delta^*\right) + \sqrt{\sinh^2\left(R/\Delta^*\right) - 1}\right)\,. \tag{4.36}$$

The parameter Δ^* is connected to the domain wall width. From an experimental point of view, it can be more convenient to define the domain wall width Δ as the radial distance between the inner radius R_i where $m_z(R_\mathrm{i}) = N \cdot 0.99$ and the outer radius R_o where $m_z(R_\mathrm{o}) = -N \cdot 0.99$. In this case, Δ^* and Δ are connected with the simple linear relation

$$\Delta^* = 0.12\,\Delta\,. \tag{4.37}$$

As an example, the magnetization structure of a Bloch skyrmion with $\psi = 3\pi/2$, $N = 1$ and a relative skyrmion wall width $\Delta = 1.2R$ is shown in Fig. 4.11A. The white arrows represent the in-plane magnetization, whereas coloring defines the m_z-component which is also indicated by the color bar at the y-axis in Fig. 4.11B. The graphs in Fig. 4.11B show the line profiles of the $\boldsymbol{m}$-components along the dotted line in Fig. 4.11A. They also shows the structural parameters R, R_i, R_o and Δ that define the skyrmion profile of the model.

The next step is to calculate the electron phase ϕ_m that is introduced by the magnetic induction resulting from the skyrmion spin structure. For this, the formalism of Mansuripur, given in Eqs. (4.6)-(4.9) in section 4.1.2 is used. To verify that the developed code is free of errors and the conversion to SI units is correct, magnetic sample structures given in Mansuripur's original work are replicated and the calculated phase is compared [173]. The obtained results are identical, which is demonstrated in appendix A.4.

Under normal electron incidence, i.e. $\hat{\boldsymbol{p}} = (0, 0, 1)$, Eq. (4.6) simplifies to the expression that is found by Belaggia et al. [205, 206]. This can be further rewritten to

$$\phi_\mathrm{m} = \frac{\mathrm{i}e\mu_0 M_\mathrm{s}\tau L}{h}\,\mathcal{F}^{-1}\left[\frac{(\tilde{m}_x k_x - \tilde{m}_y k_y)\,L}{(k_x^2 + k_y^2)\,L^2}\right]\,. \tag{4.38}$$

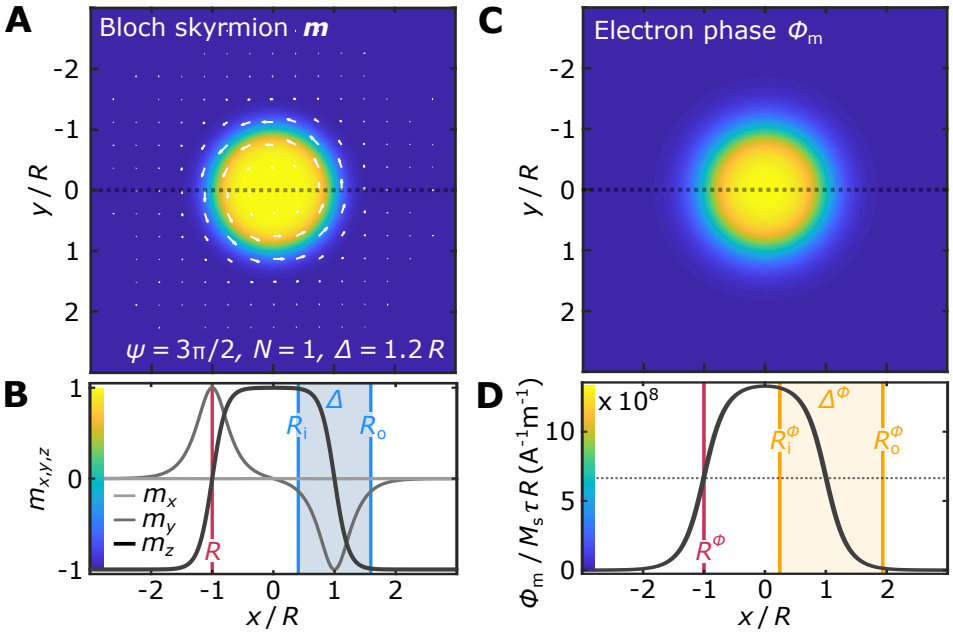

Fig. 4.11.: **(A)** Example Bloch skyrmion spin structure with indicated structural parameters. The white arrows represent the in-plane magnetization components. Coloring maps the m_z component as indicated at the y-axis of (B). **(B)** Line profile of the components of $\boldsymbol{m}$ along the dotted line in A. **(C)** Calculated 2D electron phase of the skyrmion in (A). Coloring represents the normalized phase value as indicated at the y-axis of (D). **(D)** Line profile of the normalized electron phase along the dotted line in (C).

Here, $\tilde{\boldsymbol{m}}$ is the Fourier transform of the unit magnetization and $L = L_x = L_y$ is the physical edge length of the simulation grid. The advantage of this expression is that the physical dimensions and the saturation magnetization of the system appear as scaling terms in the prefactor. Therefore, the phase calculations can be normalized with these factors which makes the results applicable to arbitrary skyrmion sizes and saturation magnetization strengths. This is a key requirement as the intention of this section is to give a general recipe to deduce the skyrmion profile from LTEM measurements without focusing on a specific sample/material with fixed magnetic and geometrical parameters.

To showcase the electron phase that is introduced by a Bloch skyrmion, the electron phase for the example Bloch skyrmion structure from Fig. 4.11A is calculated. The 2D phase map is shown in Fig. 4.11C. The color scale is given at the y-axis in Fig. 4.11D, which shows the phase's horizontal line profile at $y = 0$ as indicated by the dotted line. According to the prior discussion, the phase is normalized with the saturation magnetization, sample thickness and the skyrmion radius. This makes it easy to retrieve the phase of an actual skyrmion structure from the multiplication by these parameters. A first feature is that the shape of ϕ_m is very similar to the top

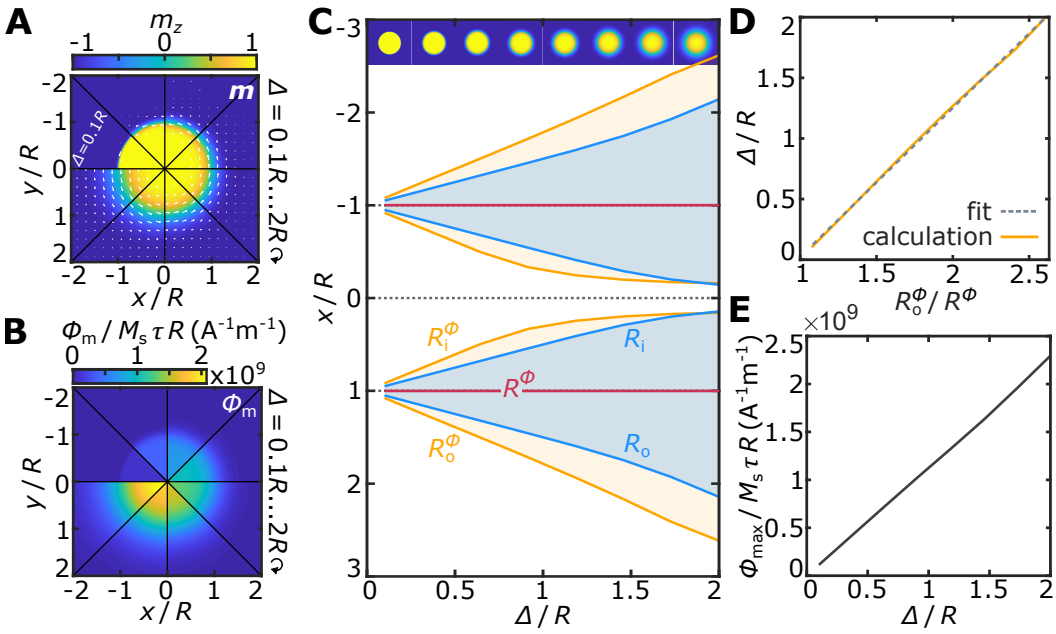

Fig. 4.12.: Electron phase in dependence of Bloch skyrmion wall width. **(A)** The segments show the Bloch skyrmion structure for different wall widths ranging from $\Delta = 0.1R$ to $\Delta = 2R$. **(B)** Electron phase of the respective spin structure shown in (A). **(C)** Structural parameters of the skyrmion structure and the electron phase with respect to the skyrmion wall width. **(D)** The outer radius of the phase R_o^ϕ shows a linear dependence with the domain wall width. **(E)** The normalized phase maximum (see text) with respect to domain wall width.

hat shape of m_z. This is slightly surprising considering that m_z does not contribute to the electron phase. In analogy to the description of the skyrmion structure it is therefore natural to define a radius R_i^ϕ with $\phi_m(R_i^\phi) = \phi_m(r_\perp \to \infty) + 0.99\phi_{max}$ and R_i^ϕ with $\phi_m(R_o^\phi) = \phi_m(r_\perp \to \infty) + 0.01\phi_{max}$. Here, $\phi_{max} = \phi_m(0) - \phi_m(r_\perp \to \infty)$. To complete the analogy, a phase wall width $\Delta^\phi = R_o^\phi - R_i^\phi$ and a radius R^ϕ at the inflection point of ϕ_m are defined. These parameters are included in Fig. 4.11D. In the shown example, R coincides with R^ϕ and $\Delta^\phi > \Delta$.

These relations are now extended for variable domain wall widths. The considered values cover the whole physical range which reaches from $\Delta = 0.1R$, corresponding to a circular domain with a very sharp domain wall that is close to the classical understanding of a magnetic bubble, up to $\Delta = 2R$, representing a domain wall that is twice the skyrmion radius and begins to overlap in the skyrmion core. The spin structures for this range are shown in Fig. 4.12A. Due to rotational symmetry of the structure, the polar direction is split into segments and each segment represents a different value of Δ. The respective calculated normalized electron phase is shown in Fig. 4.12B accordingly.

The structural parameters of $\boldsymbol{m}$ and ϕ_m are extracted and plotted for each domain wall width in Fig. 4.12C. The narrow horizontal image strip on the top shows the

m_z-component for the respective Δ on the abscissa. The ordinate also ranges to negative values of x, so it can be viewed as a crosscut through the skyrmion. The first aspect worth mentioning is that the inflection point of the phase R^ϕ coincides with the actual skyrmion radius for the whole Δ-range, i.e.

$$R = R^\phi \ . \tag{4.39}$$

In cases with the inflection point being not well accessible, alternatively the radius where the electron phase is half of its maximum value $\phi_\mathrm{m}(r_\perp \to \infty) + 0.5\phi_\mathrm{max}$ can be measured. This will only lead to a maximum overestimation of the actual skyrmion radius by 7 % when approaching $\frac{\Delta}{R} \to 2$ (The respective graph is not shown).

A second detail that is visible in Fig. 4.12C is that the phase wall indicated by the orange region extends further than the magnetic domain wall indicated by the blue region, i.e. $\Delta^\phi > \Delta$, for the whole range. By measuring R^ϕ and R^ϕ_i or R^ϕ_o, the skyrmion wall width can be extracted from this graph. It turns out that R^ϕ_o linearly depends on the domain wall width as shown in Fig. 4.12D. The fit gives the phenomenological dependence

$$\frac{\Delta}{R} = 1.23 \cdot \frac{R^\phi_\mathrm{o}}{R^\phi} - 1.21 \ . \tag{4.40}$$

Using expression (4.40) might be more convenient in some cases. Additionally, the normalized phase gain ϕ_max versus domain wall width is plotted in Fig. 4.12E. The total electron phase change that is generated by the Bloch skyrmion linearly increases with its wall width. This is due to the fact that with Δ, also the effective area in which the magnetic induction lies inside the sample plane increases. These results can be used for LTEM techniques that quantitatively measure the electron phase like electron holography or (integrated) DPC [207, 208].

A similar discussion can be applied to the Néel skyrmion. As already extensively discussed in section 4.2.1 and appendix A.3, an electron that is transmitted through a Néel skyrmion spin structure at normal incidence obtains no magnetic phase shift. For this reason, the sample needs to be tilted. An example Néel skyrmion spin structure for $\psi = 0$, $N = 1$, $\Delta = 1.2R$ and a sample tilt $\alpha = 10°$ around the indicated axis is shown in Fig. 4.13A. The uniform in-plane magnetization parallel to $\hat{\boldsymbol{y}}$ outside and in the center of the skyrmion which is obtained from the sample tilt is also visible in the m_y line profile at $y = 0$ shown in Fig. 4.13B. The structural skyrmion parameters R, R_i, R_o and Δ, which are marked in the profiles, are defined as before.

The sample tilt also removes the rotational symmetry of the problem, which is directly visible in the calculated electron phase that is displayed in Fig. 4.13C. Following the phase feature through its center in direction of the tilt axis, a patch of increased electron phase followed by a patch of decreased phase is found, which

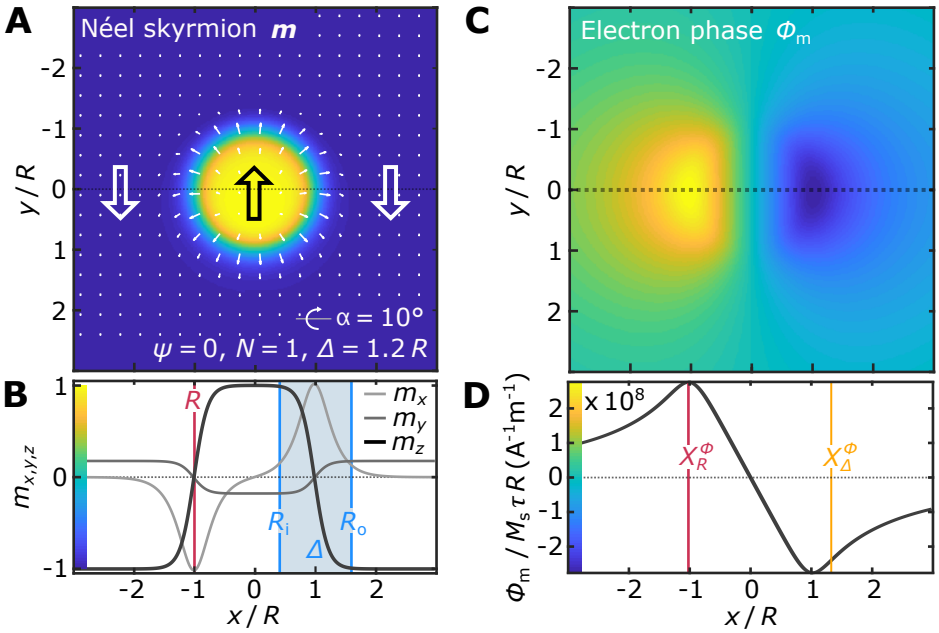

Fig. 4.13.: **(A)** Example of a tilted Néel skyrmion spin structure with indicated paramters. The arrows represent the in-plane magnetization component (the large outlined arrows highlight the in-plane magnetization directions of the skyrmion center and outer area). Color maps the m_z component as indicated at the y-axis of (B). **(B)** Line profile of the $\boldsymbol{m}$ components along the dotted line in (A). **(C)** Calculated 2D phase of the skyrmion in A. Coloring represents the normalized phase value as indicated at the y-axis of (D). **(D)** Line profile of the normalized electron phase along the dotted line in (C).

is reminiscent of the Néel skyrmion's Fresnel LTEM contrast. A line profile of this progression is shown in Fig. 4.13D. The relation of this profile with the actual spin structure is not as intuitive as it was for the Bloch skyrmion case. Two quantities are defined: The first one is the x-position X_R^ϕ where the absolute phase reaches its maximum for $y = 0$, i.e. $\left|\phi_\mathrm{m}(X_R^\phi)\right| = \max\left(\left|\phi_\mathrm{m}(X_R^\phi, 0)\right|\right)$. The second one is the x-coordinate at the point of inflection X_Δ^ϕ of $\phi_\mathrm{m}(x, 0)$ with $X_\Delta^\phi > X_R^\phi$. The values are also indicated in the graph. Note that due to the point symmetry, X_R^ϕ and X_Δ^ϕ can of course be obtained for both signs of x, however the absolute value needs to be taken for the expressions introduced later. In the shown example, X_R^ϕ coincides with the skyrmion radius. From the naming, it can be expected that X_Δ^ϕ is associated with the skyrmion wall width, which will be shown later.

Some computational tricks are involved in the phase calculation. Eq. (4.38) assumes normal electron incidence. As a sample tilt is crucial here, it is introduced by means of a rotation of each individual spin in the magnetization grid around the tilt axis and a subsequent compression of the physical dimensions perpendicular to

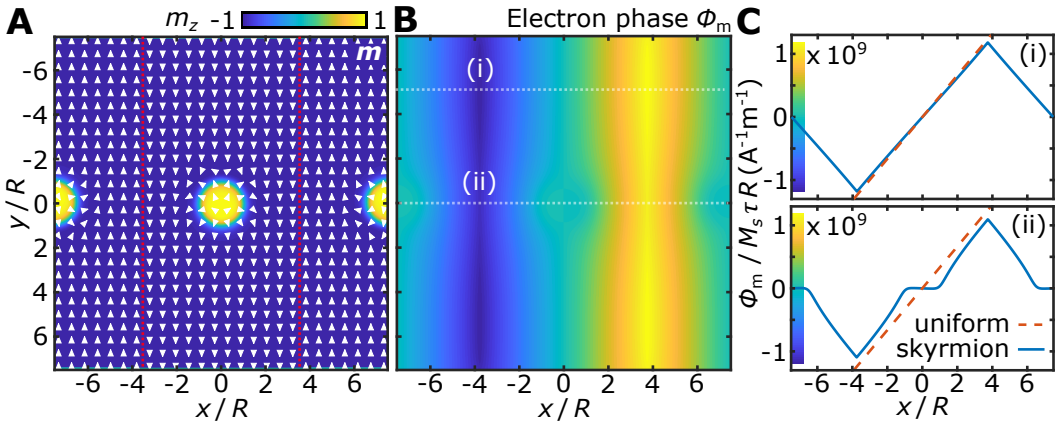

Fig. 4.14.: **(A)** Tailored magnetization structure to obtain a periodic electron phase. It consists of three sectors indicated by the red lines (see main text). **(B)** Calculated electron phase from the magnetization structure in (A). The color represents electron phase value as indicated at the y-axes in (C). **(C)** Line profiles of the phase along the dotted lines in (B) marked with (i) on the top and (ii) on the bottom. The dashed line is the expected phase ramp of the 1D case from Eq. (4.5).

the tilt axis. Such an approach is also chosen in other works[4] [209, 210]. Another important fact concerns the finite constant value of m_y in the surrounding area of the tilted Néel skyrmion. From this, a phase ramp ϕ_{ramp} in the background of ϕ_{m} with $\nabla\phi_{\mathrm{ramp}} \parallel \hat{\boldsymbol{x}}$ is expected. Some effort is necessary to properly include this in the calculation. It turns out that Mansuripur's formalism in Eq. (4.6) excludes the zero-frequency term $\boldsymbol{M}_{00}$. This term is proportional to a uniform offset of the magnetization and is non-zero with the presence of a finite net magnetization. Once this net-magnetization possesses an in-plane component, the aforementioned phase ramp is expected. This is also explained in the discussion of Fig. 4.3A. Due to this issue, Eq. (4.6) is only valid for a magnetization that produces an electron phase that is periodic within the simulation grid [197]. For this reason, a special magnetization is chosen for the calculation which is displayed in Fig. 4.14A. It is divided into three areas along $\hat{\boldsymbol{x}}$. The central area is the one shown in Fig. 4.13A. The outer two areas are obtained by a split of the central area at $x = 0$, a rotation by $180°$ around $\hat{\boldsymbol{z}}$ and a translation to the sides. This way, the electron phase along $\hat{\boldsymbol{x}}$ is expected to be periodic when integrating the magnetic induction according to Eq. (4.5).

The resulting electron phase is shown on the top of Fig. 4.14B. It features the expected symmetrical double phase ramp profile which overshadows the skyrmion signatures that are slightly visible at $y = 0$ and $x/R = -7, 0, 7$. To verify the correct slopes of the ramps, a line profile of the phase indicated by the dotted line marked

[4] In principle, it is also possible to introduce sample tilt by choosing $\hat{\boldsymbol{p}} \neq \pm\hat{\boldsymbol{z}}$ in Eq. (4.6), however it is then not possible to pull out the physical simulation grid size to the prefactor and treat the problem for arbitrary skyrmion sizes.

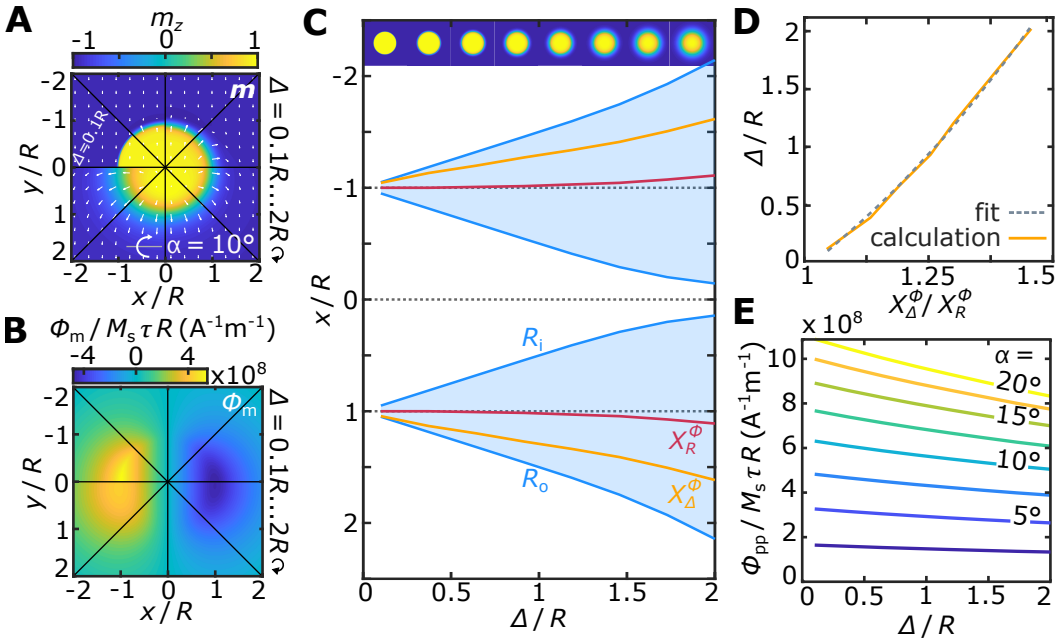

Fig. 4.15.: Electron phase in dependence of Néel skyrmion wall width. **(A)** The sectors show the Néel skyrmion spin structure for different wall widths ranging from $\Delta = 0.1R$ to $\Delta = 2R$. **(B)** Electron phase of the respective spin structures shown in (A). **(C)** Structural parameters of the magnetization and electron phase with respect to the skyrmion wall width. **(D)** The phase inflection point X_Δ^ϕ in dependence of the domain wall width. A quadratic fit is included. **(E)** The peak-to-peak phase value (see text) with respect to domain wall width and different sample tilt angles.

with (i) is shown in Fig. 4.14C. Additionally, the expected phase ramp for a uniform in-plane magnetization from Eq. (4.5) is included with a dashed line. It follows the obtained 2D result which validates the chosen approach. A line profile at $y = 0$, i.e. through the electron phase signature created by the skyrmion spin structure, is shown in the bottom of Fig. 4.14C. Here, the skyrmion signature is clearly visible. For a better visibility, this phase ramp is subtracted in the other plots like Fig. 4.13C, D. It is stressed here that the calculated phase around $x, y = 0$ obtained by this approach slightly differs from a calculation with Mansuripur's formalism on a Néel skyrmion structure that lacks the proposed double structure in Fig. 4.14A. Although in this case the phase ramp is also absent and the phase looks qualitatively the same, the exact phase values and progression at the skyrmion position slightly changes with the dimensions of the simulation grid, which is non-physical. The important consequence from this is that the following results rely on the fact that the phase ramp is subtracted. This becomes essential when the results are applied to actual measurements.

Next, the electron phase ϕ_m is related to the Néel skyrmion spin structure. Fig. 4.15A shows the magnetization for different values of the skyrmion wall width

Δ. The eight sectors show the structures for Δ-values in accordance to Fig. 4.12A. The calculated electron phase is shown below in Fig. 4.15B. Although the display method is not as adequate as in the radially symmetric Bloch skyrmion case, the essential features are discernible. In contrast to the Bloch skyrmion, the largest phase value is obtained for the smallest Δ. This is clear, considering that only the tilted out-of-plane components contribute to the generation of an electron phase. The phase ramp that was discussed before is subtracted from this signal. The relations of the electron phase structure parameters X_R^ϕ and X_Δ^ϕ are shown in Fig. 4.15C. As can be seen, the phase maximum X_R^ϕ coincides with the skyrmion radius with a maximum overestimation of 6.5 % for $\Delta = 2R$, i.e.

$$X_R^\phi \approx R \, . \tag{4.41}$$

The dependence of X_Δ^ϕ with respect to Δ is displayed in Fig. 4.15D. A phenomenological quadratic fit gives the following dependence

$$\frac{\Delta}{R} = 3.07 \left(\frac{X_\Delta^\phi}{X_R^\phi} \right)^2 - 2.93 \left(\frac{X_\Delta^\phi}{X_R^\phi} \right) - 0.2 \, . \tag{4.42}$$

These results are independent of sample tilt up to values of $\alpha < 20°$. The normalized peak to peak phase changes $\phi_{\mathrm{pp}} = \left| \phi_{\mathrm{m}}(X_R^\phi, 0) \right| + \left| \phi_{\mathrm{m}}(-X_R^\phi, 0) \right|$ with respect to Δ and different values of sample tilt α are shown in Fig. 4.15E. Again, this can be used for quantitative phase measurements.

Recently, hybrid magnetic skyrmion structures have been reported [149, 211]. Zhang et al. show that up to around 30 nm below the sample surface of the Bloch skyrmion hosting material Cu_2OSeO_3, a twisted surface state emerges. In these states, the helicity ψ in Eq. (4.33) is detached from $\pi/2$ or $3\pi/2$ and can deviate by values up to around $\pi/4$ [149]. Even more extreme cases are reported by Legrand et al., who show that in multilayer systems with interface DMI, ψ can change its value between neighboring layers to such an extent that even a chirality inversion is possible [150]. The consequences of such structures for phase contrast imaging discussed before are as follows. It turns out that a skyrmion spin structure $\boldsymbol{m}_\psi$, defined in Eq. (4.33), with arbitrary values of ψ can be written as a superposition of a Bloch and Néel skyrmion spin structure $\boldsymbol{m}_{\psi=\pi/2}$ and $\boldsymbol{m}_{\psi=0}$ as

$$\boldsymbol{m}_\psi = \begin{pmatrix} \sin(\psi) & 0 & 0 \\ 0 & \sin(\psi) & 0 \\ 0 & 0 & 0.5 \end{pmatrix} \boldsymbol{m}_{\psi=\pi/2} + \begin{pmatrix} \cos(\psi) & 0 & 0 \\ 0 & \cos(\psi) & 0 \\ 0 & 0 & 0.5 \end{pmatrix} \boldsymbol{m}_{\psi=0} \, . \tag{4.43}$$

Plugging in $\boldsymbol{m}_\psi$ into e.g. Eq. (4.31), it can be seen that the expression can be additively separated for $\boldsymbol{m}_{\psi=0}$ and $\boldsymbol{m}_{\psi=\pi/2}$. As Néel skyrmions do not produce a magnetic electron phase, the origin of ϕ_m is exclusively obtained from the Bloch part $\mathbf{m}_{\psi=0}$ without sample tilt. When $\psi(z)$ possesses a z-dependence like in the case of the hybrid skyrmions described in Refs. [149, 150, 211], an effective sample thickness τ^* can be defined as

$$\tau^* = \int_{-\tau/2}^{\tau/2} \sin\left[\psi(z)\right] \, \mathrm{d}z \; . \tag{4.44}$$

This attributes a Néel contribution of the skyrmion structure with an effectively reduced sample thickness. Note that this also allows for negative τ^*, that can occur due to a chirality inversion. Using this expression, the electron phase considerations for the Bloch skyrmion are applicable to hybrid skyrmions by exchanging τ with τ^*.

4.2.3 Aberration and contrast considerations of isolated magnetic skyrmion imaging using DPC

In a real LTEM experiment, the electron phase that is generated by a magnetic sample is the ideal measurand as it contains all of the accessible magnetic information. However, it is usually modified by electron optical aberrations and other sample interactions which introduces deviations from pure magnetic scattering. Additionally, to obtain the electron phase from some techniques, a reconstruction algorithm needs to be applied to the data which can introduce further errors. For Fresnel LTEM this is the so-called quantitative transport of intensity equation (TIE) [212, 213] or for DPC the so-called integrated DPC (iDPC) method [208, 214]. Therefore it is clear that the phase modification of each technique has to be addressed in order to apply the findings of the previous section. In this section, the expected DPC contrast for skyrmions is calculated and discussed. The influence of optical aberrations is considered and correction terms are presented, which make the application of the results in the previous section possible.

The description is started with DPC LTEM on isolated Bloch skyrmions. To show the expected DPC image contrast, the gradient of the calculated phases for the Bloch skyrmions from the last section is calculated. Fig. 4.16A shows the two components of the normalized gradient for a skyrmion with a domain wall width of $\Delta = 1.2R$. The right image shows the gradient with a color-coding as indicated by the color wheel next to it. These results match the qualitative descriptions in section 4.2.1.

To discuss the influence of electron-optical aberrations for DPC measurements, further simulations are conducted. The resolution in STEM is essentially limited by the size and shape of the electron probe in the sample plane [162, 163]. Imperfections

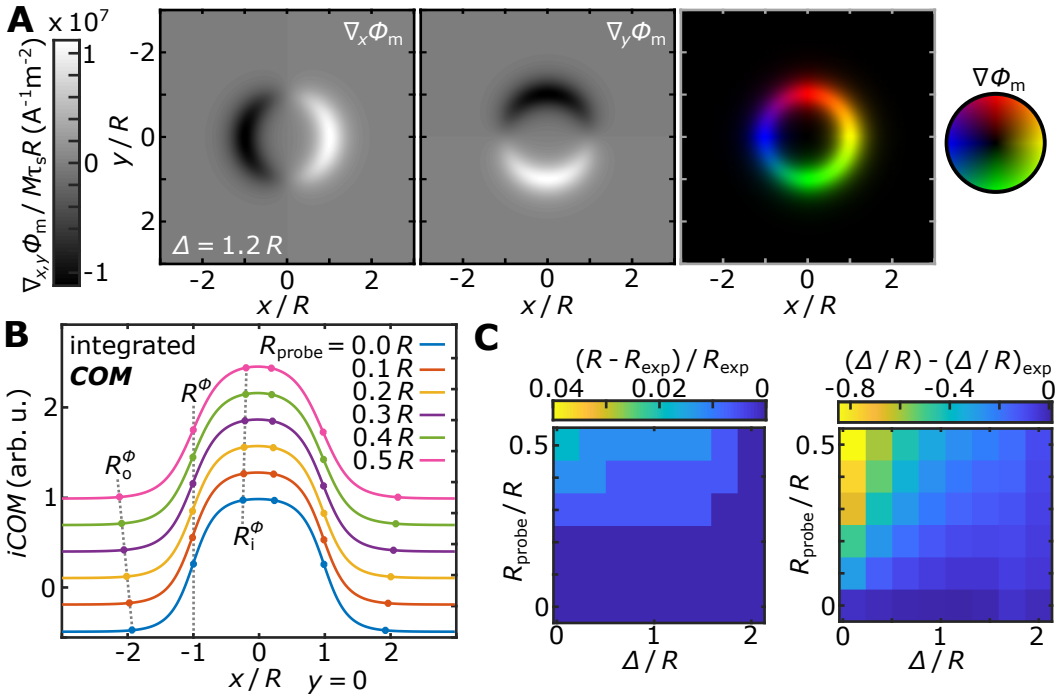

Fig. 4.16.: DPC simulation for Bloch skyrmions. **(A)** Calculated components of the electron phase gradient for a Bloch skyrmion with $\Delta = 1.2R$ and color representation on the right. **(B)** Line profiles of the integrated ***COM*** through the center of the skyrmion for different electron probe sizes. The phase parameters are marked in the plot. **(C)** Correction terms for calculated skyrmion radius and wall width with respect to finite electron probe sizes.

in the probe-forming systems can have a negative influence which results in probe enlargement and deformation. Here, the effect of enlargement of an otherwise circular electron probe is discussed. The size of the electron probe in LMSTEM is fundamentally limited by the C2 aperture radius as discussed in section 4.1.3. The probe size is further increased by a finite physical size of the electron source's emitting area, chromatic aberrations usually inferred from the thermal energy spread of the source, a defocused beam, electrical instabilities of the lenses and source or spherical aberrations of the C2 lens. Effects that lead to a radially inhomogeneous probe shape, like coma, third order spherical aberrations or astigmatism are not considered here, because these probe deformations are rather specific and a general treatment is not easily possible [215–217]. The consideration of each individual aberration is condensed to a DPC simulation for electron probes with different probe radii in terms of aperture sizes as described in Eq. (4.20).

For the simulation, the calculated magnetic electron phases from the previous section are used. Next, a probe of finite radius with respect to the skyrmion size is generated. For each pixel or probe position, the ronchigram intensity $|\Psi_{\mathrm{ronch}}|^2$ is calculated following Eqs. (4.24) and (4.25). Subsequently, the center of mass

(COM) of $|\Psi_{\mathrm{ronch}}|^2$ is calculated. For the calculation, ϕ_{m} needs to be rescaled such that the calculated shift of the $\boldsymbol{COM}$ is large enough to obtain a reasonable dynamic range but not as large that the Ronchigram is shifted to the edges of the simulation grid. The exact value is not that important as a linear scaling of ϕ_{m} also linearly scales the magnitude of the $\boldsymbol{COM}$. This can be understood by considering that a scaled electron phase ϕ can be produced by scaling the respective projected electric field or magnetic induction accordingly. These quantities are connected to the lateral electron momentum via Eqs. (4.27) and (4.29). This finally leads to a proportional scale of $\boldsymbol{COM}$ considering Eq. 4.26. Nevertheless, if the dynamical range of COM is too small in the simulation, the extraction of the structural parameters becomes erratic which may not even be clearly apparent at first glance. The investigated range of probe radii R_{probe} in the simulation is $R_{\mathrm{probe}} \in [0.1R, 0.2R, ..., 0.5R]$. Whenever $R_{\mathrm{probe}} = 0$ is discussed in the following, the result from a direct calculation of the phase gradient is considered.

The calculated components of $\boldsymbol{COM} = (COM_x, COM_y)$ for the different probe sizes look essentially the same as the pure phase gradient in Fig. 4.16A which is why they are not shown here. To extract the structural parameters R_{i}^{ϕ} and R_{o}^{ϕ}, the $\boldsymbol{COM}$ which is proportional to $\nabla\phi_{\mathrm{m}}$ needs to be integrated in order to obtain ϕ_{m}. This problem is equivalent to the calculation of the electric potential from a given 2D electric field and is called integrated DPC (iDPC). More details on iDPC can be found in Ref. [208]. Line profiles along $\hat{\boldsymbol{x}}$ of the resulting integrated $\boldsymbol{COM}$, $iCOM$, at $y = 0$ for the different probe sizes and $\Delta = 1.2R$ are shown in Fig. 4.16B. The structural parameters R_{i}^{ϕ}, R^{ϕ} and R_{o}^{ϕ} are marked with dots and labeled at the end of the dashed lines.

Now the experimental skyrmion radius R_{exp} and the relative domain wall width $(\Delta/R)_{\mathrm{exp}}$ are calculated using the relations (4.39) and (4.40). The resulting values differ from the real values known for the simulation. These differences are calculated and given as correction terms in Fig. 4.16C. The determination of the radius is nearly unaffected by an increasing electron probe size as the relative error stays below 2 %. Also the skyrmion wall width is still determined quite well and only shows large absolute deviations when domain wall widths that are around half of the probe size are measured.

A very similar discussion is conducted for the Néel skyrmion. Fig. 4.17A shows the normalized phase gradient for a Néel skyrmion with $\Delta = 1.5R$. The component of the phase gradient that is parallel to the tilt axis shows three patches of in/decreased phase, a larger one at the center and two smaller ones next to it in the direction of tilt. The phase gradient component perpendicular to the tilt axis shows four equally sized patches of in/decreased electron phase, which are situated at the edges of a square that is aligned at a 45° angle with respect to the tilt axis. The color composite

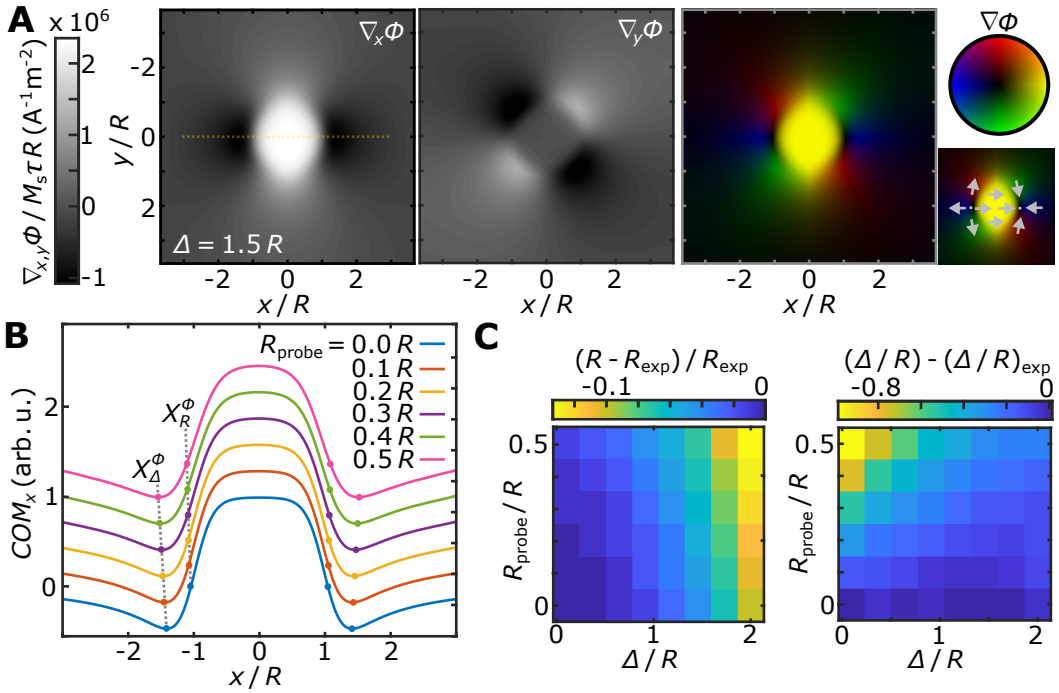

Fig. 4.17.: DPC simulation for Néel skyrmions. **(A)** Calculated components of phase gradient for a Néel skyrmion with $\Delta = 1.5R$ and color-coded phase gradient. **(B)** Line profiles of the COM_x-component for different electron probe sizes and indicated structural parameters. **(C)** Correction terms for calculated skyrmion radius and wall width with respect to finite electron probe sizes.

image on the right shows that the phase gradient actually consists of a double vortex structure (with different chiralities) that overlaps in the center of the skyrmion as indicated by the sketch on the right of Fig. 4.10A.

As before, DPC simulations are conducted for a selection of electron probe sizes. The chosen sample tilt angle for the simulations is $\alpha = 10°$, however the results are valid up to 20°, as a sample tilt up to that value only leads to a scaling of the obtained electron phase. To determine X_R^ϕ and X_Δ^ϕ, it is not necessary to integrate the differential phase as the features are already present in the derivative. The x-value where $COM_x = 0$ in the line-profile of COM_x at $y = 0$ represents the local maximum of the phase X_R^ϕ. On the other hand, the x-value at one of the minima in COM_x is the point of inflection X_Δ^ϕ. This is also indicated in Fig. 4.17B. Using expression (4.41) and (4.42), the actual skyrmion radius and domain wall width can be extracted. The correction terms for finite probe sizes are given in Fig. 4.17C. The error for the skyrmion radius is about five times larger than the one for the Bloch skyrmion. This is mainly because the given equations already showed errors for a perfect phase measurement, i.e. infinitely sharp electron probes, which can also be seen in this graph. The error for the domain wall width is again largest for very small domain wall widths and large electron probe sizes, as one would expect.

As a reminder, the results rely on the fact that the linear background of the phase that emerges due to the finite in-plane magnetization of the tilted Néel skyrmion is subtracted from the data. In DPC, a linear phase background leads to a vector offset of the whole deflection signal. The phase ramp is therefore accounted for by digitally subtracting the constant deflection value obtained from positions that are reasonably far away from any skyrmion such that the beam deflection in the skyrmion "vacuum" becomes zero. In images that contain only sparse skyrmions and have a homogeneous background, this can be achieved by subtracting the average deflection vector. Shadings in the DPC signal due to misaligned scanning or thickness gradients of the sample should be subtracted before, e.g. by subtracting a 2D polynomial fit.

4.3 LTEM measurements of (001) Cu_2OSeO_3

In this section, TEM measurements on Cu_2OSeO_3 with (001)-orientation are presented. Zero-field-cooled and field-cooled phase diagrams are recorded using Fresnel LTEM. A special focus is set on the low-temperature skyrmion phase that is already introduced in section 3.2. For lowest achievable temperatures ($T \approx 13\,\mathrm{K}$), a magnetic field dependent skyrmion interaction is observed, which is attributed to an embedding of the skyrmions in a conical background. Additionally, DPC measurements are presented that show indications of a hexagonal skyrmion distortion.

The single crystal of Cu_2OSeO_3 is grown by the chemical vapor transport method by A. Aqeel[5]. It is cut to a thin platelet with a lateral size of around $1.5 \times 1.5\,\mathrm{mm}^2$. The $[001]$ direction is oriented such that it is parallel to the sample normal. It is equivalently oriented as the sample in section 3.2 which should allow the observation of the LT-skyrmion phase. The sample is glued to a steel ring and after mechanical thinning, one of the sample edges is further thinned by Argon ion-beam-milling until some edge areas become transparent for electrons with 300 keV (usually at a thickness around 100 nm). This process resulted in two problems; the first one is that the sample becomes very fragile and the thin areas easily break off. The second one is that the surface is not satisfactorily smooth and shows terraces that probably occur due to the brittleness of the material.

To counter these problems, the thinning process described before is stopped at a sample thickness of 3 to 10 µm. At such thicknesses, breaking the sample with small shocks (e.g. from mounting it in the sample holder) proved to be unlikely. The final thinning is then manually done by using Focused-Ion-Beam (FIB) milling. For this, the steel ring is cut and a small segment is removed to be able to access to the sample

[5] Physik-Department, Technische Universität München, Garching, 85748, Germany.

from the side. Then, the sample is inserted in the Zeiss AURIGA FIB-SEM[6]. There, it is carefully thinned from the open side by an Ar-Ion beam at 30 keV. After some optimizations, an electron-transparent lamella of around $15 \times 8\,\mu m^2$ size is cut this way in reasonable times of around two hours. Due to an imperfect orientation of the sample with respect to the ion beam and the fact that the focus is not constant over the milling depth, cutting a perfectly flat lamella is not likely and thickness gradients of around 100 nm for milling depths of around 10 µm are common. The sides of the lamella are still attached to the thicker surrounding material which stabilizes and protects the sample. As Cu_2OSeO_3 is an insulator, TEM observations are problematic due to charging effects, especially at low temperatures. Therefore, a few nm of carbon are evaporated onto both sides of the sample using electric arc carbon rod evaporation. However, this can only partially compensate charging effects at low temperatures.

The sample is put into a special liquid helium TEM-holder which is inserted into the TEM. The holder has a reservoir that can be filled with liquid helium, prior to the measurement. After removal of the helium transfer rod, a total measurement time of around one hour is available. Afterwards, the holder needs to be heated up before it can be refilled again. Alternatively, the transfer rod can also be kept in place during the measurement which in principle allows for measurement times of many hours, however drastically limits stage movements and can lead to an expensive chamber vent if not handled carefully. The minimum temperatures that can be reached with this system are around 10 to 14 K. The electron energy is tuned to 300 keV and the Lorentz lens is excited to obtain a defocus of $\approx 100\,\mu m$.

First, a zero-field-cooled phase diagram is recorded using Fresnel LTEM. For this, the sample is cooled below T_c at zero externally-applied magnetic field at a rate of around $5\,K\,s^{-1}$. The cooling is stopped at some finite temperature T_m and kept constant. Then, an external magnetic field is applied along the optical axis, which is parallel to $[001]$, by weakly exciting the objective lens (below 10 % of its maximal current). The calibration of the magnetic field at the sample with respect to objective lens excitation is done using a custom-built Hall sensor TEM holder. Although the calibrations are renewed for this thesis, details on the calibration process can be found in Ref. [175]. Fresnel LTEM images are taken at different magnetic field values. Once the sample is saturated and no more magnetic contrast is obtained, it is heated above T_c. In the end, the field is reduced to zero and the cycle is repeated for a different value of T_m.

For each recorded image, the present magnetic phase is manually classified. This gives scattered points in T-H_{ext}-space each with an associated magnetic phase. Afterwards, phase borders are manually drawn. The resulting ZFC phase diagram

[6]Gratefully provided by the chair of Prof. D. Weiss at the University of Regensburg.

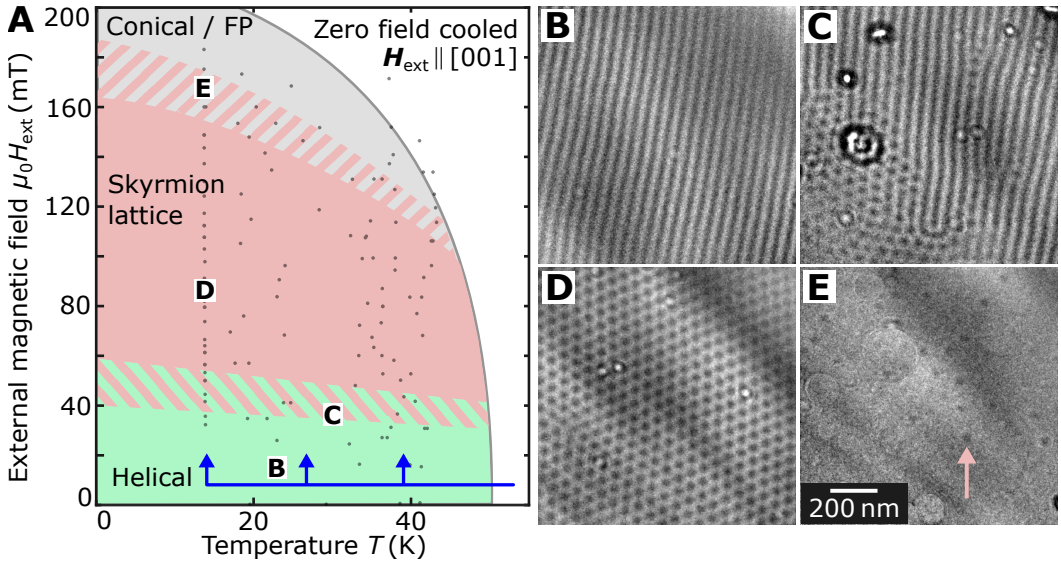

Fig. 4.18.: Zero-field-cooled phase diagram of (001)-Cu_2OSeO_3 with $\boldsymbol{H}_{\mathrm{ext}} \parallel [001]$ obtained by Fresnel LTEM. **(A)** Phase diagram with respect to temperature and externally-applied magnetic field. Each black dot represents a Fresnel LTEM image. During a magnetic field scan starting at $\mu_0 H_{\mathrm{ext}} = 0\,\mathrm{mT}$, the **(B)** helical phase, **(C)** a helical/skyrmion mixed state, **(D)** the skyrmion lattice phase and **(E)** sparse skyrmions in a conical/field-polarized background can be observed successively. The phase space positions of the images are indicated in the phase diagram. A median filter in a 3×3 neighborhood and a polynomial background subtraction is applied to the (B-E). Further, localized chunks of dirt in (E) are removed in order to retain visibility of the weak skyrmion contrast (compare with (C)).

is shown in Fig. 4.18A. Each tiny black dot represents a Fresnel LTEM image. The temperature above minimum is unstable, as the transfer rod is left in place which leads to temperature drifts during the magnetic field scan and introduces the horizontal scatter of the data points. At zero magnetic field, the helical phase is present. An example LTEM image of the mono-$\boldsymbol{q}_{\mathrm{h}}$ domain is shown in Fig. 4.18B. Upon field increase to $\approx 40\,\mathrm{mT}$, the helical phase transforms to the skyrmion phase via a mixed helical/skyrmion state shown in Fig. 4.18C. The skyrmions nucleate from defects of the helical phase, which can be seen from the A-defect in the top right part of the image [5, 31, 81, 135, 218]. The complete hexagonal skyrmion lattice, displayed in Fig. 4.18D, is obtained for externally-applied magnetic fields of around 60 mT. At large fields of around 120 to 160 mT, the skyrmion lattice vanishes, and only sparse skyrmions remain, as shown in Fig. 4.18E. Their surrounding environment does not show any magnetic contrast. The related phase can therefore either be field-polarized or conical with $\boldsymbol{q}_{\mathrm{h}} \parallel \boldsymbol{H}_{\mathrm{ext}}$. After a further increase of the external field by another 20 mT, the remaining skyrmions vanish.

Note that the phase space positions of images 4.18B-E are also highlighted in the phase diagram. The border of the conical phase cannot be determined by LTEM

and is only drawn for completeness in analogy to measurements on bulk systems. The phase borders on the right are determined from the field-cooled phase diagram shown later.

The low-temperature skyrmion phase that is reported in bulk Cu_2OSeO_3 for $\boldsymbol{H}_{\mathrm{ext}} \parallel [001]$ cannot be clearly identified from these measurements. As a comparison, the respective phase diagrams in Fig. 3.3D can be considered. A first difference is the unequal value of T_{c}. An explanation for this could be that $M_{\mathrm{s}} \to 0$ for $T \to T_{\mathrm{c}}$, and the magnetic electron phase-shifts might not be strong enough to observe Fresnel contrast with enough signal to noise ratio. The different scaling of the magnetic field axis can have two reasons. The first one is, that a thin sample has a larger demagnetization factor in $\hat{\boldsymbol{z}}$-direction than the bulk sample. Therefore, it is expected that larger external fields are necessary to obtain equivalent states than in the case of the bulk sample. The second reason is the transformation of the phase diagram when approaching small sample thicknesses which is discussed in section 2.1.3.

Comparing the result with Fig. 4.19, the obtained phase diagram is most similar to the one of a 2D B20 chiral magnet which indicates that the sample thickness τ is around the size of $\lambda_{\mathrm{h}} \approx 50$ to 70 nm [52, 73]. As the skyrmion lattice is extended to low temperatures in this case, the observation of the second independent LT-skyrmion phase might be elusive if the two phases were connected as in Fig. 4.19C. For the case that the LT-skyrmion phase is still disconnected from the extended regular skyrmion phase but is located at larger magnetic fields, the field scan for lowest $T \approx 14\,\mathrm{K}$ is extended to larger values than the shown range. At values of 180, 210, 240 and 270 mT, the externally-applied field is oscillated 100 times with an amplitude of 9 mT with a period of around 0.3 s, as suggested by Ref. [117] and the experiences from the REXS measurements in section 3.2. However, still no Fresnel LTEM contrast emerges. Another explanation for this could be that the LT-skyrmion phase is always accompanied by the initial observation of the so-called tilted conical phase. This phase is similar to the regular conical phase with $\boldsymbol{q}_{\mathrm{h}}$ tilted away from $[001]$ for a maximum of 30°[117]. However, as a thin sample is measured, conical phases with modulation vectors parallel to the sample normal are suppressed as discussed in section 2.1.3. Therefore, the tilted conical phase might not develop in the first place which ultimately forbids a further relaxation into the LT-skyrmion phase.

During the REXS measurements in section 3.2, the most consistent measurements of the LT-skyrmion phase are obtained from a field-cooled measurement protocol. Therefore, an additional field-cooled phase diagram is recorded with LTEM. For this, a constant external magnetic field H_{m} is applied at $T > T_{\mathrm{c}}$. The sample is then cooled at a rate of around $5\,\mathrm{K\,s^{-1}}$ and Fresnel images are recorded during the cooling process. Once the lowest temperature is reached, the sample is heated above

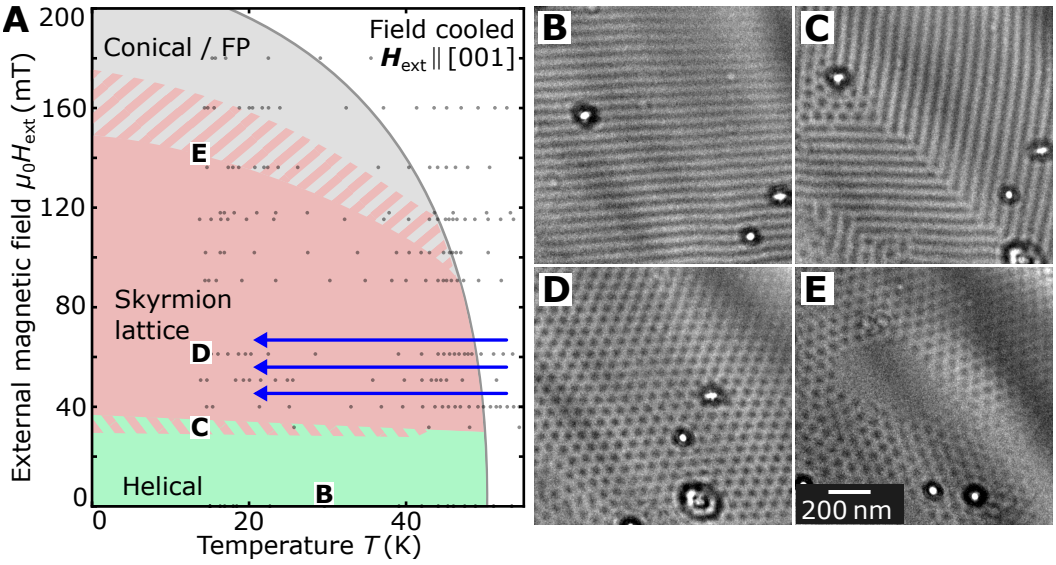

Fig. 4.19.: Field-cooled phase diagram of (001)-Cu_2OSeO_3 with $\boldsymbol{H}_{\mathrm{ext}} \parallel [001]$ obtained by Fresnel LTEM. **(A)** Phase diagram with respect to temperature and externally-applied magnetic field. Each black dot represents a Fresnel LTEM image. For increasing external magnetic field, the **(B)** helical phase, **(C)** helical/skyrmion mixed state, **(D)** skyrmion lattice phase and **(E)** mixed skyrmion and conical/field-polarized phase can be observed. The phase space positions of the images are indicated in the phase diagram. A median filter in a 3×3 neighborhood and a polynomial background subtraction are applied to (B-E).

T_{c} and the process is repeated for a different value of H_{m}. The resulting phase diagram is shown in Fig. 4.19A. Essentially, it is equivalent to the ZFC-case with a few minor differences. An image of the helical phase obtained at zero external magnetic field is shown in Fig. 4.19B. The helical/skyrmion mixture in Fig. 4.19C shows two helical domains and their domain boundary, which is also discussed in section 3.2. The hexagonal skyrmion lattice phase is shown in Fig. 4.19D and a mixture of skyrmion and field-polarized/conical phase in Fig. 4.19E. The sparse skyrmion phase is not as distinct as before; in this case the skyrmions are packed more tightly but there are patches that do not show any skyrmions. Still, a distinct LT-skyrmion phase is not found, again even for larger fields than the ones shown in the phase diagram.

A peculiarity can be observed by a closer inspection of the transformation of the skyrmion lattice phase to the sparse skyrmion state in the ZFC-phase diagram at lowest temperatures of $T \approx 14\,\mathrm{K}$. Four exemplary images that are recorded for different applied magnetic fields are shown in the top row of Fig. 4.20A. First, the skyrmion separation and decreased skyrmion count for an increase of applied magnetic field is clearly visible. If the annihilation process of skyrmions was random,

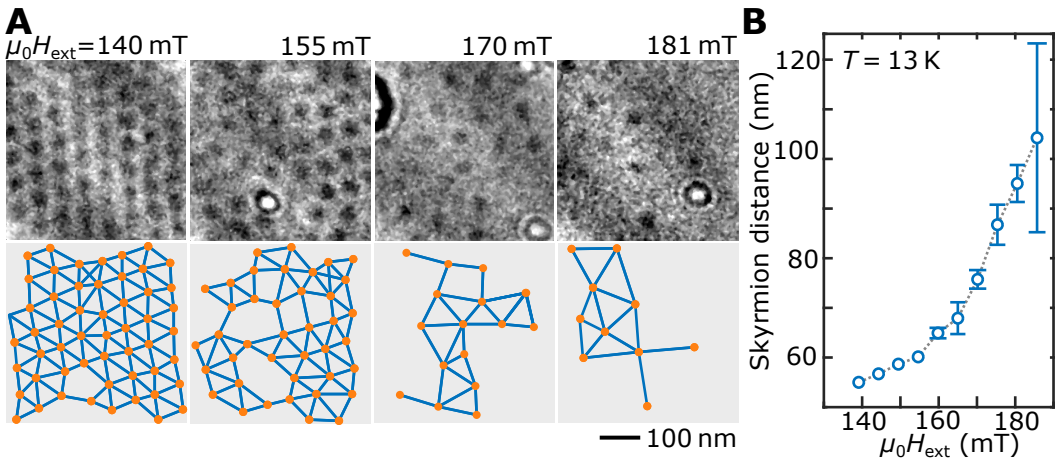

Fig. 4.20.: Skyrmion interaction in Cu_2OSeO_3 with externally-applied magnetic field. **(A)** The top row shows an LTEM image series of skyrmions at $T = 13\,\mathrm{K}$ with applied magnetic fields close to the transition to the field-polarized/conical phase. The bottom row shows the detected skyrmion position (orange dots) and skyrmion-skyrmion distances (blue lines). **(B)** Calculated average skyrmion-skyrmion-distance d_{sk} in dependence of externally-applied magnetic field. A 3×3 median filter and a Gaussian filter with $\sigma = 3\,\mathrm{px}$ is applied to the images in (A).

at least a few skyrmions arranged in small clusters would be expected. However, the impression is rather that the overall skyrmion-skyrmion distance d_{sk} is increased.

To quantify this, the skyrmion positions are detected by a computer. This is illustrated by the orange dots in the bottom row of Fig. 4.20A. Note that only sections of the images are shown as an example, and the full evaluation is done on 1 to 6 times more skyrmions. In order to calculate an average d_{sk}, the unique distance for all detected skyrmion positions is calculated. In an ideal case, a histogram of these values is proportional to the radial distribution function of the skyrmion "crystal" [219]. The data is cut off after the first maximum, which takes into account nearest neighbor distances and a mean value of d_{sk} is computed. To aid the comprehensibility, the distances that are used in the calculation are highlighted with the respective connection lines in the example panels.

The mean skyrmion-skyrmion distance with respect to externally-applied magnetic field is plotted in Fig. 4.20B. Qualitatively, the observed dependence very well matches the one from a similar LTEM experiment conducted by Du et al. in a thin FeGe stripe [220]. For largest magnetic fields, Du et al. report a doubling of d_{sk} which is similar to the measured value here. The behavior can be explained as follows: The isolated skyrmions are metastable and their background is the conical phase with $\boldsymbol{q}_{\mathrm{h}} \parallel \hat{\boldsymbol{z}}$. The spin cone is aligned along the skyrmion tube. This leads to a modulation of the skyrmion wall along $\hat{\boldsymbol{z}}$. When two skyrmions are brought close to each other, their effective magnetization volume is decreased, as parts of the

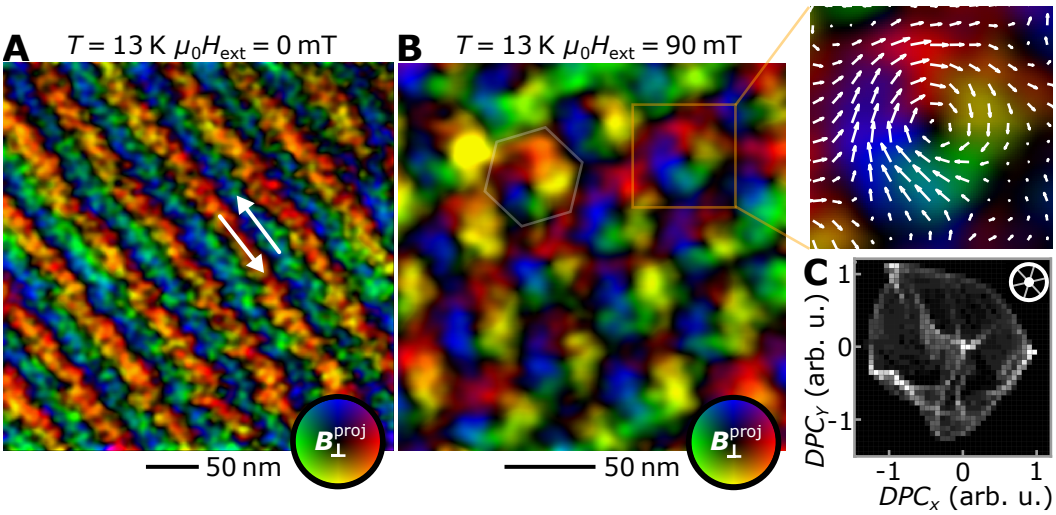

Fig. 4.21.: DPC measurements on Cu_2OSeO_3 with $\boldsymbol{H}_{\mathrm{ext}} \parallel [001]$. **(A)** The helical phase shows the two directions from the projection of the magnetization to the sample plane. **(B)** Hexagonal skyrmion lattice shows the 360° domain walls. The inset is a magnified view. The drawn hexagon illustrates hexagonal skyrmion spin distortion. **(C)** 2D histogram of the deflections measured from the skyrmion in the inset. It shows a central peak with a distorted ring around it that represent core and walls. Also streaks are visible that resemble hexagonal distortion which can be compared to the expectation in the inset on the top right. A 2D polynomial background fit is subtracted from the beam deflection signals, a median filter in a $3 \times 3\,\mathrm{pixel}^2$ neighborhood and a Gaussian filter ($\sigma = 4$ and 6 pixel for (A) and (B)) are applied to improve visibility.

structure can overlap. This attributes more magnetic volume to the conical phase, which is the actual ground state of the system and therefore reduces the energy. This corresponds to an attractive potential. On the other hand, if the two skyrmions get too close, their internal structure will get distorted, resulting in an energy increase. In combination, this gives a Lennard-Jones-like potential [220, 221]. When the field is changed, the modulation of the skyrmion wall changes, which also alters the equilibrium position of the potential and leads to the observed dependence.

In addition to the Fresnel LTEM studies, DPC LTEM images are recorded. The microscope is switched to LMSTEM mode and a C2-aperture with a diameter of 70 µm is inserted. With a camera length of 14 m, the diffraction disk is projected onto the annular segmented detector. The focused electron beam is scanned over the sample and the deflection of the diffraction disk is measured. This is done by calculating the electrical current difference of opposing detector segments. Using this detector, the electron beam deflection can be converted into a measure that is proportional to the projected magnetic induction by assuming a homogeneous Ronchigram which requires that the magnetic induction is constant in intervals of the electron probe size (see Eqs. (4.25) and (4.29)). For this simple case, the

conversion is obtained by a 90° rotation of the deflection vectors. Although this might not be exactly the case for $\lambda_\mathrm{h} \approx 50\,\mathrm{nm}$, the measured quantity is referred to as $\boldsymbol{B}_\perp^\mathrm{Proj}$ as no absolute numbers are given.

At first, the helical phase is imaged. For this, the objective lens is turned off completely to avoid field oscillations that are produced by the power supply at very weak excitations ($< 3\,\%I_\mathrm{max}$). The measured magnetic induction of the helical phase at $T = 13\,\mathrm{K}$ is shown in Fig. 4.21A. The two in-plane directions of the projected magnetization of the spin helix projection onto the sample plane are clearly visible. With an applied magnetic field of $\mu_0 H_\mathrm{ext} = 90\,\mathrm{mT}$, the skyrmion phase is imaged the same way, which is displayed in Fig. 4.21B. The DPC measurements suffer from strong charging effects, which is clearly visible in the image. However, the magnified view of a single skyrmion in the inset to the right nicely features the 360° Bloch skyrmion wall.

A small remark is added here: Usually, the zero-value of the electron deflection direction, i.e. the effective detector rotation, is not directly known as it changes e.g. with the camera length (magnetic lenses tend to rotate the image upon different excitations). A common way to retrieve the detector orientation is to use $\nabla \times \boldsymbol{B} = 0$ and minimize $\left|\int_\mathrm{image} \left[\nabla \times (A_\gamma \cdot \boldsymbol{DPC}(\boldsymbol{r}_\perp))\right] \cdot \hat{\boldsymbol{z}}\,\mathrm{d}A\right|$ with respect to a rotation A_γ of the measured deflections $\boldsymbol{DPC}$ for an angle γ around $\hat{\boldsymbol{z}}$. Finding the respective rotation angle γ_0 should give the orientation such that $A_\gamma \cdot \boldsymbol{DPC} \propto \boldsymbol{B}_\perp^\mathrm{Proj}$. However, caution is advised when using this method. It can be shown that for an arbitrary vector field $\boldsymbol{DPC}(\boldsymbol{r}_\perp)$,

$$\left|\int_\mathrm{image} \left[\nabla \times (A_\gamma \cdot \boldsymbol{DPC}(\boldsymbol{r}_\perp))\right] \hat{\boldsymbol{z}}\,\mathrm{d}A\right| \propto \left|\sin(\gamma + \gamma_0)\right| \ . \tag{4.45}$$

Therefore, the resulting dependence looks always perfect in the sense of an absent noise, which is untypical for a measurement. This fact might be deceiving and the method could be evaluated better than it is. It shows that the application of the method to 289 image sections of Fig. 4.21B with partial overlap and an individual size of $256 \times 256\,\mathrm{pixel}^2$ yields a standard deviation for γ_0 of 51°. It turns out that the method can be very sensitive to signal noise and the result should be carefully cross-checked for a few different sections of the image. Finally it should be noted that the solution $A_{\gamma 0+\pi}$ is equivalent. This means that e.g. the skyrmion chirality cannot be fixed with this method. The value for γ_0 used in Fig. 4.21B is determined from the Fresnel images which gives the correct chirality in combination with the assumption that the magnetization should be perpendicular to the radial direction of the skyrmion [48, 185, 187, 222].

Other LTEM experiments on FeGe report that the skyrmion spin structure in its lattice state can show a hexagonal distortion [187, 223]. This means that the

skyrmion wall extends further to the areas between two neighboring skyrmions, as illustrated by the hexagon in Fig. 4.21B. Indications for this distortion are also visible in Fig. 4.21B, although it is not very convincing due to the charging effects. To further analyze this, a 2D histogram of the beam deflection for the area of the single skyrmion in the inset is shown in Fig. 4.21C. For a circular skyrmion, an increased count at zero-deflection which represents the skyrmion core and perimeter that is surrounded by a ring which reflects the wall is expected. If there was a hexagonal distortion, the ring should show six pronounced points lying on the edges of a hexagon. Further as the magnetization fades out, six streaks from zero deflection in the center to these points are expected. This expectation is drawn in the inset on the top right. In the actual histogram, the central peak and the ring are visible, although strong distortions, probably due to the charging effects, are present. Clearly at least four streaks are visible, which suggests preferred directions. Therefore, the measured (001) Cu_2OSeO_3 sample shows indications of a hexagonal distortion of skyrmions in their lattice state.

4.4 LTEM imaging of room-temperature skyrmion hosting multilayer materials

In this section, measurements on room temperature magnetic skyrmion hosting multilayer systems are presented. These materials exhibit interface-DMI which leads to the generation of Néel skyrmions and cycloids as described in section 2.1.3. Results for two multilayer structures with different compositions are shown. For each of the two systems, samples with different layer thicknesses were investigated throughout the course of this thesis, however only the most promising one - in terms of maximum skyrmion numbers - are included here as an example. From a TEM imaging point of view, variations in the measurement results among the samples are not that striking. The studies in this section are a collaboration with the group of Prof. Na Lei[7], who grows the samples and perform supporting measurements like electrical spin Hall effect or magnetic hysteresis loop measurements obtained from magneto-optical-Kerr-effect (MOKE) or a superconducting quantum interference device (SQUID).

[7] Fert Beijing Institute, BDBC, School of Electronic and Information Engineering, Beihang University, Beijing, 100191, China.

4.4.1 LTEM measurements of a Pt/Co/W multilayer stack

In this section, LTEM measurements on a SiN/Ta_{1nm}/Pt_5/Co_5/W_1[Pt_1/Co_5/W_1]$_{\times 4}$/Pt_1 multilayer sample are presented. First, phase diagrams are recorded and differences to the B20 chiral magnets are shown. Afterwards, a possible way to align the $\boldsymbol{q}_{\mathrm{h}}$-vector of the cycloidal phase with an externally-applied in-plane magnetic field is shown. Finally, the experimental Fresnel contrast of the Néel skyrmions is further investigated and the skyrmion size is determined by the comparison to simulation results.

The Ta_{1nm}/Pt_5/Co_5/W_1[Pt_1/Co_5/W_1]$_{\times 4}$/Pt_1 stack is grown by magnetron sputtering at a base pressure $<4 \times 10^{-8}\,\mathrm{mbar}$ onto a 20 nm thick Si_3N_4 membrane by Lin[8]. Deposition rate and pressure are adjusted to match other work [67, 224, 225]. The polycrystalline sample is put into a liquid nitrogen TEM-holder and inserted into the TEM. The holder possesses a liquid nitrogen reservoir with an embedded Cu-rod that extends close to the holder tip where the sample is situated. As the holder can be conveniently refilled, measurement times are essentially unlimited, in contrast to the liquid helium holder described in section 4.3. Close to the sample, there is also an additional electric resistance which can be used to heat the sample which allows temperatures beyond room temperature or to counter the cooling effect of the liquid nitrogen. The effective temperature range of the holder is around 100 to 360 K. Furthermore, by using an integrated motor, the holder can tilt the sample around an axis perpendicular to the stage-tilt axis of the TEM. This can be used to realize arbitrary sample tilt axes in the plane perpendicular to the optical axis which proved particularly useful in the study of Néel skyrmion hosting materials as shown later.

For the following Fresnel LTEM measurements, the electron energy is tuned to 300 keV. To obtain magnetic contrast, the sample is tilted to 20° as explained in section 4.2.1. This value is large enough to produce sufficient magnetic electron phase-shift (see Fig. 4.15D). Although this is potentially problematic as $\boldsymbol{H}_{\mathrm{ext}}$ will be at an angle with respect to the sample normal, the results are still in agreement with hysteresis loops obtained by MOKE with $\boldsymbol{H}_{\mathrm{ext}}$ parallel to the sample normal [67]. To further quantify this, a tilt angle dependent phase scan is also presented later. In contrast to the Bloch skyrmions in section 4.3, a 30 times larger Lorentz-lens defocus of around 3 mm is necessary to obtain reasonable contrast, to which only the small in-plane projection of the tilted out-of-plane magnetization contributes.

First, magnetic phase diagrams are recorded similarly to the ones on Cu_2OSeO_3 before. However, the T_{c} of this sample is above the accessible temperature range.

[8] Fert Beijing Institute, BDBC, School of Electronic and Information Engineering, Beihang University, Beijing, 100191, China.

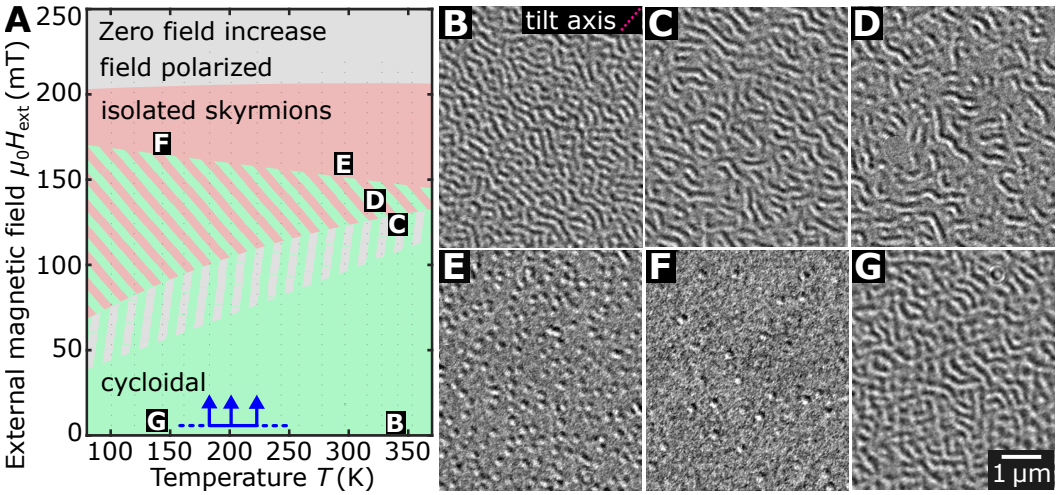

Fig. 4.22.: **(A)** Zero field increase phase diagram of the Pt/Co/W multilayer sample. At each indicated temperature, the sample is saturated and afterwards the external magnetic field is increased from zero, while the present magnetic phase is tracked. The dots represent recorded Fresnel images. **(B)** Example image of the cycloidal, **(C)** cycloidal/field-polarized mixed, **(D)** cycloidal/field-polarized/skyrmion mixed and **(E)** isolated skyrmion phase. **(F)** At lower temperatures, a skyrmion phase with less density is observed. **(G)** A cycloidal phase with less order is visible for low temperatures. The phase space positions of the example images are indicated in the phase diagram. A median filter in a 3×3 neighborhood, polynomial background subtraction and a manual removal of dirt are applied to the example Fresnel LTEM images.

Therefore, the combined temperature and magnetic field protocols for the ZFC and FC phase diagrams are not applicable to this sample. A first alternative measurement protocol produces a so-called zero-field increase (ZFI) phase diagram. For a fixed temperature value T_m, the sample is saturated with $H_\mathrm{ext} = 240\,\mathrm{mT}$ which is confirmed by the observation of a vanishing magnetic contrast. Afterwards, the external magnetic field is reduced to zero at a rate of $230\,\mathrm{mT\,s^{-1}}$. Then, $\mu_0 H_\mathrm{ext}$ is increased in steps of around 6 mT and images are recorded after each step. Finally, once the sample is again saturated, the process is repeated for a different value of T_m. After the measurement, the present magnetic phase is identified for every image. This information is used to construct the phase diagram shown in Fig. 4.22A by the manual insert of phase borders. As before, each small gray dot represents a Fresnel image.

The ZFI phase diagram is now discussed alongside the presentation of exemplary images. The phase space position of the images is also indicated inside the phase diagram. For zero magnetic field, a cycloidal phase is obtained as displayed in Fig. 4.22B. The tilt axis of the sample is indicated in the image. Note that $\boldsymbol{q}_\mathrm{h}$ is essentially parallel to the tilt axis, which is due to the magnetic history and will be discussed in more detail later. Once the externally-applied magnetic field is

increased, the magnetic domains with a magnetization parallel to the field increase their size and the anti-parallel domains start to shrink. A phase with isolated stripes in a field-polarized background is obtained, as seen in Fig. 4.22C. Upon further magnetic field increase, the isolated cycloidal domains shrink down to the size of a Néel skyrmion, and a mixed phase consisting of isolated cycloidal stripes and skyrmions is observed as shown in Fig. 4.22D.

This behavior continues until an isolated Néel skyrmion phase is obtained, see Fig. 4.22E. The isolated skyrmions are found for the whole accessible temperature range. The observation of single events shows that during this process, the stripes pinch off such that a single cycloidal stripe is the origin of many skyrmions. Such behavior is also observed in magnetic bubble-hosting materials and happens due to the presence of magnetic pinning defects inside the sample. At such a defect, magnetic parameters like the local uniaxial anisotropy can be discontinuous. This can lead to a locally strong anisotropic magnetization energy landscape that fixes or pins the magnetization at the corresponding position [5, 218, 226]. In this case, the probability of a stripe ripping off during its size reduction process is enhanced at such a defect position. The effect of pinning in this sample is investigated in more detail later.

Picturing the skyrmions as the topological remnants of the cycloidal stripes, it is unsurprising that no hexagonal lattice state is obtained. Approaching the magnetic saturation field, the topological number decreases until all skyrmions are annihilated. The maximum number of skyrmions decreases for low temperatures, which is illustrated in Fig. 4.22F. Another difference at low temperatures is observed in the cycloidal phase at zero-applied magnetic field. The image in Fig. 4.22G shows a cycloidal phase that qualitatively exhibits less order in terms of stripe continuity and shows an increased stripe width than its analogue at room temperature. This may be explained due to the decreased thermal energy that cannot overcome the topological protection of an extending isolated stripe which forbids its combination with another stripe after the initial field-decrease and leaves back a frustrated system. An alternative explanation is the modified energy landscape due to a temperature dependence of magnetic parameters like M_s.

The second phase diagram is obtained from a saturation-field-decrease (SFD) field protocol. At a certain temperature, the sample is saturated as in the ZFI case. However, then the field is decreased in steps of 6 mT down to $H_\mathrm{ext} = 0\,\mathrm{mT}$. Again, a Fresnel image is recorded after each magnetic field step. The resulting phase diagram is shown in Fig. 4.23A. At room temperature, skyrmions appear around $125\,\mathrm{mT}$ as displayed in Fig. 4.23B. In comparison to the isolated skyrmion phase in the ZFI phase diagram, these skyrmions seem slightly elongated even for largest fields, indicating that they are close to expansion. This observation

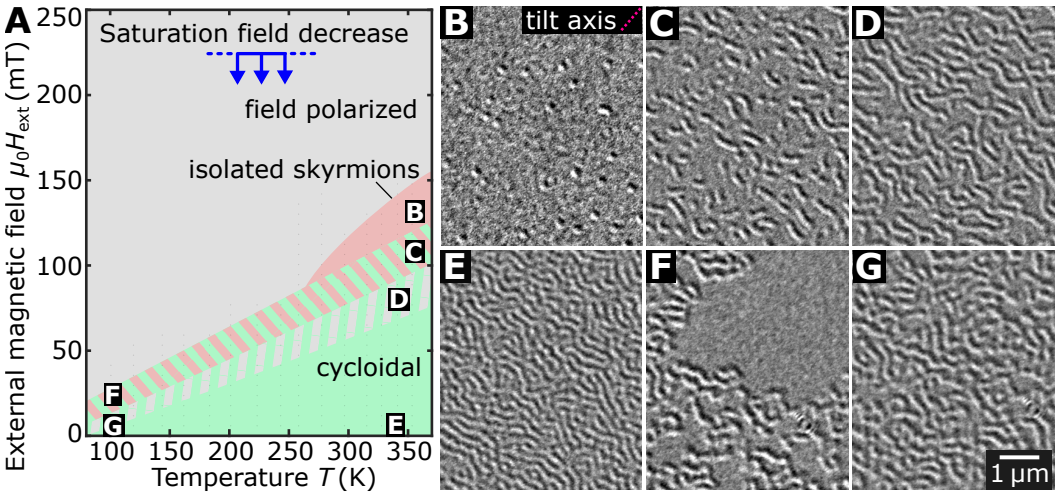

Fig. 4.23.: **(A)** Saturation field decrease phase diagram of the Pt/Co/W multilayer sample. At each indicated temperature, the sample is saturated and the external magnetic field is reduced to zero, while the present magnetic phase is tracked. The dots represent recorded Fresnel images. **(B)** Example image of the skyrmion, **(C)** cycloidal/field-polarized/skyrmion mixed, **(D)** cycloidal/field-polarized mixed and **(E)** cycloidal phase. **(F)** At lower temperatures, no skyrmion phase but a rapid cycloidal coverage of the sample is observed. **(G)** The cycloidal phase with decreased order at low temperatures that is observed in the ZFI case, is also visible for the SFD case. The phase space positions of the example images are also indicated in the phase diagram. A median filter in a 3×3 neighborhood, polynomial background subtraction and a manual removal of dirt is applied to the example Fresnel LTEM images.

matches the ZFI phase diagram, where an isolated skyrmion/cycloidal mixed phase is observed for this magnetic field range. The Fresnel contrast also suggests that at room temperature the skyrmions in the SFD case are also roughly 20 % larger than in the ZFI case, which can be explained with the different magnetic fields at which they are observed. With decreasing external magnetic field, the skyrmions expand as shown in Fig. 4.23C,D and finally form the cycloidal phase at zero field as displayed in Fig. 4.23E. This behavior changes for lower temperatures. Here no skyrmions are observed at all. Instead, at some critical field large areas of the sample instantaneously transform to a cycloidal phase as shown in Fig. 4.23F. In fact, the transformation from the field-polarized phase to the latter state is observed for a field interval smaller than 1 mT. The frustrated cycloidal structure at zero applied magnetic field and low temperatures is also observed for the SFD protocol, as shown in Fig. 4.23G.

In comparison to the ZFI phase diagram, a strong temperature dependence of the field at which the magnetic system transforms from the field-polarized to cycloidal or isolated skyrmion phase is observed. Additionally, this field is significantly lower than the one observed for the ZFI case. This might be explained as follows:

When the magnetic field is increased, the energy landscape is deformed until the thermal energy can overcome the topological protection of the metastable skyrmions. For a field decrease, a similar energy barrier needs to be overcome as also the field-polarized phase is topologically protected from the skyrmion state. However, the energy landscape that is required for this transition to take place is naturally found at lower external fields, as the skyrmion or cycloidal state needs to have a lower energy than the field-polarized phase. The required thermal energy, needed to overcome the topological protection, might also explain the temperature dependence of the transition field in the SFD case. Because of the small critical fields at low temperatures, it is also obvious why no skyrmions are observed as the skyrmion states in the ZFI phase diagram are found at field values that are around 8 times as large.

The energy barriers and the concomitant metastable phases slightly complicate a general statement about the actual magnetic ground states of the system. Nevertheless, considering that the model that leads to the theoretical phase diagram for magnetic bubble materials in Fig. 2.8C does not include mixed phases, a similarity to the phase diagrams presented here becomes quite clear, in particular when comparing it to the SFD phase diagram. This shows a resemblance of the multilayer room-temperature skyrmion hosting materials to the magnetic bubble systems.

From the example images of the cycloidal phases in both phase diagrams, a preferred $\boldsymbol{q}_\mathrm{h}$ alignment parallel to the sample tilt axis is suggested. To further investigate this, the externally-applied magnetic field is increased from zero to 135 mT to obtain a skyrmion/cycloidal mixed phase. Afterwards, the field is reduced to 35 mT and the skyrmions expand to cycloidal stripes, whose individual orientation is well discernible. This field protocol is applied for four differently oriented tilt axes with intermediate angles of 45°. The resulting Fresnel images are shown in Fig. 4.24A. As $\boldsymbol{H}_\mathrm{ext}$ is always parallel to the optical axis, an in-plane magnetic field component $\boldsymbol{H}_\mathrm{ext}^\mathrm{ip}$ is present due to the tilted sample as indicated at the top of the images. The alignment of $\boldsymbol{q}_\mathrm{h}$ parallel to the tilt axis and perpendicular to $\boldsymbol{H}_\mathrm{ext}^\mathrm{ip}$ is clearly visible.

The fact that the Fresnel contrast vanishes when $\boldsymbol{q}_\mathrm{h}$ is perpendicular to the tilt axis as discussed in section 4.2.1 slightly impairs the latter conclusion. To quantitatively capture this fact, the external magnetic field is reduced to zero after the field protocol discussed before. Further, the sample tilt angle is increased to 40°, as this increases $H_\mathrm{ext}^\mathrm{ip}$ and the effect will be stronger which is explained later. The resulting cycloidal phase at $\mu_0 H_\mathrm{ext} = 0\,\mathrm{mT}$ is shown in Fig. 4.24B. Note that the sample tilt angle is adjusted back to 20° for the recording of the image. The theoretically expected circular intensity profile of the square modulus of the Fourier transform at the radius $k_\perp = q_\mathrm{h}$ of a Fresnel image showing an unordered cycloidal phase is known from

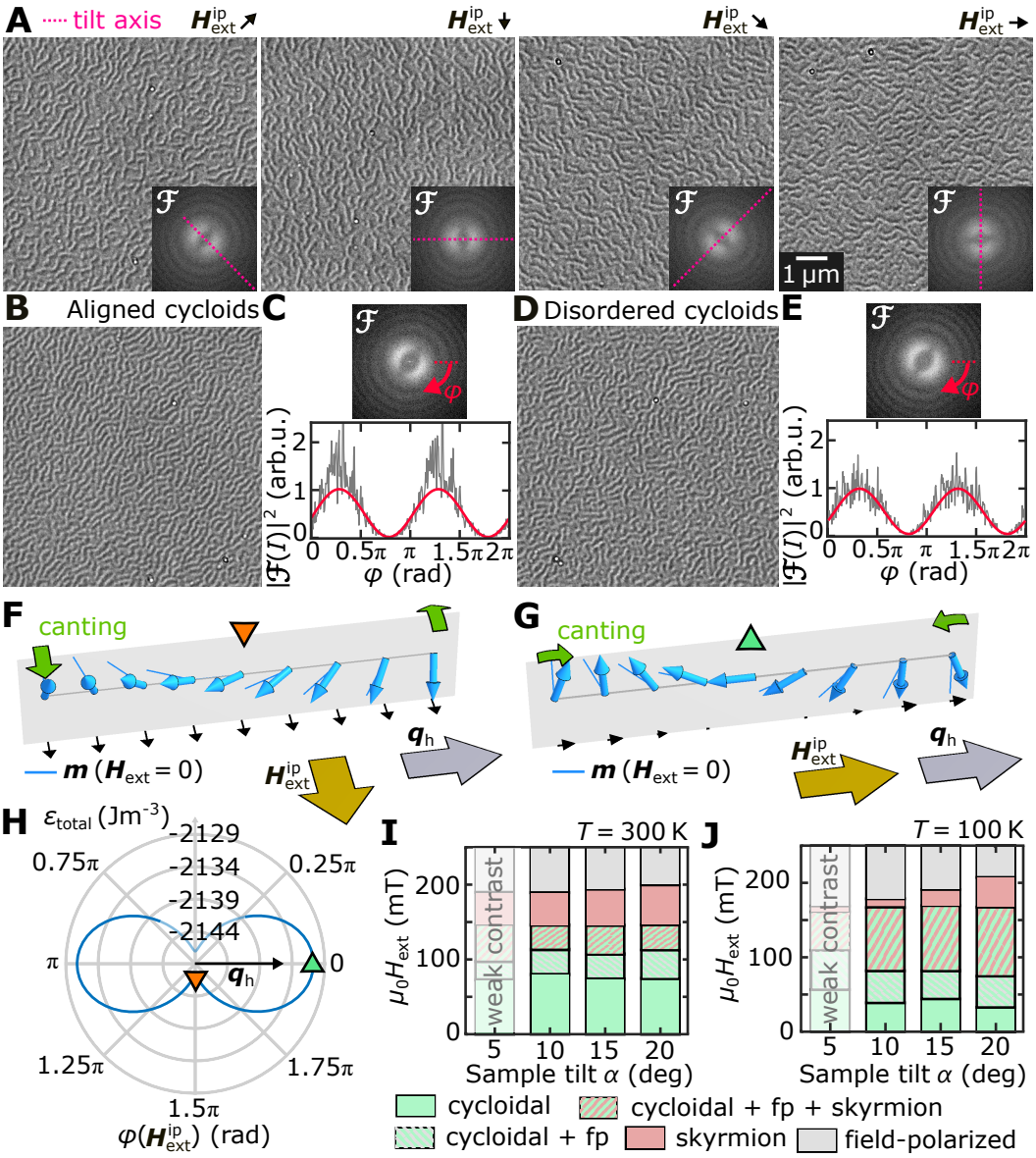

Fig. 4.24.: Effects of an in-plane magnetic field on the magnetic textures. **(A)** At $\mu_0 H_{\mathrm{ext}} = 35\,\mathrm{mT}$, $\boldsymbol{q}_{\mathrm{h}}$ aligns parallel to the tilt axis $\perp \boldsymbol{H}_{\mathrm{ext}}^{\mathrm{ip}}$. **(B)** At zero field, the alignment is also visible for tilt angles of 40° (see text). **(C)** Absolute square of the FT of (B) and circular profile. As the phase is ordered, the data deviates from the theoretical curve. **(D)** Cycloidal phase when $\boldsymbol{H}_{\mathrm{ext}}$ is reduced to zero with an untilted sample. **(E)** The circular FT profile matches the theoretical expectation. **(F)** Simulated torsion of a Néel wall for $\boldsymbol{H}_{\mathrm{ext}}^{\mathrm{ip}} \perp \boldsymbol{q}_{\mathrm{h}}$. The solid lines in the plane represent the equilibrium position for $H_{\mathrm{ext}} = 0$. The black arrows in the bottom show the projected magnetization change due to $\boldsymbol{H}_{\mathrm{ext}}^{\mathrm{ip}}$. **(G)** Néel wall compression for $\boldsymbol{H}_{\mathrm{ext}}^{\mathrm{ip}} \parallel \boldsymbol{q}_{\mathrm{h}}$. **(H)** Energy density of the simulation for the relative direction of $\boldsymbol{H}_{\mathrm{ext}}^{\mathrm{ip}}$ and $\boldsymbol{q}_{\mathrm{h}}$. The triangles mark the energies of (F) and (G). The canting of the structures in (F) and (G) is artificially amplified by factors of 5 and 2 for better visualization. **(I)** Dependence of the magnetic phases with respect to H_{ext} and sample tilt α at room temperature and **(J)** $T = 100\,\mathrm{K}$. A 3×3 median filter and a polynomial background subtraction is applied to (A,B,D).

Eq. (4.32). The respective Fourier transform and the circular profile as well as this theoretical prediction are shown in Fig. 4.24C. Clearly, the theoretical expectation does not describe the experimental data, which indicates that the $\boldsymbol{q}_\mathrm{h}$ of the cycloidal phase is indeed aligned along the tilt axis. In contrast to this, Fig. 4.24D shows the cycloidal phase when the external magnetic field protocol is applied with zero sample tilt such that $\boldsymbol{H}_\mathrm{ext}^\mathrm{ip}$ vanishes. In this case, the cycloidal phase is clearly disordered, which is visible from the image and from the circular FT profile that is shown in Fig. 4.24E which perfectly follows the theoretical expectation for a disordered cycloidal phase.

The reason for this alignment is attributed to the orientation of $\boldsymbol{H}_\mathrm{ext}^\mathrm{ip}$ during the stripe expansion process. To make this more plausible and visualize the microscopic effect, micromagnetic simulations are performed. As the exact simulation of the multilayer structure is complex and not all micromagnetic constants are known, the micromagnetic model of Cu_2OSeO_3 from section 3.3.1 is used. To apply to this case, the cubic anisotropy is dropped and the bulk DMI is replaced with an interface-DMI which transforms the magnetic structures from the Bloch to the Néel type. Without external magnetic field, a mono-$\boldsymbol{q}_\mathrm{h}$ cycloidal spin structure is obtained as the ground state. Based on this ground state, an external field $\boldsymbol{H}_\mathrm{ext}^\mathrm{ip}$ of 10 mT is applied in every in-plane direction of the simulation plane (compare Fig. 3.6A). For each in-plane magnetic field direction, the equilibrium magnetization is computed.

In the ground state without an in-plane magnetic field, $\boldsymbol{M}$ lies inside the plane of $\boldsymbol{q}_\mathrm{h}$ and the sample normal as shown by the gray plane and the solid lines in Fig. 3.6F for a single Néel wall. When now $\boldsymbol{H}_\mathrm{ext}^\mathrm{ip}$ is applied perpendicular to $\boldsymbol{q}_\mathrm{h}$, the spins are canted towards $\boldsymbol{H}_\mathrm{ext}^\mathrm{ip}$ and the state in Fig. 3.6F represented by the 3D arrows is obtained. This gives a net magnetization along $\boldsymbol{H}_\mathrm{ext}^\mathrm{ip}$ as indicated by the solid black arrows at the bottom. This canting of the spins is reminiscent of a torsion of the spin structure along the $\boldsymbol{q}_\mathrm{h}$-axis which is indicated by the green circular arrows. In contrast to that for $\boldsymbol{H}_\mathrm{ext}^\mathrm{ip} \parallel \boldsymbol{q}_\mathrm{h}$, the resulting spin structure is not canted out of the plane as shown in Fig. 3.6G. For the shown structure, the magnetization direction in the center of the Néel wall is opposite to $\boldsymbol{H}_\mathrm{ext}$. In this case, the spin canting, induced by $\boldsymbol{H}_\mathrm{ext}^\mathrm{ip}$, effectively compresses the Néel wall as indicated by the green arrows. In contrast to that, the neighboring Néel wall (not shown) has an opposite in-plane magnetization and expands due to $\boldsymbol{H}_\mathrm{ext}^\mathrm{ip}$.

Now that the two relaxed magnetization structures for $\boldsymbol{H}_\mathrm{ext}^\mathrm{ip} \parallel \boldsymbol{q}_\mathrm{h}$ and $\boldsymbol{H}_\mathrm{ext}^\mathrm{ip} \perp \boldsymbol{q}_\mathrm{h}$ are known, their energy is compared. The energy density with respect to the direction of $\boldsymbol{H}_\mathrm{ext}^\mathrm{ip}$ is given in Fig. 3.6H. It is minimized for $\boldsymbol{q}_\mathrm{h} \perp \boldsymbol{H}_\mathrm{ext}^\mathrm{ip}$. This result can explain the cycloidal alignment observed in the experiment as the torsion leads to a lower energy compared to the compression and expansion of the Néel wall.

As the effect of $H_{\mathrm{ext}}^{\mathrm{ip}}$ becomes evident, it is further checked whether the tilt of the sample with its concomitant introduction of an in-plane magnetic field affects the shape of the phase diagram. For this, field scans following the ZFI-protocol of the respective phase diagram in Fig. 4.22 are conducted for different tilt angles $\alpha = 5°, 10°, 15°, 20°$. The obtained phases at room temperature are shown in Fig. 4.24I. There is no significant dependence on the sample tilt. The same behavior is found for $T = 100\,\mathrm{K}$, which is illustrated in Fig. 4.24J. Here, a dependence of the magnetic transition field from skyrmion to field-polarized phase is indicated. This is however not very reliable due to the small skyrmion count at that temperature in combination with the small sampling area of TEM. Note that the given phases for 5° are not clearly discernible due to the weak contrast and are only hinted.

In the description of the phase diagrams, the role of pinning of the magnetic structures to magnetic defects is already briefly discussed. For a deeper analysis of this assumption, two effects are investigated at room temperature. First, the hypothesis that skyrmions get pinned during the transition from cycloidal to skyrmion phase is checked. For this, the external magnetic field is put to zero such that a cycloidal phase is obtained. Afterwards, the magnetic field is increased up to 162 mT at a rate of $15\,\mathrm{T\,s^{-1}}$ in one step which leads to a transformation of the cycloids to skyrmions (compare with the ZFI phase diagram in Fig. 4.22). A typical Fresnel image in that state is depicted in Fig. 4.25A. The same process is repeated 11 times and the resulting images are digitally aligned such that the dirt feature on the top right is exactly at the same position in all images. The skyrmion positions are then marked using an automatic skyrmion detection that relies on finding local intensity maxima in combination with some preprocessing steps including polynomial background subtraction, median, low-pass and disk filtering. The detected positions are manually checked and corrected if needed. The analysis gives a mean skyrmion count of 221 per image with a standard deviation of 13 skyrmions.

At each position, a circular skyrmion area with the skyrmion radius (determined later) is defined. For a single skyrmion, the area is indicated by the green dot in the image. A binary mask is created and a value of one is assigned to the skyrmion areas and zero to the other parts of the image. Then, all 11 masks are added up and divided by the number of images. The resulting map is shown in Fig. 4.25B. It is a measure of the space-dependent probability distribution of finding a skyrmion within a circular area of the skyrmion radius around a given position after following the described field protocol. Clearly, there are positions of enhanced skyrmion probability. Particularly striking are the locations where skyrmions are found in all of the recorded images, like the highlighted one. These points do not even make the impression that they consist of eleven points as the congruence is so precise. This is a strong indication that a pinning center is present at that point. To exclude the effect

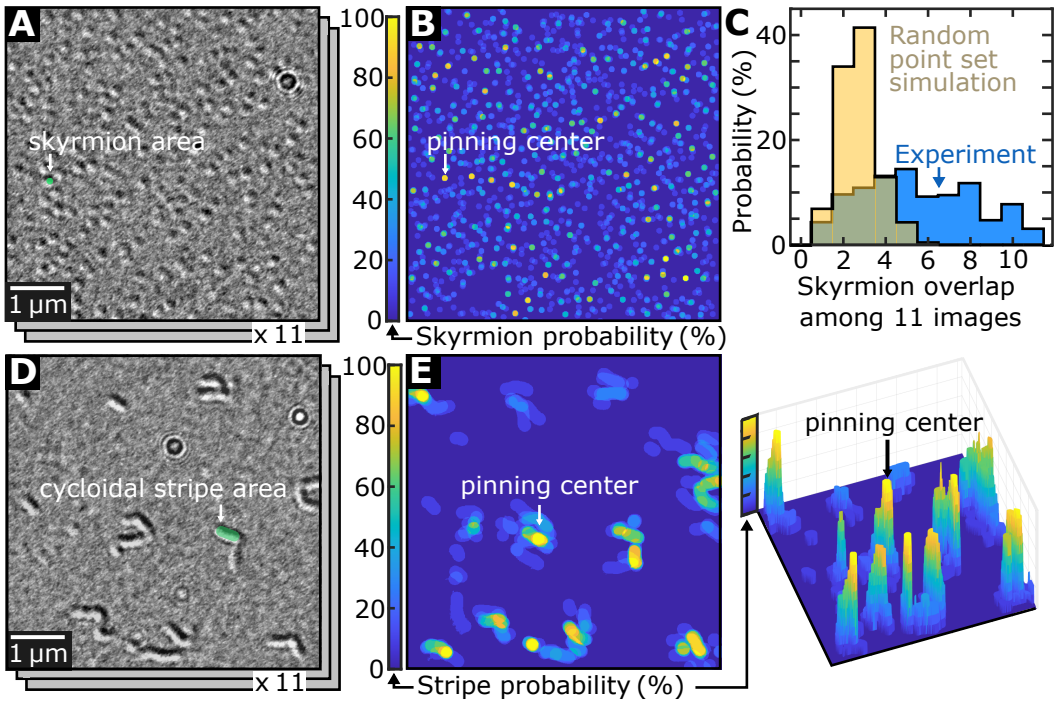

Fig. 4.25.: Pinning effects in the Pt/Co/W sample. **(A)** One of eleven images after the transition of the cycloidal to the skyrmion phase. The green dot highlights the area enclosed by the radius of the skyrmion at that position. **(B)** Probability distribution of finding a skyrmion at a specific location among the 11 images. A position where this probability is $100\,\%$ is marked and identified as a pinning location. **(C)** Histogram showing the share of skyrmions with respect to their overlap with other skyrmions among the images. The yellow distribution shows the results from a simulation that uses random points that are no subject to a potential pinning with a minimum distance of twice the skyrmion radius. It clearly deviates from the experimental data, which indicates pinning effects. **(D)** Example image after the transition of the field-polarized phase to the skyrmion/-cycloidal mixed phase. A cycloidal stripe area is highlighted. **(E)** Map of the probability density of finding a cycloidal stripe among the images. On the right, a 3D view of the map is shown, where the pinning center is most strikingly visible. A 3×3 median filter and a polynomial background subtraction is applied to images (A) and (D).

of clustering-illusion [227], a statistical cross-check is performed. In Fig. 4.25C, the proportion of skyrmions with respect to the overlap with other skyrmions from the other images is drawn. As expected from Fig. 4.25B, the histogram is non-zero up to the maximum of 11 (an overlap within a single image is not observed). This is compared to the result of the same analysis on a random set of points with the same total number. Here, the only constraint to the set is that the points lie within the range of the image and are not closer than twice the skyrmion radius. The incompatibility of the two cases is obvious, proving that the skyrmions are pinned to defects when they are generated from the cycloidal phase. Assuming that at least

the skyrmions with an overlap ≥ 6 are subject to pinning, more than 61 % of the skyrmions are affected.

The second hypothesis is that the magnetic defects serve as seeds for the modulated structures when they are generated from the field-polarized phase. The same procedure from before is conducted, only now the magnetic field is reduced from 240 mT at which the field-polarized phase is present to 126 mT where the first skyrmions and cycloidal stripes appear. An example Fresnel image of the resulting situation is shown in Fig. 4.25D. Note that in the SFD phase diagram in Fig. 4.23, the final value of H_{ext} is still within the field-polarized phase, and skyrmions without cycloidal stripes are expected. This difference is explained with the fact that the external magnetic field is reduced in one large step and not in small steps of 6 mT like during the measurement of the SFD-phase diagram. It turns out that this alters the phase diagram and the number of observed skyrmions, which is further analyzed in section 4.4.2. Similar as before, a cycloidal stripe area is defined for each of the 11 images. As the observed cycloidal structures are few in comparison to the skyrmions from before, it is sufficient to manually mark the observed contrast and define it as a cycloidal stripe area, as shown with the green patch. The probability map of obtaining a magnetically modulated texture in Fig. 4.25E shows obvious overlaps of the cycloidal stripes. These are again attributed to pinning centers. This becomes even more striking from the 3D view of the map shown on the right. In summary, strong evidence is found that the skyrmions and isolated cycloidal stripes are pinned to magnetic defects during the transition of cycloidal to skyrmion and field-polarized to skyrmion/cycloidal mixed phase.

Next, the Néel skyrmion Fresnel contrast is investigated in more detail and the skyrmion size is extracted from a comparison with simulations. Fig. 4.26A shows the isolated skyrmion phase at $\mu_0 H_{\mathrm{ext}} = 150\,\mathrm{mT}$ for different orientations of the tilt axis. The sample orientation is illustrated in the top row. The skyrmion intensities in the center row nicely follow the tilt axis as expected from the description in section 4.2.1. Again, the tilt axis is also visible in the respective FT of the images as shown in the bottom row.

Fig. 4.26B shows a magnified view of a skyrmion for tilt angles $\alpha = 20°, 0°$ and $-20°$. As expected, the contrast is inverted for opposite tilt angles and vanishes with the absence of a sample tilt. This contrast is now simulated using Eq. (4.17) in combination with Mansuripur's formalism applied to the Néel skyrmion structure as introduced in section 4.2. The parameters used in the calculation are the $M_{\mathrm{s}} = 1.4 \times 10^6\,\mathrm{A\,m^{-1}}$, a defocus of $\Delta f = 2.95\,\mathrm{mm}$, an effective sample thickness of $\tau = 9\,\mathrm{nm}$, an electron energy of $300\,\mathrm{keV}$, a spherical aberration of $C_{\mathrm{s}} = 8\,\mathrm{m}$, a beam divergence of $1 \times 10^{-5}\,\mathrm{rad}$, a skyrmion radius $R = 72.5\,\mathrm{nm}$ and a skyrmion wall width of $\Delta = 2R$.

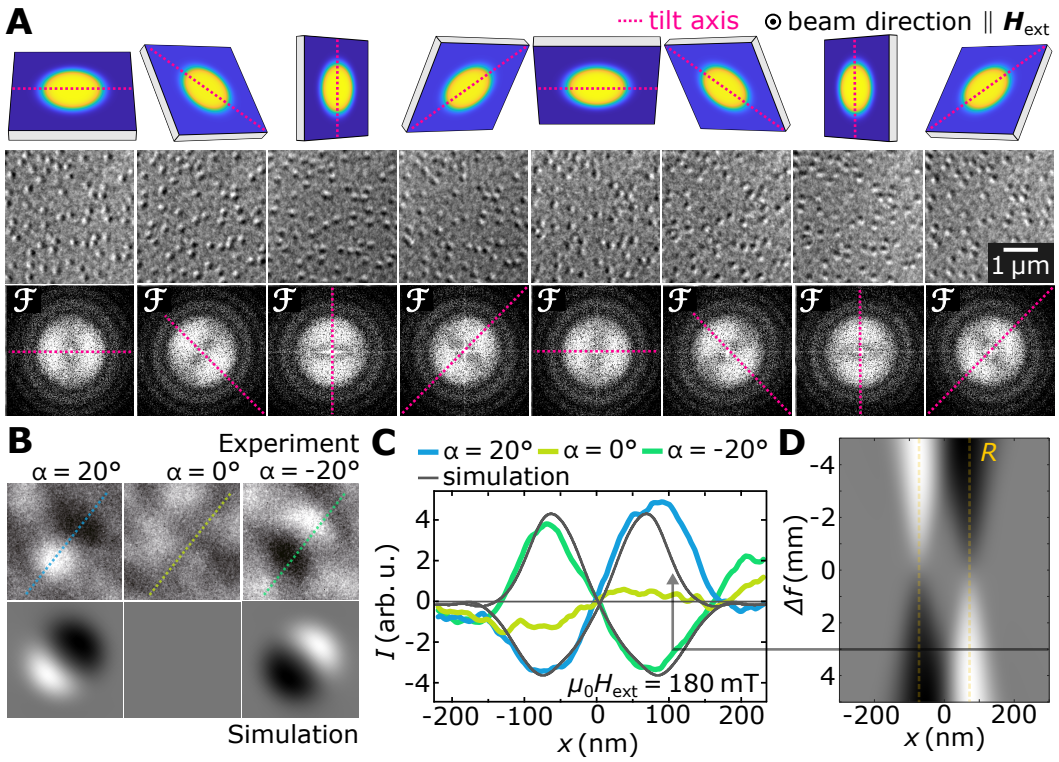

Fig. 4.26.: Fresnel contrast of Néel skyrmions in the Pt/Co/W multilayer sample. **(A)** The skyrmion signature in the Fresnel images in the central row follows the sample tilt axis that is indicated in the cartoon of the top row and the FTs in the bottom row. **(B)** Magnified view of a single skyrmion for sample tilt angles of $\alpha = 20°, 0°$ and $-20°$. Simulations in the bottom row match the images. **(C)** Line profiles along the dotted lines in (B) show a quantitative match with the simulated contrast. **(D)** Simulated cut through the central skyrmion Fresnel intensity in dependence of defocus. The general shape is conserved for the shown defocus range. A 3×3 median filter and a Gaussian filter with $\sigma = 2\,\mathrm{px}$ is applied to (A). The line profiles in (C) rely on raw data.

The resulting simulated Fresnel images qualitatively match the experimental images as seen in the bottom row of Fig. 4.26B.

There is also a quantitative agreement as proven from the image profiles along the dotted lines in Fig. 4.26B given in Fig. 4.26C. Comparing this to the proposed skyrmion in the simulation, a measured skyrmion diameter of $125\,\mathrm{nm}$ and a skyrmion wall width twice that large is obtained. However caution is advised, as the Fresnel simulation depends on a large set of parameters. If one of the parameters is erratic, there will nevertheless be a skyrmion radius/wall width combination for which the simulated Fresnel line profile matches the experimental one. In this example, a reduction of the skyrmion radius by 10 % and a simultaneous increase of defocus by 20 % essentially gives equivalent line profiles. For this reason, it is advisable to not rely on these parameter-sensitive and tedious Fresnel contrast simulations.

More consistent results can be obtained from a method like DPC that measures the electron phase more directly. This can then also be combined with the skyrmion spin structure relations introduced in sections 4.2.2 and 4.2.3. This will be demonstrated in section 4.4.2.

The simulated Fresnel intensity profile of the Néel skyrmion discussed before is now calculated for a focus range of -5 to 5 mm. The resulting dependence is drawn in Fig. 4.26D. Each horizontal line represents a cut through the profile and white (black) color resembles large (low) Fresnel intensity just like in the images. Interestingly, the typical shape of the Néel skyrmion contrast is conserved for all values of the studied defocus range. This is in contrast to observations on magnetic vortices or in-plane domain walls, where the contrast quickly disappears with defocus, shows side-fringes or is not symmetric with respect to $\Delta f = 0$ [167, 170, 175].

In section 4.2.2, the so-called hybrid skyrmions were already introduced. These are a combination of Bloch and Néel skyrmion spin structure and are among other materials also reported for Pt/Co/Ir multilayer systems which qualitatively show the same modulated structures as the Pt/Co/W system discussed in this section [150]. To check the presence of potential hybrid skyrmions, Fresnel LTEM can be used conveniently. Fallon et al. show that the contrast of hybrid cycloidal stripes of a Pt/Co/Ru multilayer stack on the bent surface of a SiN membrane does not completely vanish when the sample normal is parallel to the optical axis [198]. Considering the explanations in section 4.2.2 particularly around Eq. (4.44), the same argumentation is possible for a hybrid skyrmion, which should also give a Fresnel signature similar to Fig. 4.18D if its spin structure has a finite Bloch contribution. Considering Fig. 4.26B, this is not the case here, indicating that there is no Bloch skyrmion contribution that is large enough to be detected.

4.4.2 LTEM measurements of a Pt/Co/Tb multilayer stack

In this section, LTEM measurements on a SiN/$\mathrm{Ta}_{3\mathrm{nm}}$/$\mathrm{Pt}_5$/$[\mathrm{Co}_2/\mathrm{Tb}_1/\mathrm{Pt}_3]_{\times 5}$ multilayer stack are shown. In the beginning, ZFI and SFD phase diagrams, obtained with Fresnel LTEM, are presented. The results are similar to the ones of the Pt/Co/W multilayer stack that is investigated in the last section. After that, the phase space dependency of the topological charge N_{sk} within the field of view for both ZFI and SFD field protocols is investigated. A double peak in the temperature dependence of N_{sk} indicates a change of the parameters of the magnetic system at around $300\,\mathrm{K}$. Here, an interesting mechanism is found: When the externally-applied magnetic field is changed in a single step from zero to a target value case at which skyrmions are observed according to the phase diagram, the skyrmion density can be increased

up to a factor of 2, in comparison to the ZFI case in which the magnetic field is changed in smaller steps. Finally, first DPC measurements on Néel skyrmions are presented. The theoretical descriptions in sections 4.2.2 and 4.2.3 can be directly applied to the results.

Accordingly to the last section, the $Ta_{3nm}/Pt_5/[Co_2/Tb_1/Pt_3]_{\times 5}$ stack is grown onto the $500 \times 500\,\mu m^2$ Si_3N_4 membrane with a thickness of 20 nm by Lin[9]. An average grain size of 4.9 nm with a standard deviation of 1 nm of the polycrystalline stack is measured using HRTEM. The measurement conditions in terms of an electron energy of 300 keV, the liquid nitrogen sample holder and a sample tilt of 20° are also maintained according to the last section.

Before the data is presented, a brief motivation is given on why Pt/Co/Tb samples are particularly interesting within the heavy metal/ferromagnet/heavy metal multilayer systems. The most striking difference between the Pt/Co/W and Pt/Co/Tb stack is obviously the replacement of W with Tb. It is known that at the Tb/Co interface, the non-magnetic Tb becomes ferromagnetic due to the exchange coupling to Co [228]. In addition, this coupling is antiferromagnetic, i.e. the magnetized Tb-layer aligns anti-parallel to the Co-layer. For a skyrmion spin structure, this has the consequence that skyrmion polarity and chirality in Co and Tb are inverted. Actually, this reduces the effective electron phase that is measured with LTEM as the integrated magnetization along $\hat{z}$ is partially compensated.

The benefits of such an antiferromagnetic coupling is rooted in skyrmion transport. When the skyrmion is moved by a spin polarized current, its velocity is in general not parallel to the current direction but is inclined at an angle within the skyrmion plane. This angle is called the skyrmion-Hall angle. For opposite skyrmion chirality, the topological charge and the skyrmion-Hall angle are inverted. This is in complete analogy to the electric charge in the common Hall effect [6, 87, 99, 229]. Therefore, the antiferromagnetic coupling, described before, can reduce the effective skyrmion-Hall angle. A technical example where the skyrmion-Hall effect is problematic is the skyrmion racetrack. Here, the skyrmion-Hall effect creates a constant force that pushes the skyrmion to one of the racetrack walls, which can e.g. lead to an undesired skyrmion annihilation due to edge roughness [226]. A more scientific example can be observed during TEM observations. Here, a radially symmetric spin current is created from a temperature gradient in the sample which itself is inflicted by the circular electron beam. In this case, the skyrmion-Hall effect can lead to a rotation of the hexagonal skyrmion lattice as reported for Cu_2OSeO_3. This can be obstructing for static measurements [86, 88, 230]. In this work, the antiferromagnetic coupling of Co and Tb has been verified for a similar sample using

[9] Fert Beijing Institute, BDBC, School of Electronic and Information Engineering, Beihang University, Beijing, 100191, China.

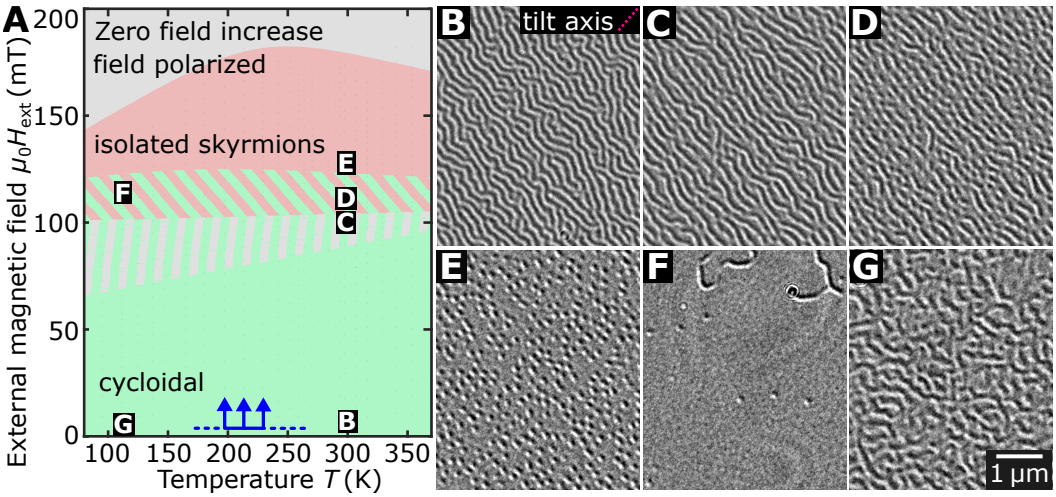

Fig. 4.27.: **(A)** Zero field increase phase diagram of the Pt/Co/Tb multilayer sample. At each indicated temperature, the sample is saturated and afterwards the external magnetic field is increased from zero, while the present magnetic phases are tracked. The dots represent recorded Fresnel images. **(B)** Example image of the cycloidal phase, **(C)** cycloidal/field-polarized mixed, **(D)** cycloidal/field-polarized/skyrmion mixed and **(E)** isolated skyrmion phase. **(F)** At lower temperatures, only few skyrmions are observed. **(G)** A cycloidal phase with less order is visible for low temperatures. The phase space positions of the example images are also indicated in the phase diagram. A median filter in a 3×3 neighborhood, polynomial background subtraction and a manual removal of dirt is applied to the example Fresnel LTEM images.

XMCD magnetic field scan measurements at the Tb and Co L_3 energies, which result in inverted hysteresis loops for Tb and Co (data not shown).

For an overview, phase diagrams are recorded. The field protocols ZFI and SFD were already established in the last section and are also applied for this sample. The step size between each image during a magnetic field scan is not fixed and is in the range of 2 to 10 mT. The field is adjusted manually and the rate of the magnetic field change is in the order of $10\,\mathrm{mT\,s^{-1}}$. The ZFI phase diagram is displayed in Fig. 4.27A. The qualitative shape is very similar to the phase diagram of the Pt/Co/W sample in Fig. 4.22A. Also the magnetic field scan at room temperature yields similar results. At zero applied magnetic field, a cycloidal phase is obtained as displayed in Fig. 4.27B. As can be seen, $\boldsymbol{q}_\mathrm{h}$ aligns parallel to the tilt axis which is attributed to the interaction with the in-plane magnetic field that was discussed in the last chapter. The effect appears to be even stronger by a qualitative comparison of the obtained order. The overall signal to noise ratio of the magnetic contrast is superior to the Pt/Co/W sample. Upon magnetic field increase, the cycloidal phase transforms to isolated cycloidal stripes in a field polarized background as shown in Fig. 4.27C. With further increase of the magnetic field, a mixed Néel skyrmion/isolated cycloidal stripe phase is obtained (Fig. 4.27D) before an isolated skyrmion phase is finally

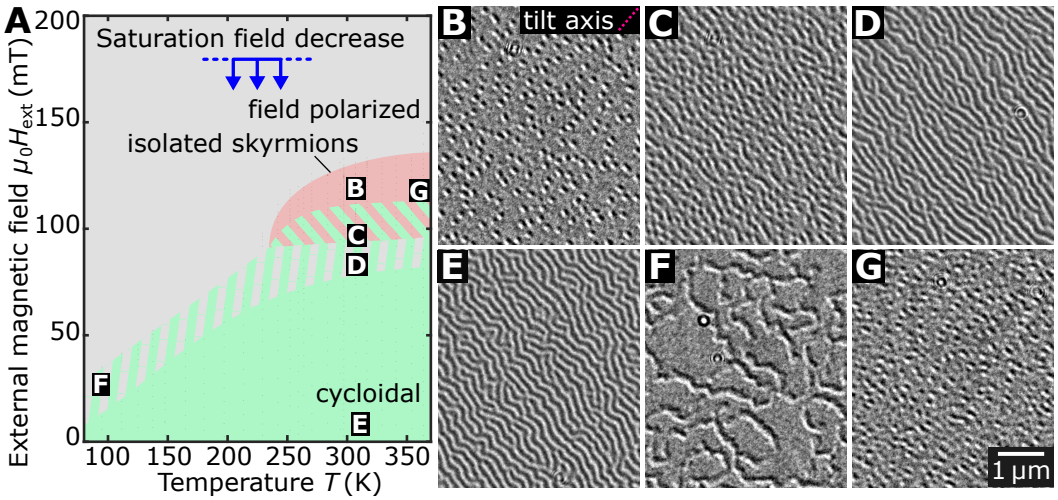

Fig. 4.28.: **(A)** Saturation field decrease phase diagram of the Pt/Co/Tb multilayer sample. At each indicated temperature, the sample is saturated and the external magnetic field is reduced to zero, while the present magnetic phase is tracked. The dots represent recorded Fresnel images. **(B)** Example image of the skyrmion phase, **(C)** cycloidal/field-polarized/skyrmion mixed, **(D)** cycloidal/field-polarized mixed and **(E)** cycloidal phase. **(F)** At lower temperatures, no skyrmion phase but an isolated cycloidal stripe phase is observed. **(G)** The cycloidal phase with less order as in the ZFI is also visible for low temperatures. The phase space positions of the example images are also indicated in the phase diagram. A median filter in a 3×3 neighborhood, polynomial background subtraction and a manual removal of dirt is applied to the example Fresnel LTEM images.

established at around 125 mT which is shown in Fig. 4.27E. Subsequently, the skyrmion number is further reduced up to a magnetic field value around 175 mT at room temperature. Beyond this limit, the field-polarized phase is obtained, showing no magnetic contrast.

At low temperatures ($\approx$110 K), the skyrmion count is drastically decreased which is shown in Fig. 4.27F. A more detailed investigation of the skyrmion count will be given later in this section. Compared to the case at room temperature, the cycloidal phase at zero-applied magnetic field is less ordered in terms of stripe continuity, which is shown in Fig. 4.27G and is in accordance with the findings of the previous section. The phase space locations of the example images are also indicated in the phase diagrams.

For the SFD phase diagram, the same saturation field of $H_{\mathrm{ext}} = 240\,\mathrm{mT}$ as in the last section is chosen. The resulting phase diagram is drawn in Fig. 4.28A. Again the general shape is similar to the SFD phase diagram of Pt/Co/W in Fig. 4.23A. Around room temperature, after the external magnetic field falls below a critical value of $\approx$130 mT, an isolated skyrmion phase is obtained as displayed in Fig. 4.28B. In contrast to the ZFI case, the skyrmions again show a clear elongation perpendicular to the tilt axis. Upon further magnetic field decrease, the magnetic texture transforms

to an isolated cycloid/skyrmion mixed phase (Fig. 4.28C) and afterwards to an isolated cycloid phase in a field-polarized background (Fig. 4.28D). Finally around 80 mT, a cycloidal phase is obtained which persists down to zero applied magnetic field (Fig. 4.28E). At 95 K, no skyrmion phase is observed, only an isolated cycloidal phase with low order is measured as displayed in Fig. 4.28F. The contrast indicates that the width of the cycloidal stripes is increased in comparison to the room temperature case. At large temperatures around 360 K, the skyrmion phase is still present, as shown in Fig. 4.28G. However, when comparing the contrast to an image at room temperature as e.g. in Fig. 4.28B, the image background around the clear skyrmion features is not homogeneous and shows an irregular magnetic contrast. This might indicate a temperature dependent change of the magnetic parameters and will be discussed later in more detail.

In the discussion of the ZFI phase diagram, the temperature dependence of the skyrmion density was already briefly mentioned. This behavior is now quantified with additional measurements. As the phase diagrams for the ZFI and SFD field-protocol vary so strongly, both methods are considered. First, the temperature dependence of the topological charge that emerges from the cycloidal phase is studied. The investigated phase space is highlighted in the ZFI phase diagram in Fig. 4.29A. Within the marked area, Fresnel LTEM images with a field of view of $6.1 \times 6.1\,\mu m^2$ are recorded. For each image, the total topological charge is determined. Due to the interface-DMI and the Néel skyrmion structure, it can be safely assumed that all the skyrmions have the same chirality, as multi-chiral bubbles are only investigated for the Bloch type with absent DMI [5]. With this assumption, the topological charge determination which is defined in Eq. (2.23) simplifies to the counting of visible skyrmions in the images. Note that also the isolated stripes that are sometimes present in the recorded images, have an absolute topological charge of one, as their spin structure is topologically equivalent to the skyrmion. Note that the sign of the topological charge cannot be determined using LTEM, as it is not sensitive to the Néel skyrmion wall. According to the last sections, the counting of skyrmions is conducted using an automatic local maximum finding algorithm in combination with a manual correction step for each image. In the 283 recorded images, 42 977 are identified this way. Due to temperature drift, the sample position changes for different temperature values and is also not perfectly constant during the magnetic field scans.

Fig. 4.29B shows the temperature dependence of the topological charge for different values of the externally-applied magnetic field. The measurement protocol begins in the cycloidal phase at zero-applied magnetic field and is increased to 118 mT at a rate of $1000\,mT\,s^{-1}$. After that, the field is further increased in steps of 6 mT at the same rate. At each step, an image is recorded. This field protocol

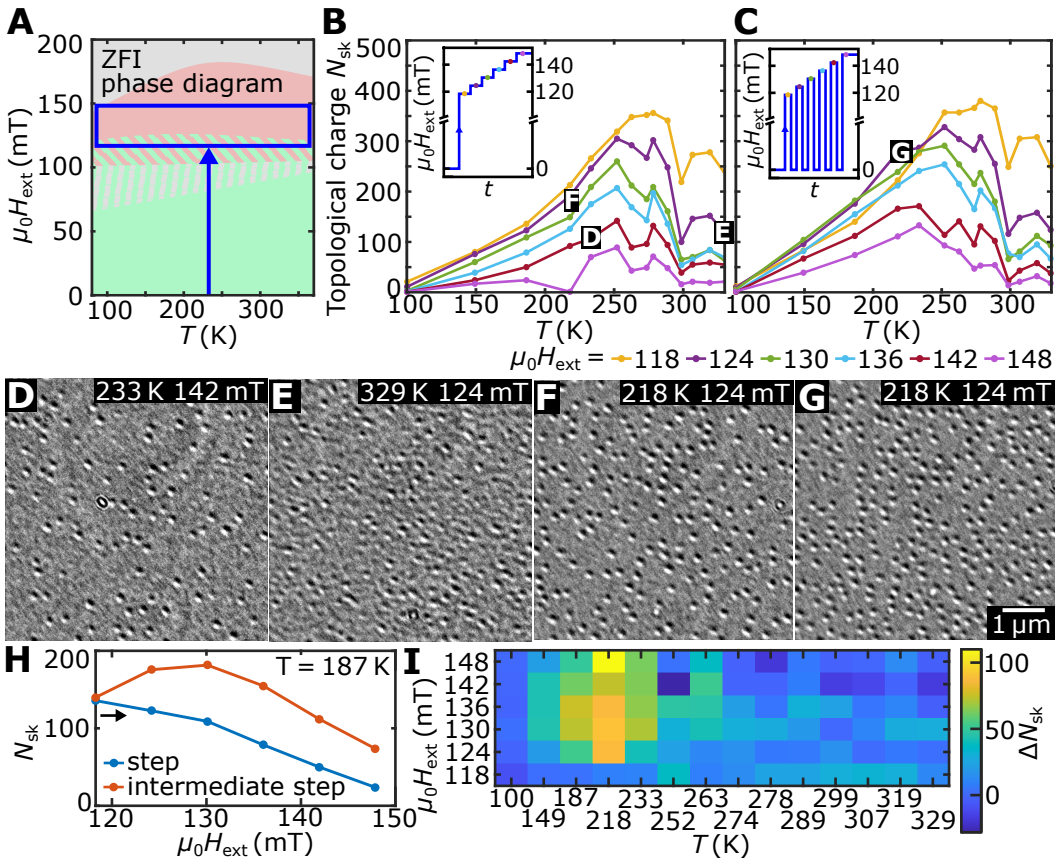

Fig. 4.29.: **(A)** Investigated phase space region for the topological charge measurements starting in the cycloidal phase. **(B)** Temperature and externally-applied magnetic field dependence of the topological charge for the step increase magnetic field protocol and the **(C)** intermediate step increase protocol. The field protocols are visualized in the insets. **(D)** Example Fresnel image of the skyrmion phase inside the first maximum and **(E)** the second maximum of the topological charge measurement. **(F)** Fresnel image resulting from the step increase field protocol compared to **(G)** the intermediate step field protocol for identical temperature and magnetic field. **(H)** Magnetic field scan of the topological charge for step increase and intermediate step increase field protocol at $T = 187\,\mathrm{K}$. **(I)** Topological charge difference of step increase and intermediate step increase field protocol for the whole investigated phase space region. A polynomial background subtraction and a 3×3 median filter is applied to the Fresnel images in (D-G)

is illustrated in the inset and is referred to as step increase. As expected from the description of the phase diagram, the topological charge decreases as the increasing externally-applied magnetic field leads to the annihilation of skyrmions at a constant temperature. From this, it becomes also directly clear that once there are no cycloidal stripes left, no further skyrmions appear, which again indicates that the skyrmions can only nucleate from the cycloidal stripes. Following the trend for a constant value of H_{ext}, a vanishing topological charge for lowest temperatures is obtained. The

value increases up to a maximum topological charge density of $9.5\,/\mu\mathrm{m}^2$ around 270 K for $\mu_0 H_{\mathrm{ext}} = 118\,\mathrm{mT}$.

Above that temperature, the skyrmion count decreases. However, a second maximum appears around 325 K. Although this is somewhat peculiar, signatures of the second maximum are visible for all magnetic field values and all four magnetic field protocols that will be shown. It is also present in a second measurement that is conducted on a different day at a different sample location. A hint concerning the second maximum can be found by the inspection of the respective LTEM images. Fig. 4.29D shows an LTEM image at $T = 233\,\mathrm{K}$ and $\mu_0 H_{\mathrm{ext}} = 142\,\mathrm{mT}$ and Fig. 4.29E shows one at $T = 329\,\mathrm{K}$ and $\mu_0 H_{\mathrm{ext}} = 124\,\mathrm{mT}$. The respective measured topological charge is indicated in Fig. 4.29B and is around 100 in both images. The first image lies within the first maximum of the topological charge data whereas the second one is found in the second maximum. Comparing the images, it is clear that the image background around the clear skyrmion signatures in Fig. 4.29D is smoother than the one in Fig. 4.29E, where a magnetic background modulation of the Fresnel intensity is visible. A closer inspection of the background shows that it is partly irregular but there are also some of the typical Néel skyrmion signatures with reduced intensity.

Without any further measurements, the reason for the modulated image background and the concomitant second peak in the topological charge measurement remains speculation. It could e.g. be caused by a temperature dependence of the magnetic parameters. A potential candidate for this is the uniaxial out-of-plane anisotropy, which is known to decrease with temperature for magnetic bubble hosting materials and forces the magnetization to align parallel to the sample plane at a certain critical temperature [5, 102, 218]. If there was a tendency for an in-plane alignment, it would be expected to be visible in an Fresnel LTEM image, as the technique is very sensitive to magnetic modulations parallel to the sample plane. Note that once the image background shows this inhomogeneity, the exact determination of the skyrmion count becomes slightly ambiguous. Here, only the skyrmion signatures with the same intensity as the ones at lower temperatures are counted. It should be noted that the weaker signatures could in principle also be skyrmions when considering the second maximum in the topological charge measurements.

The second magnetic field protocol is also started in the cycloidal phase. It is essentially equivalent to the step increase process, with the difference that after each magnetic field step, the field is reverted to zero such that the structure evolves directly from the cycloidal phase. This is depicted in the inset of Fig. 4.29C and is referred to as intermediate step increase. The temperature dependence of the topological charge measurement in Fig. 4.29C is qualitatively equal to the step increase case. However, the maximum skyrmion count for temperatures below 230 K is not found for the lowest magnetic field of 118 mT but for the intermediate values

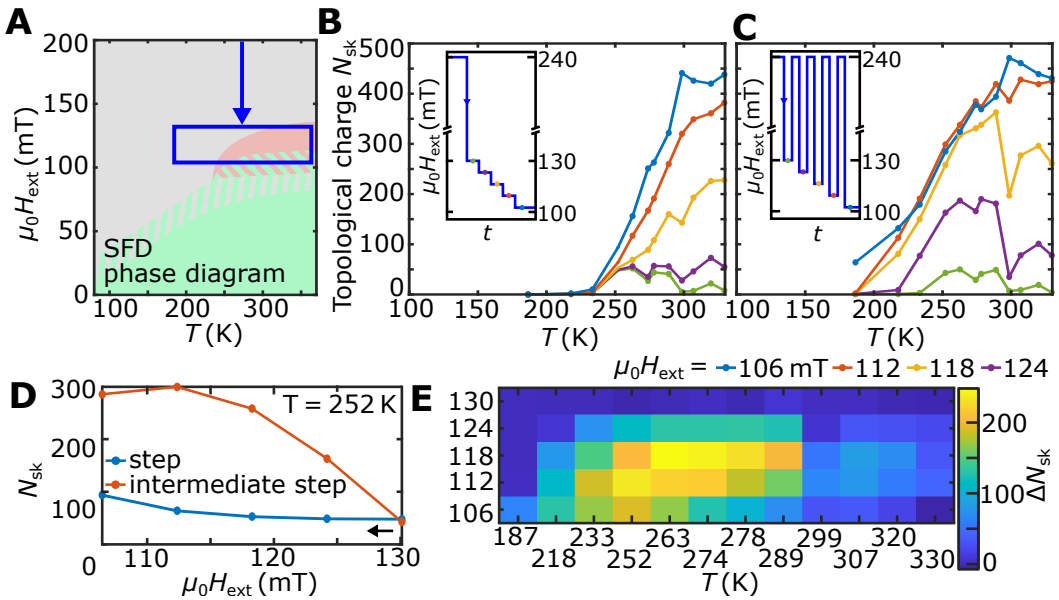

Fig. 4.30.: **(A)** Investigated phase space region for the topological charge measurements starting in the field-polarized phase. **(B)** Topological charge measurement for the step decrease magnetic field protocol and **(C)** the intermediate step decrease protocol. **(D)** Exemplary magnetic field scan of the topological charge for step decrease and intermediate step decrease field protocol at $T = 252\,\mathrm{K}$. **(E)** Topological charge difference of step decrease and intermediate step decrease field protocol for the whole investigated phase space region.

of 124 and 130 mT. In fact, the overall topological charge is increased compared to the step increase case. An example situation for this fact is shown in Figs. 4.29F, G. Both images are recorded at $T = 218\,\mathrm{K}$ and $\mu_0 H_{\mathrm{ext}} = 124\,\mathrm{mT}$. Nevertheless, Fig. 4.29G shows obviously more skyrmions as it is recorded with the intermediate step increase magnetic field protocol.

At $T = 187\,\mathrm{K}$, a field dependence of this discrepancy is further illustrated in Fig. 4.29H. For lowest magnetic field, the topological charge data agrees as the two field protocols are equivalent up to this point. Above that field, the two curves separate and roughly twice the skyrmion count is obtained for the intermediate step increase protocol. The temperature and magnetic field dependence of the total topological charge difference of the two magnetic field protocols is drawn in Fig. 4.29I. It shows a maximum around 220 K. Note that the temperature ticks are not equidistant. The discovery of this effect might turn out useful for applications where a large skyrmion count is desired.

A similar procedure is conducted for the skyrmion nucleation from the field-polarized phase at large externally-applied magnetic fields. Fig. 4.30A shows the SFD phase diagram and the investigated phase space region for the following topological charge measurements. The first field protocol investigated starts at a

saturation field of $\mu_0 H_{\mathrm{ext}} = 240\,\mathrm{mT}$. The field is then decreased to 130 mT where an isolated skyrmion phase is obtained. In complete analogy to the step increase field protocol, the field is then decreased in steps of 6 mT to 106 mT. Therefore, the field protocol is referred to as step decrease. It is displayed in the inset of Fig. 4.30B. The topological charge increases with temperature and reaches its maximum around 320 K. Indications for the second maximum are visible in the graphs recorded at lower magnetic field.

The second field protocol is also in complete analogy to the intermediate step increase protocol with the exception that the field is brought up to 240 mT at the intermediate steps instead of zero. Therefore, it is referred to as intermediate step decrease. It is depicted in the inset of Fig. 4.30C. Again, the qualitative shapes of the respective topological charge dependence are equal to the step decrease protocol, however the skyrmion count is drastically increased. This can be also seen from the magnetic field scan at $T = 252\,\mathrm{K}$ in Fig. 4.30D. Here, the topological charge is around three times as large for the intermediate step magnetic field protocol. The topological number difference for the two protocols is plotted in Fig. 4.30E. The maximum difference is found around 250 K.

An issue arises during the measurement using the intermediate step decrease. It turns out that for a decreasing field step larger than $50\,\mathrm{mT}$, the magnetic field undershoots the target field value. In the measured range, the magnetic field drops 50 mT below the target value for a duration of 60 ms. This flaw in the electronics of the objective lens power supply of the TEM is irrelevant for the optics and is therefore not addressed by the manufacturer. This behavior only occurs during the decrease of the magnetic field but might affect the absolute skyrmion numbers in Fig. 4.30C.

Finally, DPC measurements on the isolated Néel skyrmion phase at room temperature are conducted. The sample tilt of 20° is maintained and the external magnetic field is increased from zero to $\mu_0 H_{\mathrm{ext}} = 120\,\mathrm{mT}$. The electron beam deflection is measured using the annular segmented detector. The electron beam is scanned over the sample within a field of view of 11.1 $\mu\mathrm{m}^2$. Fig. 4.31A shows the beam deflection signal in x- and y-direction DPC_x and DPC_y. In both directions, the intensity signature of around 30 skyrmions is visible. As expected, the intensity in x-direction is larger than in y-direction. In fact, these are the first reported DPC measurements on Néel skyrmions that match the theoretical expectations [155]. To showcase the measured contrast, the average skyrmion signature is calculated from the 14 skyrmions highlighted with the yellow boxes. The resulting skyrmion intensities are shown on the right side of Fig. 4.31B. In the bottom row, the beam deflection is represented by color. Under the assumption of a homogeneous ronchigram, the DPC_x and DPC_y signal is proportional to the gradient of the electron phase. As a

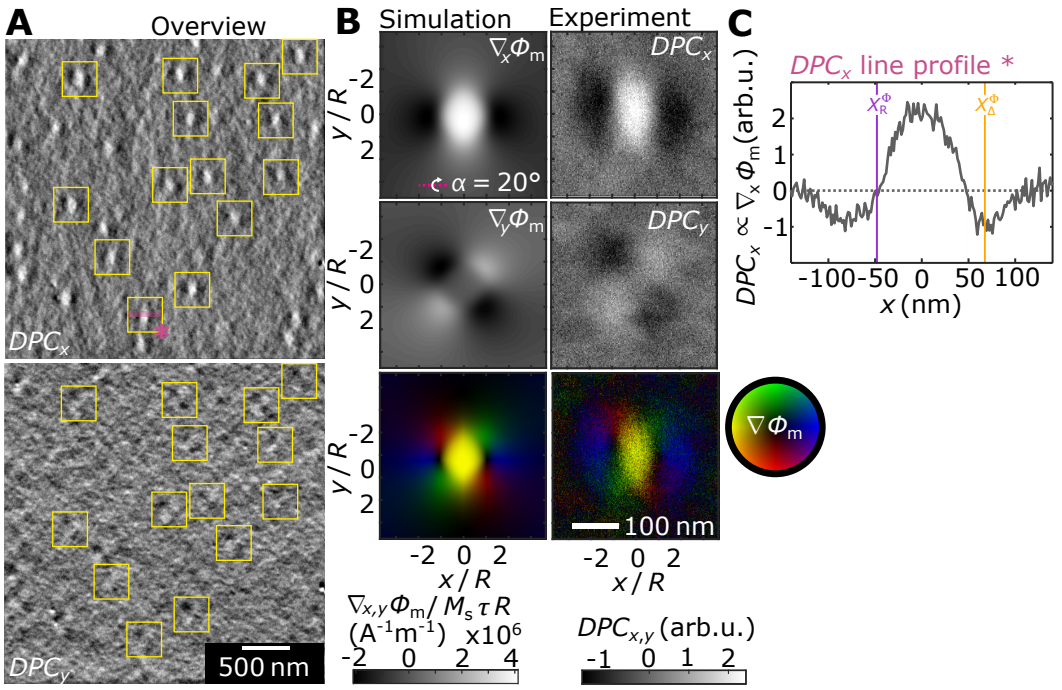

Fig. 4.31.: DPC measurements on the Pt/Co/Tb sample. **(A)** The two components of the measured beam deflection of the skyrmion phase in the Pt/Co/Tb sample. **(B)** Simulated Néel skyrmion contrast (left) compared to the experimental data (right), which is obtained by taking the average skyrmion intensity of the marked skyrmions in (A). In the bottom row, the deflection is represented by color as indicated in the color wheel. **(C)** Image profile through the center of the marked skyrmion in the DPC_x signal in (A). The parameters X_R^ϕ and X_Δ^ϕ are highlighted. To enhance the visibility of skyrmions, a polynomial background subtraction, a 3×3 median filter and a Gaussian filter with $\sigma = 2\,\mathrm{px}$ is applied to (A). The line profile in (C) relies on the raw data.

reminder, the simulated DPC contrast of a Néel skyrmion with the experimentally measured structural skyrmion parameters (given later) is displayed on the left. It is in good agreement with the measured data.

Fig. 4.31C shows a horizontal image profile of the DPC_x signal across the center of the highlighted skyrmion in Fig. 4.31A. Using the relations from section 4.2.2, the structural skyrmion parameters can be obtained. In order to do so, the zero deflection value must be manually shifted such that the regions around the skyrmions show a zero-phase gradient, as discussed. Assuming $\boldsymbol{DPC} \propto \nabla_\perp \phi_\mathrm{m}$, the phase maximum at X_R^ϕ is found at the zero-intersection of the line profile. The position of the inflection point of the phase X_Δ^ϕ on the other hand is found at the minimum of DPC_x, as highlighted in the profile. Using Eqs. (4.41) and (4.42), a skyrmion radius of $R = (48 \pm 3)\,\mathrm{nm}$ and a wall width of $\Delta = (84 \pm 27)\,\mathrm{nm}$ is found.

This result holds for probe sizes that are much smaller than the actual skyrmion radius. In the experiment, an aperture of $70\,\mu\mathrm{m}$ led to a rather low resolution

of 25 nm. This value is determined by checking at which frequency the square modulus of the FT of the image approaches zero. From this, the probe diameter is expected to be around 50 nm. As explained in section 4.2.3, the model does not give precise results for such large probe sizes. In this case, the correction terms given in Fig. 4.17C have to be applied. With them, a 13 % smaller skyrmion radius of $R = (42 \pm 3)\,\mathrm{nm}$ and a domain wall width of $(72 \pm 27)\,\mathrm{nm}$ is obtained.

5 Summary

In this thesis, static and dynamic properties of magnetic skyrmions and chiral magnetic textures are investigated. Two experimental techniques are used: The first one is REXS which probes magnetically modulated structures in reciprocal space. For the first time, this technique is combined with FMR to detect magnetic excitations of the chiral system. The second experimental technique is Fresnel and DPC LTEM which produces real space images of the skyrmions and the various other magnetic structures.

The first experimental part of the thesis covers reciprocal space imaging of the magnetically modulated phases of bulk single-crystalline (001)-Cu_2OSeO_3 by means of REXS in combination with FMR measurements. Experimental reciprocal space maps of the helical, conical, skyrmion and LT-skyrmion phase are shown. Before the actual FMR measurements are discussed, the expected skyrmion eigenmodes - breathing, clockwise and counter-clockwise gyrating modes - are extracted from micromagnetic simulations. The resonance frequencies of the helical, conical, field-polarized and skyrmion phase are then experimentally measured by tracking the scattered X-ray intensity of the Bragg peak as well as its satellite peaks under excitation by means of an oscillating external magnetic field. The resulting resonance frequencies and their dependence on the externally applied magnetic field are in good agreement with conventional FMR experiments performed on equivalent crystals.

These results are the foundation of a novel technique that is called REXS-FMR [51]. It inherits the element-specific character of REXS and further allows the selection of the FMR-signal from a specific magnetic phase. This is particularly useful in systems that show complex magnetic environments like phase-coexistence as in the case of the novel LT skyrmion phase in Cu_2OSeO_3 which is always accompanied by the tilted conical phase [117, 118]. Further examples for this are the multidomain skyrmion states in lacunar spinels [74, 151, 152] or the glassy skyrmion textures in Co-Mn-Zn compounds [24, 153, 154].

Still, the full potential of REXS-FMR is not yet reached. A logical next step is to perform stroboscopic measurements, i.e. that the microwave excitation field is phase-coupled to the probing X-ray pulses. An additional analysis of the simulations in chapter 3.3.1 shows that the resonant oscillation of the skyrmion magnetization exhibits different phase shifts with respect to the microwave excitation field depen-

dent on the driven mode. This means that during the excitation of the breathing mode, an in-phase oscillation of all six satellite spots is expected. In contrast to that, when a gyrating mode is excited, the satellite peak intensity is expected to be phase-shifted by 120° with respect to each other. From such an experiment, the skyrmion modes could be detected unambiguously, without the need of assisting theoretical calculations.

The second experimental part of the thesis concerns real-space imaging of skyrmions by means of LTEM. A rich qualitative overview of the expected Fresnel and DPC LTEM image contrasts of the various magnetic phases that are investigated in this thesis is given. The electron phase that is introduced by the magnetic structure of arbitrary Bloch and Néel skyrmions is calculated and related to the original skyrmion structure. This gives phenomenological strategies for the extraction of the skyrmion spin structure from an electron phase measurement. Although these relations are in principle applicable to all LTEM techniques, it is necessary to further consider the effect of electron-optical aberrations for each Lorentz technique separately. This is performed explicitly for DPC LTEM, which leads to the introduction of correction terms [155].

Then, LTEM measurements of (001)-Cu_2OSeO_3 are presented. Phase diagrams are recorded which show the commonly expected phases. However, they lack the observation of an LT-skyrmion phase, which is attributed to the low thickness of the sample which is in the order of the helical modulation length λ_h of Cu_2OSeO_3 [52, 54]. At a temperature of $T = 13\,\mathrm{K}$, an externally applied magnetic field dependence of the skyrmion-skyrmion interaction is found. This is in accordance with reports on FeGe and is attributed to a surrounding conical background of the skyrmions [220]. Finally, DPC measurements of the helical and skyrmion lattice phase are presented and show traces of a hexagonal distortion of the skyrmion lattice.

Further, LTEM measurements of two room-temperature skyrmion hosting multilayer samples are shown. The first one is a Pt/Co/W system [67]. Measured phase diagrams show that the skyrmions appear as relics of the cycloidal phase upon magnetic field increase from zero. They feature a skyrmion phase within the whole temperature range of around 100 to 360 K. A process that allows the alignment of isolated cycloidal stripes and the cycloidal phase with an in-plane magnetic field is found. Further, an independence of the phase diagram with respect to sample tilt up to 20° away from the externally applied magnetic field direction is found. In addition to that, it is shown that the magnetic structures in the sample are subject to pinning. This affects the system during the skyrmion generation from an initial cycloidal as well as an initial field-polarized phase. Further, a tilt and defocus dependent simulation of the Fresnel skyrmion contrast is presented which is used to estimate the actual skyrmion size.

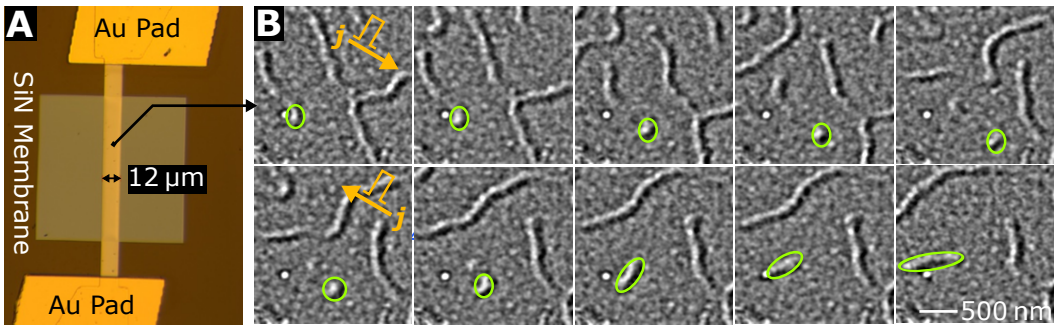

Fig. 5.1.: **(A)** Structured Pt/Co/Tb multilayer strip with gold contacts. **(B)** LTEM images of isolated cycloids pushed by electrical current pulses whose polarity is reversed in the bottom row.

The second sample is a Pt/Co/Tb multilayer system. The measured phase diagrams are qualitatively equivalent to the Pt/Co/W sample. A topological charge measurement shows a maximum skyrmion count just below room temperature. It is found that the total topological charge density can be greatly increased (by factors larger than 2) by approaching the final external magnetic field in one step opposed to several small steps. Finally, first DPC measurements on Néel skyrmions that match the theoretically predicted contrast are presented. From this data, the skyrmion structure is extracted, showcasing an application of the calculations presented in the beginning of the chapter.

The TEM part gives a broad overview of potential contrast signatures that can be encountered when measuring Néel or Bloch skyrmion hosting materials. It also provides a method to extract the skyrmion parameters from an LTEM measurement. This link is key e.g. for comparative LTEM studies in material research that aims for engineered skyrmion magnetization structures. This is clearly an important aspect considering that LTEM became one of the most import tools for real-space imaging of magnetic skyrmions. A next logical step that goes beyond the imaging of static structures is the in-situ TEM observation of the current driven motion of skyrmions. Preliminary work on this has already been conducted. Fig. 5.1A shows a structured Pt/Co/Tb multilayer stack featuring a contactable microstrip across a SiN membrane, which was fabricated by Yiming Sun[1]. In Fig. 5.1B, images of an isolated cycloidal phase at $H_{\mathrm{ext}} = 30\,\mathrm{mT}$ are shown. Between each snapshot, an average of 16 electrical current pulses with a current density of $<7 \times 10^{10}\,\mathrm{A\,m^{-2}}$ and a pulse length of 20 ns is applied along the indicated direction. Clear unidirectional shifts of the cycloids are visible. These shifts are opposite upon current polarity reversal, as shown in the bottom row. Once issues like pinning can be further reduced, this yields a large potential for future applications.

[1]Fert Beijing Institute, BDBC, School of Electronic and Information Engineering, Beihang University, Beijing, 100191, China.

Appendix

A

A.1 Magnetization extraction from REXS Bragg intensity

To extract the actual magnetization profile from the externally applied magnetic field dependence of the Bragg intensity, the theoretical description by van der Laan et al. is applied [121].

The scattering cross section is (Eq. (15) in Ref. [121])

$$I(\Delta\boldsymbol{k}) = I_{\mathrm{c}}(\Delta\boldsymbol{k}) + I_{\mathrm{m}}(\Delta\boldsymbol{k}) + I_{\mathrm{i}}(\Delta\boldsymbol{k}) \; . \tag{A.1}$$

Here $\Delta\boldsymbol{k} = \boldsymbol{k}_{\mathrm{f}} - \boldsymbol{k}_{\mathrm{i}}$, with incident wave vector $\boldsymbol{k}_{\mathrm{i}}$ and final wave vector $\boldsymbol{k}_{\mathrm{f}}$, alongside their unit vectors $\hat{\boldsymbol{k}}_{\mathrm{i}}$ and $\hat{\boldsymbol{k}}_{\mathrm{f}}$. The cross-section consists of three contributions. First is charge scattering which is given by (Eq. (16) in Ref. [121])

$$I_{\mathrm{c}}(\Delta\boldsymbol{k}) = \frac{1}{2}\left|\tilde{f}_0\tilde{\rho}\right|^2 \left[P_\sigma + P_\pi \left|\hat{\boldsymbol{k}}_{\mathrm{f}} \cdot \hat{\boldsymbol{k}}_{\mathrm{i}}\right|^2\right] \; , \tag{A.2}$$

with the Fourier transform of the charge density $\tilde{\rho}$ and the monopole contribution of the energy dependent resonance amplitude $\tilde{f}_0$. Further $P_\sigma = P_0 + P_1$ and $P_\pi = P_0 - P_1$ with the Poincaré vector which is given by $\boldsymbol{P}^{\mathsf{T}} = (1, 0, 0, \pm 1)$ for circularly polarized light which is used in the experiment. The contribution of I_{c} is independent of $\boldsymbol{M}$ (and its Fourier transform $\tilde{\boldsymbol{M}}$.

The second contribution I_{m} describes pure magnetic scattering. For $\tilde{\boldsymbol{M}}$ inside the scattering ($\boldsymbol{k}_{\mathrm{i}}$-$\boldsymbol{k}_{\mathrm{f}}$)-plane, it can be written as (Eq. (19) in Ref. [121])

$$I_{\mathrm{m}}(\Delta\boldsymbol{k}, \tilde{\boldsymbol{M}}) = \frac{1}{2}\left|\tilde{f}_1\right|^2 \left[P_\sigma \left|\hat{\boldsymbol{k}}_{\mathrm{f}} \cdot \tilde{\boldsymbol{M}}\right|^2 + P_\pi \left|\hat{\boldsymbol{k}}_{\mathrm{i}} \cdot \tilde{\boldsymbol{M}}\right|^2\right] \; . \tag{A.3}$$

Here, $\tilde{f}_1$ is the Fourier transform of the magnetic dipolar contribution to the energy dependent resonance amplitude.

Third is the interference term between charge and magnetic scattering. Again for $\tilde{\boldsymbol{M}}$ inside the scattering plane and circularly polarized light, it is given by (Eq. (21) in Ref. [121])

$$I_{\mathrm{i}}(\Delta\boldsymbol{k}, \tilde{\boldsymbol{M}}) = P_3 \,\mathrm{Re}\left[\tilde{f}_0^* \tilde{\rho}^* \tilde{f}_1^* \left(\hat{\boldsymbol{k}}_{\mathrm{i}} \cdot \tilde{\boldsymbol{M}} + (\hat{\boldsymbol{k}}_{\mathrm{f}} \cdot \tilde{\boldsymbol{M}})(\hat{\boldsymbol{k}}_{\mathrm{f}} \cdot \hat{\boldsymbol{k}}_{\mathrm{i}})\right)\right] \; . \tag{A.4}$$

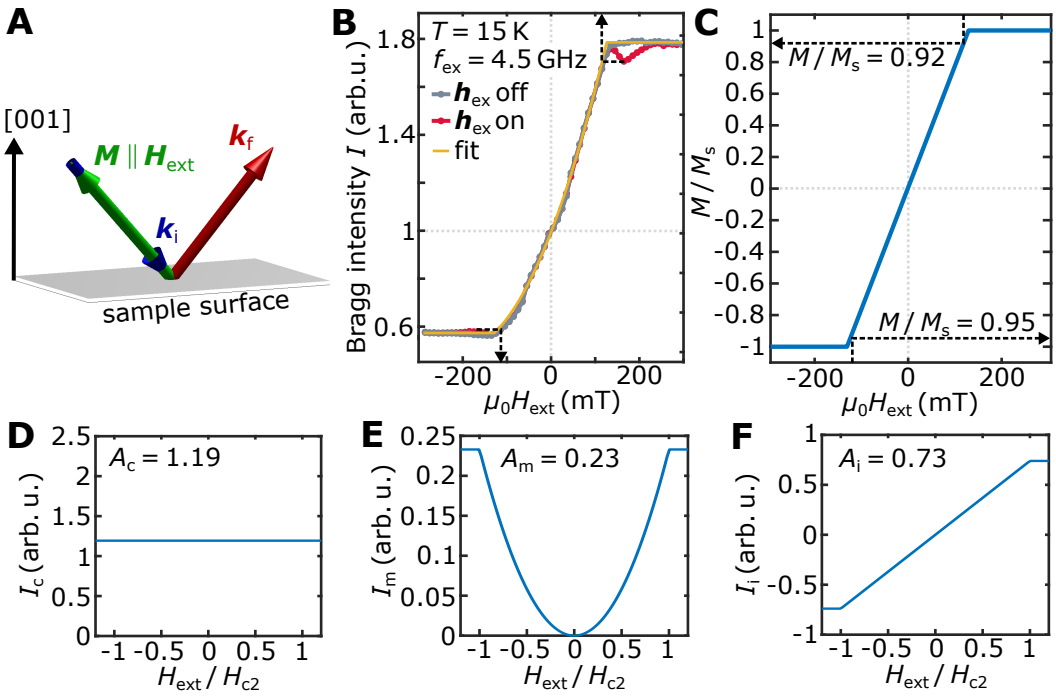

Fig. A.1.: Extraction of magnetization trace from magnetic field dependence of Bragg scattering intensity. **(A)** Scattering condition. **(B)** Bragg intensity with externally applied magnetic field for excitation on and off (see main text) and theoretical fit. **(C)** Extracted magnetization trace with expected values at resonance. **(D)** Charge, **(E)** magnetic, **(F)** interference scattering contribution and parameters of the fit.

In the experimental situation described in the main text, the magnetization and externally applied magnetic field is parallel to $\boldsymbol{k}_\mathrm{i}$. The wave vectors $\boldsymbol{k}_\mathrm{i}$ and $\boldsymbol{k}_\mathrm{f}$ are fixed to the (001)-Bragg condition at the Cu L_2-edge with $2\theta = 95.8°$. A sketch of the scattering condition is shown in Fig. A.1A. For circularly polarized light $P_\sigma = P_\pi = 1$, $P_3 = \pm 1$ and by using the substitutions $A_\mathrm{c} = I_\mathrm{c}$, $A_\mathrm{m} = \frac{1}{2}\left|\tilde{f}_1\right|^2$ and $A_\mathrm{i} = \mathrm{Re}(\tilde{f}_0^* \tilde{\rho}^* \tilde{f}_1^*)$, Eq. (A.1) can be rewritten to

$$I(\tilde{\boldsymbol{M}}) = A_\mathrm{c} + A_\mathrm{m}\left(\left|\hat{\boldsymbol{k}}_\mathrm{f}\cdot\tilde{\boldsymbol{M}}\right|^2 + \left|\hat{\boldsymbol{k}}_\mathrm{i}\cdot\tilde{\boldsymbol{M}}\right|^2\right) \pm A_\mathrm{i}\left(\hat{\boldsymbol{k}}_\mathrm{i}\cdot\tilde{\boldsymbol{M}} + (\hat{\boldsymbol{k}}_\mathrm{f}\cdot\tilde{\boldsymbol{M}})(\hat{\boldsymbol{k}}_\mathrm{f}\cdot\hat{\boldsymbol{k}}_\mathrm{i})\right) \quad \text{(A.5)}$$

The assumed net magnetization results from Eq. (2.21)

$$\boldsymbol{M}(\boldsymbol{H}_\mathrm{ext}) = \begin{cases} M_\mathrm{s}\boldsymbol{H}_\mathrm{ext}/H_\mathrm{c2} \text{for } H_\mathrm{ext} < H_\mathrm{c2} \\ M_\mathrm{s}\boldsymbol{H}_\mathrm{ext}/H_\mathrm{ext} \text{ otherwise} \end{cases} . \quad \text{(A.6)}$$

The experimental Bragg intensity dependence in Fig. 3.8A is fitted with Eq. (A.5), with the parameters A_c, A_m, A_i and H_c2. The result is displayed in Fig. A.1B. Using Eq. A.6 with the fit paramters, the expected magnetization trace is extracted which

is shown in Fig. A.1C. To retrieve the net reduction of $\boldsymbol{M}$ in resonance, the field values within the linear range in Fig. A.1B that match the reduced intensities at the resonance features are determined. Finding the respective value for M in Fig. A.1C gives the expected reduction of $\boldsymbol{M}$ in resonance. This process is indicated by the dashed arrows. A mean value of $\Delta M/M_\mathrm{s} \approx 6.5\,\%$ is obtained. The individual contributions of charge, magnetic and interference scattering to the fit are shown in Fig. A.1D-F.

A.2 Electron momentum transfer measurement by DPC for a magnetic sample

The calculation in this chapter is based on the work of Müller et al., adapted for magnetic fields [183]. The starting point is Ehrenfest's theorem [231]

$$\frac{\mathrm{d}}{\mathrm{d}t}\langle \boldsymbol{p}\rangle = \frac{1}{\mathrm{i}\hbar}\left\langle \left[\hat{H},\boldsymbol{p}\right]\right\rangle + \left\langle \frac{\partial \boldsymbol{p}}{\partial t}\right\rangle \,, \tag{A.7}$$

with the expectation value of the momentum operator $\langle \boldsymbol{p}\rangle$. For an electron in the magnetic vector potential $\boldsymbol{A}$, the Hamilton operator is given by $\hat{H} = \frac{1}{2m_\mathrm{e}}\left(\boldsymbol{p} + \frac{e}{c}\boldsymbol{A}\right)^2$. Plugging in the commutator $\left[\hat{H},\boldsymbol{p}\right]$, one obtains

$$\frac{\mathrm{d}}{\mathrm{d}t}\langle \boldsymbol{p}\rangle = -\frac{e}{2}\left\langle (\boldsymbol{v}\times\boldsymbol{B} - \boldsymbol{B}\times\boldsymbol{v})\right\rangle \,, \tag{A.8}$$

with the velocity operator $\boldsymbol{v}$ and the magnetic induction operator $\boldsymbol{B}$. Assuming that the electron velocity along the optical axis v_z is approximately constant and $B_z = 0$, the change of lateral momentum $\boldsymbol{p}_\perp$ can be written as

$$\frac{\mathrm{d}}{\mathrm{d}t}\langle \boldsymbol{p}_\perp\rangle = -ev_z\left[\langle B_y\rangle\,\hat{\boldsymbol{x}} + \langle B_x\rangle\,\hat{\boldsymbol{y}}\right] \,. \tag{A.9}$$

The expectation value of $\langle \boldsymbol{B}_\perp(z)\rangle = \langle \Psi_\mathrm{probe}(z)\,|\boldsymbol{B}_\perp(z)|\,\Psi_\mathrm{probe}(z)\rangle$ at some depth z, is evaluated using the wave-function of the electron probe Ψ_probe. Substituting $\mathrm{d}t = \mathrm{d}z/v_z$, this gives

$$\langle \boldsymbol{p}_\perp\rangle = -e\iint I_\mathrm{probe}(\boldsymbol{r}_\perp,z)\left[B_y(\boldsymbol{r}_\perp,z)\hat{\boldsymbol{x}} + B_x(\boldsymbol{r}_\perp,z)\hat{\boldsymbol{y}}\right]\,\mathrm{d}z\,\mathrm{d}r_\perp \,. \tag{A.10}$$

Dropping the probe's z-dependence

$$I_\mathrm{probe}(\boldsymbol{r}_\perp,z) \approx I_\mathrm{probe}(\boldsymbol{r}_\perp,0) \,, \tag{A.11}$$

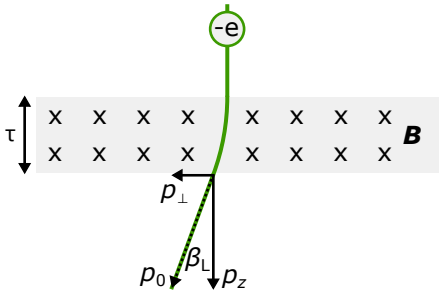

Fig. A.2.: Classical consideration of the generation of lateral electron momentum during its traversal through a region (gray) with finite magnetic induction.

which only holds for thin specimens (around 1 to 2 nm [183]) and defining the average projected magnetic field

$$\boldsymbol{B}_\perp^{\mathrm{proj}}(\boldsymbol{r}_\perp) = \frac{1}{\tau}\int \boldsymbol{B}_\perp^{\mathrm{proj}}(\boldsymbol{r}_\perp, z)\,\mathrm{d}z\ , \tag{A.12}$$

equation 4.29 of the main text is finally obtained and is repeated here:

$$-\frac{1}{e\tau}\langle \boldsymbol{p}_\perp \rangle = \left[B_y^{\mathrm{proj}}(\boldsymbol{r}_\perp)\hat{\boldsymbol{x}} + B_x^{\mathrm{proj}}(\boldsymbol{r}_\perp)\hat{\boldsymbol{y}}\right] \otimes I_{\mathrm{probe}}(\boldsymbol{r}_\perp)\ . \tag{A.13}$$

This result is similar to the classical result which is now briefly shown. Assuming the situation that is displayed in Fig. A.2, the lateral momentum of the electron after it is transmitted through the region with finite magnetic induction is given by

$$p_\perp = p_0 \sin(\beta_\mathrm{L}) \approx p_0 \beta_\mathrm{L}\ . \tag{A.14}$$

Here, p_0 is the initial absolute electron momentum and $\beta_\mathrm{L} = e\lambda_\mathrm{e} B\tau/h$ is the electron deflection angle given in Eq. (4.2). As $\beta_\mathrm{L} \ll 1°$, the small-angle approximation is valid. Using $\lambda_\mathrm{e} = h/p_0$, Eq. (A.14) can be rewritten to

$$\frac{1}{e\tau}p_\perp = B\ , \tag{A.15}$$

which is a classical analogue to Eq. (A.13).

A.3 Proof of zero magnetic electron phase from a cycloid and Néel skyrmion without sample tilt

First, it is shown that a cycloidal spin structure does not produce an electron phase under normal incidence. A cycloidal spin structure with $\boldsymbol{q}_\mathrm{h} \parallel \hat{\boldsymbol{x}}$ can be written as

$$\boldsymbol{m} = \cos\left(\frac{2\pi x}{L_x}\right)\hat{\boldsymbol{x}} + \sin\left(\frac{2\pi x}{L_x}\right)\hat{\boldsymbol{z}}\ . \tag{A.16}$$

It can be shown that $\boldsymbol{M}_{mn}$ from Eq. 4.8 is zero except for $n = 0$ and $m = \pm 1$. $\boldsymbol{M}_{\pm 10}$ is then given by

$$\boldsymbol{M}_{\pm 10} = 0.5\,\hat{\boldsymbol{x}} \pm \mathrm{i}0.5\,\hat{\boldsymbol{z}}\ . \tag{A.17}$$

Further is $\boldsymbol{k}_{\pm 10} = \pm\frac{1}{L_x}\hat{\boldsymbol{x}}$, $\hat{\boldsymbol{p}} = \hat{\boldsymbol{z}}$ (normal incidence) and $G_p(\tau\boldsymbol{k}_{\pm 10}) = 1$. Plugging this into Eq. 4.6 one sees that $\boldsymbol{k}_{\pm 10} \times \hat{\boldsymbol{z}} = \pm\frac{1}{L_x}\hat{\boldsymbol{y}}$ and $\hat{\boldsymbol{p}} \times [\hat{\boldsymbol{p}} \times \boldsymbol{M}_{\pm 10}] = \mp 0.5\hat{\boldsymbol{x}}$. As the scalar product $\hat{\boldsymbol{x}} \cdot \hat{\boldsymbol{y}} = 0$, the whole terms become zero and $\phi_\mathrm{m} = 0$.

To show it for the Néel skyrmion an analytical solution of Eq. 4.6 is impossible or at least very tedious. Rather, Eq. 4.31 is used. The skyrmion spin structure is given in Eq. 4.33. The substitutions $\sin[\theta(r)] = f(r)$ and $\sin[\theta(r)] = g(r)$ are made which gives

$$\boldsymbol{m}(r,\varphi) = f(r)\cos(\varphi + \psi)\,\hat{\boldsymbol{x}} + f(r)\sin(\varphi + \psi)\,\hat{\boldsymbol{y}} + g(r)\,\hat{\boldsymbol{z}}\ . \tag{A.18}$$

For now the helicity $\psi = 0$, which gives a Néel skyrmion but the result also holds for the other chirality $\psi = \pi/2$. The magnetization can be transformed to a polar coordinate system which gives

$$\boldsymbol{m}(r) = f(r)\hat{\boldsymbol{r}} + g(r)\,\hat{\boldsymbol{z}}\ . \tag{A.19}$$

In Eq. 4.31, the z-component of the curl of the magnetization needs to be calculated, which can be expressed using the curl in polar coordinates

$$\hat{\boldsymbol{z}} \cdot \nabla \times \boldsymbol{m} = \frac{1}{r}\left[\frac{\partial(r m_\varphi)}{\partial r} - \frac{\partial m_r}{\partial \varphi}\right] \overset{\text{A.19}}{=} 0\ , \tag{A.20}$$

which is zero and gives gives $\phi_\mathrm{m} = 0$.

A.4 Verification of the magnetic electron phase algorithm

In this section, the calculated phase of the implementation of Mansuripur's technique is verified. For this, the equivalence of the code written in this work with some examples given in the original work is checked. The validity in terms of a comparison to experimental data is deduced from Mansuripur's manuscript [173].

The first magnetic example structure are two side-by-side walls with in-plane magnetization. The domain walls are of Néel type. Such a structure is also called head-to-head or tail-to-tail walls, as the magnetization vectors in the uniform regions face each other. Fig. A.3A shows the spin structure (top) and a line profile of the calculated phase along x-direction (bottom). Next to it in Fig. A.3B, the result of this

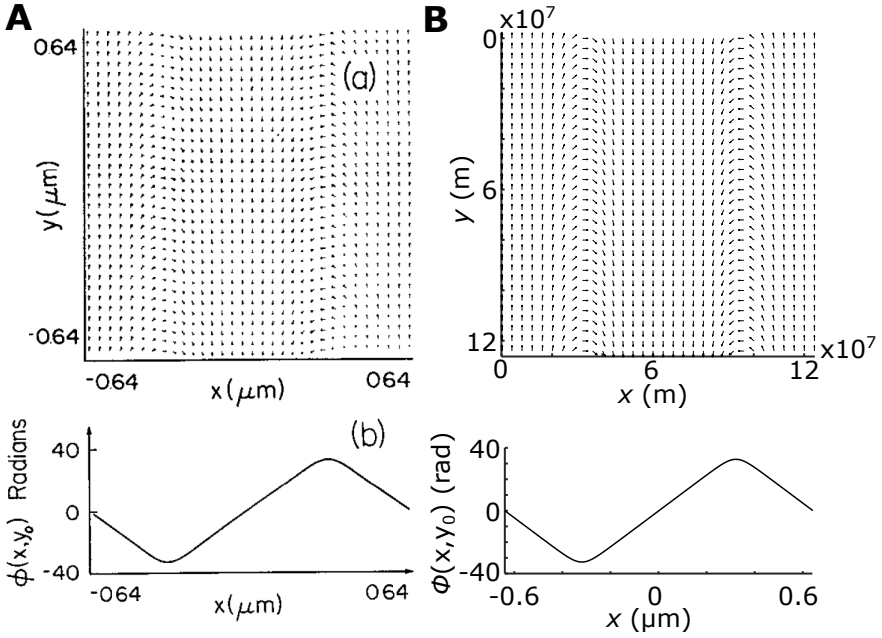

Fig. A.3.: Verification of the phase calculation algorithm example 1. **(A)** Spin structure and horizontal phase profile taken from the original work [173]. **(B)** Spin structure and horizontal phase profile from the implementation of this work.

work's implementation is shown and qualitatively matches very well. Fortunately, also quantitative, the phase change is identical.

As the first example can be reduced to a 1D problem, a second magnetic sample structure is shown in A.4A (left). It is the same magnetic structure that is however cut off in horizontal directions at the top and bottom. This is then called a narrow track. On the right, a contour plot, as well as a 3D surface plot of the calculated phase is shown. The phase variation is non-zero outside of the sample, which is attributed to magnetostatic stray fields. These results again qualitatively match the results obtained using the algorithm from this work very well, as can be seen in Fig. A.4B. For this case, Mansuripur actually gives the maximum and minimum phase value which is $\pm 16.65\,\mathrm{rad}$. Taking into account the reverse engineering that is neccessary to reconstruct the sample's track dimensions, the obtained maximum phase values of $\pm 16.7\,\mathrm{rad}$ matches perfectly.

Beside the two shown cases, the examples B and E of the original work are also compared, but are not shown here.

Below, the minimal matlab code is found. It expects a quadratic magnetization grid with $\boldsymbol{m} = (m_x, m_y, m_z)$, the saturation magnetization M_s, the three member array $\boldsymbol{p} = (p_x, p_y, p_z)$ that holds the incident electron beam vector and the grid spacings dx, dy and dz. Note that there exists a similar implementation by Walton et al., however it turned out to yield errors, which is why an own implementation

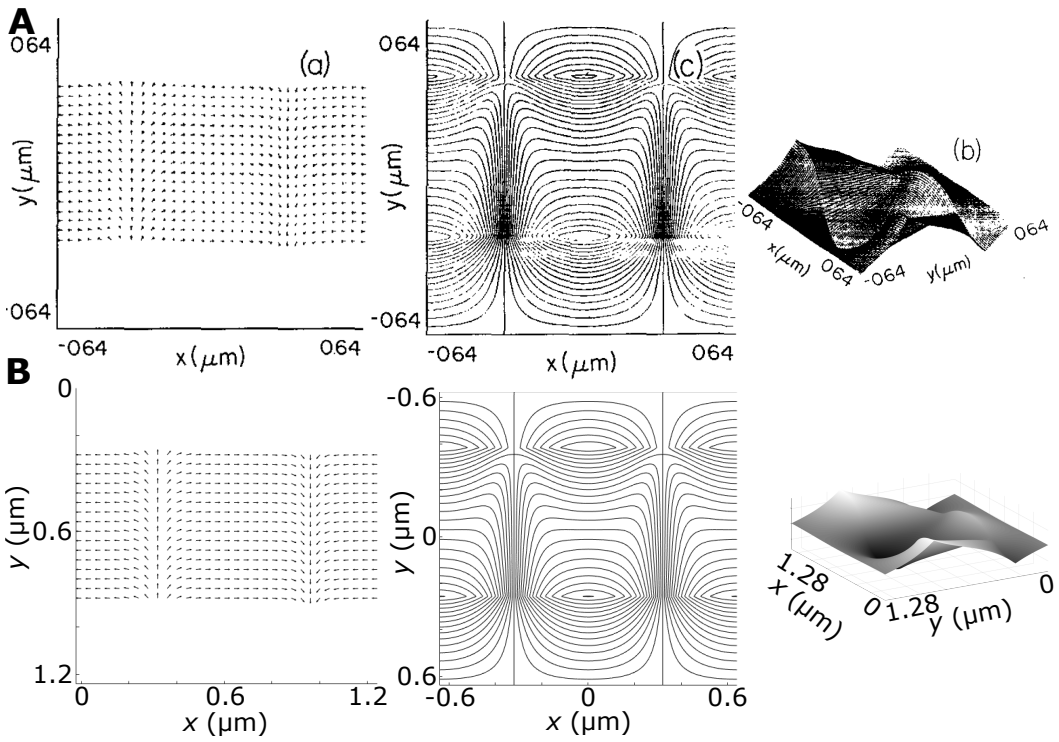

Fig. A.4.: Verification of the phase calculation algorithm example 2. **(A)** Spin structure and contour as well as 3D plot of the phase taken from the original work [173]. **(B)** Spin structure and contour as well as 3D plot of the phase from the implementation of this work.

based on the Mansuripur algorithm is chosen [209]. Another one was made by Haug et al.; however it is written in an outdated language and did not provide the required extensibility and flexibility as the provided concise matlab code [232].

```
function phase = phase_mansuripur(mx, my, mz, Ms, p, dx, dy, dz)
% Get grid size (grid must be quadratic!)
[N,~,Nz] = size(mx);
% Normalize incident vector
p = p./norm(p);
% Prefactor
A_pre = 1.60217662E-19*1.2566E-6*Ms*dz/6.62607004E-34;

% 1D array of k-vectors
kkx = fftshift( (-N/2:N/2-1)./N ) ./ dx;
kky = fftshift( (-N/2:N/2-1)./N ) ./ dy;
% Get gridded data of k-vectors
[kx,ky] = meshgrid(kkx,kky);
% Calculate length of k-vectors on grid
k2 = kx.^2 + ky.^2;
k = sqrt(k2);
% Calculate unit vectors of k-vectors on grid
```

```
qx = kx ./ k;
qy = ky ./ k;

% Dot product p*z
pz = p(3);
% Dot product p*q (qz = 0)
pq = p(1) .* qx + p(2) .* qy;
% Calculate sine Argument + Denominator
x = pi * dz .* k .* (pq) ./ (pz);
% Finally calculate G_p
G_p = 1 ./ (pq.^2 + pz.^2) .* sin(x)./x;
G_p(x==0) = 1 ./ (pq(x==0).^2 + pz.^2);
% If p is normal to sample surface pq = 0, pz = 1, G_p -> 1
if abs(pz) == 1
G_p = ones(N,N);
end
% Set G_p(0) = 0, as it is not summed
G_p(1,1) = 0;

% Fourier transform magnetization
mxft = fft2(mx);
myft = fft2(my);
mzft = fft2(mz);

% p x Ft(m) <- Three component vector
pxFTmx = p(2)*mzft-p(3)*myft;
pxFTmy = p(3)*mxft-p(1)*mzft;
pxFTmz = p(1)*myft-p(2)*mxft;
% p x p x FT(m)
pxpxFTmx = p(2)*pxFTmz-p(3)*pxFTmy;
pxpxFTmy = p(3)*pxFTmx-p(1)*pxFTmz;
v = qy .* pxpxFTmx + (-qx) .* pxpxFTmy;

% Calculate the FT phase
phase = 1./k .* G_p .* v;
% Remove constant phase contribution (divergence in calculation)
phase(1,1) = 0;
% Transform back
phase =  -A_pre .* real(1i * (ifft2(phase));
```

References

1. Mühlbauer, S., Binz, B., Jonietz, F., Pfleiderer, C., Rosch, A., Neubauer, A., Georgii, R. & Böni, P. Skyrmion Lattice in a Chiral Magnet. *Science* **323,** 915 (2009).
2. Everschor-Sitte, K., Masell, J., Reeve, R. M. & Kläui, M. Perspective: Magnetic skyrmions–Overview of recent progress in an active research field. *J. Appl. Phys.* **124,** 240901 (2018).
3. Foster, D., Kind, C., Ackerman, P. J., Tai, J.-S. B., Dennis, M. R. & Smalyukh, I. I. Two-dimensional skyrmion bags in liquid crystals and ferromagnets. *Nat. Phys.* **15,** 655 (2019).
4. Shibata, K., Yu, X. Z., Hara, T., Morikawa, D., Kanazawa, N., Kimoto, K., Ishiwata, S., Matsui, Y. & Tokura, Y. Towards control of the size and helicity of skyrmions in helimagnetic alloys by spin-orbit coupling. *Nat. Nanotechnol.* **8,** 723 (2013).
5. Meier, T. N. G. *Static and dynamic properties of chiral magnetic textures in systems with broken inversion symmetry*. PhD thesis (Universität Regensburg, 2018).
6. Schulz, T., Ritz, R., Bauer, A., Halder, M., Wagner, M., Franz, C., Pfleiderer, C., Everschor, K., Garst, M. & Rosch, A. Emergent electrodynamics of skyrmions in a chiral magnet. *Nat. Phys.* **8,** 301 (2012).
7. Schütte, C. & Garst, M. Magnon-skyrmion scattering in chiral magnets. *Phys. Rev. B* **90,** 094423 (2014).
8. Schroeter, S. & Garst, M. Scattering of high-energy magnons off a magnetic skyrmion. *Low Temp. Phys.* **41,** 817 (2015).
9. Jonietz, F., Mühlbauer, S., Pfleiderer, C., Neubauer, A., Münzer, W., Bauer, A., Adams, T., Georgii, R., Böni, P., Duine, R. A., Everschor, K., Garst, M. & Rosch, A. Spin Transfer Torques in MnSi at Ultralow Current Densities. *Science* **330,** 1648 (2010).
10. Caretta, L., Mann, M., Büttner, F., Ueda, K., Pfau, B., Günther, C. M., Hessing, P., Churikova, A., Klose, C., Schneider, M., Engel, D., Marcus, C., Bono, D., Bagschik, K., Eisebitt, S. & Beach, G. S. D. Fast current-driven domain walls and small skyrmions in a compensated ferrimagnet. *Nat. Nanotechnol.* **13,** 1154 (2018).
11. Tomasello, R., Martinez, E., Zivieri, R., Torres, L., Carpentieri, M. & Finocchio, G. A strategy for the design of skyrmion racetrack memories. *Sci. Rep.* **4,** 6784 (2014).
12. Müller, J. Magnetic skyrmions on a two-lane racetrack. *New J. Phys.* **19,** 025002 (2017).
13. Sampaio, J., Cros, V., Rohart, S., Thiaville, A. & Fert, A. Nucleation, stability and current-induced motion of isolated magnetic skyrmions in nanostructures. *Nat. Nanotechnol.* **8,** 839 (2013).

14. Fert, A., Cros, V. & Sampaio, J. Skyrmions on the track. *Nat. Nanotechnol.* **8,** 152 (2013).

15. Yu, G., Upadhyaya, P., Shao, Q., Wu, H., Yin, G., Li, X., He, C., Jiang, W., Han, X., Amiri, P. K. & Wang, K. L. Room-Temperature Skyrmion Shift Device for Memory Application. *Nano Lett.* **17,** 261 (2017).

16. Zhang, S., Wang, J., Zheng, Q., Zhu, Q., Liu, X., Chen, S., Jin, C., Liu, Q., Jia, C. & Xue, D. Current-induced magnetic skyrmions oscillator. *New J. Phys.* **17,** 023061 (2015).

17. Xing, X., Pong, P. W. T. & Zhou, Y. Skyrmion domain wall collision and domain wall-gated skyrmion logic. *Phys. Rev. B* **94,** 054408 (2016).

18. Luo, S., Song, M., Li, X., Zhang, Y., Hong, J., Yang, X., Zou, X., Xu, N. & You, L. Reconfigurable Skyrmion Logic Gates. *Nano Lett.* **18,** 1180 (2018).

19. Garcia-Sanchez, F., Sampaio, J., Reyren, N., Cros, V. & Kim, J.-V. A skyrmion-based spin-torque nano-oscillator. *New J. Phys.* **18,** 075011 (2016).

20. Zhang, X., Zhou, Y., Ezawa, M., Zhao, G. P. & Zhao, W. Magnetic skyrmion transistor: skyrmion motion in a voltage-gated nanotrack. *Sci. Rep.* **5,** 11369 (2015).

21. Woo, S., Litzius, K., Krüger, B., Im, M.-Y., Caretta, L., Richter, K., Mann, M., Krone, A., Reeve, R. M., Weigand, M., Agrawal, P., Lemesh, I., Mawass, M.-A., Fischer, P., Kläui, M. & Beach, G. S. D. Observation of room-temperature magnetic skyrmions and their current-driven dynamics in ultrathin metallic ferromagnets. *Nat. Mater.* **15,** 501 (2016).

22. Nayak, A. K., Kumar, V., Ma, T., Werner, P., Pippel, E., Sahoo, R., Damay, F., Rößler, U. K., Felser, C. & Parkin, S. S. P. Magnetic antiskyrmions above room temperature in tetragonal Heusler materials. *Nature* **548,** 561 (2017).

23. Gilbert, D. A., Maranville, B. B., Balk, A. L., Kirby, B. J., Fischer, P., Pierce, D. T., Unguris, J., Borchers, J. A. & Liu, K. Realization of ground-state artificial skyrmion lattices at room temperature. *Nat. Commun.* **6,** 8462 (2015).

24. Tokunaga, Y., Yu, X. Z., White, J. S., Rønnow, H. M., Morikawa, D., Taguchi, Y. & Tokura, Y. A new class of chiral materials hosting magnetic skyrmions beyond room temperature. *Nat. Commun.* **6,** 7638 (2015).

25. Moreau-Luchaire, C., Moutafis, C., Reyren, N., Sampaio, J., Vaz, C. A. F., Van Horne, N., Bouzehouane, K., Garcia, K., Deranlot, C., Warnicke, P., Wohlhüter, P., George, J.-M., Weigand, M., Raabe, J., Cros, V. & Fert, A. Additive interfacial chiral interaction in multilayers for stabilization of small individual skyrmions at room temperature. *Nat. Nanotechnol.* **11,** 444 (2016).

26. Zheng, F., Rybakov, F. N., Borisov, A. B., Song, D., Wang, S., Li, Z.-A., Du, H., Kiselev, N. S., Caron, J., Kovács, A., Tian, M., Zhang, Y., Blügel, S. & Dunin-Borkowski, R. E. Experimental observation of chiral magnetic bobbers in B20-type FeGe. *Nat. Nanotechnol.* **13,** 451 (2018).

27. Yu, X. Z., Tokunaga, Y., Kaneko, Y., Zhang, W. Z., Kimoto, K., Matsui, Y., Taguchi, Y. & Tokura, Y. Biskyrmion states and their current-driven motion in a layered manganite. *Nat. Commun.* **5,** 3198 (2014).

28. Zhang, S., Kronast, F., van der Laan, G. & Hesjedal, T. Real-Space Observation of Skyrmionium in a Ferromagnet-Magnetic Topological Insulator Heterostructure. *Nano Lett.* **18,** 1057 (2018).

29. Jena, J., Göbel, B., Ma, T., Kumar, V., Saha, R., Mertig, I., Felser, C. & Parkin, S. S. P. Elliptical Bloch skyrmion chiral twins in an antiskyrmion system. *Nat. Commun.* **11,** 1115 (2020).

30. Hagemeister, J., Romming, N., von Bergmann, K., Vedmedenko, E. Y. & Wiesendanger, R. Stability of single skyrmionic bits. *Nat. Commun.* **6,** 8455 (2015).

31. Wild, J., Meier, T. N. G., Pöllath, S., Kronseder, M., Bauer, A., Chacon, A., Halder, M., Schowalter, M., Rosenauer, A., Zweck, J., Müller, J., Rosch, A., Pfleiderer, C. & Back, C. H. Entropy-limited topological protection of skyrmions. *Sci. Adv.* **3,** e1701704 (2017).

32. Bessarab, P. F., Müller, G. P., Lobanov, I. S., Rybakov, F. N., Kiselev, N. S., Jónsson, H., Uzdin, V. M., Blügel, S., Bergqvist, L. & Delin, A. Lifetime of racetrack skyrmions. *Sci. Rep.* **8,** 3433 (2018).

33. Büttner, F., Lemesh, I. & Beach, G. S. D. Theory of isolated magnetic skyrmions: From fundamentals to room temperature applications. *Sci. Rep.* **8,** 4464 (2018).

34. Stosic, D., Mulkers, J., Van Waeyenberge, B., Ludermir, T. B. & Milošević, M. V. Paths to collapse for isolated skyrmions in few-monolayer ferromagnetic films. *Phys. Rev. B* **95,** 214418 (2017).

35. Flovik, V., Qaiumzadeh, A., Nandy, A. K., Heo, C. & Rasing, T. Generation of single skyrmions by picosecond magnetic field pulses. *Phys. Rev. B* **96,** 140411 (2017).

36. Romming, N., Hanneken, C., Menzel, M., Bickel, J. E., Wolter, B., von Bergmann, K., Kubetzka, A. & Wiesendanger, R. Writing and Deleting Single Magnetic Skyrmions. *Science* **341,** 636 (2013).

37. Je, S.-G., Vallobra, P., Srivastava, T., Rojas-Sánchez, J.-C., Pham, T. H., Hehn, M., Malinowski, G., Baraduc, C., Auffret, S., Gaudin, G., Mangin, S., Béa, H. & Boulle, O. Creation of Magnetic Skyrmion Bubble Lattices by Ultrafast Laser in Ultrathin Films. *Nano Lett.* **18,** 7362 (2018).

38. Legrand, W., Maccariello, D., Reyren, N., Garcia, K., Moutafis, C., Moreau-Luchaire, C., Collin, S., Bouzehouane, K., Cros, V. & Fert, A. Room-Temperature Current-Induced Generation and Motion of sub-100 nm Skyrmions. *Nano Lett.* **17,** 2703 (2017).

39. Koshibae, W. & Nagaosa, N. Creation of skyrmions and antiskyrmions by local heating. *Nat. Commun.* **5,** 5148 (2014).

40. Litzius, K., Leliaert, J., Bassirian, P., Rodrigues, D., Kromin, S., Lemesh, I., Zazvorka, J., Lee, K.-J., Mulkers, J., Kerber, N., Heinze, D., Keil, N., Reeve, R. M., Weigand, M., Van Waeyenberge, B., Schütz, G., Everschor-Sitte, K., Beach, G. S. D. & Kläui, M. The role of temperature and drive current in skyrmion dynamics. *Nat. Electron.* **3,** 30 (2020).

41. Woo, S., Song, K. M., Zhang, X., Zhou, Y., Ezawa, M., Liu, X., Finizio, S., Raabe, J., Lee, N. J., Kim, S.-I., Park, S.-Y., Kim, Y., Kim, J.-Y., Lee, D., Lee, O., Choi, J. W., Min, B.-C., Koo, H. C. & Chang, J. Current-driven dynamics and inhibition of the skyrmion Hall effect of ferrimagnetic skyrmions in GdFeCo films. *Nat. Commun.* **9,** 959 (2018).

42. Hayashi, M., Thomas, L., Moriya, R., Rettner, C. & Parkin, S. S. P. Current-Controlled Magnetic Domain-Wall Nanowire Shift Register. *Science* **320,** 209 (2008).

43. Zhang, S. L., Wang, W. W., Burn, D. M., Peng, H., Berger, H., Bauer, A., Pfleiderer, C., van der Laan, G. & Hesjedal, T. Manipulation of skyrmion motion by magnetic field gradients. *Nat. Commun.* **9,** 2115 (2018).

44. Mochizuki, M. Spin-Wave Modes and Their Intense Excitation Effects in Skyrmion Crystals. *Phys. Rev. Lett.* **108,** 017601 (2012).

45. Schwarze, T., Waizner, J., Garst, M., Bauer, A., Stasinopoulos, I., Berger, H., Pfleiderer, C. & Grundler, D. Universal helimagnon and skyrmion excitations in metallic, semiconducting and insulating chiral magnets. *Nat. Mater.* **14,** 478 (2015).

46. Garst, M., Waizner, J. & Grundler, D. Collective spin excitations of helices and magnetic skyrmions: review and perspectives of magnonics in non-centrosymmetric magnets. *J. Phys. D* **50,** 293002 (2017).

47. Onose, Y., Okamura, Y., Seki, S., Ishiwata, S. & Tokura, Y. Observation of Magnetic Excitations of Skyrmion Crystal in a Helimagnetic Insulator Cu_2OSeO_3. *Phys. Rev. Lett.* **109,** 037603 (2012).

48. Yu, X. Z., Onose, Y., Kanazawa, N., Park, J. H., Han, J. H., Matsui, Y., Nagaosa, N. & Tokura, Y. Real-space observation of a two-dimensional skyrmion crystal. *Nature* **465,** 901 (2010).

49. Langner, M. C., Roy, S., Mishra, S. K., Lee, J. C. T., Shi, X. W., Hossain, M. A., Chuang, Y.-D., Seki, S., Tokura, Y., Kevan, S. D. & Schoenlein, R. W. Coupled Skyrmion Sublattices in Cu_2OSeO_3. *Phys. Rev. Lett.* **112,** 167202 (2014).

50. Zhang, S. L., Bauer, A., Burn, D. M., Milde, P., Neuber, E., Eng, L. M., Berger, H., Pfleiderer, C., van der Laan, G. & Hesjedal, T. Multidomain Skyrmion Lattice State in Cu_2OSeO_3. *Nano Lett.* **16,** 3285 (2016).

51. Pöllath, S., Aqeel, A., Bauer, A., Luo, C., Ryll, H., Radu, F., Pfleiderer, C., Woltersdorf, G. & Back, C. H. Ferromagnetic Resonance with Magnetic Phase Selectivity by Means of Resonant Elastic X-Ray Scattering on a Chiral Magnet. *Phys. Rev. Lett.* **123,** 167201 (2019).

52. Seki, S., Yu, X. Z., Ishiwata, S. & Tokura, Y. Observation of Skyrmions in a Multiferroic Material. *Science* **336,** 198 (2012).

53. Bos, J.-W. G., Colin, C. V. & Palstra, T. T. M. Magnetoelectric coupling in the cubic ferrimagnet Cu_2OSeO_3. *Phys. Rev. B* **78,** 094416 (2008).

54. Adams, T., Chacón Roldán, A., Wagner, M., Bauer, A., Brandl, G., Pedersen, B., Berger, H., Lemmens, P. & Pfleiderer, C. Long-Wavelength Helimagnetic Order and Skyrmion Lattice Phase in Cu_2OSeO_3. *Phys. Rev. Lett.* **108,** 237204 (2012).

55. Heisenberg, W. Zur Theorie des Ferromagnetismus. *Zeitschrift für Physik* **49,** 619 (1928).

56. Blundell, S. *Magnetism in Condensed Matter* (Oxford University Press, 2001).

57. Coey, J. M. D. *Magnetism and Magnetic Materials* (Cambridge University Press, 2009).

58. Meier, T. N. G., Kronseder, M., Zimmermann, M. & Back, C. H. Quantification of thermal fluctuations in stripe domain patterns. *Phys. Rev. B* **93,** 064424 (2016).

59. Zimmermann, M. *Static and dynamic properties of hexagonally shaped magnetic nanotubes.* PhD thesis (Universität Regensburg, 2018).

60. Butenko, G. *Phenomenological theory of chiral states in magnets with Dzyaloshinskii-Moriya interactions.* PhD thesis (Technische Universität Dresden, 2013).

61. Moriya, T. Anisotropic Superexchange Interaction and Weak Ferromagnetism. *Phys. Rev.* **120,** 91 (1960).

62. Dzyaloshinsky, I. A thermodynamic theory of "weak" ferromagnetism of antiferromagnetics. *J. Phys. Chem. Solids* **4,** 241 (1958).

63. Münzer, W., Neubauer, A., Adams, T., Mühlbauer, S., Franz, C., Jonietz, F., Georgii, R., Böni, P., Pedersen, B., Schmidt, M., Rosch, A. & Pfleiderer, C. Skyrmion lattice in the doped semiconductor $Fe_{1-x}Co_xSi$. *Phys. Rev. B* **81,** 041203 (2010).

64. Yu, X. Z., Kanazawa, N., Onose, Y., Kimoto, K., Zhang, W. Z., Ishiwata, S., Matsui, Y. & Tokura, Y. Near room-temperature formation of a skyrmion crystal in thin-films of the helimagnet FeGe. *Nat. Mater.* **10,** 106 (2011).

65. Janson, O., Rousochatzakis, I., Tsirlin, A. A., Belesi, M., Leonov, A. A., Rößler, U. K., van den Brink, J. & Rosner, H. The quantum nature of skyrmions and half-skyrmions in Cu_2OSeO_3. *Nat. Commun.* **5,** 5376 (2014).

66. Meunier, G. & Bertaud, M. Constantes cristallographiques de $CuSe_2O_5$, $CuSeO_3$ et Cu_2SeO_4. *J. Appl. Cryst.* **9,** 364 (1976).

67. Lin, T., Liu, H., Pöllath, S., Zhang, Y., Ji, B., Lei, N., Yun, J. J., Xi, L., Yang, D. Z., Xing, T., Wang, Z. L., Sun, L., Wu, Y. Z., Yin, L. F., Wang, W. B., Shen, J., Zweck, J., Back, C. H., Zhang, Y. G. & Zhao, W. S. Observation of room-temperature magnetic skyrmions in Pt/Co/W structures with a large spin-orbit coupling. *Phys. Rev. B* **98,** 174425 (2018).

68. Wang, L., Liu, C., Mehmood, N., Han, G., Wang, Y., Xu, X., Feng, C., Hou, Z., Peng, Y., Gao, X. & Yu, G. Construction of a Room-Temperature Pt/Co/Ta Multilayer Film with Ultrahigh-Density Skyrmions for Memory Application. *ACS Appl. Mater. Interfaces* **11,** 12098 (2019).

69. McVitie, S., Hughes, S., Fallon, K., McFadzean, S., McGrouther, D., Krajnak, M., Legrand, W., Maccariello, D., Collin, S., Garcia, K., Reyren, N., Cros, V., Fert, A., Zeissler, K. & Marrows, C. H. A transmission electron microscope study of Néel skyrmion magnetic textures in multilayer thin film systems with large interfacial chiral interaction. *Sci. Rep.* **8,** 5703 (2018).

70. Uchida, M., Onose, Y., Matsui, Y. & Tokura, Y. Real-Space Observation of Helical Spin Order. *Science* **311,** 359 (2006).

71. Bauer, A., Garst, M. & Pfleiderer, C. History dependence of the magnetic properties of single-crystal $\mathrm{Fe}_{1-x}\mathrm{Co}_x\mathrm{Si}$. *Phys. Rev. B* **93,** 235144 (2016).

72. Beille, J., Voiron, J. & Roth, M. Long period helimagnetism in the cubic B20 $\mathrm{Fe}_x\mathrm{Co}_{1-x}\mathrm{Si}$ and $\mathrm{Co}_x\mathrm{Mn}_{1-x}\mathrm{Si}$ alloys. *Solid State Commun.* **47,** 399 (1983).

73. Rajeswari, J., Huang, P., Mancini, G. F., Murooka, Y., Latychevskaia, T., McGrouther, D., Cantoni, M., Baldini, E., White, J. S., Magrez, A., Giamarchi, T., Rønnow, H. M. & Carbone, F. Filming the formation and fluctuation of skyrmion domains by cryo-Lorentz transmission electron microscopy. *Proc. Natl. Acad. Sci. U.S.A.* **112,** 14212 (2015).

74. Kézsmárki, I., Bordács, S., Milde, P., Neuber, E., Eng, L. M., White, J. S., Rønnow, H. M., Dewhurst, C. D., Mochizuki, M., Yanai, K., Nakamura, H., Ehlers, D., Tsurkan, V. & Loidl, A. Néel-type skyrmion lattice with confined orientation in the polar magnetic semiconductor $\mathrm{GaV}_4\mathrm{S}_8$. *Nat. Mater.* **14,** 1116 (2015).

75. Wilson, M. N., Butenko, A. B., Bogdanov, A. N. & Monchesky, T. L. Chiral skyrmions in cubic helimagnet films: The role of uniaxial anisotropy. *Phys. Rev. B* **89,** 094411 (2014).

76. Bauer, A., Chacon, A., Wagner, M., Halder, M., Georgii, R., Rosch, A., Pfleiderer, C. & Garst, M. Symmetry breaking, slow relaxation dynamics, and topological defects at the field-induced helix reorientation in MnSi. *Phys. Rev. B* **95,** 024429 (2017).

77. Everschor, K. *Current-Induced Dynamics of Chiral Magnetic Structures.* PhD thesis (Universität zu Köln, 2012).

78. Nagaosa, N. & Tokura, Y. Topological properties and dynamics of magnetic skyrmions. *Nat. Nanotechnol.* **8,** 899 (2013).

79. Feldtkeller, E. & Thomas, H. Struktur und Energie von Blochlinien in dünnen ferromagnetischen Schichten. *Physik der kondensierten Materie* **4,** 8 (1965).

80. Shinjo, T., Okuno, T., Hassdorf, R., Shigeto, K. & Ono, T. Magnetic Vortex Core Observation in Circular Dots of Permalloy. *Science* **289,** 930 (2000).

81. Milde, P., Köhler, D., Seidel, J., Eng, L. M., Bauer, A., Chacon, A., Kindervater, J., Mühlbauer, S., Pfleiderer, C., Buhrandt, S., Schütte, C. & Rosch, A. Unwinding of a Skyrmion Lattice by Magnetic Monopoles. *Science* **340,** 1076 (2013).

82. Zhang, S. L., van der Laan, G. & Hesjedal, T. Direct experimental determination of the topological winding number of skyrmions in $\mathrm{Cu}_2\mathrm{OSeO}_3$. *Nat. Commun.* **8,** 14619 (2017).

83. Pfleiderer, C. Surfaces get hairy. *Nat. Phys.* **7,** 673 (2011).

84. Neubauer, A., Pfleiderer, C., Binz, B., Rosch, A., Ritz, R., Niklowitz, P. G. & Böni, P. Topological Hall Effect in the A Phase of MnSi. *Phys. Rev. Lett.* **102,** 186602 (2009).

85. Meynell, S. A., Wilson, M. N., Loudon, J. C., Spitzig, A., Rybakov, F. N., Johnson, M. B. & Monchesky, T. L. Hall effect and transmission electron microscopy of epitaxial MnSi thin films. *Phys. Rev. B* **90,** 224419 (2014).

86. Everschor, K., Garst, M., Binz, B., Jonietz, F., Mühlbauer, S., Pfleiderer, C. & Rosch, A. Rotating skyrmion lattices by spin torques and field or temperature gradients. *Phys. Rev. B* **86,** 054432 (2012).

87. Jiang, W., Zhang, X., Yu, G., Zhang, W., Wang, X., Benjamin Jungfleisch, M., Pearson, J. E., Cheng, X., Heinonen, O., Wang, K. L., Zhou, Y., Hoffmann, A. & te Velthuis, S. G. E. Direct observation of the skyrmion Hall effect. *Nat. Phys.* **13,** 162 (2017).

88. Pöllath, S., Wild, J., Heinen, L., Meier, T. N. G., Kronseder, M., Tutsch, L., Bauer, A., Berger, H., Pfleiderer, C., Zweck, J., Rosch, A. & Back, C. H. Dynamical Defects in Rotating Magnetic Skyrmion Lattices. *Phys. Rev. Lett.* **118,** 207205 (2017).

89. Parkin, S. S. P., Hayashi, M. & Thomas, L. Magnetic Domain-Wall Racetrack Memory. *Science* **320,** 190 (2008).

90. Schryer, N. L. & Walker, L. R. The motion of 180° domain walls in uniform dc magnetic fields. *J. Appl. Phys.* **45,** 5406 (1974).

91. Karube, K., White, J. S., Reynolds, N., Gavilano, J. L., Oike, H., Kikkawa, A., Kagawa, F., Tokunaga, Y., Rønnow, H. M., Tokura, Y. & Taguchi, Y. Robust metastable skyrmions and their triangular-square lattice structural transition in a high-temperature chiral magnet. *Nat. Mater.* **15,** 1237 (2016).

92. Ishikawa, Y. & Arai, M. Magnetic Phase Diagram of MnSi near Critical Temperature Studied by Neutron Small Angle Scattering. *J. Phys. Soc. Jpn.* **53,** 2726 (1984).

93. Buhrandt, S. & Fritz, L. Skyrmion lattice phase in three-dimensional chiral magnets from Monte Carlo simulations. *Phys. Rev. B* **88,** 195137 (2013).

94. Wilhelm, H., Baenitz, M., Schmidt, M., Rößler, U. K., Leonov, A. A. & Bogdanov, A. N. Precursor Phenomena at the Magnetic Ordering of the Cubic Helimagnet FeGe. *Phys. Rev. Lett.* **107,** 127203 (2011).

95. Rybakov, F. N., Borisov, A. B., Blügel, S. & Kiselev, N. S. New Type of Stable Particlelike States in Chiral Magnets. *Phys. Rev. Lett.* **115,** 117201 (2015).

96. Yi, S. D., Onoda, S., Nagaosa, N. & Han, J. H. Skyrmions and anomalous Hall effect in a Dzyaloshinskii-Moriya spiral magnet. *Phys. Rev. B* **80,** 054416 (2009).

97. Pöllath, S. *Dynamic defects and grain boundaries in the skyrmion lattice of* Cu_2OSeO_3. MA thesis (Universität Regensburg, 2016).

98. Ishizuka, H. & Nagaosa, N. Spin chirality induced skew scattering and anomalous Hall effect in chiral magnets. *Sci. Adv.* **4,** eaap9962 (2018).

99. Litzius, K., Lemesh, I., Krüger, B., Bassirian, P., Caretta, L., Richter, K., Büttner, F., Sato, K., Tretiakov, O. A., Förster, J., Reeve, R. M., Weigand, M., Bykova, I., Stoll, H., Schütz, G., Beach, G. S. D. & Kläui, M. Skyrmion Hall effect revealed by direct time-resolved X-ray microscopy. *Nat. Phys.* **13,** 170 (2017).

100. Jiang, W., Zhang, S., Wang, X., Phatak, C., Wang, Q., Zhang, W., Jungfleisch, M. B., Pearson, J. E., Liu, Y., Zang, J., Cheng, X., Petford-Long, A., Hoffmann, A. & te Velthuis, S. G. E. Quantifying chiral exchange interaction for Néel-type skyrmions via Lorentz transmission electron microscopy. *Phys. Rev. B* **99,** 104402 (10 2019).

101. Schäfer, A. H. Ř. *Magnetic Domains: The Analysis of Magnetic Microstructures* (Springer-Verlag Berlin Heidelberg, 2009).

102. Saratz, N. A. *Inverse symmetry breaking in low-dimensional systems.* PhD thesis (ETH Zürich, 2009).

103. Saratz, N., Lichtenberger, A., Portmann, O., Ramsperger, U., Vindigni, A. & Pescia, D. Experimental Phase Diagram of Perpendicularly Magnetized Ultrathin Ferromagnetic Films. *Phys. Rev. Lett.* **104,** 077203 (2010).

104. Wong, C. K. & Wong, C. K. in *Algorithmic Studies in Mass Storage Systems* 225–406 (Springer Berlin Heidelberg, Berlin, Heidelberg, 1983).

105. Abanov, A., Kalatsky, V., Pokrovsky, V. L. & Saslow, W. M. Phase diagram of ultrathin ferromagnetic films with perpendicular anisotropy. *Phys. Rev. B* **51,** 1023 (1995).

106. Baltz, V., Marty, A., Rodmacq, B. & Dieny, B. Magnetic domain replication in interacting bilayers with out-of-plane anisotropy: Application to CoPt multilayers. *Phys. Rev. B* **75,** 014406 (2007).

107. Andelman, D. & Rosensweig, R. E. Modulated Phases: Review and Recent Results. *J. Phys. Chem. B* **113,** 3785 (2009).

108. Bernand-Mantel, A., Camosi, L., Wartelle, A., Rougemaille, N., Darques, M. & Ranno, L. The skyrmion-bubble transition in a ferromagnetic thin film. *SciPost Phys.* **4,** 027 (2018).

109. Bogatyrëv, A. B. & Metlov, K. L. What makes magnetic skyrmions different from magnetic bubbles? *J. Magn. Magn. Mater.* **465,** 743 (2018).

110. Büttner, F. *Topological mass of magnetic Skyrmions probed by ultrafast dynamic imaging.* PhD thesis (Johannes Gutenberg-Universität Mainz, 2013).

111. Heinrich, B. & Cochran, J. F. Ultrathin metallic magnetic films: magnetic anisotropies and exchange interactions. *Adv. Phys.* **42,** 523 (1993).

112. Landau, L. D. & Lifshitz, E. On the theory of the dispersion of magnetic permeability in ferromagnetic bodies. *Phys. Z. Sowjetunion* **8,** 101 (1935).

113. Gilbert, T. L. *Formulation, foundations and applications of the phenomenological theory of ferromagnetism.* PhD thesis (Graduate School of Illinois Institute of Technology, 1956).

114. Mayergoyz, I., Bertotti, G. & Serpico, C. *Nonlinear Magnetization Dynamics in Nanosystems* (Elsevier, 2009).

115. Süli, E. *An introduction to numerical analysis* (Cambridge Univ. Press, 2007).

116. Vansteenkiste, A., Leliaert, J., Dvornik, M., Helsen, M., Garcia-Sanchez, F. & Van Waeyenberge, B. The design and verification of MuMax3. *AIP Advances* **4,** 107133 (2014).

117. Chacon, A., Heinen, L., Halder, M., Bauer, A., Simeth, W., Mühlbauer, S., Berger, H., Garst, M., Rosch, A. & Pfleiderer, C. Observation of two independent skyrmion phases in a chiral magnetic material. *Nat. Phys.* **14,** 936 (2018).

118. Halder, M., Chacon, A., Bauer, A., Simeth, W., Mühlbauer, S., Berger, H., Heinen, L., Garst, M., Rosch, A. & Pfleiderer, C. Thermodynamic evidence of a second skyrmion lattice phase and tilted conical phase in Cu_2OSeO_3. *Phys. Rev. B* **98,** 144429 (2018).

119. Qian, F., Bannenberg, L. J., Wilhelm, H., Chaboussant, G., Debeer-Schmitt, L. M., Schmidt, M. P., Aqeel, A., Palstra, T. T. M., Brück, E., Lefering, A. J. E., Pappas, C., Mostovoy, M. & Leonov, A. O. New magnetic phase of the chiral skyrmion material Cu_2OSeO_3. *Sci. Adv.* **4,** eaat7323 (2018).

120. Chen, C. T., Idzerda, Y. U., Lin, H.-J., Smith, N. V., Meigs, G., Chaban, E., Ho, G. H., Pellegrin, E. & Sette, F. Experimental Confirmation of the X-Ray Magnetic Circular Dichroism Sum Rules for Iron and Cobalt. *Phys. Rev. Lett.* **75,** 152 (1995).

121. Van der Laan, G. Soft X-ray resonant magnetic scattering of magnetic nanostructures. *Comptes Rendus Physique* **9,** 570 (2008).

122. *Magnetism and Synchrotron Radiation* (eds Beaurepaire, E., Bulou, H., Scheurer, F. & Jean-Paul, K.) (Springer Berlin Heidelberg, 2010).

123. *Modern Techniques for Characterizing Magnetic Materials* (ed Zhu, Y.) (Springer-Verlag, 2005).

124. Noll, T. & Radu, F. *The Mechanics of the Vekmag Experiment.* in *Proceedings of the 9th Mechanical Engineering Design of Synchrotron Radiation Equipment and Instrumentation Conference (MEDSI2016)* Barcelona, Spain 2016 (JACoW, Geneva, Switzerland, 2017), 370.

125. Farle, M. Ferromagnetic resonance of ultrathin metallic layers. *Rep. Prog. Phys.* **61,** 755 (1998).

126. Hoffmann, F. *Magnetic Anisotropies of (Ga,Mn)As films and nanostructures.* PhD thesis (Universität Regensburg, 2010).

127. *Metrology and Diagnostic Techniques for Nanoelectronics* (eds Ma, Z. & Seilder, D.) (New York: Jenny Stanford Publishing, 2016).

128. Zhang, S. L., Bauer, A., Berger, H., Pfleiderer, C., van der Laan, G. & Hesjedal, T. Resonant elastic x-ray scattering from the skyrmion lattice in Cu_2OSeO_3. *Phys. Rev. B* **93,** 214420 (2016).

129. Zhang, S. L., Bauer, A., Berger, H., Pfleiderer, C., van der Laan, G. & Hesjedal, T. Imaging and manipulation of skyrmion lattice domains in Cu_2OSeO_3. *Appl. Phys. Lett.* **109,** 192406 (2016).

130. Zhang, S. L., van der Laan, G. & Hesjedal, T. Direct experimental determination of spiral spin structures via the dichroism extinction effect in resonant elastic soft x-ray scattering. *Phys. Rev. B* **96,** 094401 (2017).

131. Van der Laan, G., Thole, B. T., Sawatzky, G. A., Goedkoop, J. B., Fuggle, J. C., Esteva, J.-M., Karnatak, R., Remeika, J. P. & Dabkowska, H. A. Experimental proof of magnetic x-ray dichroism. *Phys. Rev. B* **34,** 6529 (1986).

132. Schütz, G., Wagner, W., Wilhelm, W., Kienle, P., Zeller, R., Frahm, R. & Materlik, G. Absorption of circularly polarized x rays in iron. *Phys. Rev. Lett.* **58,** 737 (1987).

133. Bearden, J. A. & Burr, A. F. Reevaluation of X-Ray Atomic Energy Levels. *Rev. Mod. Phys.* **39,** 125 (1967).

134. Templeton, D. H. & Templeton, L. K. Tetrahedral anisotropy of x-ray anomalous scattering. *Phys. Rev. B* **49,** 14850 (1994).

135. Müller, J., Rajeswari, J., Huang, P., Murooka, Y., Rønnow, H. M., Carbone, F. & Rosch, A. Magnetic Skyrmions and Skyrmion Clusters in the Helical Phase of Cu_2OSeO_3. *Phys. Rev. Lett.* **119,** 137201 (2017).

136. Okamura, Y., Kagawa, F., Seki, S. & Tokura, Y. Transition to and from the skyrmion lattice phase by electric fields in a magnetoelectric compound. *Nat. Commun.* **7,** 12669 (2016).

137. Bauer, A., Chacon, A., Halder, M. & Pfleiderer, C. in (eds Zang, J., Cros, V. & Hoffmann, A.) 151 (Springer, New York, 2018).

138. Seki, S., Okamura, Y., Shibata, K., Takagi, R., Khanh, N. D., Kagawa, F., Arima, T. & Tokura, Y. Stabilization of magnetic skyrmions by uniaxial tensile strain. *Phys. Rev. B* **96,** 220404 (2017).

139. Aqeel, A., Sahliger, J., Taniguchi, T., Mändl, S., Mettus, D., Berger, H., Bauer, A., Garst, M., Pfleiderer, C. & Back, C. H. Microwave spectroscopy of the low-temperature skyrmion state in Cu_2OSeO_3. *in review* (2020).

140. Stasinopoulos, I., Weichselbaumer, S., Bauer, A., Waizner, J., Berger, H., Maendl, S., Garst, M., Pfleiderer, C. & Grundler, D. Low spin wave damping in the insulating chiral magnet Cu_2OSeO_3. *Appl. Phys. Lett.* **111,** 032408 (2017).

141. Okamura, Y., Kagawa, F., Mochizuki, M., Kubota, M., Seki, S., Ishiwata, S., Kawasaki, M., Onose, Y. & Tokura, Y. Microwave magnetoelectric effect via skyrmion resonance modes in a helimagnetic multiferroic. *Nat. Commun.* **4,** 2391 (2013).

142. Miao, B. F., Wen, Y., Yan, M., Sun, L., Cao, R. X., Wu, D., You, B., Jiang, Z. S. & Ding, H. F. Micromagnetic study of excitation modes of an artificial skyrmion crystal. *Appl. Phys. Lett.* **107,** 222402 (2015).

143. Stasinopoulos, I., Weichselbaumer, S., Bauer, A., Waizner, J., Berger, H., Garst, M., Pfleiderer, C. & Grundler, D. Linearly polarized GHz magnetization dynamics of spin helix modes in the ferrimagnetic insulator Cu_2OSeO_3. *Sci. Rep.* **7,** 7037 (2017).

144. Versteeg, R. B., Vergara, I., Schäfer, S. D., Bischoff, D., Aqeel, A., Palstra, T. T. M., Grüninger, M. & van Loosdrecht, P. H. M. Optically probed symmetry breaking in the chiral magnet Cu_2OSeO_3. *Phys. Rev. B* **94,** 094409 (2016).

145. Bauer, H. G., Majchrak, P., Kachel, T., Back, C. H. & Woltersdorf, G. Nonlinear spin-wave excitations at low magnetic bias fields. *Nat. Commun.* **6,** 8274 (2015).

146. Woltersdorf, G. *Spin-pumping and two-magnon scattering in magnetic multilayers.* PhD thesis (Simon Fraser University, 2004).

147. Vonsovskii, S. V. *Ferromagnetic Resonance* (Pergamon Press, Oxford, 1966).

148. Härtinger, M. O. *Untersuchung magnetischer Materialien mit Methoden der Ferromagnetischen Resonanz.* PhD thesis (Universität Regensburg, 2016).

149. Zhang, S. L., van der Laan, G., Wang, W. W., Haghighirad, A. A. & Hesjedal, T. Direct Observation of Twisted Surface skyrmions in Bulk Crystals. *Phys. Rev. Lett.* **120,** 227202 (2018).

150. Legrand, W., Chauleau, J.-Y., Maccariello, D., Reyren, N., Collin, S., Bouzehouane, K., Jaouen, N., Cros, V. & Fert, A. Hybrid chiral domain walls and skyrmions in magnetic multilayers. *Sci. Adv.* **4,** eaat0415 (2018).

151. Ehlers, D., Stasinopoulos, I., Tsurkan, V., Krug von Nidda, H.-A., Fehér, T., Leonov, A., Kézsmárki, I., Grundler, D. & Loidl, A. Skyrmion dynamics under uniaxial anisotropy. *Phys. Rev. B* **94,** 014406 (2016).

152. Okamura, Y., Seki, S., Bordács, S., Butykai, Á., Tsurkan, V., Kézsmárki, I. & Tokura, Y. Microwave Directional Dichroism Resonant with Spin Excitations in the Polar Ferromagnet GaV_4S_8. *Phys. Rev. Lett.* **122,** 057202 (2019).

153. Takagi, R., Morikawa, D., Karube, K., Kanazawa, N., Shibata, K., Tatara, G., Tokunaga, Y., Arima, T., Taguchi, Y., Tokura, Y. & Seki, S. Spin-wave spectroscopy of the Dzyaloshinskii-Moriya interaction in room-temperature chiral magnets hosting skyrmions. *Phys. Rev. B* **95,** 220406 (2017).

154. Karube, K., White, J. S., Morikawa, D., Dewhurst, C. D., Cubitt, R., Kikkawa, A., Yu, X., Tokunaga, Y., Arima, T.-h., Rønnow, H. M., Tokura, Y. & Taguchi, Y. Disordered skyrmion phase stabilized by magnetic frustration in a chiral magnet. *Sci. Adv.* **4,** eaar7043 (2018).

155. Pöllath, S., Lin, T., Lei, N., Zhao, W., Zweck, J. & Back, C. H. Spin structure relation to phase contrast imaging of isolated magnetic Bloch and Néel skyrmions. *Ultramicroscopy* **212,** 112973 (2020).

156. Abbe, E. Beiträge zur Theorie des Mikroskops und der mikroskopischen Wahrnehmung. *Archiv für mikroskopische Anatomie* **9,** 413 (2009).

157. Hell, S. W. & Wichmann, J. Breaking the diffraction resolution limit by stimulated emission: stimulated-emission-depletion fluorescence microscopy. *Opt. Lett.* **19,** 780 (1994).

158. Klar, T. A. & Hell, S. W. Subdiffraction resolution in far-field fluorescence microscopy. *Opt. Lett.* **24,** 954 (1999).

159. Knoll, M. & Ruska, E. Das Elektronenmikroskop. *Z. Phys. A* **78,** 318 (1932).

160. Tillmann, K., Barthel, J. & Houben, L. FEI titan G3 50-300 PICO. *Journal of large-scale research facilities* **1** (2015).

161. Thomas, J. & Gemming, T. *Analytische Transmissionselektronenmikroskopie* (Springer-Verlag Wien, 2013).

162. Williams, D. B. & Carter, C. B. *Transmission Electron Microscopy* (Plenum Press, New York, 1996).

163. Reimer, L. & Kohl, H. *Transmission Electron Microscopy* (ed Rhodes, W. T.) (Springer Science+Business Media, 2008).

164. Marton, L. & Lachenbruch, S. H. Electron Optical Mapping of Electromagnetic Fields. *J. Appl. Phys.* **20,** 1171 (1949).

165. Marton, L. Electron Optical "Schlieren" Effect. *J. Appl. Phys.* **19,** 687 (1948).

166. Marton, L. Electron Optical Observation of Magnetic Fields. *J. Appl. Phys.* **19,** 863 (1948).

167. Zweck, J. Imaging of magnetic and electric fields by electron microscopy. *J. Phys. Condens. Matter* **28,** 403001 (2016).

168. Wohlleben, D. Diffraction Effects in Lorentz Microscopy. *J. Appl. Phys.* **38,** 3341 (1967).

169. Fuller, H. W. & Hale, M. E. Determination of Magnetization Distribution in Thin Films Using Electron Microscopy. *J. Appl. Phys.* **31,** 238 (1960).

170. Chapman, J. N. The investigation of magnetic domain structures in thin foils by electron microscopy. *J. Phys. D* **17,** 623 (1984).

171. Spence, C. H. J. *High-Resolution Electron Microscopy* (Oxford University Press, 2003).

172. Lichte, H. & Lehmann, M. Electron holography–basics and applications. *Rep. Prog. Phys.* **71,** 016102 (2007).

173. Mansuripur, M. Computation of electron diffraction patterns in Lorentz electron microscopy of thin magnetic films. *J. Appl. Phys.* **69,** 2455 (1991).

174. Zweck, J. & Bormans, B. The CM30 Lorentz lens. *Philips Electron Opt. Bull.* **132,** 1 (1992).

175. Wild, J. *Lorentz-Transmissionselektronenmikroskopie und Differentielle Phasenkontrastmikroskopie an magnetischen Skyrmionen.* PhD thesis (Universität Regensburg, 2017).

176. Dekkers, N. & de Lang, H. Differential Phase Contrast in a STEM. *Optik* **41,** 452 (1974).

177. Rose, H. Phase Contrast in Scanning Transmission Electron Microscopy. *Optik* **39,** 416 (1974).

178. Chapman, J. N., Batson, P. E., Waddell, E. M. & Ferrier, R. P. The direct determination of magnetic domain wall profiles by differential phase contrast electron microscopy. *Ultramicroscopy* **3,** 203 (1978).

179. Lohr, M., Schregle, R., Jetter, M., Wächter, C., Wunderer, T., Scholz, F. & Zweck, J. Differential phase contrast 2.0–Opening new "fields" for an established technique. *Ultramicroscopy* **117,** 7 (2012).

180. Bauer, B., Hubmann, J., Lohr, M., Reiger, E., Bougeard, D. & Zweck, J. Direct detection of spontaneous polarization in wurtzite GaAs nanowires. *Appl. Phys. Lett.* **104,** 211902 (2014).

181. Shibata, N., Findlay, S. D., Sasaki, H., Matsumoto, T., Sawada, H., Kohno, Y., Otomo, S., Minato, R. & Ikuhara, Y. Imaging of built-in electric field at a p-n junction by scanning transmission electron microscopy. *Sci. Rep.* **5,** 10040 (2015).

182. Lohr, M., Schregle, R., Jetter, M., Wächter, C., Müller-Caspary, K., Mehrtens, T., Rosenauer, A., Pietzonka, I., Strassburg, M. & Zweck, J. Quantitative measurements of internal electric fields with differential phase contrast microscopy on InGaN/GaN quantum well structures. *Phys. Status Solidi B* **253,** 140 (2015).

183. Müller, K., Krause, F. F., Béché, A., Schowalter, M., Galioit, V., Löffler, S., Verbeeck, J., Zweck, J., Schattschneider, P. & Rosenauer, A. Atomic electric fields revealed by a quantum mechanical approach to electron picodiffraction. *Nat. Commun.* **5,** 5653 (2014).

184. Shibata, N., Findlay, S. D., Kohno, Y., Sawada, H., Kondo, Y. & Ikuhara, Y. Differential phase-contrast microscopy at atomic resolution. *Nat. Phys.* **8,** 611 (2012).

185. Matsumoto, T., So, Y.-G., Kohno, Y., Sawada, H., Ikuhara, Y. & Shibata, N. Direct observation of $\Sigma 7$ domain boundary core structure in magnetic skyrmion lattice. *Sci. Adv.* **2,** e1501280 (2016).

186. Matsumoto, T., So, Y.-G., Kohno, Y., Sawada, H., Ishikawa, R., Ikuhara, Y. & Shibata, N. Jointed magnetic skyrmion lattices at a small-angle grain boundary directly visualized by advanced electron microscopy. *Sci. Rep.* **6,** 35880 (2016).

187. McGrouther, D., Lamb, R. J., Krajnak, M., McFadzean, S., McVitie, S., Stamps, R. L., Leonov, A. O., Bogdanov, A. N. & Togawa, Y. Internal structure of hexagonal skyrmion lattices in cubic helimagnets. *New J. Phys.* **18,** 095004 (2016).

188. Chapman, J. N., Morrison, G. R., Jakubovics, J. P. & Taylor, R. A. Determination of domain wall structures in thin foils of soft magnetic alloy. *J. Magn. Magn. Mater.* **49,** 277 (1985).

189. Schwarzhuber, F., Melzl, P., Pöllath, S. & Zweck, J. Introducing a non-pixelated and fast centre of mass detector for differential phase contrast microscopy. *Ultramicroscopy* **192,** 21 (2018).

190. Schwarzhuber, F., Melzl, P. & Zweck, J. On the achievable field sensitivity of a segmented annular detector for differential phase contrast measurements. *Ultramicroscopy* **177,** 97 (2017).

191. Zweck, J., Schwarzhuber, F., Wild, J. & Galioit, V. On detector linearity and precision of beam shift detection for quantitative differential phase contrast applications. *Ultramicroscopy* **168,** 53 (2016).

192. Chapman, J. N., McFadyen, I. R. & McVitie, S. Modified differential phase contrast Lorentz microscopy for improved imaging of magnetic structures. *IEEE Transactions on Magnetics* **26,** 1506 (1990).

193. Ishikawa, R., Findlay, S. D., Seki, T., Sánchez-Santolino, G., Kohno, Y., Ikuhara, Y. & Shibata, N. Direct electric field imaging of graphene defects. *Nat. Commun.* **9,** 3878 (2018).

194. Fang, S., Wen, Y., Allen, C. S., Ophus, C., Han, G. G. D., Kirkland, A. I., Kaxiras, E. & Warner, J. H. Atomic electrostatic maps of 1D channels in 2D semiconductors using 4D scanning transmission electron microscopy. *Nat. Commun.* **10,** 1127 (2019).

195. Tonomura, A., Yu, X., Yanagisawa, K., Matsuda, T., Onose, Y., Kanazawa, N., Park, H. S. & Tokura, Y. Real-Space Observation of Skyrmion Lattice in Helimagnet MnSi Thin Samples. *Nano Lett.* **12,** 1673 (2012).

196. Yu, X., DeGrave, J. P., Hara, Y., Hara, T., Jin, S. & Tokura, Y. Observation of the Magnetic Skyrmion Lattice in a MnSi Nanowire by Lorentz TEM. *Nano Lett.* **13,** 3755 (2013).

197. McVitie, S. & White, G. S. Imaging Amperian currents by Lorentz microscopy. *J. Phys. D* **37,** 280 (2003).

198. Fallon, K., McVitie, S., Legrand, W., Ajejas, F., Maccariello, D., Collin, S., Cros, V. & Reyren, N. Quantitative imaging of hybrid chiral spin textures in magnetic multilayer systems by Lorentz microscopy. *Phys. Rev. B* **100,** 214431 (2019).

199. Smith, D. O. & Harte, K. J. Noncoherent Switching in Permalloy Films. *J. Appl. Phys.* **33,** 1399 (1962).

200. Portier, X. & Petford-Long, A. K. The formation of 360° domain walls in magnetic tunnel junction elements. *Appl. Phys. Lett.* **76,** 754 (2000).

201. Jiang, W., Upadhyaya, P., Zhang, W., Yu, G., Jungfleisch, M. B., Fradin, F. Y., Pearson, J. E., Tserkovnyak, Y., Wang, K. L., Heinonen, O., te Velthuis, S. G. E. & Hoffmann, A. Blowing magnetic skyrmion bubbles. *Science* **349,** 283 (2015).

202. Heinze, S., von Bergmann, K., Menzel, M., Brede, J., Kubetzka, A., Wiesendanger, R., Bihlmayer, G. & Blügel, S. Spontaneous atomic-scale magnetic skyrmion lattice in two dimensions. *Nat. Phys.* **7,** 713 (2011).

203. Romming, N., Kubetzka, A., Hanneken, C., von Bergmann, K. & Wiesendanger, R. Field-Dependent Size and Shape of Single Magnetic Skyrmions. *Phys. Rev. Lett.* **114,** 177203 (2015).

204. Boulle, O., Vogel, J., Yang, H., Pizzini, S., de Souza Chaves, D., Locatelli, A., Menteş, T. O., Sala, A., Buda-Prejbeanu, L. D., Klein, O., Belmeguenai, M., Roussigné, Y., Stashkevich, A., Chérif, S. M., Aballe, L., Foerster, M., Chshiev, M., Auffret, S., Miron, I. M. & Gaudin, G. Room-temperature chiral magnetic skyrmions in ultrathin magnetic nanostructures. *Nat. Nanotechnol.* **11,** 449 (2016).

205. Beleggia, M., Fazzini, P. F. & Pozzi, G. A Fourier approach to fields and electron optical phase-shifts calculations. *Ultramicroscopy* **96,** 93 (2003).

206. Beleggia, M., Schofield, M. A., Zhu, Y., Malac, M., Liu, Z. & Freeman, M. Quantitative study of magnetic field distribution by electron holography and micromagnetic simulations. *Appl. Phys. Lett.* **83,** 1435 (2003).

207. Gabor, D. A New Microscopic Principle. *Nature* **161,** 777 (1948).

208. Lazić, I., Bosch, E. G. T. & Lazar, S. Phase contrast STEM for thin samples: Integrated differential phase contrast. *Ultramicroscopy* **160,** 265 (2016).

209. Walton, S. K., Zeissler, K., Branford, W. R. & Felton, S. MALTS: A tool to simulate Lorentz Transmission Electron Microscopy from micromagnetic simulations. *IEEE Trans. Magn.* **49,** 4795 (2013).

210. Pollard, S. D., Garlow, J. A., Yu, J., Wang, Z., Zhu, Y. & Yang, H. Observation of stable Néel skyrmions in cobalt/palladium multilayers with Lorentz transmission electron microscopy. *Nat. Commun.* **8,** 14761 (2017).

211. Rybakov, F. N., Borisov, A. B. & Bogdanov, A. N. Three-dimensional skyrmion states in thin films of cubic helimagnets. *Phys. Rev. B* **87,** 094424 (2013).

212. Beleggia, M., Schofield, M. A., Volkov, V. V. & Zhu, Y. On the transport of intensity technique for phase retrieval. *Ultramicroscopy* **102,** 37 (2004).

213. McVitie, S. & Cushley, M. Quantitative Fresnel Lorentz microscopy and the transport of intensity equation. *Ultramicroscopy* **106,** 423 (2006).

214. Yücelen, E., Lazić, I. & Bosch, E. G. T. Phase contrast scanning transmission electron microscopy imaging of light and heavy atoms at the limit of contrast and resolution. *Sci. Rep.* **8,** 2676 (2018).

215. Rose, H. *Geometrical Charged-Particle Optics* (ed Rhodes, W. T.) (Springer-Verlag Berlin Heidelberg, 2009).

216. Erni, R. *Aberration-Corrected Imaging in Transmission Electron Microscopy: An Introduction* (2010).

217. Lazić, I., Bosch, E. G. T. & Hawkes, P. W. in *Advances in Imaging and Electron Physics* 75–184 (Elsevier, 2017).

218. Kronseder, M. *Pattern evolution and fluctuations in a magnetic model system.* PhD thesis (Universität Regensburg, 2013).

219. Hunklinger, S. *Festkörperphysik* (Oldenbourg Wissenschaftsverlag GmbH, 2014).

220. Du, H., Zhao, X., Rybakov, F. N., Borisov, A. B., Wang, S., Tang, J., Jin, C., Wang, C., Wei, W., Kiselev, N. S., Zhang, Y., Che, R., Blügel, S. & Tian, M. Interaction of Individual Skyrmions in a Nanostructured Cubic Chiral Magnet. *Phys. Rev. Lett.* **120,** 197203 (2018).

221. Leonov, A. O., Monchesky, T. L., Loudon, J. C. & Bogdanov, A. N. Three-dimensional chiral skyrmions with attractive interparticle interactions. *J. Phys. Condens. Matter* **28,** 35LT01 (2016).

222. Schneider, S., Wolf, D., Stolt, M. J., Jin, S., Pohl, D., Rellinghaus, B., Schmidt, M., Büchner, B., Goennenwein, S. T. B., Nielsch, K. & Lubk, A. Induction Mapping of the 3D-Modulated Spin Texture of Skyrmions in Thin Helimagnets. *Phys. Rev. Lett.* **120,** 217201 (2018).

223. Kovács, A., Caron, J., Savchenko, A. S., Kiselev, N. S., Shibata, K., Li, Z.-A., Kanazawa, N., Tokura, Y., Blügel, S. & Dunin-Borkowski, R. E. Mapping the magnetization fine structure of a lattice of Bloch-type skyrmions in an FeGe thin film. *Appl. Phys. Lett.* **111,** 192410 (2017).

224. Weerasekera, I. A., Shah, S. I., Baxter, D. V. & Unruh, K. M. Structure and stability of sputter deposited beta-tungsten thin films. *Appl. Phys. Lett.* **64,** 3231 (1994).

225. Hao, Q., Chen, W. & Xiao, G. Beta (β) tungsten thin films: Structure, electron transport, and giant spin Hall effect. *Appl. Phys. Lett.* **106,** 182403 (2015).

226. Müller, J. & Rosch, A. Capturing of a magnetic skyrmion with a hole. *Phys. Rev. B* **91,** 054410 (2015).

227. Clarke, R. D. An application of the Poisson distribution. *Journal of the Institute of Actuaries* **72,** 481 (1946).

228. Richter, M. Band structure theory of magnetism in 3d-4f compounds. *J. Phys. D* **31,** 1017 (1998).

229. Hrabec, A., Sampaio, J., Belmeguenai, M., Gross, I., Weil, R., Chérif, S. M., Stashkevich, A., Jacques, V., Thiaville, A. & Rohart, S. Current-induced skyrmion generation and dynamics in symmetric bilayers. *Nat. Commun.* **8,** 15765 (2017).

230. Mochizuki, M., Yu, X. Z., Seki, S., Kanazawa, N., Koshibae, W., Zang, J., Mostovoy, M., Tokura, Y. & Nagaosa, N. Thermally driven ratchet motion of a skyrmion microcrystal and topological magnon Hall effect. *Nat. Mater.* **13,** 241 (2014).

231. Ehrenfest, P. Bemerkung über die angenäherte Gültigkeit der klassischen Mechanik innerhalb der Quantenmechanik. *Z. Phys. A* **45,** 455 (1927).

232. Haug, T., Otto, S., Schneider, M. & Zweck, J. Computer simulation of Lorentz electron micrographs of thin magnetic particles. *Ultramicroscopy* **96,** 201 (2003).

Back matter

B

B.1 List of publications

Publications with leading authorship

1. **Pöllath, S.**, Wild, J., Heinen, L., Meier, T. N. G., Kronseder, M., Tutsch, L., Bauer, A., Berger, H., Pfleiderer, C., Zweck, J., Rosch, A. & Back, C. H. Dynamical Defects in Rotating Magnetic Skyrmion Lattices. *Phys. Rev. Lett.* **118**, 207205, ***Editor's Suggestion*** (2017)

2. **Pöllath, S.**, Aqeel, A., Bauer, A., Luo, C., Ryll, H., Radu, F., Pfleiderer, C., Woltersdorf, G. & Back, C. H. Ferromagnetic Resonance with Magnetic Phase Selectivity by Means of Resonant Elastic X-Ray Scattering on a Chiral Magnet. *Phys. Rev. Lett.* **123**, 167201, ***Editor's Suggestion*** (2019)

3. **Pöllath, S.**, Lin, T., Lei, N., Zhao, W., Zweck, J. & Back, C. H. Spin structure relation to phase contrast imaging of isolated magnetic Bloch and Néel skyrmions. *Ultramicroscopy* **212**, 112973 (2020)

Publications with contributed authorship

4. Wild, J., Meier, T. N. G., **Pöllath, S.**, Kronseder, M., Bauer, A., Chacon, A., Halder, M., Schowalter, M., Rosenauer, A., Zweck, J., Müller, J., Rosch, A., Pfleiderer, C. & Back, C. H. Entropy-limited topological protection of skyrmions. *Sci. Adv.* **3**, e1701704 (2017)

5. Lin, T., Liu, H., **Pöllath, S.**, Zhang, Y., Ji, B., Lei, N., Yun, J. J., Xi, L., Yang, D. Z., Xing, T., Wang, Z. L., Sun, L., Wu, Y. Z., Yin, L. F., Wang, W. B., Shen, J., Zweck, J., Back, C. H., Zhang, Y. G. & Zhao, W. S. Observation of room-temperature magnetic skyrmions in Pt/Co/W structures with a large spin-orbit coupling. *Phys. Rev. B.* **98**, 174425 (2018)

6. Srichandan, S., Wimmer, S., **Pöllath, S.**, Kronseder, M., Ebert, H., Back, C. H. & Strunk, C. Magnon scattering in the transport coefficients of CoFe thin films. *Phys. Rev. B.* **98**, 020406 (2018)

7. Schwarzhuber, F., Melzl, P., **Pöllath, S.** & Zweck, J. Introducing a non-pixelated and fast centre of mass detector for differential phase contrast microscopy. *Ultramicroscopy* **192**, 21 (2018)

8. Sandl, S., Schwarzhuber, F., **Pöllath, S.**, Zweck, J. & Jacobi von Wangelin, A. Olefin-Stabilized Cobalt Nanoparticles for C=C, C=O, and C=N Hydrogenations. *Chem. Eur. J.* **24**, 3403 (2018)

9. Jacobi von Wangelin, A., Gregori, B., Schwarzhuber, F., **Pöllath, S.**, Zweck, J., Fritsch, L., Schoch, R. & Bauer, M. Stereoselective Alkyne Hydrogenation by a Simple Iron Catalyst. *ChemSusChem.*, **12**, 3864 (2019)

10. Taylor, J. M., Lesne, E., Markou, A., Dejene, F. K., Sivakumar, P. K., **Pöllath, S.**, Rana K. G., Kumar N., Luo, C., Ryll, H., Radu F., Kronast, F., Werner, P., Back, C. H., Felser C. & Parkin S. S. P. Magnetic and electrical transport signatures of uncompensated moments in epitaxial thin films of the non-collinear antiferromagnet Mn_3Ir. *Appl. Phys. Lett.*, **115**, 062403 (2019)

11. Wangelin, A. J., Gregori, B. J., Nowakowski, M., Schoch, A., Bauer, M., Zweck, J. & **Pöllath, S.** Stereoselective Chromium-Catalyzed Semi-Hydrogenation of Alkynes. *ChemCatChem*, accepted, 10.1002/cctc.202000994 (2020)

Conference contributions

1. Pöllath, S., Luo, C., Schön, M., Radu, F., Ryll, H. & Back, C. H. Poster: Soft X-Ray Resonant Magnetic Scattering from the helical phase in Cu_2OSeO_3 at VEKMAG. *HZB User Meeting 2016*, Berlin, Germany (2016)

2. Pöllath, S., Luo, C., Schön, M., Radu, F., Ryll, H. & Back, C. H. Poster: Resonant Elastic X-ray Scattering (REXS) from the helical phase in Cu_2OSeO_3 at VEKMAG. *DPG Spring Meeting 2017*, Dresden, Germany (2017)

3. Pöllath, S., Wild, J., Heinen, L., Meier, T. N. G., Kronseder, M., Tutsch, L., Bauer, A., Berger, H., Pfleiderer, C., Zweck, J., Rosch, A. & Back, C. H. Talk: Time resolved Lorentz-TEM measurements of dynamical skyrmion lattice defects in Cu_2OSeO_3. *Microscopy Conference 2017*, Lausanne, Switzerland (2017)

4. S., Wild, J., Heinen, L., Meier, T. N. G., Kronseder, M., Tutsch, L., Bauer, A., Berger, H., Pfleiderer, C., Zweck, J., Rosch, A. & Back, C. H. Talk: Time resolved Lorentz-TEM measurements of dynamical skyrmion lattice defects in Cu_2OSeO_3. *DPG Spring Meeting 2018*, Berlin, Germany (2018)

5. Pöllath, S., Aqeel, A., Luo, C., Ryll, H., Radu, F. & Back, C. H., Poster: Resonant Soft X-Ray Scattering Ferromagnetic Resonance in the chiral magnet Cu_2OSeO_3. *DPG Spring Meeting 2018*, Berlin, Germany (2018)

6. Wild, J., Meier, T. N. G., Pöllath, S., Kronseder, M., Bauer, A., Chacon, A., Halder, M., Schowalter, M., Rosenauer, A., Zweck, J., Müller, J., Rosch, A., Pfleiderer, C. & Back, C. H. **Invited Talk:** Entropy limited topological protection of skyrmions in $Fe_{1-x}Co_xSi$. *SPIE 2018*, San Diego, USA (2018)

7. Pöllath, S., Wild, J., Meier, T. N. G., Kronseder, M., Bauer, A., Chacon, A., Halder, M., Schowalter, M., Rosenauer, A., Zweck, J., Müller, J., Rosch, A., Pfleiderer, C. & Back, C. H. Talk: Time resolved Lorentz-TEM measurements of topological skyrmion decay in $Fe_{0.5}Co_{0.5}Si$. *IMC19*, Sydney, Australien (2018)

8. Pöllath, S., Schwarzhuber, F., Wild, J., Bauer, B., Vogel, M., Back, C. H., Zweck J. Talk: Introduction to Differential Phase Contrast Microscopy. *DPC Workshop*, Regensburg, Germany, (2018)

9. Pöllath, S., Aqeel, A., Sahliger, J., Back, C. H., Woltersdorf G. & Zweck J. Poster: Manipulation of single skyrmions and skyrmion cluster with current, heat, microwaves and magnons. *Retreat-Meeting SPP2137*, München, Germany (2019)

10. Pöllath, S., Lin, T., Liu, H., Zhang, Y., Ji, B., Lei, N., Yun, J. J., Xi, L., Yang, D. Z., Xing, T., Wang, Z. L., Sun, L., Wu, Y. Z., Yin, L. F., Wang, W. B., Shen, J., Zweck, J., Back, C. H., Zhang, Y. G. & Zhao, W. S. Talk: LTEM and DPC measurements on room temperature magnetic skyrmions in Pt/Co/W multilayers. *DPG Spring Meeting 2019*, Regensburg, Germany (2019)

11. Pöllath, S. **Invited Talk:** Fresnel and DPC LTEM imaging of magnetic skyrmions. *StEM Workshop at Ringberg Castle*, Kreuth, Germany (2019)

12. Pöllath, S., Lin, T., Liu, H., Zhang, Y., Ji, B., Lei, N., Yun, J. J., Xi, L., Yang, D. Z., Xing, T., Wang, Z. L., Sun, L., Wu, Y. Z., Yin, L. F., Wang, W. B., Shen, J., Zweck, J., Back, C. H., Zhang, Y. G. & Zhao, W. S. **Best Poster award:** LTEM and DPC measurements on room temperature magnetic skyrmions in Pt/Co/W and Pt/Co/Tb multilayers. *MC2019*, Berlin, Germany (2019)

B.2 Acknowledgments

Last but not least I wanna thank all of the kind people who helped me so much during this thesis.

- **Prof. Dr. Joe Zweck**, die Physik Frohnatur, dem man auf einer nahbaren Ebene begegnen durfte, der beim Radeln noch über meine physikalischen Probleme grübelte und einfach eine einzigartige heimische Gruppenatmosphäre schuf. An dieser Stelle bin ich auch dankbar in einer von seinen unzähligen Geschichten Einzug zu halten und Jülich überlebt zu haben.
- **Prof. Dr. Christian Back**, der mir den Einstieg in die Promotion überhaupt erst ermöglichte und sich für mich einsetzte. Und auch während der Promotion immer interessiert, ermutigend und produktiv auf mich einwirkte und bei jeder Gelegenheit mich zu fördern an mich dachte. Vielen, vielen Dank.
- Dem restlichen Prüfungsausschuss bestehend aus **Prof. Dr. Dieter Weiss** und **Dr. Juan-Diego Urbina**.
- **Felix Schwarzhuber** Ein Bürokollege, der schnell zum Freund wurde, mit dem man über alles reden konnte und mit dem die Arbeit einfach um ein Vielfaches lustiger ablief.
- **Prof. Dr. Na Lei**, **Tao Lin** and **Yiming Sun** for the very pleasant cooperation on the multilayer room-temperature skyrmion samples. Maybe some day we can eat Weisswürst again!
- **Dr. Matthias Kronseder** Weil er mir so oft half und die Arbeit korrekturgelesen hat. Außerdem war er einfach die beste USA-Begleitung die man sich hätte wünschen können.
- **Dr. Florin Radu, Dr. Chen Luo** und **Dr. Hanjo Ryll** für ihre tolle Unterstützung bei den Messungen in Berlin.
- **Dr. Aisha Aqeel** for the preparation of the Cu_2OSeO_3 samples and her pleasant company at BESSY in Berlin. I still enjoy drinking from that secret mug!
- **Prof. Dieter Weiss** für das Benutzen des AURIGA SEM und des Wirebonders.
- Der **DFG**, die meine Stelle und meine Forschung unter dem Schwerpunktsprogramm SPP2137 Skyrmionics größtenteils finanzierte.

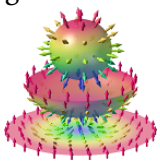

- **Dr. Hannes Wild, Elli, Peter, Julius, Franz und Tobi**, die einfach eine spitzen nette Gruppe waren.
- Meine ehemaligen Back'schen Bürokollegen: **Dr. Thomas NG Meier**, das Original, den man alles fragen konnte und der mir dann auch noch immer bereitwillig half. Und natürlich **Dr. Michael Zimmermann**, von dem man lernte, auch mal Fünfe grade sein zu lassen. Ich bin mir nicht sicher, ob ich jemals wieder so eine Büroatmosphäre haben werde.
- **Markus Hollnberger** für die immer nette und schnelle Hilfe entweder bei der Konstruktion eines neuen apparatus oder einer anderen Ingenieurstechnischen Frage meinerseits. Außerdem **Olga Ganitcheva** für so manche Probenpräparation.
- Allen anderen Lehrstuhlmitgliedern für die ganzen Feiern und die angenehme Atmosphäre.
- Den Sekretärinnen **Magdalena Pfleger** und **Doris Meier**, die mir immer so lieb geholfen haben, insbesondere am Anfang meiner Arbeit.
- **Dr. Kerstin Pöllath** für das Finden der letzten (?) Fehlerchen in der Arbeit.
- Meinen Eltern **Bernadette** und **Josef** und meiner Freundin **Aylin** für das lange Aushalten bis zur Beendigung dieser Arbeit.

> *If you happen to be looking at a magnetic material, then this can cause major problems for both you and the TEM and you might want to switch to studying aluminum.*
>
> **— D. B. Williams and C. B. Carter [162]**

FAKULTÄT FÜR PHYSIK
LEHRSTUHL FÜR MAGNETISMUS UND MAGNETOELEKTRONIK
INSTITUT FÜR EXPERIMENTELLE UND ANGEWANDTE PHYSIK
AG ZWECK ELEKTRONENMIKROSKOPIE